

UNIVERSIDADE DE LISBOA
FACULDADE DE CIÊNCIAS



**Ciências
ULisboa**

Is the Earth currently in a Global tidal maximum? 500 Ma of coupled tectonic and tidal modelling.

“ Documento Definitivo ”

Doutoramento em Geologia
Geodinâmica Interna

Hannah Sophia Davies

Tese orientada por:
João C. Duarte & J. A. Mattias Green

Documento especialmente elaborado para a obtenção do grau de doutor

UNIVERSIDADE DE LISBOA

FACULDADE DE CIÊNCIAS



**Ciências
ULisboa**

Is the Earth currently in a Global tidal maximum? 500 Ma of coupled tectonic and tidal modelling.

Doutoramento em Geologia

Geodinâmica Interna

Hannah Sophia Davies

Tese orientada por:

João C. Duarte & J. A. Mattias Green

Júri:

Presidente:

- Doutora Maria da Conceição Pombo de Freitas, Professora Catedrática e Presidente do Departamento de Geologia da Faculdade de Ciências da Universidade de Lisboa

Vogais:

- Doutor Ralph Dietmar Müller, Professor da Faculty of Science da University of Sydney (Austrália)
- Doutor Peter Anthony Allison, Professor da Faculty of Engineering do Imperial College London (Reino Unido)
- Doutor Rui Manuel Soares Dias, Professor Associado com Agregação da Escola de Ciências e Tecnologia da Universidade de Évora
- Doutor Pedro Manuel Alberto de Miranda, Professor Catedrático da Faculdade de Ciências da Universidade de Lisboa
- Doutor Rui Pires de Matos Taborda, Professor Associado com Agregação da Faculdade de Ciências da Universidade de Lisboa
- Doutor João Daniel Casal Duarte, Professor Auxiliar da Faculdade de Ciências da Universidade de Lisboa (Orientador)

Documento especialmente elaborado para a obtenção do grau de doutor

This research has been supported by the Fundação para a Ciência e a Tecnologia through grant no. UIDB/50019/2021 – Instituto Dom Luiz, grant no. IF/00702/2015, and PhD grant no. PD/BD/135068/2017.

Abstract

Earth's continents in the present day are the dispersed fragments of the former supercontinent Pangea which existed from 330 - 180 Ma. In around 200 - 250 Myr, following the progression of the current supercontinent cycle, the Earth's continents will reform into another supercontinent. The supercontinent cycle is closely linked to the Wilson cycle which describes the life cycle of oceans as they form, grow, shrink, and eventually close. As oceans grow and shrink with the Wilson cycle the tides within them are affected. The present day North Atlantic ocean, which formed as a result of the breakup of Pangea, is resonant with the M_2 tide, causing macrotidal (>4m) tidal amplitudes and strengthening the global M_2 tidal dissipation rate to 2.5 TW. Is this a unique occurrence in the present supercontinent cycle or is the tide periodically buoyed by resonance in ocean basins because of geometry changes brought about by the progression of the Wilson cycle? Here we will reconstruct predictions of the progression of the current supercontinent cycle into the future (+250 Ma) with GPlates which we will then use as a boundary condition for tidal modelling at 20 Myr intervals with OTIS (Oregon state Tidal Inversion Software). We present four unique scenarios of the Earth's future, each arguing a different style of supercontinent formation. In all scenarios of the future, we find that the Atlantic continues to widen over the next 25 Myrs, causing the tide within it to weaken as resonance is lost. However, we find several other occurrences of tidal resonance during the future scenarios, which causes tidal dissipation rates to increase to 70 – 250% of the present-day value. This periodic increase in tidal amplitudes and dissipation affects the evolution of the Earth-Moon system over geological time and has implications for ocean circulation, climate and the ocean's ability to host and support life in the past and future.

Keywords: Supercontinent Cycle, Wilson Cycle, Tectonic-tidal modelling, Tides, Tidal Resonance.

Resumo

Os continentes que observamos hoje na superfície da Terra são os fragmentos de um supercontinente que existiu há cerca de 300-200 milhões de anos atrás, a Pangeia. A ruptura deste supercontinente marcou o início de um novo ciclo dos supercontinentes em que os continentes, após um período de dormência, voltaram a separar-se. Estes ciclos ocorrem ao longo de períodos de cerca de 500 milhões de anos. Tendo em conta que a separação da Pangeia se iniciou há cerca de 180 milhões de anos, prevê-se que o próximo supercontinente ir-se-á formar daqui a cerca de 200-250 milhões de anos. O ciclo dos supercontinentes está intimamente ligado ao ciclo de Wilson, que descreve o ciclo de vida dos oceanos. Sempre que os supercontinentes se formam e se separam, terminam e iniciam-se novos ciclos de Wilson. Tanto o ciclo dos supercontinentes, como o ciclo de Wilson, são controlados pelo afundamento da litosfera oceânica no manto. À medida que as placas oceânicas envelhecem e arrefecem, tornam-se mais espessas e densas, e acabam por afundar no manto subjacente. O afundamento ocorre ao longo de zonas de subducção, arrastando consigo as placas e os continentes que nelas estão contidos. Este processo leva a que as placas oceânicas sejam recicladas, que os oceanos fechem e que os continentes acabem por voltar a colidir. O planeta atualmente não contém placas oceânicas com idades superiores a 200 milhões de anos, e pensa-se que esta é a idade máxima que uma placa oceânica pode atingir antes de começar a subductar.

Atualmente, o Oceano Pacífico é quase totalmente rodeado por zonas de subducção (o “Anel de Fogo” do Pacífico), levando vários autores a prever que este irá ser o próximo grande oceano a fechar, formando um novo supercontinente nos antípodas da Pangeia chamado Novopangeia. Um cenário alternativo considera que será o Oceano Atlântico a fechar, isto porque as placas oceânicas no Atlântico estão perto de atingir os 200 milhões de anos, e há evidências do início de formação e propagação de novas zonas de subducção no seu interior (nos arcos da Nova Escócia e das Pequenas Antilhas, e na Margem Sudoeste Ibérica). O alastramento destas zonas de subducção a todo o oceano poderá levar ao seu fecho e à consequente formação de um supercontinente a que se chamou Pangeia Ultima. Combinando a lógica dos cenários anteriores, é possível que ambos os oceanos fechem simultaneamente, reciclando totalmente as placas oceânicas do Atlântico e do Pacífico. Para tal é necessário que um novo grande oceano se desenvolva eventualmente a partir do Oceano Índico e fraturando a Eurásia. O supercontinente resultante deste cenário foi denominado Aurica. Embora a subducção das placas oceânicas seja a principal causa para o movimento das placas tectónicas, pensa-se que as cicatrizes deixadas

no manto pela Pangeia (e pelo oceano circundante Panthalassa) podem ter um efeito na forma e local de formação do próximo supercontinente. Segundo este cenário, os supercontinentes formam-se a 90° do supercontinente anterior, pelo que o próximo supercontinente se deverá formar junto ao polo Norte. O supercontinente resultante deste cenário foi denominado de Amásia.

O primeiro objetivo deste trabalho consistiu em reconstruir os quatro cenários, acima mencionados, propostos para a formação do próximo supercontinente, utilizando o software GPlates, de forma a obter uma melhor compreensão acerca da dinâmica do ciclo dos supercontinentes e dos ciclos de Wilson associados. Estudar estes ciclos a partir de um ponto de partida comum e conhecido (o Presente), permitiu-nos explorar de que forma estes ciclos funcionam e manipular os diferentes cenários. Começámos por construir um conjunto de modelos da Terra futura que fossem comparáveis e sobre os quais fosse possível modelar outras componentes do Sistema Terra, como as marés, circulação oceânica e o clima.

O segundo objetivo deste trabalho foi tentar compreender, no contexto dos ciclos dos supercontinentes e ciclos de Wilson, o como e porquê do Oceano Atlântico estar em ressonância com a maré M_2 . Esta ressonância leva a que as marés no Atlântico atinjam amplitudes superiores a 4 metros, com taxas de dissipação na ordem dos 2,5 TW, as mais altas dos últimos 250 milhões de anos. A questão que se levantou foi: se a maré atualmente é a mais energética desde a fractura da Pangeia, será que é a mais energética de todo o atual ciclo dos supercontinentes? Para resolver esta questão, utilizaram-se os quatro cenários tectónicos acima referidos como base para a modelação de marés utilizando o software OTIS (Oregon State University Tidal Inversion Software). Os resultados mostraram que em todos os cenários, à medida que o Oceano Atlântico continua a abrir, a energia dissipada pela maré irá diminuir (nos próximos 25 milhões de anos). No entanto, a partir deste ponto os cenários começam a divergir, sendo que nalguns cenários surgem novos períodos de ressonância. O cenário que leva à formação da Pangea Última (com fecho do Oceano Atlântico) é o que possui maior número de períodos de ressonância, com ambos os oceanos Atlântico e Pacífico a passarem por dois períodos de ressonância cada. No cenário “Aurica” os oceanos passam por três períodos de ressonância, ao passo que no cenário “Novopangea” apenas surge um. No cenário “Amasia” não ocorre nenhum período de ressonância. O aumento da energia dissipada difere entre os vários cenários, sendo que os picos podem variar entre 70 e 250% da energia dissipada no presente. Estes resultados demonstram que existe um ciclo de “super” marés associado ao ciclo dos supercontinentes, caracterizado

pelo aumento cíclico da energia dissipada pelas marés, devido às bacias oceânicas atingirem dimensões nas quais as marés sofrem processos de ressonância. Estes ciclos não estão, no entanto, perfeitamente sincronizados, sendo que cada ciclo dos supercontinentes pode conter, em média, entre um a três ciclos de supermarés. Esta dessincronização deve-se à relação complexa que existe entre os ciclos dos supercontinentes e os ciclos de Wilson.

Foram também desenvolvidos modelos de marés específicos para o Criogénico e o Arcaico. No Criogénico o sinal da maré apresentou uma redução drástica generalizada, devido às glaciações globais (“Terra Bola de Neve”) que ocorreram neste período. O enfraquecimento das marés durante os períodos de glaciação podem ter reduzido a mistura de água sob o gelo, permitindo a formação de uma camada de água doce e fria, isolando-o e prevenindo o degelo. Este efeito, embora reduzido, poderá ter produzido um feedback positivo que contribuiu para prolongar as glaciações. No Arcaico foram também identificados períodos de supermarés. O estudo referente a este período mostrou que as marés eram, em geral, 1.5 vezes mais energéticas que atualmente, em parte devido à Lua se encontrar mais próxima da Terra. Os resultados também mostram que terá havido períodos de ressonância, sendo que nesta fase da história do planeta, a tectónica de placas seria ainda muito primitiva e o ciclo dos supercontinentes poderia ainda não existir. Estas marés energéticas poderão ter tido um papel importante no aparecimento e evolução da vida.

Os resultados referentes à modelação de marés realizados no âmbito desta tese mostram que a Terra, durante a sua evolução, poderá ter passado por vários períodos de supermarés (cerca de 9% do total da sua idade). Estas supermarés podem estender-se por períodos de tempo na ordem dos 25 milhões de anos, e têm um papel importante na variação da velocidade de recessão da Lua, que aumenta sempre que a Terra passa por um período de supermarés.

Um outro objectivo desta tese foi tentar compreender o efeito do ciclo dos supercontinentes e das supermarés noutras componentes do Sistema Terra, como, por exemplo, a sua influência no clima. Neste âmbito, o clima dos supercontinentes Aurica e Amasia foi simulado com um General Circulation Model (GCM), o ROCKE-3D. Os resultados mostraram que os dois potenciais supercontinentes apresentam climas muito distintos. A Aurica seria um supercontinente equatorial com um clima quente e árido, ao passo que a Amásia teria um clima mais frio que o atual, com grandes áreas cobertas por gelo, devido à aglomeração dos continentes junto ao polo Norte.

Todos estes modelos ajudam-nos a compreender como o Sistema Terra funciona em longas

escalas de tempo e ao longo de períodos em que o planeta apresentava características significativamente diferentes das atuais. Isto permite, por exemplo, testar os diferentes estados pelos quais um planeta semelhante à Terra pode passar, o que nos pode ajudar a compreender os outros planetas do sistema solar e até mesmo os exoplanetas que estamos a começar a descobrir e observar.

Palavras-chave: ciclo dos supercontinentes, ciclo de Wilson, modelação tectónica-maré, marés, ressonância das marés.

Acknowledgements

This work would not have been possible without the support of many people.

First and foremost I would like to thank my supervisors João C. Duarte and J. A. Mattias Green for their support and advice. I am grateful to you both for the moral and intellectual support you were always happy to provide.

This work would not have been possible without support from Instituto Dom Luiz (IDL) and the Earthsystems doctoral school who among other things, provided me the financial support via the Fundação para a Ciência e a Tecnologia grant no. UIDB/50019/2021 – Instituto Dom Luiz, grant no. IF/00702/2015, and PhD grant no. PD/BD/135068/2017.

I would like to thank the University of Lisbon Faculty of Sciences and Geology Department for providing me with access to literature and IDL for providing me with an appropriate work space.

This PhD would not have been possible without the regular and attentive support of Pedro Miranda, Ricardo Trigo, João Cabral, Filipe Rosas, and Célia Lee who each provided regular encouragement, advice and support to this work.

I would like to acknowledge the support of the Supercomputing Wales project, which is part-funded by the European Regional Development Fund (ERDF) via Welsh Government.

I am fortunate to be part of the informal "deep-time tidal research group" made up of numerous members from many different countries, I thank each and every one of you for stimulating discussions.

I would like to extend a thanks to the Earthbyte team for their support and tutorials with the GPlates software.

I am also grateful to my colleagues and friends in the Earthsystems PhD group and department of geology: David Schlaphorst, Martin Wronna, Juan Pinzon, Jaime Almeida, and Inês Machado.

To the friends I made along the way, Claire Reed, João Santos, Xu Wang, you each helped me in your own way and so I thank you here for your support.

To my fiancée Mary Pacheco for help with coding, translating, spellchecking, as an infinitely patient ear to hear my ideas, and above all, your unwavering love and support.

Finally I would like to thank my family: my mother, Diane Davies, my father, Jonathan Davies, and my brother Alec Davies. Thank you for the support you have provided me with despite being so far away.

Contents

Abstract	I
Resumo	II
1 Introduction	1
1.1 Thesis structure	3
2 Background	4
2.1 Plate Tectonics	4
2.2 The origins of Plate Tectonics	8
2.2.1 Continental drift	8
2.2.2 Seafloor spreading	8
2.2.3 Plate boundaries	9
2.3 The Wilson cycle	10
2.4 The Supercontinent cycle	12
2.5 Modes of Supercontinent formation	14
2.6 Earth's interior	15
2.7 Tides	16
2.7.1 Half wavelength open ocean resonance	18
2.7.2 Tidal energy	19
2.7.3 Lunar recession and tidal friction	20
3 Methods	22
3.1 GPlates	22
3.2 Oregon State Tidal Inversion Software - OTIS	26
3.2.1 Using the GPlates kinematic model with OTIS	28
3.3 ROCKE3-D	29
3.3.1 Using the GPlates kinematic model with ROCKE-3D	30
4 Back to the future: Testing different scenarios for the next supercontinent gathering	32
4.1 Summary	32
4.2 Abstract	33

4.3	Introduction	34
4.4	Main concepts	35
4.4.1	Supercontinent Cycles and Wilson Cycles (modes of aggregation) . . .	35
4.4.2	How do oceans start to close? The problem of subduction initiation . .	36
4.4.3	Plate tectonics and mantle convection	38
4.5	Methodology	40
4.6	Back to the future	43
4.6.1	Introversion: Pangea Ultima	43
4.6.2	Extroversion: Novopangea	45
4.6.3	Combination: Aurica	48
4.6.4	Orthoversion: Amasia	50
4.6.5	Ocean Divergence and convergence rates	52
4.7	Discussion	53
5	Back to the future II: Tidal evolution of four supercontinent scenarios	56
5.1	Summary	56
5.2	Abstract	57
5.3	Introduction	58
5.4	Methods	59
5.4.1	Tidal Modelling	59
5.4.2	Mapping of the future tectonic scenarios	61
5.5	Results	62
5.5.1	Pangea Ultima	64
5.5.2	Novopangea	66
5.5.3	Aurica	67
5.5.4	Amasia	68
5.6	Discussion	69
6	Analysing the tidal state of a pre-Plate tectonic Earth during the Archean Eon (3.9 Ga)	72
6.1	Preface	72
6.2	Introduction	72
6.3	Methods	73

6.3.1	Mapping of the Archean conceptual scenarios	73
6.3.2	Tidal modelling	74
6.4	Results	75
6.5	Discussion	79
7	Co-authored papers	81
7.1	Is there a tectonically driven supertidal cycle?	81
7.1.1	Abstract	81
7.1.2	Summary	82
7.1.3	Results - Tidal Amplitudes	84
7.1.4	Results - Tidal Dissipation	86
7.1.5	My contribution	87
7.2	Weak tides during Cryogenian glaciations	88
7.2.1	Abstract	88
7.2.2	Summary	89
7.2.3	Results - Tidal Amplitudes	89
7.2.4	Results - Tidal Dissipation	90
7.2.5	My contribution	92
7.3	Deep Future Climate on Earth: effects of tectonics, rotation rate, and insolation	93
7.3.1	Abstract	93
7.3.2	Summary	94
7.3.3	My contribution	95
8	Discussion	97
8.1	Future work	106
	Appendix	125
	A1 Is there a tectonically driven supertidal cycle?	125
	A2 Weak tides during Cryogenian glaciations	135
	A3 The climates of Earth's next supercontinent: effects of tectonics, rotation rate, and insolation	143

List of Tables

2.1	Tidal constituents covered in this work	16
4.1	A complete list of all the supercontinents believed to have existed during the period of active plate tectonics on Earth up to the present-day and their modes of formation, along with the four scenarios of the formation of the next supercontinent.	41
4.2	Average velocities in cm yr^{-1} for each of the major continents in each scenario, and total average plate velocity for each of the scenarios	43
5.1	Summary of the number of super-tidal peaks for each scenario	69
5.2	Summary of the total time each scenario was in a super-tidal state.	69
6.1	Global average and standard deviation of the Archean ensemble maps' tidal dissipation (in TW) for the M_2 , S_2 , K_1 , and O_1 tidal constituents, along with the dissipation for Present day simulation with PD forcing and PD bathymetry.	76
6.2	Global average of the Archean ensemble maps' amplitude (in meters) for the M_2 , S_2 , K_1 , and O_1 tidal constituents, along with the amplitude for Present day simulation with PD forcing and PD bathymetry.	76

List of Figures

1.1	Global plate tectonic map illustrating the major tectonic plates and their boundaries and velocities (in cm yr^{-1}). Convergent boundaries are marked by black and grey segments with triangles, divergent boundaries are red and transform boundaries are green (Duarte and Schellart, 2016).	2
2.1	Figure 1 from Cawood et al. (2018) illustrating plate boundaries of the world. Note that the transform boundaries discussed by Wilson (1965) are referred to as "strike-slip" boundaries in this figure.	4
2.2	From Torsvik et al. (2014) a schematic of Earth's mantle from a southern polar perspective, the lower mantle is dominated by two antipodal large low shear wave velocity provinces (LLSVPs) beneath Africa (Tuzo) and the Pacific (Jason). They sit under two areas with a residual geoid (red dashed lines) and at their margins have zones of plume generation (PGZs) which are the principal source of large igneous provinces (LIPs).	6
2.3	A modified version of Figure 1 from Cawood (2020) illustrating the primary planetary geodynamic regimes and supercontinent cycles throughout Earth history.	6
2.4	From (Stern, 2016), possible geodynamic regimes for large silicate bodies with examples from our solar system.	7
2.5	A sketch of the Indian ocean (left) and East Pacific ocean (right) showing the mobile belts of the regions, thick dashes denoting ridges, solid lines for mountains and thin dashed lines for shears (transform faults) (Wilson, 1965).	9
2.6	From Wilson (1966) illustrating the North Atlantic region in lower Paleozoic time (~ 250 Ma) shaded regions are distinct faunal realms.	10
2.7	From Wilson et al. (2019) illustrating the life cycle of an ocean according to the Wilson cycle.	11
2.8	From Bradley (2011) timings of proposed supercontinents in Earth history. See Bradley (2011) for a full discussion.	13

2.9	From Pastor-Galán et al. (2019), three modes of supercontinent formation - a) Extroversion - Supercontinent formation through closure of an old external ocean b) Introversion - Supercontinent formation through closure of a new in- ternal ocean c) Orthoversion - Remnant subduction girdle left in the mantle from previous supercontinent forces the next supercontinent to form 90° away from the previous one, closing an old ocean.	14
2.10	Age area distribution of the ocean floor (Müller et al., 2008).	15
2.11	A schematic of the Earth's tidal bulges risen by the gravitation of the Moon and the centrifugal force of the Earth's orbit around the Lunar axis (http://www.oc.nps.edu/nom/day1/partc.html).	17
2.12	Tidal patterns of the Earth classified by amplitude and predominant type from (Pinet, 2008).	18
2.13	Figure 8-9 from McCully (2006a) illustrating harmonic resonance in guitar strings.	19
2.14	From Munk and Wunsch (1998), tidal and wind energy input to the oceans of Earth.	20
3.1	From https://data.nodc.noaa.gov/cgi-bin/iso?id=gov.noaa.ngdc.mgg.dem:316 , global relief map of the Earth.	22
3.2	Feature description of selected plate (here Africa is shown) on the GPlates work space.	23
3.3	A schematic illustration of the motion of an object from point A to point B along a great circle. In this illustration the great circle is the equator and the pole is the true North pole.	24
3.4	A screenshot of the GPlates work space while Africa is being manipulated. The “reconstruction pole” menu on the right-hand side of the image shows the calculates Euler pole for the manipulation being carried out (the solid continent would move to the position of the outline). If the "apply" button is pressed and the rotation file is loaded, the plate will assume this position from it's original position for the time displayed "300".	25
3.5	The GPlates workspace showing how to calibrate plate motions using raster images. The shape files are outlined in blue and the raster image is in black and white.	26

3.6	Grey-scale image of the Present day Earth once it is colour coded to be used as the boundary condition for the OTIS model.	29
4.1	GPlates set-up of present-day Earth used as the initial condition for each of the future scenarios. White lines represent mid-ocean ridges: Ma, Mid- Atlantic ridge; Swir, SW Indian Ridge; Cir, Central Indian ridge; Seir, SE Indian Ridge; Pa, Pacific- Antarctic spreading centre; Na, Nazca-Antarctic spreading center; Pn, Pacific-Nazca spreading center; Cn, Cocos-Nazca spreading centre; Pcs, Pacific-Cocos spreading center; Ar, Arctic Ridge. Black lines represent subduction zones: A, Aleutian trench; Ca, Central American trench; C, Cascadia subduction zone; H, Hikurangi trench; Im, Izu-Marianas trench; J, Japan trench; K, Kurile Trench; La, Lesser Antilles arc; M, Macquarie subduction zone; Nh, New Hebrides subduction zone; P, Philippine trench; R, Ryukyu subduction zone; Sa, Scotia arc; St, Sumatra trench. Brown dashed lines represent the extents of the LLSVPs discussed in (Torsvik et al., 2016), marked above as Tuzo and Jason. (For interpretation of the references to colour in this figure legend, the reader is referred to the web version of this article).	39
4.2	(a–d): A map of the development of Pangea Ultima, showing 50 Ma, 100 Ma, 200 Ma and 250 Ma. Speculative subduction zones and ridges are represented in red and white, respectively. Brown represents LLSVP extents as in (Torsvik et al., 2016). The centre point of the map is along the Greenwich meridian (0°). Eas, East American subduction zone; Ma, Mid-Atlantic ridge; E. Ant, East Antarctica; W. Ant, West Antarctica. (e): An illustration of the development of the supercontinent Pangea Ultima since the break-up of Pangaea. The major oceans of the Pacific, Atlantic, and Trans-Antarctic are presented. Other oceans and seas have been omitted (see figure 4.2 a–d). The oceans widths have been normalized between values of 0 and 10, representing the smallest and largest extent of each ocean.	41

4.3	(a–d): Maps of Novopangea from top left to bottom right 50 Ma, 100 Ma, 150 Ma and 200 Ma respectively. Speculative subduction zones and ridges are represented in red and white respectively. Yellow represents LLSVP extents as in Torsvik et al. (2016). The centre point of this map is along the international date line (180°). Ear, East African rift; Sp, Somalia plate; St, Sumatra trench; Ant, Antarctica; Eas, East American subduction zone; Ma, Mid Atlantic. (e): A graphical illustration of the development of the supercontinent of Novopangea. The major oceans of the Pacific, Atlantic and New African are presented. Other oceans and seas have been omitted (see Fig. 4.3a–d).	45
4.4	(a–d): Maps of Aurica from top left to bottom right 50 Ma, 100 Ma, 200 Ma and 250 Ma, respectively. Speculative subduction zones and ridges are represented in red and white, respectively. Yellow represents LLSVP extents as in Torsvik et al. (2016). The centre point of this map is along the international date line (180°). Par, Pan-Asian rift, Epr, East Pacific rise; Eas, East American subduction zone; Gs, Gibraltar subduction zone; Epas, East Pan-Asian subduction zone (e): A graphical illustration of the development of the supercontinent of Aurica. The major oceans of the Pacific, Atlantic and Pan-Asian are presented. Other oceans and seas have been omitted.	48
4.5	(a–d): Maps of Amasia from top left to bottom right 50 Ma, 100 Ma, 150 Ma and 200 Ma, respectively. Speculative subduction zones and ridges are represented in red and white, respectively. Yellow represents LLSVP extents as in Torsvik et al. (2016). The centre point of this map is along the Greenwich meridian (0°). Eas, East American subduction zone; Ma, Mid-Atlantic ridge; Zr, Zonal ridge; Cs, Circumferential Antarctic subduction zone (e): A graphical illustration of the development of the supercontinent of Amasia. The major oceans of the Pacific, Atlantic and Arctic are presented. Other oceans and seas have been omitted.	50
4.6	Divergence (positive) and Convergence (negative) rates in cm yr^{-1} for the Atlantic ocean (triangles), Pacific ocean (squares), Indian ocean (filled circles), Arctic ocean (empty circles), and new oceans (Trans-Antarctic – Pangea Ultima, East African - Novopangea, and Pan-Asia – Aurica)(Diamonds).	52

5.1	(a) The PD bathymetry in m. Panel (b) is the same as (a) but for the degenerate PD bathymetry (see text for details). (c–d) The simulated M_2 amplitudes (in m) for the control PD (c) and degenerate PD (d) bathymetries. Note that the colour scale saturates at 2 m. Panels (e–f) are the same as (c)–(d) but show M_2 dissipation rates in $W m^{-2}$	62
5.2	Global M_2 amplitudes for six representative time slices of the Pangaea Ultima scenario. The colour scale saturates at 2 m. For the full set of time slices covering every 20 Myr, see the Supplement. Additionally, note that the figures presented for each scenario display different time slices to highlight periods with interesting tidal signals and that the centre longitude varies between panels to ensure the supercontinent forms in the middle of each figure (where possible). 64	64
5.3	Normalized (against PD degenerate) globally integrated dissipation rates for the Pangaea Ultima (a), Novopangaea (b), Aurica (c), and Amasia (d) scenarios. The lines refer to total (solid line), deep (dashed line), and shelf (dotted–dashed line) integrated dissipation values. Each super-tidal peak is marked where it reaches its peak. Pac stands for Pacific and Atl stands for Atlantic.	65
5.4	The same as in Fig. 5.2 but for the Novopangaea scenario.	66
5.5	The same as in Fig. 5.2 but for the Aurica scenario.	67
5.6	The same as in Fig. 5.2 but for the Amasia scenario.	68
6.1	R versus the globally integrated dissipation rate for the M_2 (top left), S_2 (top right), K_1 (bottom left), and O_1 (bottom right) tide. The triangle marks present day dissipation and R value, and circle is present day with Archean tidal forcing. Note the discontinuous x-axis on all figures, also the y-scale is different for the M_2 tidal constituent.	77
6.2	M_2 tidal amplitudes for (a) present day bathymetry with present day tidal forcing, (b) present day bathymetry and Archean tidal forcing, and (c) a representative map selected from the Archean ensemble because it has median tidal amplitudes.	78

7.1	Figure 1 from Green et al. (2018) showing the progression of the next 250 Ma of Plate tectonics on Earth according to the Aurica scenario. The top two panels show present day (PD) and PD-reduced bathymetries respectively. Light blue is 200 m, intermediate blue (the ridges) is 2500 m and the majority of the ocean is <4000 m deep.	83
7.2	Figure 2 from Green et al. (2018) showing M_2 tidal amplitudes in meters for PD (top left) and PD-reduced (top right) simulations, along with the amplitudes at each time modelled in the future. The colour scale saturates at 2 m.	84
7.3	Figure 3 from Green et al. (2018) showing the same as Fig. 2, but for the K_1 constituent of the tide.	85
7.4	Figure 4 from Green et al. (2018) (a), Relative (to PD) tidal amplitudes for the K_1 (dashed line) and M_2 (Solid line) tidal constituents. (b), Globally integrated relative (to PD) dissipation rates for the M_2 tide. (c), Evolution of Lunar semi-major axis a over the scenario time frame, for the modelled (solid line) dissipation rate, and the present day (dashed) dissipation rate.	86
7.5	Figure 1 from Green et al. (2020) simulated M_2 tidal amplitudes for the 9 time slices represented in Fig. 7.3. Note that the colour scale saturates at 2 m. The grey arrow at 630 Ma is pointing to the Elatina formation in present day Aurstalia (Williams, 2000).	90
7.6	Figure 2 from Green et al. (2020) a) Globally averaged M_2 amplitudes and b) Globally averaged M_2 dissipation rates. The light grey shaded areas and data points marked by red dots are for interglacial periods, and the dark shaded areas and data points marked with blue dots are results for glacial periods. The black solid line represents simulations with conversion and no sea level change during interglacial periods, no conversion, and increased bed friction during the glacial periods. The "x" and "+" symbols represent sensitivity simulations for the onset of glaciations (although non-glacial paramaters were used) and for interglacial periods with no tidal conversion respectively. The dashed line marked with blue circles represents a simulation with slushball conditions and an ice free band within 10° of the equator.	91

7.7	Figure 3 from Green et al. (2020) Ocean bathymetry for 9 key time slices. Land is shown in white and the ocean bathymetry in colour. Note the lack of (yellow) shelf seas during glaciations. The green lines in the oceans mark the peaks of the oceanic spreading centers and dark grey lines show subduction zones. . . .	92
7.8	Figure 2 from Way et al. (2019), individual grid cell snow and ice fractional values for simulations 2 (Aurica_rand_PD), 5 (Amasia_rand_PD), and 7 (PD_control) show northern hemisphere winter (Dec, Jan & Feb) on the top row and northern hemisphere summer (Jun, Jul & Aug) on the bottom row).	95
7.9	Figure 1 from Way et al. (2019) Land masks (grey) and ocean (white) used for this study, present day continental configurations have been overlain for reference.	96
8.1	Relative tidal dissipation (Present-Day = 1) from 1500 Million years ago to 250 Million years in the future, dashed black lines represent supercontinent tenures, and blue dots represent ice ages (Green personal communication, Feb, 2020). .	98
8.2	650 Ma ago as represented by (Scotese, 2017) illustrating the landmasses, oceans, and seas of the time.	100

Table : List of Acronyms/Abbreviations

Abbreviation/Acronym	Definition
Ma	Mega annum or Million years ago
Myr(s)	Million years
LLSVP	Large Low shear wave Velocity Provinces
PGZ	Plume Generation Zones
LIP	Large Igneous Province
GW	Giga Watts
TW	Tera Watts
Ga	Giga annum or billion years ago
lh	Lhasa craton
OTIS	Oregon state Tidal Inversion Software
ROCKE-3D	Resolving Orbital and Climate Keys of Earth and Extraterrestrial Environments
GIS	Geographic Information System
GCM	General Circulation Model
SST	Sea Surface Temperature
Abbreviations from Fig. 4.1	
Ma	Mid-Atlantic ridge
Swir	SW Indian Ridge
Cir	Central Indian ridge
Seir	SE Indian Ridge
Pa	Pacific-Antarctic spreading centre
Na	Nazca-Antarctic spreading center
Pn	Pacific-Nazca spreading center
Cn	Cocos-Nazca spreading centre
Pcs	Pacific-Cocos spreading center
Ar	Arctic Ridge
A	Aleutian trench
Ca	Central American trench
C	Cascadia subduction zone
H	Hikurangi trench
Im	Izu-Marianas trench
J	Japan trench
K	Kurile Trench
La	Lesser Antilles arc
M	Macquarie subduction zone
Nh	New Hebrides subduction zone
P	Philippine trench
R	Ryukyu subduction zone
Sa	Scotia arc
St	Sumatra trench
Abbreviations from Figs. 4.2, 4.3, 4.4, and 4.5	
E. Ant	East Antarctica
W. Ant	West Antarctica
Ear	East African Rift
Sp	Somalia plate
Ant	Antarctica
Eas	East American Subduction zone
Par	Pan-Asian Rift
Epr	East Pacific Rise
Gs	Gibraltar subduction zone
Epas	East Pan-Asian subduction zone
Zr	Zonal ridge
Cs	Circumferential Antarctic subduction zone
PD	Present Day
Pac	Pacific Ocean
Atl	Atlantic Ocean
PCR	Polymerase Chain Reactions

Table : List of symbols

Symbol	Definition
Half wavelength resonance	
g	Force of gravity
H	Ocean depth
T	Tidal period
Eqn. 2.1 - Equilibrium tide	
M_L	Mass of Moon
M_E	Mass of Earth
a	Earth Radius
R_L	Semi major axis of Moon
θ	The longitude of the Moon's advance around the Earth
Eqns. 3.1 and 3.2 - Great circle length on a sphere	
ϕ	Latitude
λ	longitude
Φ	bearing (clockwise from North)
δ	Angular distance d/R
d	Distance travelled
R	Earth's radius
Eqns. 3.3 and 3.4 - Linearised shallow water equations*	
\mathbf{U}	Tidal volume transport vector defined as $\mathbf{u}h$
\mathbf{u}	Horizontal velocity vector
h	Water depth
f	Coriolis parameter
g	Acceleration due to gravity
η	Sea surface elevation
η_{SAL}	Self-attraction and loading elevation
η_{EQ}	Elevation of the equilibrium tide
\mathbf{F}	Energy dissipation term defined as $\mathbf{F} = \mathbf{F}b + \mathbf{F}w$
$\mathbf{F}b$	$Cd\mathbf{u}\ \mathbf{u}\ $
Cd	Drag coefficient
$\mathbf{F}w$	CU which represents losses dur to tidal conversion
C	conversion coefficient

*These equations appear multiple times in the text in sections (3.2, 5.4.1, and 6.3.2) so have only been defined for their first appearance.

Table : List of symbols contd.

Symbol	Definition
Eqn. 3.5 - Conversion coefficient	
Υ	50
N_H	Buoyancy frequency (N) at seabed
\bar{N}	Vertically averaged buoyancy frequency
ω	Frequency of the M_2 tidal constituent
N	Buoyancy frequency given by $N(x,y) = 0.00524 \exp(-z/1300)$
z	Vertical coordinate counted positive upwards from the sea floor
Eqns. 3.6, 3.7, and 3.8 - Calculating tidal dissipation*	
W	Tide generating force
\mathbf{P}	Divergence of the horizontal energy flux
Rossby radius of deformation	
N	Brunt Väisälä or buoyancy frequency
H	Scale height
f	Coriolis frequency
Fermi approximation of Supertidal frequency through Earth history	
N_{sc}	Number of supercontinent cycles that have occurred on Earth
N_{wc}	Number of Wilson cycles per supercontinent cycle
N_t	Number of tidal maxima per Wilson cycle
T_{tm}	Representative time duration for each tidal maximum (20 Myr)
T_E	Age of the Earth
Non-dimensional R value	
L_{tot}	Total coastline length
A_{ocean}	Ocean surface area

*These equations appear multiple times in the text in sections (3.2, 5.4.1, and 6.3.2) so have only been defined for their first appearance.

1 Introduction

The Earth is the only planet we know of which has an active, deforming mobile surface made up of a series of mobile plates - plate tectonics (Fig. 1.1). Earth is also unique because it possesses a large Moon which exerts an influential tidal force on the planet. The link between these two features is the Supercontinent cycle and the closely related Wilson cycle. Both cycles are manifestations of plate tectonics, the supercontinent cycle is the periodic gathering and dispersal of continents, and the Wilson cycle describes the life cycle of an ocean from initial rifting to eventual closure (Wilson, 1966; Dewey and Burke, 1974).

Earth's continents in the present day are the dispersed fragments of a former supercontinent which existed from 330 to 180 Ma (Ma - Mega annum, or Million years ago), called Pangea (Scotese, 1991; Matthews et al., 2016). As Pangea broke up it formed the Atlantic ocean, and as the next supercontinent forms in approximately 200 - 250 Myr (Yoshida and Santosh, 2018; Davies et al., 2018) it will close one or more ocean basins (i.e., the Atlantic, and/or Pacific, or other future basins).

Earth's Moon has a mass of 7.3×10^{22} Kg ($\sim 1\%$ of Earth) and an orbital radius of 384400 Km (~ 60 Earth Radii) (<https://nssdc.gsfc.nasa.gov/planetary/factsheet/moonfact.html>). This high mass and proximity causes uniquely large lunar tides on Earth. The tidal energy the Moon imparts on the Earth's oceans is important for ocean circulation and mixing and life in the ocean (Green, 2010; Green et al., 2017). The amount of energy the tide dissipates in each ocean is dictated by its geometry which is altered by the Wilson cycle over geological time.

The tide in the present day is anomalously high when compared to the past 250 Myr since the breakup of Pangea (Green et al., 2017). This is because the North Atlantic has the correct morphology to be harmonically resonant with the M_2 (principle Lunar semi-diurnal) tide. This occurs when an ocean basin's width (L) and depth (H) is equal to a multiple of half wavelength of the M_2 tidal wave $\lambda = \sqrt{gHT}$ (where T is the tidal period, and g is gravity) (Egbert et al., 2004; Arbic and Garrett, 2010; Green, 2010). As the Atlantic is currently opening (due to Africa/Eurasia and the Americas drifting apart), we expect it to move through its harmonic width and depth within the next 25 Myr or so (Green et al., 2018; Davies et al., 2020).

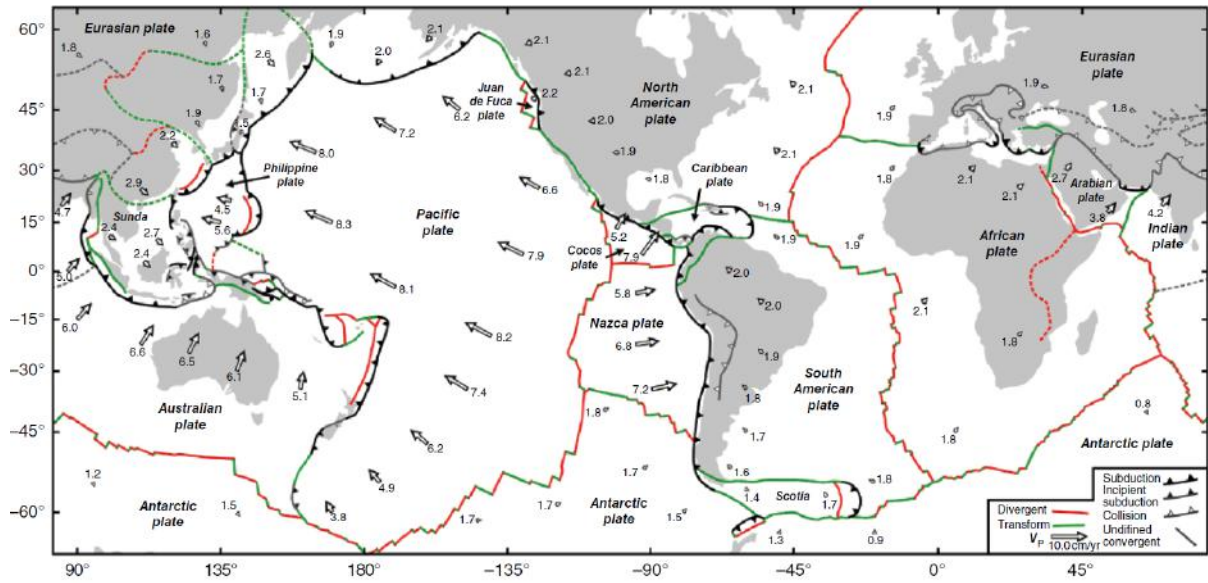


Figure 1.1: Global plate tectonic map illustrating the major tectonic plates and their boundaries and velocities (in cm yr^{-1}). Convergent boundaries are marked by black and grey segments with triangles, divergent boundaries are red and transform boundaries are green (Duarte and Schellart, 2016).

We would expect other ocean basins to become harmonically resonant as they either open or close as the next supercontinent coalesces. Once the next supercontinent has formed it will likely be tidally quiescent as observed for Pangea in Green et al. (2017) because the hemisphere-spanning superocean surrounding the supercontinent would be far too wide to support any kind of resonance.

It appears there is a relationship between the tide and the Supercontinent cycle. Periods of Supercontinent tenure are marked by tidal quiescence, because the ocean basins at these times are too large to host large tides, where periods of dispersed continents are marked by increased average tidal energies. During the dispersed continent phase of the supercontinent cycle, when oceans are changing size due to the Wilson cycle, they can occasionally reach a geometry which is resonant with the tide (Arbic et al., 2009; Green, 2010; Green et al., 2017, 2018; Davies et al., 2018). This tidal resonance (or Super-tide) typically lasts for (~ 20 Ma) (Green et al., 2018), and increases total global dissipation and regional tidal amplitudes, which in turn affects other components of the hydrosphere such as ocean circulation (Gerkema, 2019). These Super-tides have been identified in several periods of Earth history (Green, 2010; Green et al., 2017; Byrne et al., 2020; Green et al., 2020).

The initial aim of this work is to answer the question of if the present day is in a global tidal maximum. Our initial objective was to use GPlates to create kinematic tectonic reconstructions of Earth to couple them with a tidal model OTIS (Oregon state Tidal Inversion Software).

We then present coupled tidal tectonic modelling of four predicted scenarios of the Earth's near geological future (250 Myrs) ending in the formation of the next supercontinent. This will allow us to analyse the evolution of the tide over the ~ 500 Myr period of the present supercontinent cycle. We will then present coupled tidal tectonic modelling results of several periods in Earth's history to establish a deep time average of tidal energy input to Earth, to identify periods of Earth's history (and potential future) where enhanced resonant tides have occurred and may occur. Furthermore, we aim to establish a method to predict when ocean basins may become harmonically resonant with the tide during their Wilson cycle, and for how long they remain resonant. Then we will analyse tidal modelling results of the very young Earth during the Achaean to assess how global tides are affected by a moon in close proximity to Earth (meaning much stronger equilibrium tides) and how resonance may occur without plate tectonics, and therefore no supercontinent cycle or Wilson cycle.

Finally, we will use the kinematic tectonic model with a climate model to assess the further link between topography and climate in the Earth's potential future. Supercontinent accretion and dispersal is precipitated by large changes in land topography which can alter weathering and atmospheric circulation (Raymo and Ruddiman, 1992). Understanding the role of plate tectonics, the tide, and the climate will further our understanding of not only the Earth system but the planetary systems of Earth-like exoplanets, allowing us to better predict their potential habitability and improve the search for extra-terrestrial life.

1.1 Thesis structure

The manuscript is structured as eight chapters, an introduction (chapter 1), a background (chapter 2), methods (chapter 3), and a collection of works, published or submitted during my PhD (chapter 4, 5, 6, 7.1, 7.2, 7.3) followed by a complete overarching discussion (chapter 8) and the full published papers in the appendix.

2 Background

2.1 Plate Tectonics

Plate tectonics is a unifying theory of all the layers of the solid Earth and their interactions. It states that the surface of the Earth is made up of lithospheric plates that move in relation to each other, and that most of the geological processes on the surface occur where they meet (plate boundaries), i.e., earthquakes, volcanism, ore genesis (Fig. 2.1; Wilson (1966); McKenzie and Parker (1967); Le Pichon (1968); Morgan (1972)). The theory built upon the earlier theories of continental drift and seafloor spreading to create a full geodynamical picture of the Earth (Wegener, 1912; Holmes, 1931; Hess, 1962; Vine and Matthews, 1963; Morley and Larochelle, 1964; Dietz, 1977). At the surface, plate tectonics manifests as the motion of several distinct plates which incorporate the crust and part of the upper mantle (collectively known as the lithosphere (Le Pichon, 1968)).

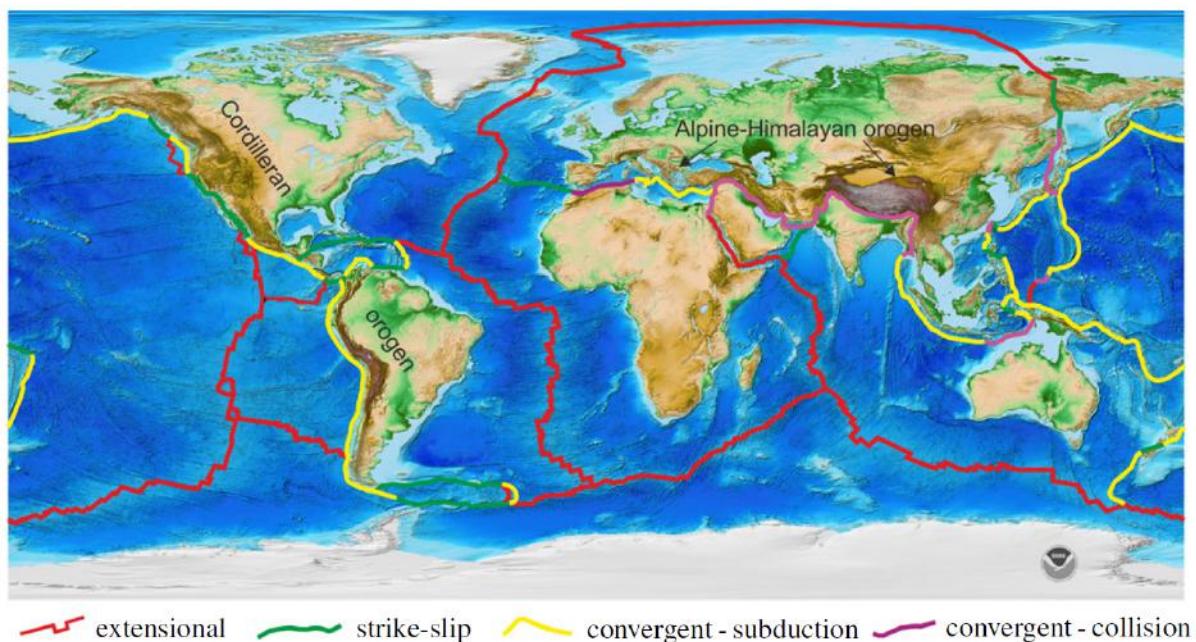


Figure 2.1: Figure 1 from Cawood et al. (2018) illustrating plate boundaries of the world. Note that the transform boundaries discussed by Wilson (1965) are referred to as "strike-slip" boundaries in this figure.

The interior of the Earth is hot (because of radioisotope decay) and the outside of Earth - the surface is relatively cooler. This establishes a thermal gradient which facilitates convection. Plate tectonics accounts for around 66% of the heat lost by Earth (Condie, 1997) in the form of convection. This convection is well illustrated in the mantle (Fig. 2.2) but the oceanic lithosphere is also part of the convective system. When new oceanic plate is made at the mid

ocean ridge it cools, emitting heat from the Earth's interior. It is then pulled away from the ridge before eventually subducting into the mantle (at the ocean trench). When it enters the mantle it diffuses. This is the upper most part of the convective system. It is forced by gravitational pull of old cold ocean plate into the mantle (Lithgow-Bertelloni and Richards, 1995; Schellart and Rawlinson, 2010).

The upper most layer of the solid Earth - the lithosphere - is made up of two layers, the crust and part of the upper mantle. Most of the lithosphere at the Earth's surface is oceanic, with the rest being continental and a small fraction being transitional (e.g., island arcs) (Condie, 1997) (for a full explanation of crustal types and a discussion of transitional crust see Condie (1997)). Both continental and oceanic lithosphere types are geologically and morphologically distinct, because of this continental crust is buoyant relative to the mantle for its entire lifetime, where oceanic crust is only buoyant relative to the sub-lithospheric mantle for the first 20 Myrs or so after its formation (Condie, 1997). After 20 Myrs it has cooled and thickened making it denser than the underlying mantle, and therefore more likely to subduct, provided it comes into contact with a subduction zone. Typically all ocean crust on the Earth's surface will be recycled within 200 Myr, although occasionally, a small amount of oceanic crust will be preserved in ophiolites, (small fragments of oceanic crust which break off and are emplaced on top of continental crust in the process of subduction) (Bradley, 2008, 2011).

The constant recycling of ocean plate through creation at mid ocean ridges and destruction through partial melt and diffusion once subducted affects the surface and mantle in separate ways. On the surface the effect of ocean plate creation and destruction, forces oceans (and therefore continental plates) to move in the Supercontinent cycle, and Wilson Cycle as described in sections 2.3, and 2.4.

In the mantle subducting ocean plate affects the temperature and chemical makeup of the mantle. The mantle is not thermally and chemically uniform (Torsvik et al., 2010, 2016). It possesses two regions of lower shear wave velocity (LLSVP) which are chemically and/or thermally distinct from the mantle. Because they are hotter and/or chemically distinct from the surrounding mantle, they tend to upwell. In contrast there are also regions of higher shear wave velocity, generally cooler or more dense mantle material which is usually caused by sinking slab. The sinking ocean plate makes up a fundamental part of this thermo-chemical stratification of the mantle - hot mantle feeds mid ocean ridges as it upwells and cold sinking slab introduces temperature and chemical differences (see Fig. 2.2).

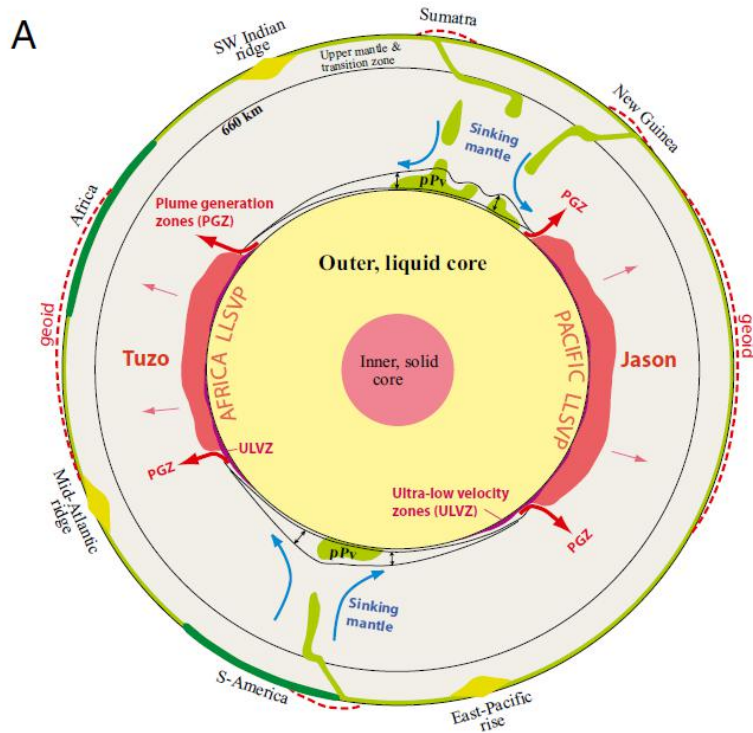


Figure 2.2: From Torsvik et al. (2014) a schematic of Earth's mantle from a southern polar perspective, the lower mantle is dominated by two antipodal large low shear wave velocity provinces (LLSVPs) beneath Africa (Tuzo) and the Pacific (Jason). They sit under two areas with a residual geoid (red dashed lines) and at their margins have zones of plume generation (PGZs) which are the principal source of large igneous provinces (LIPs).

The Earth is unique among the known terrestrial planets for presently having an active regularly deforming mobile surface composed of rock. However, as Fig. (2.3) shows, Earth has moved through a number of geodynamic regimes through geological time. Looking at other planets in our solar system can help us understand what Earth was like in the deep past and how the Earth may evolve geodynamically in the future.

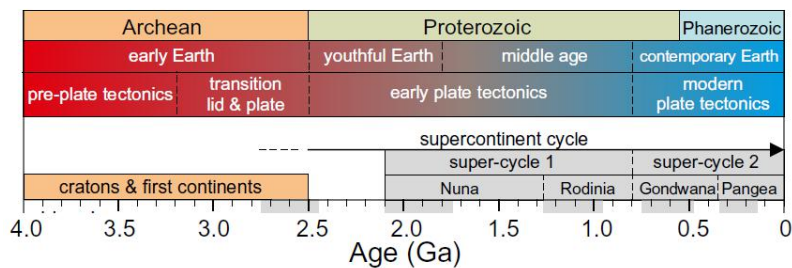


Figure 2.3: A modified version of Figure 1 from Cawood (2020) illustrating the primary planetary geodynamic regimes and supercontinent cycles throughout Earth history.

Plate tectonics has been the primary geodynamic regime of Earth for at least 2.5 - 3 Ga (Ga = Giga annum or Billion years ago) (Cawood et al., 2018; Palin et al., 2020). When looking

at the very early history of Earth, we must consider the other planetary geodynamic regimes. Plate tectonics is one of several primary regimes observed on rocky planets, and appears to be a middle ground between very hot and very cool regimes. Fig. (2.4) shows hotter regimes resemble the planets of Io and Venus - heat pipe and large scale overturning via surface melt (Moresi and Solomatov, 1998; King, 2018). With cooler regimes resembling Mars and Mercury with small scale intrusions into an otherwise stagnant lid (Nimmo and Stevenson, 2000). For a review of the types of geodynamic regimes observed in the solar system see Stern et al. (2018).

The potential for a planet to develop plate tectonics appears important for the maintenance of long term habitability. This is because plate tectonics affords Earth the ability to cycle elements, compounds, minerals, and heat from the Earth’s interior to the surface, all of which are important for Earth’s habitability (Foley and Driscoll, 2016; Waltham, 2019). Why Earth is the only planet we know of with plate tectonics, and how important plate tectonics is to the long term habitability of a planet are both important questions we will touch upon in this work, however also require much more investigation before a definitive answer can be made.

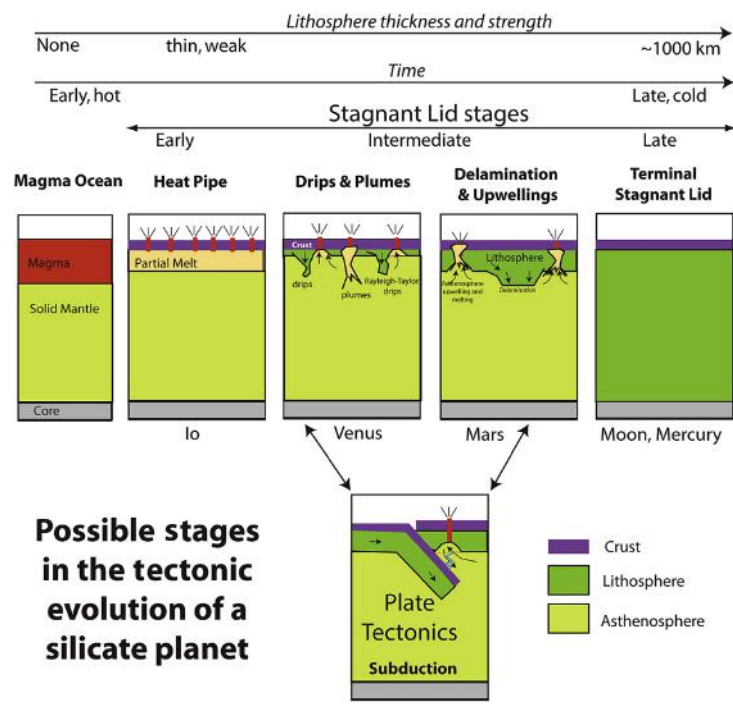


Figure 2.4: From (Stern, 2016), possible geodynamic regimes for large silicate bodies with examples from our solar system.

2.2 The origins of Plate Tectonics

2.2.1 Continental drift

Continental drift was proposed initially by Abraham Ortelius in the 16th century and later developed by Alfred Wegener (Wegener, 1912). Wegener (1912) acknowledged the observations of several scholars and cartographers before him in his 1912 work which argued the Earth's continents were once joined in one singular supercontinent. There were several lines of evidence for this, as well as the common argument that South America and Africa appeared to fit together in a "jigsaw" fit, the geological evidence also showed distant continents possessing similar fossils, geology, and glacial evidence. Wegener's theory was not widely accepted because while there was ample evidence for the argument, Wegener could not provide a mechanism for how the continents moved.

2.2.2 Seafloor spreading

The development of radar, sonar, and magnetic detection systems in the Early 20th was crucial for the development of plate tectonic theory and geoscience as a discipline. Initially used in a strictly military setting to detect enemy vessels and ordnance in the air and sea, they would later be used extensively for land and sea mapping. With sonar it was now much easier to map the ocean floor. Expeditions in the 19th century used simple sounding technologies which usually involved lowering a length of rope to the ocean floor to determine depth (Bossard, 2004), however after the development of sonar, the ships could collect echo and sonar soundings electronically much faster and with more precision. Large scale surveys of the ocean were carried out post WW2 and into the latter half of the 20th century. The most famous discovery to come from this mapping campaign was the largest feature on the surface of the Earth, mid ocean ridges. Mapped diligently by Marie Tharp and publicised by Harry Hess (Hess, 1962).

Magnetic analysis of the mid ocean ridge systems revealed they had linear magnetic anomalies. Vine and Matthews (1963) explained that as the new lithosphere forms at these mid ocean ridges, and ferrous materials in the rock cool, they orient themselves parallel to the natural magnetic field of the Earth. Regularly in Earth history the magnetic pole has flipped. This means ocean lithosphere formed in these times of magnetic reversal had a flipped magnetisation (either N-S or S-N). This proved ocean plate was being made at these ridge systems and moving away like a conveyor belt, and being destroyed and recycled at the ocean's edge in sub-

duction zones. This constant creation and destruction of ocean plate at mid ocean ridges and subduction zones respectively is known as seafloor spreading and the sinking of ocean plate at subduction zones represents the major driving force of plate tectonic motion (Stern, 2002).

2.2.3 Plate boundaries

By the 1960s it was clear that the Earth's surface was dynamic (Wilson, 1965; Dewey and Burke, 1974; Nance et al., 1988). The oceans and continents moved over geological time in what was referred to as mobile belts, i.e., major faults and mid ocean ridges. The picture wasn't complete though because there were points on the Earth where these mobile belts appeared to abruptly come to a stop, with one example being on the West coast of North America where the ocean plate appeared to stop at the continental margin (Fig. 2.5). Wilson (1965) argued that the mobile belts were connected and very rarely came to a complete stop, he explained the Earth was made up of "plates" with boundaries between them which allowed all mobile belts to interact. Two types of plate boundaries which we have already covered above are divergent boundaries (mid ocean ridges), and convergent boundaries (subduction zones/trenches), however there is another boundary type. Wilson (1965) presents the third type of plate boundary, the transform boundary, where the plate boundary may be transformed into either a divergent or convergent type i.e., again on the West coast of North America where the transform boundary is bordered to the North and south by subduction zones (Fig. 2.5).

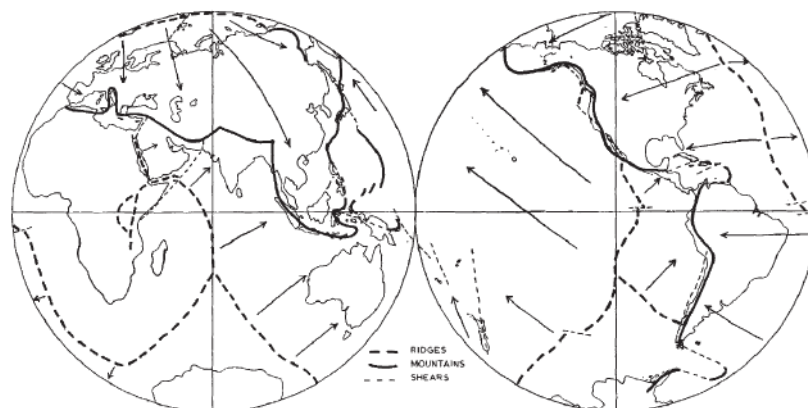


Figure 2.5: A sketch of the Indian ocean (left) and East Pacific ocean (right) showing the mobile belts of the regions, thick dashes denoting ridges, solid lines for mountains and thin dashed lines for shears (transform faults) (Wilson, 1965).

2.3 The Wilson cycle

Along with the transform fault concept, Wilson also first suggested the idea of the Wilson cycle, which describes the life-cycle of ocean basins. The name was first coined by Dewey and Burke (1974) and named after Tuzo Wilson. Its inception is in Wilson (1966), where he argues that an ancient Atlantic ocean existed in the past before Pangea. The ancient ocean basin opened, reached its zenith and then closed before re-opening to form the Atlantic ocean. Wilson (1966) used geological evidence such as faunal realms (the paleo-distribution of species) in the fossil record to argue for the existence of a paleo-ocean - now known as the Iapetus ocean - which existed before Pangea formed. These faunal realms were found on both the American and European coast of the Atlantic and unlike the fossil assemblages of Pangea, where the same fossils were found on both sides of the ocean (indicating ocean opening), they were different (indicating ocean closing) (Fig. 2.6).

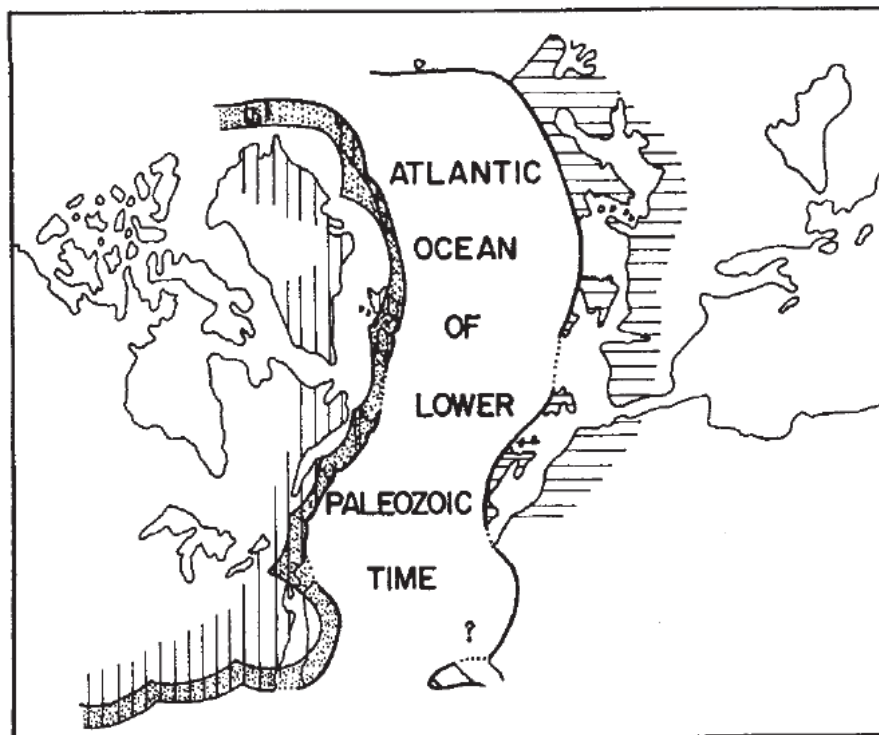


Figure 2.6: From Wilson (1966) illustrating the North Atlantic region in lower Paleozoic time (~250 Ma) shaded regions are distinct faunal realms.

The proximity of these previously distinct faunal realms on either side of the ancient ocean can be explained by continental collision. Wilson (1966) reconstructed the coastline of the Paleozoic ocean and it appeared to have a similar shape and location to the Atlantic giving rise to the argument that the Atlantic is a re-opened paleo-ocean. Wilson was right, the ancient

ocean was the Iapetus ocean, which closed in what we now know as the Caledonian orogeny (Cocks and Torsvik, 2011; Nance et al., 2012). The Iapetus (and Rheic) closed to form Pangea and the Atlantic opened to disperse Pangea, ending and beginning a Wilson cycle respectively.

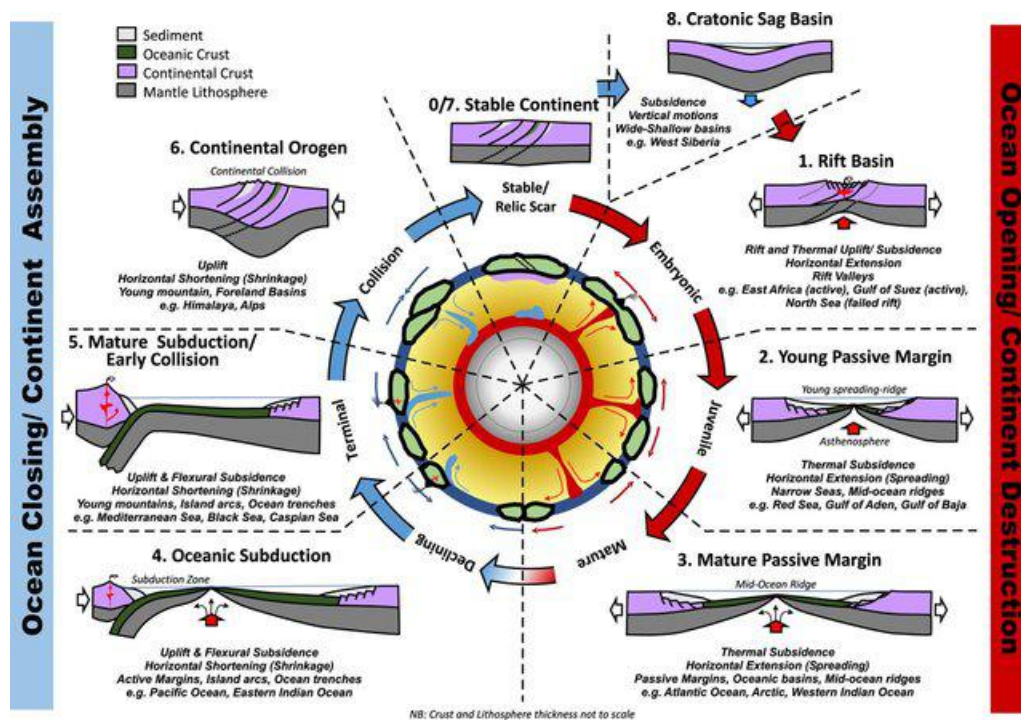


Figure 2.7: From Wilson et al. (2019) illustrating the life cycle of an ocean according to the Wilson cycle.

Fig. (2.7) illustrates the full Wilson cycle from opening to closure. A rift basin forms, progressively opens and matures into a young ocean. At this point oceanic subduction will begin to occur, although the exact method by which subduction first develops in an ocean is still debated (Stern and Gerya, 2018; Duarte et al., 2018). From this point the ocean will begin to close ending in a continental orogeny and possible supercontinent formation. While Fig. (2.7) illustrates the major phases of the Wilson cycle it does not detail the timing of each phase. The diagram shows how a Wilson cycle will progressively move through each phase, however this is not the full picture. Between phase 1 to 3 <200 Myr will pass, (provided the ocean does not fail to open as it may do (e.g., Dannowski et al. (2020))). Between phases 4 and 6 hundreds of millions of years can occur and orogenesis is not the only outcome. The Pacific ocean was formed from a plate renewal in the Panthalassic ocean (Boschman and van Hinsbergen (2016)) thereby renewing the old plate in the already 400 Myr old ocean basin.

Furthermore, one may assume that once phase 6 was completed a Supercontinent would be assembled, however this is not strictly true, the Mediterranean ocean is a remnant of the Tethys sea (currently just before stage 6 in the diagram) and will likely close in the next 25

- 50 Ma (Schellart et al., 2008), however its closure will not mark the formation of the next supercontinent, that will not happen for at least another 200 - 250 Myr (Yoshida, 2016; Davies et al., 2018).

2.4 The Supercontinent cycle

The Supercontinent cycle is the periodic gathering and dispersing of continents as they move due to plate tectonics over geological time (Nance et al., 2014; Conrad and Lithgow-Bertelloni, 2002). As geological techniques improved, evidence of more ancient supercontinents deeper in Earth history began to emerge. As Fig. (2.3) and Table (4.1) show, there have been a number of supercontinents in Earth history. Geological evidence for supercontinent assembly and breakup can be found in a number of proxies, namely detrital zircons, passive margin area, eclogites, and granites (Fig. 2.8). Each of these proxies identifies the formation and dispersal of a supercontinent, however none actually define a supercontinent. What a "Supercontinent" exactly is is a matter of debate among the scientific community. Some simple approaches label a supercontinent as an assemblage of "nearly all" of Earth's continental blocks (Hoffman, 1999). Others assign a percentage, i.e., any land mass which contains greater than 75% of the available continental crust (Meert, 2012). These prerequisites are useful for attaining a definition but are not grounded in any scientific reasoning. When attempting to answer this question some (e.g., Pastor-Galán et al. (2019)) have asked "When does a collection of continents become a supercontinent?" and vice versa.

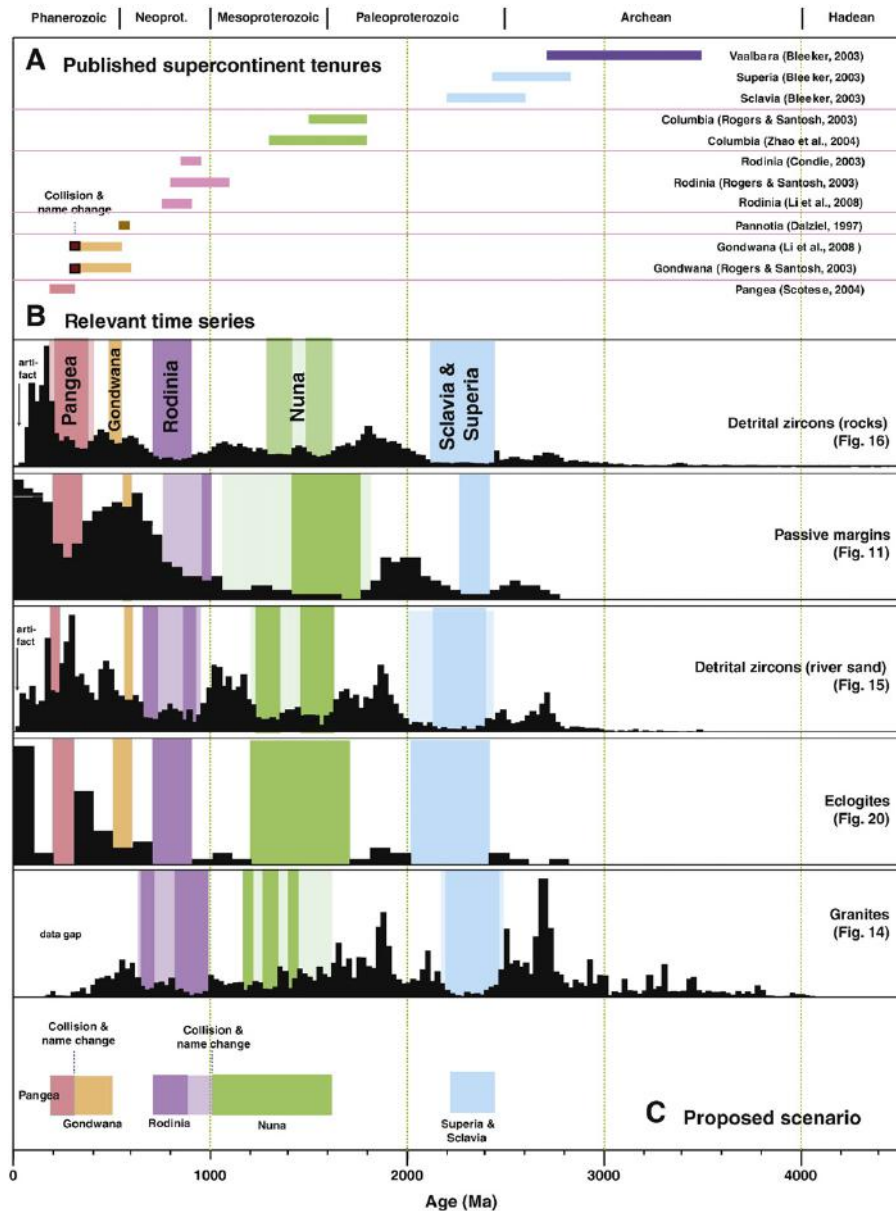


Figure 2.8: From Bradley (2011) timings of proposed supercontinents in Earth history. See Bradley (2011) for a full discussion.

As discussed in the sections above, the Earth's lithosphere is a fundamental part of the circulation of material on and in Earth. It has therefore been argued as prudent to label a supercontinent as having an effect on the mantle below. Pastor-Galán et al. (2019) provides a concise description: "A supercontinent is a single continental plate of a size capable of influencing mantle convection patterns and core-mantle boundary processes". While a supercontinent is capable of altering mantle processes, continents play a mostly passive role in plate tectonics. Ocean lithosphere is the more dynamic part of the plate system, and the creation and destruction of ocean lithosphere as part of the Wilson cycle forms and breaks supercontinents.

Whether the supercontinent cycle is as clear cut as it sounds - gathering due to closing

one or more oceans (Wilson cycle termination), followed by a period of supercontinent tenure before mantle insulation causes upwelling and breakup is very much debated in the literature. Fig. (2.8) shows each supercontinent tenure is not easily defined and furthermore, Wang et al. (2020) argues that orogeny leading to supercontinent formation typically occurs in a phase of megacontinent formation before final supercontinent formation, arguing Pannotia/Gondwana was actually just a precursor "megacontinent" which led to the final formation of Pangea.

2.5 Modes of Supercontinent formation

There are four ways to assemble a supercontinent, extroversion, introversion, orthoversion, (Fig. 2.9) and combination (Duarte et al., 2018).

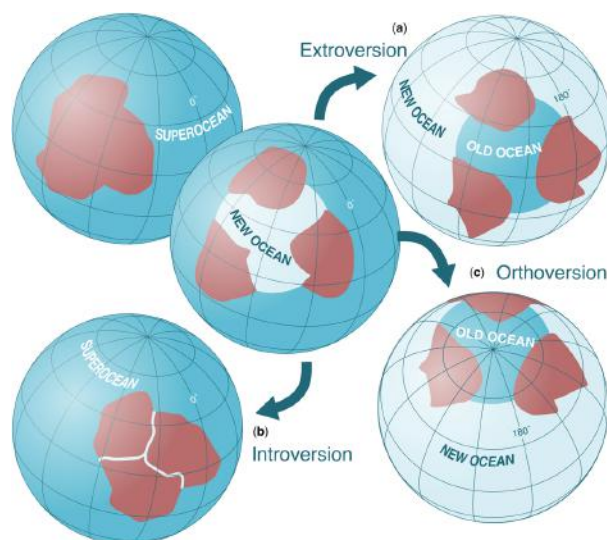


Figure 2.9: From Pastor-Galán et al. (2019), three modes of supercontinent formation - a) Extroversion - Supercontinent formation through closure of an old external ocean b) Introversion - Supercontinent formation through closure of a new internal ocean c) Orthoversion - Remnant subduction girdle left in the mantle from previous supercontinent forces the next supercontinent to form 90° away from the previous one, closing an old ocean.

If a supercontinent forms via extroversion, it will coalesce as the ocean which surrounded the previous supercontinent closes. In this mode the supercontinent will appear to turn inside out as the ocean that formed during the breakup of the previous supercontinent continues to grow and surround the entire supercontinent (Murphy and Nance, 2005). If a supercontinent forms via introversion, the ocean that formed during the break up of the previous supercontinent will reach its zenith before closing and reforming the supercontinent in much the same configuration as the previous one (Murphy and Nance, 2005). If a supercontinent forms via orthoversion, neither the aforementioned new or old ocean closes, but another separate ocean

closes to form the successive supercontinent 90° away from the previous supercontinent. This is caused by a remnant subduction girdle left in the mantle from the previous supercontinent, which forces the next supercontinent to form 90° away from the previous one (Mitchell et al., 2012). The fourth mode of supercontinent formation not detailed in Fig. (2.9) is combination (Duarte et al., 2018; Davies et al., 2018). In a combination scenario any number of extant oceans can close to form the next supercontinent. The other three modes assume only one ocean closes to form a supercontinent however, it is likely more than one ocean will close to form the next supercontinent as both the Atlantic and Pacific both have ocean plate >180 Ma old (Fig. 2.10) suggesting both oceans will either close in the future (Duarte et al., 2018) or undergo plate renewal (Boschman and van Hinsbergen, 2016).

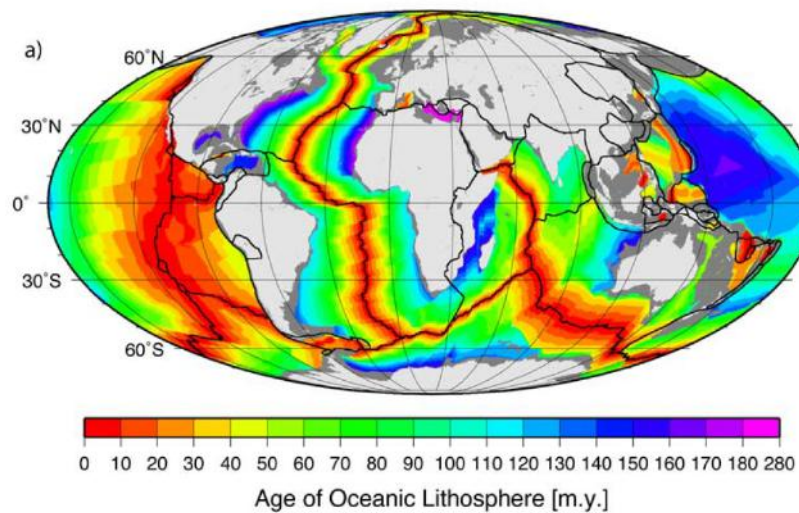


Figure 2.10: Age area distribution of the ocean floor (Müller et al., 2008).

2.6 Earth's interior

By the late 20th century, plate tectonic theory had explained the majority of the mechanisms of Earth, including how oceans form and die, how supercontinents coalesce and disperse, and how the plates interact with each other on the surface and in the Earth's interior. Until the invention of seismic tomography, there was no way to directly observe the interior of the Earth. According to the theory of seafloor spreading, the crust was a conveyor belt creating and destroying ocean plate. However the system includes the whole Earth. The recycling of ocean plate is part of a circulation system which begins at the outer core and ends at the ocean floor Torsvik et al. (2016). Ocean plate is created at the mid ocean ridge (Smith and Cann, 1993). It is then pulled away from the mid ocean ridge by motion of adjoined neighbouring plates,

or by slab pull from a subduction zone (Stern and Gerya, 2018). In the latter case the ocean plate subducts and enters the mantle, the age, chemical makeup, and width (i.e., how long the subduction zone is) affects how quickly the slab will sink through the mantle (Billen, 2008; Schellart et al., 2008). Eventually it will either diffuse or sink all the way through the mantle, where it will coalesce at the frontier of the outer core (Fig. 2.2). The chemical and thermal gradient caused by the presence of the oceanic lithosphere causes plumes of hotter or chemically distinct material to rise up through the mantle in a plume at plume generation zones (PGZs) (Torsvik et al., 2016). There is still some debate on the exact mechanisms of mantle convection but nonetheless it makes up a fundamental part of plate tectonic theory as it unifies the manifestations of plate tectonics on the surface of the planet with its interior (Torsvik et al., 2016; Condie, 1997).

This is plate tectonic theory, it is an intrinsic part of the Earth, and probably every other habitable planet in the universe (Waltham, 2019). Plate tectonics affects many aspects of the Earth system from the atmosphere to the deep oceans. Understanding plate tectonics and its place in the Earth system is fundamental to understanding the Earth as a whole.

2.7 Tides

The tide is one of the most distinguishable manifestations of gravitation - the phenomenon of attraction between objects - in nature. The ocean tide is caused by a combination of the gravitation of the Moon and Sun. Many texts explain the tides and all the constituents in detail, (see for example Pugh and Woodworth (2014)) so here we will focus on only the primary constituents listed in Table (2.1).

Table 2.1: Tidal constituents covered in this work

Principle constituents	Tidal period (hours)	Short description
M ₂	12.42	The principle Lunar semidiurnal constituent
S ₂	12.00	The principle Solar semidiurnal constituent
K ₁	23.93	The Lunisolar diurnal constituent
O ₁	25.82	The principle Lunar diurnal constituent

If we imagine the Earth was completely covered in water, with no continents then by equilibrium tidal theory (Eqn. 2.1) the tide would raise the surface of the global ocean by around 0.25 m in two tidal bulges antipodal to each other on the surface of Earth (Fig. 2.11).

$$\epsilon_L = \frac{3 M_L a^4}{2 M_E R_L^3} \left(\cos^2 \theta - \frac{1}{3} \right) \quad (2.1)$$

where M_L , and M_E are the mass of the Moon and the Earth respectively, a is the radius of Earth, R_L is the semi major axis of the Moon, θ is the longitude of the Moon's advance around the Earth which will cause a maximum at the relative position of the Moon.

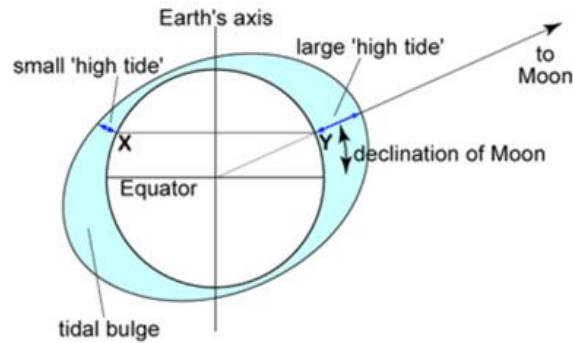


Figure 2.11: A schematic of the Earth's tidal bulges risen by the gravitation of the Moon and the centrifugal force of the Earth's orbit around the Lunar axis (<http://www.oc.nps.edu/nom/day1/partc.html>).

Fig. (2.11) shows the Moon raising two tidal bulges on Earth which cause two high and low tides a day, i.e., semi-diurnally (the M_2 tide). The same interaction occurs for the Sun and the Earth (the S_2 tide).

Diurnal tides (e.g., K_1 & O_1 , Table 2.1) are primarily caused by the influence of Lunar and Solar declination and eccentricity - the angle the orbits of the Earth and Moon in relation to the plane of the solar system, and how eccentric their orbits are respectively. This causes uneven distributions of the tidal force on the surface of the Earth creating regions of diurnal, semi-diurnal and mixed tides (Fig. 2.12). The predominant tidal signal of a region is mainly affected by its basin morphology i.e., the Gulf of Mexico, which has a strong diurnal tide due to the seiche effect (McCully, 2006b), where the gulf is the correct width to allow a diurnal oscillation of the tide within it, much like sloshing water in a bathtub.

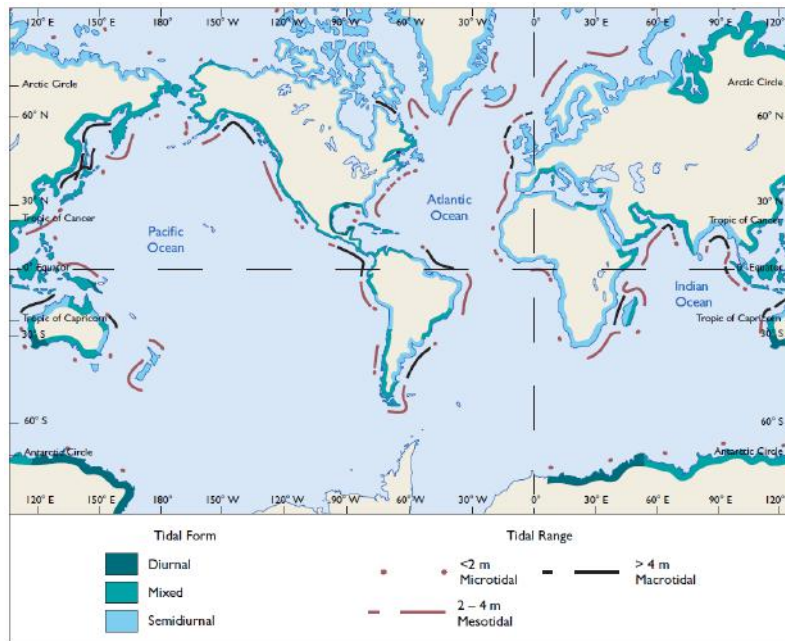


Figure 2.12: Tidal patterns of the Earth classified by amplitude and predominant type from (Pinet, 2008).

Ocean basin and coastal morphology not only affects the tidal period, it also affects the tidal amplitude and dissipation. It is known that in some areas of the Earth, the tidal range can be several meters (Fig. 2.12). Which is far higher than the amplitude described by equilibrium theory above. This is because the tide is affected by the geometry of the coast and on a larger scale ocean basins themselves. Tidal amplification and resonance are what enhances the tide in some areas of the world (e.g., the North Atlantic ocean) (Arbic et al., 2009).

2.7.1 Half wavelength open ocean resonance

The amplification of the tide under the correct conditions (e.g., correct ocean basin morphology) can cause an ocean to be resonant with a constituent of the tide. The principle is the same as in music and acoustics, if you induce a sound in a tuning fork of note "C" then bring it close to a flute with the correct finger placement to play "C" then the flute will hum the "C" note along with the tuning fork, however this will only work if the instrument and fork are aligned on the same note. In other words the tuning fork is inducing resonance in the flute. If we liken this to the tidal gravitation of the Moon (inputting energy to a system like the tuning fork) the motion can also be described with a waveform (or a note) - the tidal wave. While middle C has a wavelength of around 256 Hz, the semi-diurnal tide has a wavelength of around half a day (12.42 h), but it is still a wave. When this waveform "interacts" with an ocean which is a width and depth "aligned" to a multiple of the "note" of the tide (i.e., a half or quarter or the

wavelength) it will resonate (Fig. 2.13).

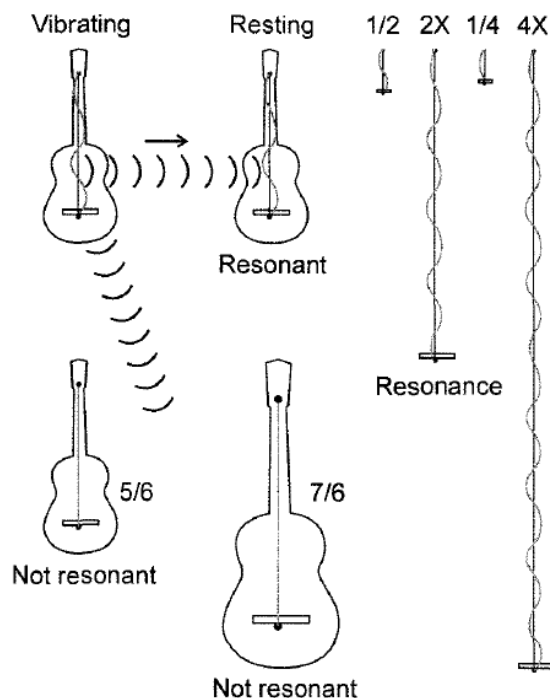


Figure 2.13: Figure 8-9 from McCully (2006a) illustrating harmonic resonance in guitar strings.

2.7.2 Tidal energy

Tidal energy is imparted to the oceans via tidal dissipation which can be divided into two mechanisms, dissipation via bottom friction which occurs mostly in continental shelf seas, and via transfer of energy from surface tides to internal tides (Gerkema, 2019). This occurs when surface tides pass over a slope in the ocean floor. The movement up and down the slope forces areas of equal density in the water column into motion which generates internal waves. These internal tides then "break" near bottom slopes or against strong shear currents causing turbulent mixing.

The equilibrium M_2 tidal dissipation rate is 2.3 GW however, the present day tidal dissipation rate for M_2 is around 2.5 TW. This is because of the current continental configuration allowing for resonance in the North Atlantic. The effect of the present day Atlantic being resonant with the M_2 tide can be seen in the tidal energy dissipated to the ocean. Tidal energy is dissipated in all areas of the ocean however, it is helpful to separate the ocean into shallow <200 m, and deep components >200 m. The global tidal energy budget (Lunar and Solar) is illustrated in Fig. (2.14). As we can see 75% of the tide is dissipated in marginal seas, with the rest of the tide being dissipated in the deep ocean at ridges and seamounts.

Because of Atlantic resonance, the present day tides are anomalously energetic when compared to the last 250 Myrs (Green et al., 2017). Since the breakup of Pangea to the present day the tidal dissipation rate has been less than half the present day value.

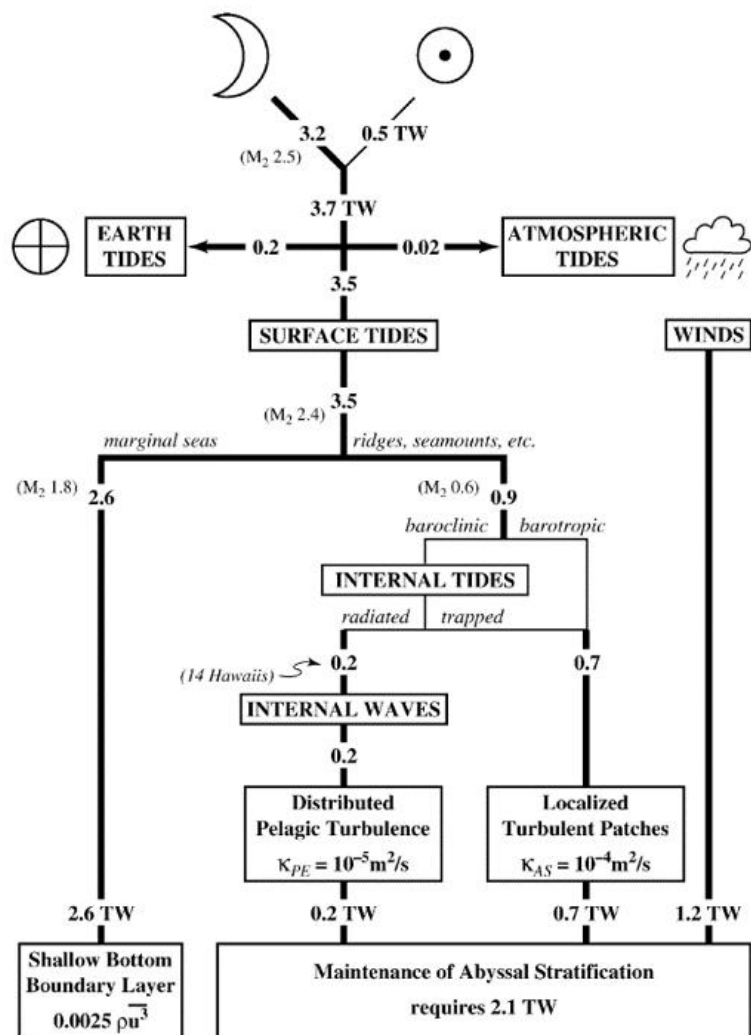


Figure 2.14: From Munk and Wunsch (1998), tidal and wind energy input to the oceans of Earth.

2.7.3 Lunar recession and tidal friction

Lunar recession is the phenomenon of the Moon slowly receding from the Earth as a result of tidal friction (Gerkema, 2019). As the Moon "pulls" on the Earth's oceans (and rock and atmosphere) to produce the tide, it imparts energy to the Earth system, this is taken from the Moon's orbital momentum. Objects in less distant orbits move faster - and therefore have a greater momentum - than those in more distant orbits, so as the Moon loses momentum due to the friction of the tide it slows and its orbit increases in distance. As the Moon recedes, its distance to Earth increases and as gravitational pull decreases with the inverse square of the

orbital distance, the tides progressively weaken. Eventually the Moon will recede to an orbit where the orbital energy it is losing due to tidal friction is negligible meaning its orbit will stabilise and not increase further.

This tidal friction has an effect on the Earth too, the tidal force of the Moon acts to slow the Earth's rotation. This affects the period of the tide. There are always two tidal bulges raised on Earth, however in the past when the Earth was rotating faster, the time between high and low tide was less frequent which may have had an effect on life and evolution in Earth history (Lathe, 2004, 2006; Balbus, 2014). Over human time scales the effect of tidal friction on slowing the Earth is minuscule (2.3 ms per century) however, over geological timescales the Earth's rotation slows measurably. Over the Phanerozoic (the last 2.5 Ga) the Earth rotation rate is estimated to have slowed by around $1.79 \text{ e}^{-5} \text{ s yr}^{-1}$. Meaning at 2.5 Ga the day was only 17.067 hours long. This Lunar recession and Earth despinning has not been constant over time. The present Lunar recession rate is around 3.82 cm yr^{-1} per year (Riofrio, 2012). If this rate was used to extrapolate the Moon's orbit back in time, the Moon's orbit would be within the Earth's Roche limit at around 1.5 Ga - suggesting it formed then, however the Moon has been radioisotope dated to be ~ 4.5 Ga old (Kleine et al., 2005). This means Lunar recession and Earth despinning must have been weaker in Earth history.

3 Methods

The work presented in this thesis is a product of a combination of the GPlates, OTIS, and ROCKE-3D (Resolving Orbital and Climate Keys of Earth and Extraterrestrial Environments with Dynamics) software. GPlates is primarily a GIS (Geographic Information System) visualisation and presentation software, and OTIS and ROCKE-3D are both modelling softwares which simulate their respective aspects of the Earth system (tides and climate when put simply). How each software was utilised for the work and coupled to produce the results presented in this thesis is detailed below.

3.1 GPlates

GPlates is an open source software which allows interactive manipulation of tectonic reconstructions, GIS functionality and raster data visualisation (Müller et al., 2018). The primary usage of GPlates is to visualise tectonic plates on a sphere - a virtual Earth - over geological time. By importing data to the GPlates work space, or using that already provided in the sample data folder on download of the program, two or more types of data can be visualised in unison, e.g., geolocations, rotation poles, plate motions, and magnetic data.

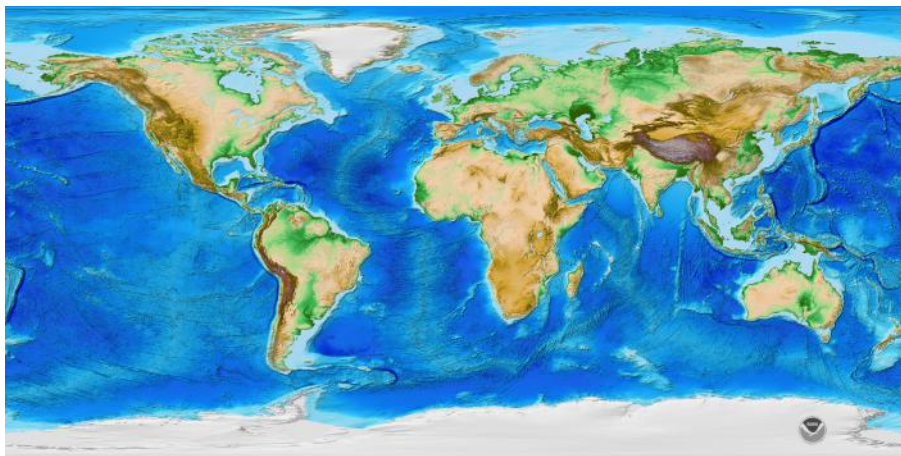


Figure 3.1: From <https://data.nodc.noaa.gov/cgi-bin/iso?id=gov.noaa.ngdc.mgg.dem:316>, global relief map of the Earth.

The first step in visualising tectonic reconstructions is to either import a georeferenced raster image (meaning it is the correct scale and projection to represent the Earth correctly) e.g., Fig. (3.1), or create or import a shapefile of a continent, plate, or other feature (generally shapefiles are compiled into collections of geological features - feature collections). Rasters are used to visualise a map on a sphere and to digitise said map by using it as the base from which

to create shapefiles. Shapefiles are the individual parts of a feature collection, they can be either lines (e.g., to depict ridges or subduction zones) or polygons (e.g., to depict three dimensional features such as a craton or a plate boundary). To draw these features in the GPlates work space find the tools "Digitise new polygon geometry" or "Digitise new polyline geometry" and begin drawing your feature, either free hand or tracing over an imported raster. Before creating either a line or polygon, the feature must have a type, a name, a plate ID, a timeframe, a geometry and a feature collection, (Fig. 3.2). The "type" is a description of the geological/geodynamic feature which here is a "coastline". The "name" is the name of the shapefile. The "plate ID" is a unique identifier for use with rotation files which will be explained below. The feature must be assigned a beginning and end, this can be infinite, as seen here, the feature begins at 300 Ma and ends in "future". A plate with a set beginning and end will only be present on the map for that time, e.g., in a reconstruction spanning 0 - 300 Myr, if a shapefile in that reconstruction has a time of 0 - 25 Myr, it will only be visible on the map during those times, and will disappear from the visualisation at 26 Ma. Clicked geometry is the latitude and longitude points used to make the shapefile, this can be any number from 1 upwards, and the feature collection is the collection the feature is saved into, here it is saved as part of the "HD world map (coastlines)" which includes all other coastlines of the other continents in one feature collection. If you are using the sample data which is provided with the GPlates download then this information will already be in the feature collections, however if you are making any new shape files you will need to define this data for each feature you create.

Current Feature

Type:

Name:

Plate ID:

Valid time:
 from to

Clicked geometry:

Feature collection:

Figure 3.2: Feature description of selected plate (here Africa is shown) on the GPlates work space.

Once the shapefiles/feature collection is present or created, it can be animated with the use

of a rotation file. This is a simple .txt file which dictates the movement of features over the surface of the planet. GPlates can process plate motions (shapefile animations) in two ways; relative plate motion, i.e., moving a plate relative to a fixed point - usually another shapefile or feature, or motion along an Euler pole. An Euler pole is the point on a sphere which intersects a great circle on the sphere at 90° . The North pole is the Euler pole for the Equator. Every plate motion in GPlates can be described as movement along a great circle (see Fig. 3.3 for an illustration).

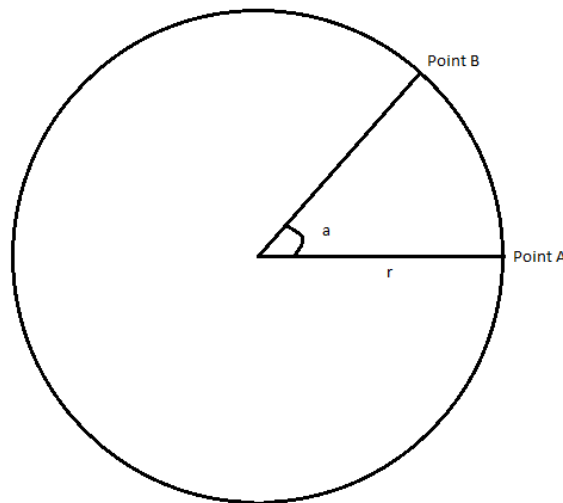


Figure 3.3: A schematic illustration of the motion of an object from point A to point B along a great circle. In this illustration the great circle is the equator and the pole is the true North pole.

If we take the present day locations as an initial point for each continent, and as long as we know the plate velocity (speed and direction) of each plate we can calculate where each plate will move to in a prescribed amount of time. The present day average plate velocity is $\sim 6 \text{ cm yr}^{-1}$ (Young et al., 2019). With this, we can begin to calculate great circle plate motions. If we know Australia is moving North at a rate of $\sim 6 \text{ cm yr}^{-1}$ it will move 60 Km in 1 million years. However, it will not move in a straight line from its initial point (point A) to its +1 Ma point (point B), it will move over the surface of the Earth, which is a sphere not a flat surface. The continent will move not in a straight line but in a "great circle" line. With an initial position, distance (velocity over time) and an azimuth (direction of plate movement) it is possible to determine the destination along the great circle:

$$\phi_2 = \arcsin(\sin \phi_1 \cdot \cos \delta + \cos \phi_1 \cdot \sin \delta \cdot \cos \Phi) \quad (3.1)$$

$$\lambda_2 = \lambda_1 + \arctan 2(\sin \Phi \cdot \sin \delta \cdot \cos \phi_1, \cos \delta - \sin \phi_1 \cdot \sin \phi_2) \quad (3.2)$$

Where ϕ is latitude, λ is longitude, Φ is bearing (clockwise from North), δ is the angular distance d/R where d is the distance travelled and R is the Earth's radius.

We now have the point A and point B for a shape file at it's beginning and end locations. To input this in GPlates either the rotation file can be edited directly, or the shape file can be moved in the GPlates work space. The rotation files do not use simple geographical coordinates, they use Euler pole coordinates. This means Euler pole coordinates must be calculated alongside the geographical coordinates. In simple cases (i.e. Australia moving almost straight north for many millions of years) the Euler pole remains fixed, however in more complex scenarios the Euler pole also moves, which complicates the calculation. In the GPlates program, Euler poles are calculated dynamically and as long as the rotation file is loaded and the time period correctly selected, the program will add the Euler pole coordinates for each rotation (plate motion).

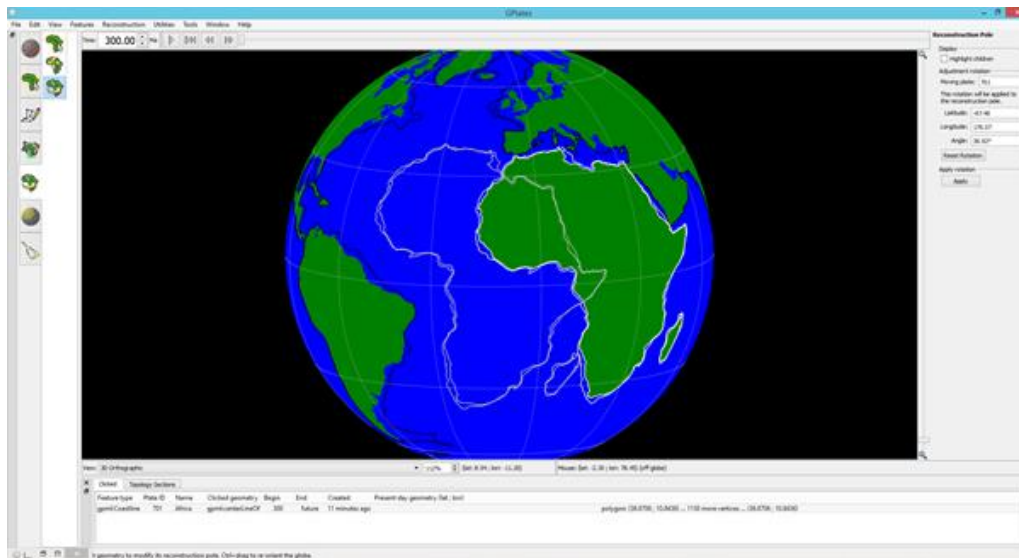


Figure 3.4: A screenshot of the GPlates work space while Africa is being manipulated. The “reconstruction pole” menu on the right-hand side of the image shows the calculates Euler pole for the manipulation being carried out (the solid continent would move to the position of the outline). If the "apply" button is pressed and the rotation file is loaded, the plate will assume this position from it's original position for the time displayed "300".

This work presents kinematic tectonic reconstructions of the past and constructions of the future. Creating reconstructions of the past with GPlates for this work mainly involved using pre-existing reconstructions and raster images of Earth's geological past to in creating reconstructions that could be used with the tidal model OTIS. There is no need to calculate Euler pole rotations for point A and point B of a continent in the past if raster images of both those time periods exist and can be used to georeference the shapefile. In this instance the same method as Fig. (3.4) is used, however instead of moving the shape file to a pre-calculated position it is

moved to the position that the same object occupies in the raster image for each time period Fig. (3.5) shows a raster image of 180 Ma and the corresponding shape files overlain (blue outlines). Here the Lhasa craton (Lh) is being moved to represent it's location at 180 Ma. This method and the one described above can be used for models of any complexity from regional models of drift of one craton to global models which include many different geological features.

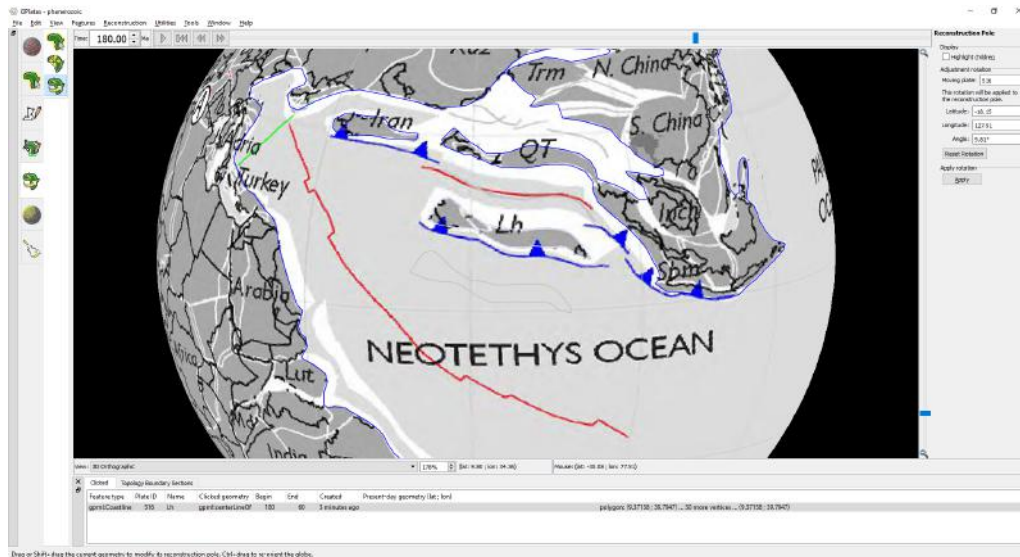


Figure 3.5: The GPlates workspace showing how to calibrate plate motions using raster images. The shape files are outlined in blue and the raster image is in black and white.

The method described above was used to create all of the kinematic tectonic models presented in this work. For the constructions of the future scenarios presented in chapter 4, the coastline and continental shelf extent was created from the NOAA ETOPO1 global relief model of the Earth (see <https://data.nodc.noaa.gov/cgi-bin/iso?id=gov.noaa.ngdc.mgg.dem:316#> for details). This was done because the version of GPlates used to create the model of the future scenarios was not able to model deformation (GPlates version 2.2 is capable), and because trying to estimate depletion and accretion of continental lithosphere over the period modelled requires too many assumptions to be accurate.

3.2 Oregon State Tidal Inversion Software - OTIS

A large part of the work involved in this project was done via global tidal modelling with the tidal inversion software OTIS (Oregon State Tidal Inversion Software) (Egbert et al., 1994). We use OTIS to provide a solution to the linearised shallow water equations:

$$\frac{\delta U}{\delta t} + f\mathbf{U} = gh\nabla(\eta - \eta_{SAL} - \eta_{EQ}) - \mathbf{F} \quad (3.3)$$

$$\frac{\delta \eta}{\delta t} - \nabla \cdot \mathbf{U} = 0 \quad (3.4)$$

Here, \mathbf{U} is the tidal volume transport vector defined as $\mathbf{u}h$, where \mathbf{u} is the horizontal velocity vector and h is the water depth, f is the Coriolis parameter, g the acceleration due to gravity, η the sea surface elevation, η_{SAL} the self-attraction and loading elevation used from (Green et al., 2017) (see Egbert et al. (2004) for a more detailed methodology), η_{EQ} the elevation of the equilibrium tide, and \mathbf{F} the energy dissipation term. The latter is defined as $\mathbf{F} = \mathbf{F}_b + \mathbf{F}_w$, where $\mathbf{F}_b = Cd\mathbf{u}\|\mathbf{u}\|$ parameterises energy due to bed friction using a drag coefficient, $Cd=0.003$, and $\mathbf{F}_w = C\mathbf{U}$ represents losses due to tidal conversion. The conversion coefficient, C , is based on Zaron and Egbert (2006) and modified by Green and Huber (2013), computed from:

$$C(x,y) = \Upsilon \frac{N_H \bar{N}}{8\pi\omega} (\nabla H)^2 \quad (3.5)$$

In Eq. 3.5 $\Upsilon = 50$ is a dimensionless scaling factor accounting for unresolved bathymetric roughness, N_H is the buoyancy frequency (N) at seabed (taken from Green et al. (2017)), \bar{N} is the vertically averaged buoyancy frequency, and ω is the frequency of the M_2 tidal constituent (NB. the frequency of the tidal constituent(s) changes depending on when in Earth history the tide is modelled, e.g., the Cryogenian M_2 tide is 10.98 h). The buoyancy frequency, N , is based on a statistical fit to present day climatology (Zaron and Egbert, 2006), and given by $N(x,y) = 0.00524 \exp(-z/1300)$, where z is the vertical coordinate counted positive upwards from the sea floor.

For the tidal analysis conducted in Green et al. (2018) both the M_2 and K_1 tidal constituents were simulated. In Davies et al. (2020), and Green et al. (2020) only the M_2 was simulated. In chapter 6 the M_2 , K_1 , S_2 , and O_1 were simulated.

In every chapter where tidal modelling is presented the same method of harmonic analysis was done - each run simulated 14 days, of which 5 days were used for harmonic analysis of the tide. The model output consists of amplitudes and phases of the sea surface elevations and transports, which was used to compute tidal dissipation rates, D , as the difference between the time average of the work done by the tide generating force (W), and the divergence of the

horizontal energy flux (\mathbf{P} ; see Egbert and Ray (2001) for details):

$$D = W - \nabla \cdot \mathbf{P} \quad (3.6)$$

where W and \mathbf{P} are given by:

$$W = g\rho\mathbf{U} \cdot \nabla (\eta_{EQ} + \eta_{SAL}) \quad (3.7)$$

$$\mathbf{P} = g\rho\mathbf{U}\eta \quad (3.8)$$

3.2.1 Using the GPLates kinematic model with OTIS

The GPLates kinematic model, when converted to a depth grid can be used as the bathymetry mask for OTIS. All of the OTIS tidal modelling results presented in this work except for the Archean work (presented in chapter 6, are used with a GPLates kinematic tectonic model converted to a $1/4^\circ$ resolution depth grid. The GPLates kinematic model represents a boundary condition which is not dynamically affected by the OTIS model, the coupling is strictly one-way. A preliminary investigation into the feasibility of the coupling was done by a masters student whom I supervised in 2017.

The Masters student (Joe Molloy) and I developed a methodology of colour coding the GPLates shapefile maps of Earth in so their RGB values could be converted into depth values in MATLAB i.e., White (RGB = 0 0 0) was reserved for the continents as they are assigned 0 m depth or "sea level", all other depths - shelf, mid ocean ridges, and subduction zones were assigned their own colour coded depths (see Fig. 3.6 for an illustration). This same methodology has been used in the modelling presented in chapter 5, and sections 7.2 and 7.3. It was used to create a simplified bathymetry map for each time slice in the kinematic tectonic model(s). Land is defined as 0 m, continental shelf at 200 m, mid ocean ridge is set to a depth around 2000 m deepening along it's long axis towards abyssal plain depth until the average width of the ridge is 5° , subduction zones are set to a depth of around 6000 m, and, the abyssal plain depth is set to preserves ocean volume.

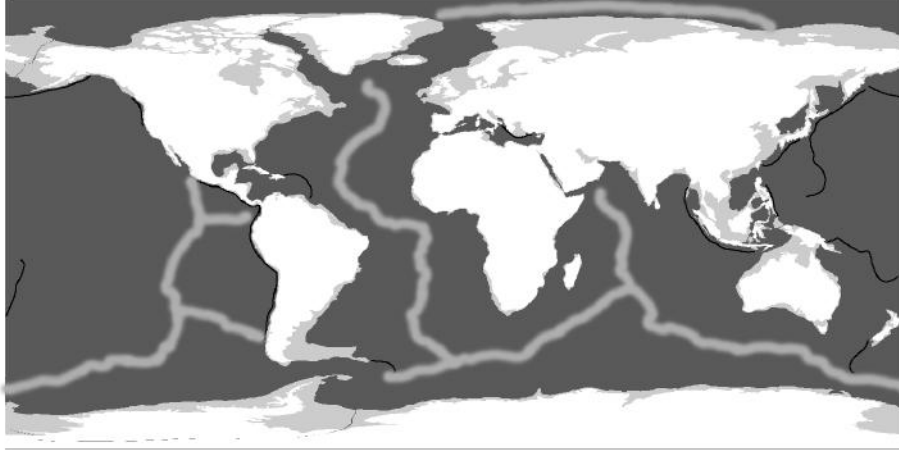


Figure 3.6: Grey-scale image of the Present day Earth once it is colour coded to be used as the boundary condition for the OTIS model.

The primary concern when coupling the models was that the kinematic tectonic models would not have a sufficiently complex bathymetry to accurately model the tide. The kinematic tectonic models when converted into a format compatible with GPlates are what is referred to as a "bathtub" because there is very little differentiation in the morphology of the ocean, furthermore, the morphology transitions from one depth to another abruptly (except for the ridges which do slope). The modelling work done by Joe was successful and the results were written up for publication (Green et al., 2018) (see section 7.1), demonstrating it was possible to couple the tectonic and tidal models.

3.3 ROCKE3-D

ROCKE-3D (Resolving Orbital and Climate Keys of Earth and Extraterrestrial Environments with Dynamics) is a three dimensional General Circulation Model (GCM). Its primary use is to model the atmospheres of solar system and extra-solar terrestrial planets. All of the modelling work with ROCKE-3D presented in this thesis was carried out by Michael Way, however the tidal and tectonic models and outputs were used as the input for the ROCKE-3D modelling presented. ROCKE-3D is still being iteratively improved to model more diverse environments, however for now it is capable of modelling the terrestrial planets of our solar system in the past and present (Way et al., 2017). For the work presented here, ROCKE-3D version Planet 1.0 is used.

ROCKE-3D in the scope of this work was ran with a Cartesian grid point latitude longitude resolution of $4^\circ \times 4.5^\circ$ which covers 20 or 40 layers of atmosphere and 13 ocean layers.

The atmospheric resolution is this so it can resolve the dominant scales of atmospheric motion. The prescribed resolution above equates to grid boxes of around 400 - 450 Km which is capable of resolving the ~ 1000 km scale radii of Rossby deformations on Earth like planets. The Rossby radius of deformation ($L_d = NH/f$) where N is the Brunt Väisälä or buoyancy frequency and is proportional to the static stability (https://glossary.ametsoc.org/wiki/Static_stability), H is the scale height which is dependant on temperature, gravity and atmospheric composition, and f which is the Coriolis frequency which is linked to the planet's rotation rate.

To accurately recreate a planet's climate system in a 4D model, oceans must be included in the parameterisation. ROCKE-3D planet 1.0 allows for three different modes of ocean interaction, each of varying complexity from lowest - specified sea surface temperature (SST), to thermodynamic upper ocean mixed layer, to coupled dynamic ocean GCM, which is the most complex mode (for a detailed explanation of each see Way et al. (2017)). A fully coupled dynamic ocean was used when using ROCKE-3D for this work.

3.3.1 Using the GPlates kinematic model with ROCKE-3D

ROCKE-3D was used with the future kinematic scenarios of Aurica and Amasia in a similar way to when they were used with OTIS (one-way as boundary conditions). While OTIS required detailed ocean bathymetry and no land detail (except for telling OTIS where land was), ROCKE-3D required ocean bathymetry and land topography, albeit at a lower resolution than OTIS. To create maps that were compatible with ROCKE-3D topography had to be added. Assuming topography into the future is very subjective and to counteract this three different sets of topographies were made: A control - where land is close to sea level with no mountains, a Present day analogue where the land is close to present day average topographic elevation and a mountainous analogue where land is close to sea level everywhere except for in regions with mountains.

The control is meant to simulate a supercontinent which has existed for long enough to be almost completely eroded, the lack of mountains and large changes in elevation shows the effect these regions have on the result when it is ran through ROCKE-3D. This was made by applying a random topography to the land mask of the scenario with a normal distribution (mean of 1 m, standard deviation of 50 m) the highest elevation in this analogue is 200 m.

The present day analogue was made by applying a random topography with a normal dis-

tribution which is close to present day values (mean of 612 m and standard deviation of 712 m) this produces a "rough" land mask which has an elevation varying from 1 - 4000 m.

In the mountainous analogue the same land mask normal distribution of elevations between 1 - 200 m is applied (as in the control) however regions where mountains would geodynamically occur or persist are added to the land mask. They can be divided into three types, Himalaya type, which represent collisional orogens and are the mountains that would form when the next supercontinent coalesced, they have an average peak elevation of 7500 m, Andes type which are cordilleran type mountains, forming as a result of compressional forces from subduction. These would border the supercontinent as a ring of subduction surrounded the land mass, these mountains have an average peak elevation of 4000 m. The third type of ocean is Appalacian type, these are the mountains which are Andean and Himalayan in the present day but have eroded in the interim. They have an average peak elevation of 2000 m. Every mountain was configured to be no wider than 5° at their widest point (at the base).

The original maps for the Aurica and Amasia scenario are in $1/4^\circ \times 1/4^\circ$. This had to be down-sampled to the $4^\circ \times 5^\circ$ resolution used in the ROCKE-3D model. Once the maps have been down-sampled river pathways are calculates from the final topography, they exit to the ocean where possible. Ocean grids larger than 15 contiguous grids are redefined as lakes to allow them to become more or less voluminous in equilibrium with the regional evaporation and precipitation. The GCM can allow lakes to form and disappear also, and can only do this with lakes (ocean cells are permanently defined as ocean) so it is beneficial to redefine inland seas as such. To prevent an issue with the ocean freezing solid and crashing the model any ocean grid cell with a depth of <150 m was deepened to 204 m.

4 Back to the future: Testing different scenarios for the next supercontinent gathering

Hannah S. Davies, J. A. Mattias Green, & João C. Duarte

(This chapter is presented in paper format as published in *Global and Planetary Change*,
Davies et al. (2018))

4.1 Summary

The subject of this chapter is a review of four predicted scenarios of the next supercontinent gathering in approximately 200 - 250 Myr. Each scenario presents a unique evolution of plate tectonic drift and ocean closure (via the Wilson cycle) and thereby the subsequent supercontinent formed as a result of all four of these scenarios is also unique. We explore the tectonic mechanisms which may cause these scenarios, namely the ocean opening and closing events which each scenario requires, and the feasibility of the four scenarios from a conceptual standpoint. Not only does this work present digitised reconstructions of the original predictions, which are simple sketched maps, but the work also represents a test of the state of the art of plate tectonics. To test our understanding of how the Earth may develop tectonically over the rest of the current supercontinent cycle.

4.2 Abstract

The theory of plate tectonics and the discovery of large scale, deep-time cycles, such as the Supercontinent cycle and Wilson cycle, has contributed to the identification of several supercontinents in Earth's history. Using the rules of plate tectonic theory, and the dynamics of subduction zones and mantle convection, it is possible to envisage scenarios for the formation of the next supercontinent, which is believed to occur around 200 – 300 Ma into the future. Here, we explore the four main proposed scenarios for the formation of the next supercontinent by constructing them, using GPlates, in a novel and standardised way. Each scenario undergoes different modes of Wilson and Supercontinent cycles (i.e., introversion, extroversion, orthoversion, and combination), illustrating that the relationship between them is not trivial and suggesting that these modes should be treated as end-members of a spectrum of possibilities. While modelling the future has limitations and assumptions, the construction of the four future supercontinents here has led to new insights into the mechanisms behind Wilson and Supercontinent cycles. For example, their relationship can be complex (in terms of being of the same or different order, or being in or out of phase with each other) and the different ways they can interact may lead to different outcomes of large-scale mantle reorganization. This work, when combined with geodynamical reconstructions since the Mesozoic allows the simulation of the entire present-day Supercontinent cycle and the respectively involved Wilson cycles. This work has the potential to be used as the background for a number of studies, it was just recently used in tidal modelling experiments to test the existence of a Supertidal cycle associated with the Supercontinent cycle.

4.3 Introduction

The present-day Earth is currently about halfway through a Supercontinent cycle (Matthews et al., 2016), which is defined as the recurring gathering and dispersion of the continents throughout Earth's history (Nance et al., 1988). 200 Ma ago all most of the continental masses were joined in a supercontinent called Pangea (Scotese, 1991; Wegener, 1912). The fragmentation of Pangea led to the formation of the Atlantic Ocean \sim 180 Ma ago. Wilson (1966) suggested that the Atlantic opened along a suture zone where another ocean once existed. This led to the concept of the Wilson cycle (Dewey and Spall, 1975), which describes the history of a given oceanic basin in three phases: opening and spreading, transformation of the passive margins (Atlantic-type margins) into active margins (Pacific-type margins), and consumption and closure (Nance et al., 1988). The fragmentation of supercontinents always leads to the formation of internal oceans (e.g., the present-day Atlantic) and the partial consumption of the surrounding oceans (e.g., the present-day Pacific). For a new supercontinent to form, one or more oceanic basins must close. The closure of an ocean corresponds to the termination of a Wilson cycle, and the final aggregation of all (or almost all) continental masses results in the end of a Supercontinent cycle. Therefore, Wilson cycles may be of different order than, and out of phase with, Supercontinent cycles (see Duarte et al. (2018) for discussion).

There is evidence that other supercontinents existed prior to Pangea (\sim 250 Myr ago; Rogers and Santosh, 2003 and references therein): Pannotia (\sim 600 Myr ago), Rodinia (\sim 1 Gyr), Columbia/Nuna (\sim 1.7 Gyr), Kenorland (\sim 2.4 Gyr) and Ur (\sim 3 Gyr; see Meert (2014) for details). This suggests a pattern of cyclicity, despite the lack of a well-defined period for the cycle (Bradley, 2011; Meert, 2014). The semantics regarding the definition of a supercontinent, and when exactly each formed and broke up, further complicates the situation (see Bradley (2011) for a discussion). Nevertheless, since Pangea broke up around 180 Myr ago (Scotese, 1991; Golonka, 2007) it is expected that a new supercontinent will form sometime in the future, within the next 200 – 300 Myr (e.g., Yoshida and Santosh (2011, 2018); Duarte et al. (2018) and references therein). For this to happen, at least one present day ocean must close: Which one, however? Four different scenarios have been proposed to achieve this: 1) closure of the Atlantic, leading to a new supercontinent called Pangea Ultima (Scotese, 2003); 2) closure of the Pacific forming Novopangea (Nield, 2007); 3) closure of both the Atlantic and the Pacific oceans, forming Aurica (Duarte et al., 2018); and 4) the closure the Arctic leading to the formation of Amasia (Mitchell et al., 2012).

The overall aim of this paper is to revisit the previously proposed scenarios to consistently simulate and standardise them using GPlates, a dedicated tectonic software (Qin et al., 2012). GPlates allows us to recreate different scenarios of supercontinent formation in parallel, allowing a direct comparison between them - including checks for advantages/plausibility and disadvantages/implausibility in each - and therefore provides new insights on how supercontinents form, how the next supercontinent will form and how supercontinents may have formed in the past.

4.4 Main concepts

4.4.1 Supercontinent Cycles and Wilson Cycles (modes of aggregation)

After the fragmentation of a supercontinent, the continental masses spread over the Earth's surface. For the next supercontinent to reform, these masses must come together again. There are several ways in which this can happen geometrically. When a supercontinent breaks up, new Atlantic-type internal oceans must form, after which either the new internal oceans close through introversion, or the old external Pacific-type ocean which surrounds the supercontinent closes through extroversion.

Introversion is the scenario that best illustrates a Wilson cycle. An interior ocean opens as the supercontinent breaks up. It then grows for a certain period of time - usually for a few hundred million years - after which subduction zones form at (or propagate into) the passive continental margins, leading to the closure of the basin. The supercontinent may then reform in much the same position and orientation as the preceding supercontinent. In this case, the Wilson cycle and Supercontinent cycle terminate simultaneously. In the second mode of closure, extroversion, the external ocean closes. After the breakup of the supercontinent, the interior Atlantic-type ocean starts by expanding in much the same way as it does during introversion. However, the interior ocean does not close in on itself, but instead continues to open while the external Pacific-type ocean closes. As a consequence, the previous internal ocean becomes the new external ocean. In this scenario, the Wilson cycle of the initial internal ocean is not completed upon the formation of the supercontinent. Instead, it may only close when the new supercontinent breaks up again during the next Supercontinent cycle. This is the case with the present-day Pacific, which is the remainder of the external ocean (Panthalassa) that formed during a previous Supercontinent cycle as the result of the breakup of Rodinia ~750 Myr ago

(Scotese, 2009). The Pacific basin evolution is a good example of a “prolonged” Wilson cycle that is out of phase with the Supercontinent cycle, i.e., it forms during the break up of a supercontinent, but it does not close during the formation of the next one.

The introversion and extroversion scenarios assume that Earth only has two major oceans involved in the Supercontinent cycle, and they assume that one ocean opens and the other closes. However, if more than two oceans are present (i.e., as in the Present; see Figure 4.1), other, more complex, scenarios are possible (Murphy and Nance, 2003; Duarte et al., 2018). For example, it would be possible to envisage a scenario in which both the Atlantic-type and Pacific-type oceans close simultaneously (Duarte et al., 2018). This would correspond to a combination scenario (Murphy and Nance, 2003; Duarte et al., 2018). In such a case, more than one Wilson cycle may occur during the lifetime of a Supercontinent cycle.

It may also be possible to have a situation where neither the internal nor external oceans close. At least one ocean must close to facilitate supercontinental assembly, however that ocean need not be the internal or external oceans. Mitchell et al. (2012) proposes a scenario, called orthoversion, in which the Arctic Ocean closes. This leads to the next supercontinent forming 90° away from the opening (rifting) point of the previous supercontinent, i.e., gathered around the North Pole.

4.4.2 How do oceans start to close? The problem of subduction initiation

To close oceans subduction zones must form around the continental margins to recycle the oceanic lithosphere back into the mantle. While this is a fundamental and accepted aspect of the decline and eventual closure of an ocean, the question arises as to how oceans develop subduction zones? This is crucial because it may control which mode of closure a Supercontinent cycle will undergo.

New oceanic lithosphere is formed at mid-ocean ridges and then carried away as the two intervening plates drift apart. When new lithosphere forms it is hot and more buoyant than the underlying asthenosphere. As it ages and cools, the oceanic lithosphere eventually becomes denser than the asthenosphere and thus negatively buoyant; this occurs around ~10 Myr after it forms (Cloos, 1993). Consequently, the lithosphere slightly sags into the mantle, forming deep abyssal plains. In an Atlantic-type ocean, oceanic plates are attached to mid oceanic ridges and continental blocks (both of which are buoyant), preventing the lithosphere from starting to sink into the mantle – a requirement for an ocean to close. Notwithstanding, observations show that

on the present-day Earth there is almost no oceanic lithosphere older than 200 Myr (Müller et al., 2008; Bradley, 2008), the exception being a portion of 350 Ma old oceanic lithosphere in the Herodotus basin west of Cyprus (Granot, 2016). Furthermore, after investigating 76 ancient passive margins, Bradley (2008) concluded that they had a mean lifespan of 178 Ma and only 5 of them had a lifespan of over 350 Ma. This suggests that, somehow, subduction zones must form at passive margins before they reach 200-300 Ma. However, as oceanic lithosphere cools, it also becomes stronger, and calculations show that there are no forces at passive margins to start a subduction spontaneously, i.e., oceanic lithosphere foundering due to their own weight (see Stern and Gerya (2018) and references therein). If oceanic lithosphere does not spontaneously subduct, a paradox develops: how do subduction zones form at passive margins of pristine Atlantic-type oceans?

It has been proposed that instead of starting spontaneously (due to their own weight), subduction zones can propagate from ocean to ocean or be forced by stresses transmitted from nearby subduction and/or collision zones (Duarte et al., 2013; Stern and Gerya, 2018). We can thus think of subduction initiation as a sort of invasive or infectious mechanism (e.g., Mueller and Phillips (1991); Scotese (2003); Duarte et al. (2018)). In fact, there are already two fully developed subduction zones in the Atlantic, the Scotia and the Lesser Antilles arcs, that seemed to have been propagated from, or induced by, subduction zones in the Pacific Ocean: (see fig. 4.1). Though, the exact mechanism by which they developed is still debated (see e.g., Eagles and Jokat (2014) for the Scotia Arc; and Wright and Wyld (2011) for the Lesser Antilles). A third place where this may be happening is in the Gibraltar Arc (Duarte et al., 2013). In this case, the subduction system is migrating from the Mediterranean into the Atlantic. Moreover, it is possible that if subduction zones do not invade an ocean over timescales of 200 – 300 Myr, some sort of weakening mechanism can come into play (e.g., hydration of oceanic lithosphere; Duarte et al. (2018)) and thus start subduction. Note that even though oceanic lithosphere must be consumed within $\sim 200 - 300$ Myr after it forms, the ocean basin can exist on the surface of the Earth for longer (e.g, the present-day Pacific; Bradley (2008)). This can happen if a balance between spreading ridges and subduction zones enter a quasi-steady state (e.g., as happened for the Panthalassa or Pacific Ocean Scotese (2009)). However, it can be argued that such a quasi-steady state would not last for longer than 600 – 700 Myr because ridges will eventually be subducted (Thorkelson, 1996).

4.4.3 Plate tectonics and mantle convection

Wilson cycles and Supercontinent cycles, and their associated processes, are an expression of plate tectonics and mantle convection. Plate tectonics is sometimes portrayed as the unifying theory of solid Earth. It describes the Earth's surface as being composed of several independently moving lithospheric plates, which incorporate the crust and a part of the upper mantle (lithospheric mantle; e.g., Wilson (1965); McKenzie and Parker (1967); Le Pichon (1968)). The present-day velocities of each of the major plates are well known and illustrated in, e.g., (Schellart et al., 2007), even though there is some debate about which reference frame is best (Schellart et al., 2008).

Recently, a more dynamic view of plate tectonics has emerged, which not only incorporates the useful kinematic description but also its driving and resisting mechanisms/forces (see Schellart and Rawlinson (2010) and references therein). It is now relatively accepted that the main driver of the plates' movement is the slab pull force of sinking lithosphere as it sinks into the mantle and, the less efficient, ridge push - a force arising from the differential of potential energy across the oceanic lithosphere. Recently, some authors have proposed that plumes can also exert an additional lateral push on the plates (see e.g., Cande and Stegman (2011); Iaffaldano et al. (2018)). Such plume push may only have a relatively localized effect, though they can have an important role during the break-up phase of supercontinents. This new dynamic framework also implies that plate tectonics is not an independent system with plates floating as solid crust on a boiling pot (the mantle), but that tectonic plates should actually be considered a part of a larger mantle circulation system that is cooling and convecting (i.e., as a cooler part of the fluid inside the pot). In this system, part of the material is heated from within, although there are still two thermal boundaries: one hot at the bottom of the mantle (near the core-mantle boundary) that generates upwelling zones and plumes and another cold at its surface (the lithosphere) where downwelling zones form (subduction zones).

A simple explanation of mantle circulation is as follows. Material in the mantle is heated from within but also at the core-mantle boundary layer. Here, less dense hot material accumulates, which begins to rise in upwellings due to thermal buoyancy. This material eventually rises through the mantle, feeding mid-ocean ridges and forming oceanic lithosphere. The oceanic lithosphere then remains at the surface for a few hundred million years before eventually being subducted and sinking back into the mantle as cold and dense lithospheric slabs, eventually cascading back to the core-mantle boundary. These slabs may carry lighter chemical compounds

that will provide an additional chemical buoyancy to the material that accumulates in this lower layer and helping to kick-start the next mantle upwelling.

In the present-day Earth's mantle there are two major regions of upwelling and two of downwelling that roughly define two convective systems (with four cells). Using seismic tomography, two areas with low shear-wave velocity anomalies below the Atlantic (the Tuzo upwelling) and the Pacific (the Jason upwelling) have been identified (e.g., Torsvik et al. (2016) and references therein). The anomalies have been interpreted as regions of low density/high temperature that seem to correspond to hot ascending material, and they are referred to as Large Low Shear Velocity Provinces (LLSVPs). In turn, there are two major downwellings composed of descending slabs in the Eastern and Western Pacific margins (the Andean/Cascadia and the Marianas/Japan/Tonga subduction systems, respectively). These are also well imaged in tomography data as (high shear-wave velocity) anomalies, which correspond to cold/dense material.

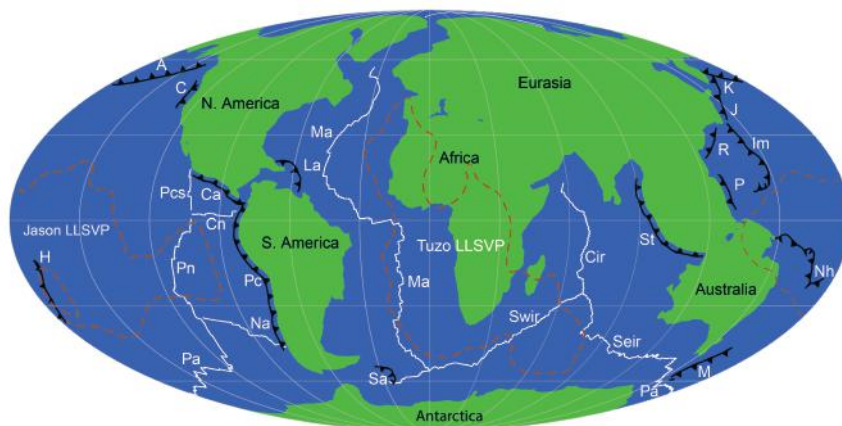


Figure 4.1: GPlates set-up of present-day Earth used as the initial condition for each of the future scenarios. White lines represent mid-ocean ridges: Ma, Mid- Atlantic ridge; Swir, SW Indian Ridge; Cir, Central Indian ridge; Seir, SE Indian Ridge; Pa, Pacific- Antarctic spreading centre; Na, Nazca-Antarctic spreading center; Pn, Pacific-Nazca spreading center; Cn, Cocos-Nazca spreading centre; Pcs, Pacific-Cocos spreading center; Ar, Arctic Ridge. Black lines represent subduction zones: A, Aleutian trench; Ca, Central American trench; C, Cascadia subduction zone; H, Hikurangi trench; Im, Izu-Marianas trench; J, Japan trench; K, Kurile Trench; La, Lesser Antilles arc; M, Macquarie subduction zone; Nh, New Hebrides subduction zone; P, Philippine trench; R, Ryukyu subduction zone; Sa, Scotia arc; St, Sumatra trench. Brown dashed lines represent the extents of the LLSVPs discussed in (Torsvik et al., 2016), marked above as Tuzo and Jason. (For interpretation of the references to colour in this figure legend, the reader is referred to the web version of this article).

At present, the plates are driven by these descending slabs of dense oceanic lithosphere, while the two major upwellings feed or have fed the Atlantic and Pacific mid-ocean ridges. For example, the break-up of Pangea may have been caused by one of these upwellings penetrating through the continental crust and initiating the formation of the Atlantic (Murphy et al., 2009;

Torsvik et al., 2010). However, some ridges seem to be offset from the upwelling regions, meaning that these ridges may presently be passive and fed by upper mantle material. Moreover, it is also recognized today that the ascending material does not correspond to the classic idea of mantle plumes. Instead, the position of the plumes may be controlled by the aforementioned upwellings: mantle plumes seem to be generated at the boundaries of these upwellings. These boundaries are known as plume generation zones (PGZs; Burke et al. (2008)) and the plumes generated there feed the majority of hotspots on Earth (Torsvik et al., 2016). Understanding of the formation, behaviour, and tenure of these LLSVPs and PGZs will be crucial in the determination of their role in the breakup of supercontinents and the maintenance of oceans (Boschman and van Hinsbergen, 2016).

4.5 Methodology

Because of an abundance of previous investigations into past supercontinents and cycles ((Rogers and Santosh, 2003; Murphy and Nance, 2003, 2005; Bradley, 2011; Merdith et al., 2017) see Table 4.1), we have gained an insight on how supercontinents form and evolve. Furthermore, since we know that there was a somewhat regular pattern in the disaggregation and formation of past supercontinents, it is reasonable to assume that this pattern may repeat itself in the future. Although there are a number of predictions about the future supercontinent (e.g., Hoffman (1999)), with many nuances, we choose to present here the four potential scenarios that illustrate the main modes of oceanic closure and supercontinent formation described in section 4.4.1. Each of these predictions independently reaches supercontinent accretion within the next 300 Ma, highlighting that we are close to the mid-point of the current Supercontinent cycle. The four explored scenarios, along with past supercontinents are summarised in Table (4.1).

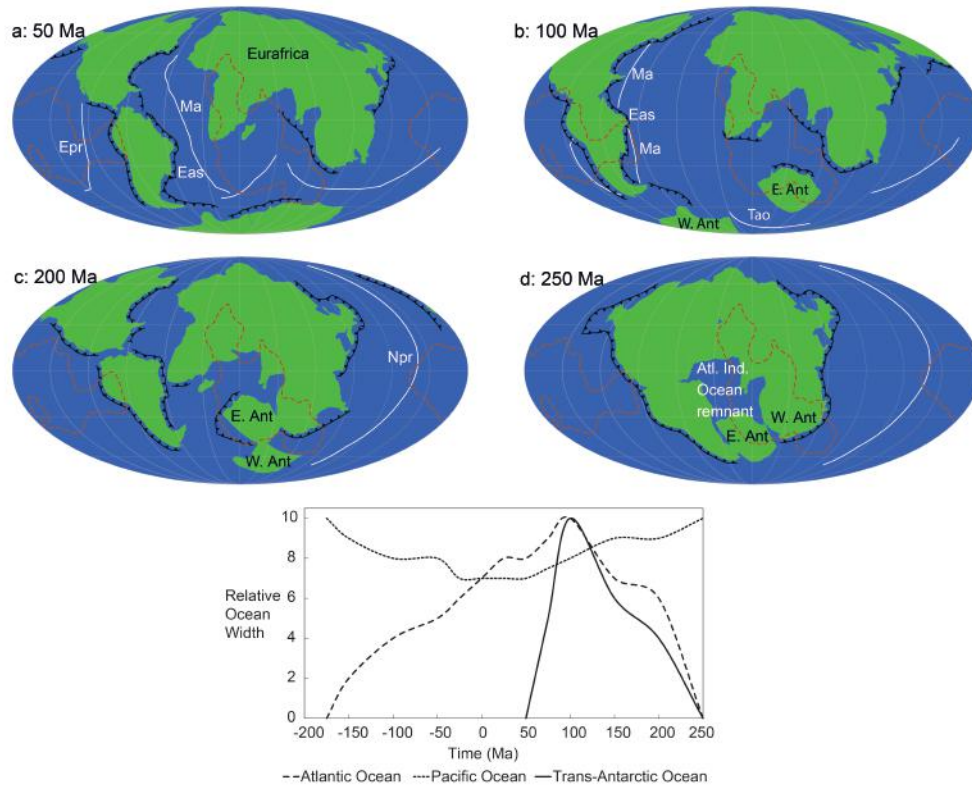


Figure 4.2: (a–d): A map of the development of Pangea Ultima, showing 50 Ma, 100 Ma, 200 Ma and 250 Ma. Speculative subduction zones and ridges are represented in red and white, respectively. Brown represents LLSVP extents as in (Torsvik et al., 2016). The centre point of the map is along the Greenwich meridian (0°). Eas, East American subduction zone; Ma, Mid-Atlantic ridge; E. Ant, East Antarctica; W. Ant, West Antarctica. (e): An illustration of the development of the supercontinent Pangea Ultima since the break-up of Pangaea. The major oceans of the Pacific, Atlantic, and Trans-Antarctic are presented. Other oceans and seas have been omitted (see figure 4.2 a–d). The oceans widths have been normalized between values of 0 and 10, representing the smallest and largest extent of each ocean.

Table 4.1: A complete list of all the supercontinents believed to have existed during the period of active plate tectonics on Earth up to the present-day and their modes of formation, along with the four scenarios of the formation of the next supercontinent.

Supercontinent	Tenure (Ma)	Mode of Formation	Supporting References
Ur	~3000 Myr	Not Known	Rogers and Santosh (2003)
Kenorland/Superia/Scavia	~2500 Myr	Not Known	Meert (2014)
Columbia/Nuna	1800 - 1500 Myr	Introversion	Rogers and Santosh (2003); Murphy and Nance (2003)
Rodinia	1100 - 800 Myr	Extroversion	Merdith et al. (2017); Dalziel et al. (2000); Murphy and Nance (2003)
(Greater) Gondwana/Pannotia	650 - 560 Myr	Extroversion/Orthoversion	Merdith et al. (2017); Murphy and Nance (2005)
Pangea	250 - 180 Myr	Introversion/Orthoversion	Golonka (2007); Murphy and Nance (2005); Mitchell et al. (2012)
Pangea Ultima	+250 Myr - Distant future	Introversion	Scotese (2003); Yoshida and Santosh (2018)
Novopangea	+200 Myr - Distant future	Extroversion	Nield (2007); Yoshida and Santosh (2018)
Aurica	+250 Myr - Distant future	Combination	Duarte et al. (2018); Yoshida and Santosh (2018)
Amasia	+200 Myr - Distant future	Orthoversion	Mitchell et al. (2012); Yoshida and Santosh (2018)

All the explored future scenarios were proposed independently at different times by different authors (see Table 4.1). Because of this, each of the scenarios have their own details and were originally explored using different space and time scales. There is therefore an issue when

comparing the scenarios because they are not standardised and do not necessarily resolve the same time periods. For example, the prediction of the future Pangea Ultima by (Scotese, 2003) is presented at time slices for 50, 100 and 250 Ma into the future, whereas Aurica by (Duarte et al., 2018) is presented for 20, 150 and 300 Ma. Consequently, direct comparisons between each scenario for specific time slices is difficult, and to compare the future scenarios directly, we need to standardise them with respect to projections and time slices investigated. This is the main aim of this paper.

Consequently, we will reproduce all four scenarios for the formation of the next supercontinent in a standardised environment using a state-of-the-art software that allows the kinematic manipulation of tectonic plates and continents – GPLates (see Qin et al. (2012) see <https://www.gplates.org/> for the original files; also the modified files with our different scenarios are provided as supplementary material <https://www.sciencedirect.com/science/article/abs/pii/S0921818118302054>). GPLates can be used for a number of different types of tectonic and geodynamical modelling endeavours, e.g., to visualise geolocations, as boundary conditions for geodynamical modelling, to reconstruct plate motions (kinematics), or to visualise predictions of the tectonic future of the Earth. The software is able to move plates and continents through time using editable rotation files (.rot) enabling the joining kinematic and geodynamic (conceptual) models. These models can be exported from the GPLates program in a large number of formats compatible with other GIS software, or simply as images presented in various widely used planetary map projections.

For our study, continental lithospheric extents were taken from Matthews et al. (2016), imported from the GPLates user database. Subduction zones and ridge extents were then drawn in as schematic geological features in GPLates. Therefore, all geological features included in this work were annotated in GPLates with timings, plate id's and descriptions. The models created do not explicitly incorporate continental deformation, but allow some overlap between continents, which somewhat mimics intercontinental deformation. We also did not simulate continental accretion or erosion (e.g., forearc accretion or erosion at subduction zones). Each of the scenarios was modelled from the same initial geometric conditions shown in Fig. (4.1). Between 0 and 25 Ma, the continents follow present-day drift velocities based on (Schellart et al., 2007). Rotation files for each of the scenarios using these velocities were written as a tab delimited text file readable by GPLates. After 25 Myr, each scenario was constructed as faithfully as possible to the original published work. To do this, we have visually moved the

continental blocks to their future locations based on each author’s construction. When manually manipulating the continents, GPlates then automatically writes those instructions to the rotation files. Note that then GPlates can provide scenarios that are continuous in space and time (see supplementary material <https://www.sciencedirect.com/science/article/abs/pii/S0921818118302054>). However, these continuous animations only show the continental blocks. The positions of ridges and subduction zones are not animated and were only drawn in schematically for specific time slices (see Figs. 4.2 to 4.5). The computed velocities for each continental block in each scenario are provided in Table (4.2). The average velocities, 3.9 cm yr^{-1} , are close to the paleo Meso-Cenozoic plate velocities reported in Young et al. (2019), though slightly lower (in particular Amasia). This means that the timing of the next supercontinent accretion may be overestimated in all the scenarios (see section 5.6).

Table 4.2: Average velocities in cm yr^{-1} for each of the major continents in each scenario, and total average plate velocity for each of the scenarios

	Pangea Ultima	Novopangea	Aurica	Amasia
Africa	4.5	3.9	7.9	1.4
Australia	6.2	4.5	1.8	6.0
East Antarctica	3.7	4.9	2.9	0.2
East Asia	N/A	N/A	0.8	N/A
Eurasia	4.2	3.8	7.7	0.6
Greenland	2.3	3.0	4.3	0.6
North America	4.0	3.4	4.0	0.8
Somalia plate	N/A	6.5	N/A	N/A
South America	5.5	5.8	5.5	5.3
West Antarctica	6.0	N/A	N/A	N/A
Average total	4.5	4.5	4.4	2.1

4.6 Back to the future

4.6.1 Introversion: Pangea Ultima

Pangea Ultima is an introversion scenario in which the Atlantic Ocean closes in an asymmetrical fashion (Scotese, 2003). This is because it is assumed that the two already existing subduction zones in the Atlantic will propagate along the Eastern margins of the Americas. The Atlantic then continues to open at the present-day rates until a large subduction system develops, possibly in the next 25-50 Myr (see Fig. 4.2a). During this period Africa continues to move north and fully collides with Eurasia forming the mega-continent Eurafica, whereas the Americas and Eurafica continue to drift apart.

After 50 Myr, although the new Atlantic subduction system is fully developed, the Atlantic mid-ocean ridges may continue to spread, delaying the point at which the bordering continents start to converge. Therefore, the Atlantic continues to open until 100 Ma because the mid-Atlantic ridge continues to produce oceanic lithosphere that can compensate lithospheric consumption at subduction zones. The lithosphere lying on the Western side of the ridge is eventually subducted whereas the lithosphere on the Eastern side of the ridge is not, as it is attached to the passive margins of the Eurafrikan mega-continent. By this time, Australia has collided with South-East Asia terminating the Mariana trench and a small portion of the Pacific Ocean. Antarctica has also begun to drift north into the Indian Ocean basin (see Fig. 4.2b).

By 100 Ma the mid-Atlantic ridge starts to undergo subduction at the East American subduction zones (Fig. 4.2b). This marks the midpoint of the Atlantic Wilson cycle because with the subduction of the ridge, the ocean can no longer continue to open and must close. At this point, Antarctica has rifted into two separate parts generating a small actively spreading new ocean. East Antarctica is still drifting north closing the southern Indian Ocean. However, the western Antarctic fragment remains in the Southern Ocean, following the same path as East Antarctica but at a significantly slower rate because of the spreading of the new Trans-Antarctic Ocean.

In 200 Myr, the Atlantic Ocean will be partially closed. South Africa is now less than a 1000 km from South America (Fig. 4.2c). The subduction of the Mid-Atlantic ridge, the advanced age of the Atlantic oceanic lithosphere, the propagation of subduction zones to the southern tip of Africa, and the generation of a new meridional spreading centre in the Arctic and Pacific Ocean all contributed to a rapid closure of the Atlantic Ocean. Antarctica has also started to reform at this time. The trans-Antarctic ocean was very short lived: when it ceased spreading, the Antarctic fragments could reunite as they combined with Indonesia, shutting down the Sumatra subduction zone in the process.

In 250 Myr, Pangea Ultima has formed, with a remnant of ancient Indian and Atlantic Ocean forming an inland sea of the supercontinent. At this time, an almost complete ring of subduction zones surrounds the supercontinent. Because the coasts of Pangea Ultima are the remnants of the coast of the Pacific Ocean, it has formed over the Tuzo LLSVP.

In Pangea Ultima the Supercontinent cycle and the Wilson cycle are in phase for the Atlantic (Fig. 4.2e). The new Antarctic Ocean formed develops a Wilson cycle out of phase with the Supercontinent cycle however, as it does not fully close with the formation of Pangea Ultima.

Fig. (4.2e) also shows that the Pacific remains the dominant ocean for the duration of the scenario despite the other oceans presented growing and shrinking over the 500 Myr presented in Fig. (4.2e).

4.6.2 Extroversion: Novopangea

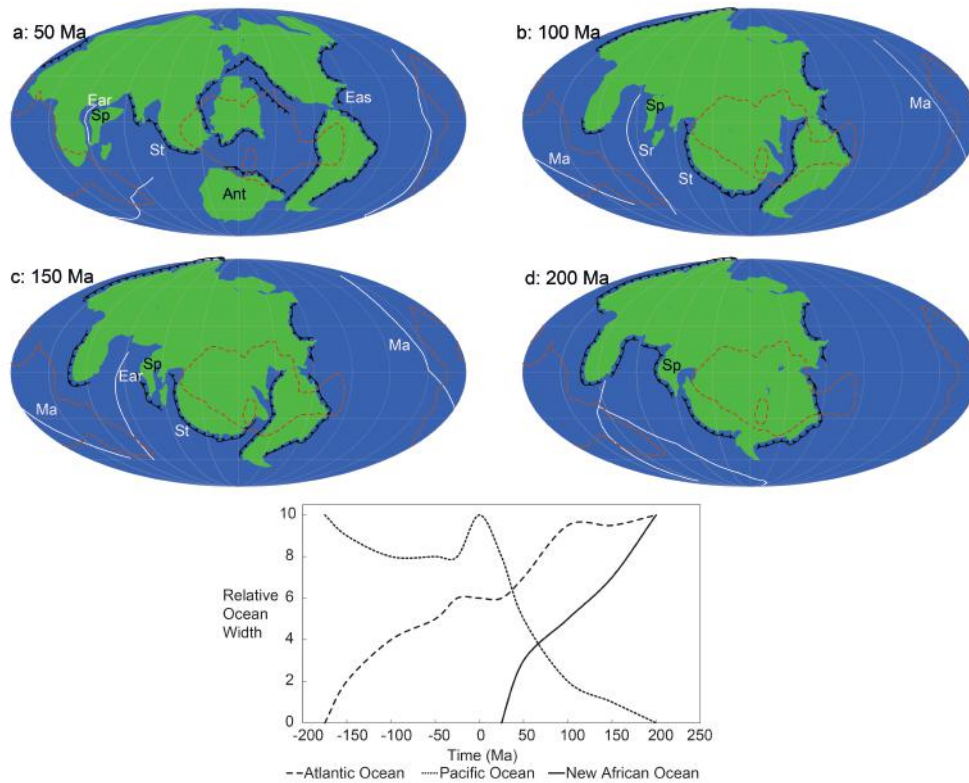


Figure 4.3: (a–d): Maps of Novopangea from top left to bottom right 50 Ma, 100 Ma, 150 Ma and 200 Ma respectively. Speculative subduction zones and ridges are represented in red and white respectively. Yellow represents LLSVP extents as in Torsvik et al. (2016). The centre point of this map is along the international date line (180°). Ear, East African rift; Sp, Somalia plate; St, Sumatra trench; Ant, Antarctica; Eas, East American subduction zone; Ma, Mid Atlantic. (e): A graphical illustration of the development of the supercontinent of Novopangea. The major oceans of the Pacific, Atlantic and New African are presented. Other oceans and seas have been omitted (see Fig. 4.3a–d).

Novopangea is an extroversion scenario in which the Pacific Ocean closes. It is based on the fact that the Pacific is an old oceanic basin (older than Pangea) surrounded by subduction zones that are presently converging (Hatton, 1997; Murphy and Nance, 2003). Conversely, the present-day Atlantic is a new ocean and home to the largest mid-ocean ridge on Earth and only a few short subduction zones that may not develop into a large-scale subduction system (Dalziel et al., 2013; Stern and Gerya, 2018). Therefore, in this scenario the continents will continue to drift apart at approximately the same velocities as present-day for the next 200

Myr (see Schellart et al. (2008) for details). The East African rift system will also continue to develop, eventually becoming an ocean basin that replaces the Indian Ocean. See Fig. (4.3) for the illustrations related to the discussion below.

In 50 Myr, the Pacific Ocean will be a series of seaways between Asia, Australia, Antarctica and the Americas. The northward drift of Australia and Antarctica, together with the convergent drift of Asia, and the Americas due to the continued opening of the Atlantic, reduces the area of the Pacific Ocean. Conversely, the highly active Mid-Atlantic ridge, combined with the closure of the Pacific and little to no subduction in the Atlantic, allows it to grow quickly: by 50 Myr, the Atlantic Ocean is over three times its present-day width. Some subduction zones have developed at the basin's edges, particularly along the West coast of Europe and North-west Africa (Duarte et al., 2013). The opening of the East African Ocean has already started and is in a similar state to the Red sea at present. The Red Sea and the Mediterranean, however, have both closed after 50 Myr.

In 100 Ma, the Pacific is mostly closed, except for an area west of South America (Fig. 4.3b). The Atlantic has continued to open, as has the East African Ocean. However, the almost complete closure of the Indian and Pacific Ocean basins, and the near complete assembly of Novopangea, means that the Atlantic can no longer continue to open. The closure of the Pacific Ocean also shuts down a significant length of subduction zones. However, because of the way that the Indian Ocean closes and the development of the subduction zones in the Atlantic Ocean, the planet retains a considerable extent of subduction zones throughout (See fig. 4.3d).

By 150 Myr the Pacific is nearly closed, with very little oceanic lithosphere left (Fig. 4.3b-c). The ongoing continental collisions between the Americas and Eastern Asia will likely slow down oceanic closure, much like the Mediterranean is doing today. During this time a portion of the Indian Ocean is almost fully recycled as consequence of the migration of the Somalia plate towards the Sumatra subduction zone and the continued opening of the East African Ocean (Fig. 4.3c). At this point, the Atlantic has developed a large-scale subduction system. Some of these subduction zones may also propagate into the margins of the East African Ocean.

In 200 Ma, Novopangea is fully formed; Somalia and Madagascar have closed the majority of the Northern Indian Ocean, and the Pacific Ocean has completely closed leaving the Atlantic to be the surrounding ocean of the supercontinent (Fig. 4.3d).

The closure of the Pacific leads to the elimination of a large amount of subduction zones, and if new subduction systems do not start continuously in the ocean surrounding the super-

continent (i.e., the Atlantic), Earth may undergo a period of tectonic quiescence (see Silver and Behn (2008) for details on the topic). However, new subduction zones are invading the Atlantic (Duarte et al., 2013, 2018), and it is therefore likely that when Novopangea forms, these subduction systems have already propagated along the margins of the Atlantic and eventually of the Eastern African Ocean. The Sumatra subduction system may also propagate into the Eastern African Ocean as the collision of the Somalia block may not fully shut this system down.

Novopangea forms over the Jason LLSVP. The closure of the Pacific Ocean marks the end of its Wilson cycle, which in this case lasted for over a billion years (Scotese (2009); Merdith et al. (2017) and references therein), from the breakup of Rodinia ~ 750 Ma ago to the formation of Novopangea. The Pacific Ocean (and the former Panthalassa) thus persisted over several full Supercontinent cycles. This is a special case in which the ocean's Wilson cycle is in phase with, but of different order than, the Supercontinent cycle. Note, however, that even though the Pacific (and Panthalassa) basins were long-lived, its oceanic lithosphere underwent several phases of renewal (Boschman and van Hinsbergen, 2016).

4.6.3 Combination: Aurica

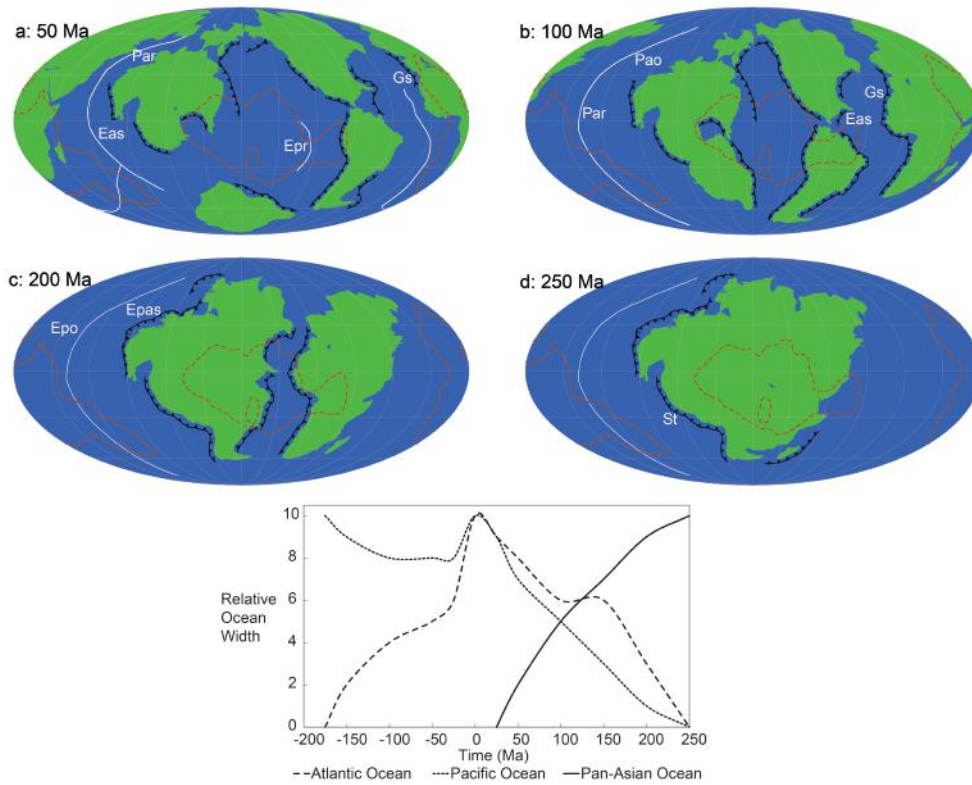


Figure 4.4: (a–d): Maps of Aurica from top left to bottom right 50 Ma, 100 Ma, 200 Ma and 250 Ma, respectively. Speculative subduction zones and ridges are represented in red and white, respectively. Yellow represents LLSVP extents as in Torsvik et al. (2016). The centre point of this map is along the international date line (180°). Par, Pan-Asian rift, Epr, East Pacific rise; Eas, East American subduction zone; Gs, Gibraltar subduction zone; Epas, East Pan-Asian subduction zone (e): A graphical illustration of the development of the supercontinent of Aurica. The major oceans of the Pacific, Atlantic and Pan-Asian are presented. Other oceans and seas have been omitted.

Aurica is a combination scenario where both the Atlantic and Pacific Oceans close. Such conjecture is based on the fact that both the Atlantic and the Pacific Oceans already have portions of oceanic lithosphere with ages close to 200 Myr, and the average age of the present-day oceanic lithosphere is around 60 Myr old, with only a few regions older than this (Müller et al., 2008). Moreover, during Earth’s history, oceanic lithosphere older than a few hundred million years can hardly persist at its surface (Bradley, 2011). This is consubstantiated by the observation that subduction zones are propagating into and inside the Atlantic, meaning that, similarly to the Pacific, the Atlantic may be fated to close. To achieve this, at least one new ocean must be created. In this scenario, a large intracontinental rift develops along the border of India and Pakistan between the Eurasia and several East Asian tectonic blocks/subplates, which propagates along the Himalaya and through the Baikal rift and Kamchatka plate boundary forming

the Pan-Asian Ocean (see Fig. 4.4 and Duarte et al., 2018).

In 50 Ma, subduction zones have propagated in the Atlantic (Fig. 4.4a). However, a balance between spreading and consumption allows it to continue to open for some time. The Pacific accelerates its closure due to the continued subduction of the East Pacific rise and the now fully developed Pan-Asian Rift. Furthermore, much like in the extroversion scenario described in section 4.6.2, Antarctica continues drifting north into the Pacific Ocean, contributing to the ocean's closure. At this time, Australia has fully collided with the Eastern Asian continent. In 100 Ma, both the Atlantic and the Pacific spreading centres have been subducted (see Fig. 4.4b), meaning that they can no longer compensate consumption at subduction zones. The Pan-Asian Ocean becomes the largest ocean on Earth, while the Pacific and the Atlantic have closed significantly. At this point, Antarctica also starts to collide with the Eastern Asian continent. Subduction zones have now formed in the two Atlantic margins, leading to an Atlantic "ring of fire". Fig. (4.4c) shows the 200 Ma time slice, in which the Pacific has fully closed, and the Atlantic is entering a terminal stage of closure. The Pan-Asian Ocean continues to open and is fully merged with the former Indian Ocean. At this point, it is almost fully surrounded by passive margins, with the exception of the Sumatra subduction system that may propagate into the Pan-Asian basin with time. By 250 Ma, the Atlantic has completely closed forming Aurica surrounded by the Pan-Asian Ocean (Fig. 4.4d). Aurica forms near the antipodes of Pangea, precisely over the Jason LLSVP. A large-scale subduction system does not fully form around the continent, potentially leading to a period of tectonic quiescence. Nevertheless, subduction systems such as Sumatra can propagate along Aurica's margins re-establishing plate recycling rates to that of normal functioning of plate tectonics. This scenario involves the termination of the Wilson cycles of the Atlantic and the Pacific, and the beginning of the one for the Pan-Asian Ocean (see Fig. 4.4e). The Aurica scenario thus involves two Wilson cycles in phase with the Supercontinent cycle, although the Atlantic one is of same order and the Pacific one of different order to the Supercontinent cycle, whereas the Pan-Asian Wilson cycle is out of phase with the Supercontinent cycle.

4.6.4 Orthoversion: Amasia

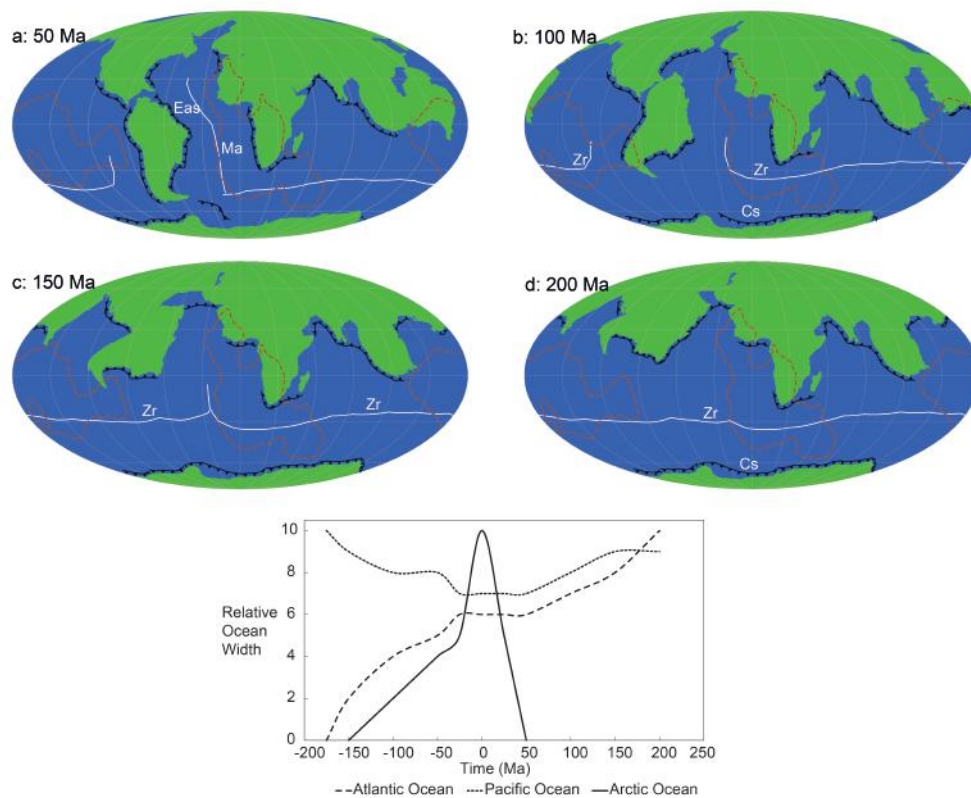


Figure 4.5: (a–d): Maps of Amasia from top left to bottom right 50 Ma, 100 Ma, 150 Ma and 200 Ma, respectively. Speculative subduction zones and ridges are represented in red and white, respectively. Yellow represents LLSVP extents as in Torsvik et al. (2016). The centre point of this map is along the Greenwich meridian (0°). Eas, East American subduction zone; Ma, Mid-Atlantic ridge; Zr, Zonal ridge; Cs, Circumferential Antarctic subduction zone (e): A graphical illustration of the development of the supercontinent of Amasia. The major oceans of the Pacific, Atlantic and Arctic are presented. Other oceans and seas have been omitted.

In the orthoversion scenario the new supercontinent forms by the closure of the Arctic Ocean (Mitchell et al., 2012). This is based on the rationale that supercontinents form at 90° from the previous supercontinent because of a bias on the mantle structure left by the preceding supercontinent. Pangea’s subduction zones left a remnant volume of downwelling mantle, a “ring of slabs”, that may confer a positive bias in plate drift towards a segment of this ring. Also, according to the present-day drift of the continents, it is likely that they will (on large scales) continue moving north.

In 50 Myr, the Mediterranean, Arctic, and part of the East China and Philippine seas have been closed by the collision of Africa with Eurasia, Asia with the Americas and Australia with East China, respectively (see Fig. 4.5a). Subduction zones propagate along the margins of the Atlantic and Indian oceans, and the Mid-Atlantic ridge has lost some of its northern extent. The

Americas split, temporarily forming a new gateway between the Pacific and Atlantic Oceans.

In 100 Ma, South America begins rotating clockwise, pulled by the Peru-Chile trench (Fig. 4.5b). This drift represents the only major large-scale reorganisation of continental lithosphere; all other continents, with exception of Antarctica, experience only slow northward drift. Subduction zones continue to propagate along the Antarctic, African, South American and the East Asian margins, while a southern hemisphere ridge system becomes dominant.

In 150 Ma, the Northern Atlantic and the Pacific Ocean have partially closed due to the aggregation of the continents around the North Pole and the continued rotation of South America. At this point, Australia collides with Asia closing the Sea of Okhotsk (Fig. 4.5c).

In 200 Myr, Amasia has formed by aggregating all continental masses, with the exception of Antarctica, as South America completes its rotation and collides with North America (Fig. 4.5d). Note that in this scenario oceans containing old lithosphere, such as the Pacific, the Atlantic, and the Indian Oceans, do not close. Therefore, it is likely that a large-scale subduction system develops along the southern margins of Amasia.

This is also the only supercontinent that does not form over a present-day LLSVP. However, it is debatable if LLSVPs persist in the same region over large periods of time, or if they are rearranged as a function of the reorganization of plates and continents (Torsvik et al., 2010). Also, Antarctica remains near its current location, meaning that Amasia technically is not a complete supercontinent (Bradley, 2011).

In the orthoversion scenario, the Atlantic and the Pacific Wilson cycles do not terminate with the formation of the supercontinent, and the Arctic Ocean undergoes a short Wilson cycle (see Fig. 4.5e). All the Wilson cycles are out of phase with the Supercontinent cycle.

4.6.5 Ocean Divergence and convergence rates

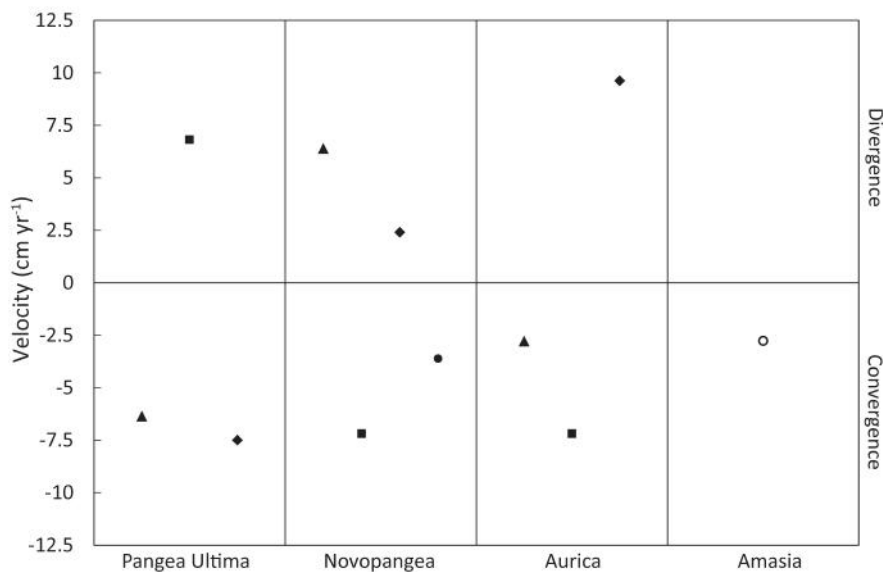


Figure 4.6: Divergence (positive) and Convergence (negative) rates in cm yr^{-1} for the Atlantic ocean (triangles), Pacific ocean (squares), Indian ocean (filled circles), Arctic ocean (empty circles), and new oceans (Trans-Antarctic – Pangea Ultima, East African - Novopangea, and Pan-Asia – Aurica)(Diamonds).

In Table (4.2) we present the drift velocities of the continental blocks in each scenario. With the values in Table (4.2), and other data from GPlates, we were able to calculate the rates of divergence and convergence for each of the oceans in each scenario (see Fig. 4.6). In the Pangea Ultima scenario the divergence rate of the Pacific Ocean is around 6.8 cm yr^{-1} , which is approximately the convergence rate at which the Atlantic closes (6.3 cm yr^{-1}). This is because the Atlantic closure is only being compensated by the opening of the Pacific, with no other major oceans involved. This is an expression of the classical view of the Wilson cycle and Supercontinent cycle in which only two major oceans are involved, and one closes at the expense of the other. The Novopangea scenario also shows similar values of divergence and convergence, in this case the Pacific closes at a rate of 7.1 cm yr^{-1} while the Atlantic opens at a rate of 6.3 cm yr^{-1} . Here again, the scenario is mostly controlled by the opening and closure of two major oceans (the Pacific and the Atlantic) and therefore their divergence and convergence rates are almost balanced. However, this scenario also involves the opening of the East African Ocean (2.4 cm yr^{-1}) at the expense of the Indian ocean (3.6 cm yr^{-1}). In the Aurica scenario, both the Atlantic and the Pacific close; the Atlantic at a rate of $\sim 2.8 \text{ cm yr}^{-1}$ and the Pacific at a rate of 7.2 cm yr^{-1} . This simultaneous closure has to be balanced by the development of the Pan-Asian Ocean, which opens at a rate of 9.6 cm yr^{-1} . This explains the high divergence rate

of the Pan-Asian Ocean. In the Amasia scenario only the Arctic Ocean closes, at a rate of 2.8 cm yr^{-1} . This is a result of both the small size of the Arctic basin and the fact that the timing of supercontinent formation was set to 200 Ma.

4.7 Discussion

The aim of this paper is to reconcile the scenarios of the formation of the next supercontinent as proposed by (Scotese, 2003; Nield, 2007; Duarte et al., 2018; Mitchell et al., 2012). Using GPlates and the general rules of plate tectonics, we have recreated the four scenarios from the same initial condition, leading to a new insight into the dynamics of Supercontinent and Wilson cycles. Due to the limited geological record the past supercontinents are poorly resolved, and the number of cycles are limited by the age of the Earth (and eventually by the emergence of plate tectonics). This is particularly true for the Wilson cycles because most of the oceanic basins are destroyed over the corresponding Supercontinent cycle(s). Studying these cycles from a known (and excellently resolved) starting position (i.e., the present day) and running the current Supercontinent cycle forward has allowed us to better understand how these cycles work, how they interact with each other, and how they affect the configuration of the Earth's surface and the dynamics of the mantle. It should be noted that the degrees of freedom increase as we move forward into the Future and that it is why we have considered several end member scenarios.

There are several advantages and limitations to the approach we used. The main advantage is that we, for the first time, used a single software to simulate all the four proposed scenarios for the formation of the future supercontinents. This allowed us to carry out standardised models with similar initial and boundary conditions using the available GPlates data and capacities, providing us with new tools to discuss these scenarios in parallel and better understand the geodynamic processes involved in each one of them. The objective of modelling the future is not just trying to guess what is going to occur but instead is a way of pushing the boundaries of our knowledge and trying to understand what the main processes operating at these long-time scales are.

Obviously, this approach also involves simplifications, leading to limitations. For example, we explored scenarios previously proposed by other authors that may not be up-to-date with new knowledge and techniques. They also often rely on only a few (and different) time slices. This implied a significant amount of interpretation, completion and smoothing within

and between the different scenarios. We also assume that there is a Supercontinent cycle (even if not with a constant period), which implies that a new supercontinent should form within the next ~ 200 - 300 Myr. But, the idea of a supercontinent, and the cycle itself, is an idealization (Bradley, 2011). It may well be that not all the continental masses come together in one Supercontinent cycle, as in the Amasia scenario. Furthermore, periods of Supercontinent assembly and break up are highly diachronic and often overlap (Bradley, 2011). The concept of Wilson cycles is also partially an idealization. It works well on interior oceanic basins that open and close during one Supercontinent cycle, such as the classical opening and closing of the Atlantic. However, it starts losing its meaning when we apply it to exterior oceans and oceans that do not precisely fit either the definition of exterior or interior (e.g., the Indian Ocean). Furthermore, some Wilson cycles may be incomplete, for example if a basin does not fully close, or if it closes in a subsequent Supercontinent cycle, in which case it would be severely delayed (e.g., in Pangea Ultima).

Another issue is subduction initiation in Atlantic-type oceans; we have just assumed that it can happen. This is a controversial topic and the driving mechanisms of subduction initiation are still fundamentally unknown (see, e.g., Duarte et al. (2013); Marques et al. (2014); Stern and Gerya (2018)). In any case, we have considered that passive margins are the most likely place for subduction zones to develop, either spontaneously or by invasion (Duarte et al., 2013), and even if they form intra-oceanically, they will quickly migrate (retreat) to passive margins (Whattam and Stern, 2011). This level of discussion, however, is out of the scope of this paper, but will be further investigated at a later date.

In our reasoning, it is also explicitly implied that oceanic lithosphere much older than ~ 200 Ma is gravitationally unstable and will be removed from the Earth's surface. This is supported by present-day observations of the seafloor age (Müller et al., 2008) and observation of the age of oceanic lithosphere in past cycles (Bradley, 2008, 2011). We have also assumed simple dynamics for mantle convection that considers major subduction systems as large-scale mantle downwellings and accounts for the existence of major mantle upwellings, defining two major convection systems. In our scenarios, these systems can split or merge, but the geometric constraints imposed by the Supercontinent cycle may force the Earth to be close to the two-convection-system mode. Further work should be pursued in order to understand the feedbacks between mantle convection and Supercontinent cycles (recent attempts are provided by Rolf et al. (2014); Coltice et al. (2012); Yoshida and Santosh (2018)).

In Table (4.2) we have plotted all of the continent's velocities for each of the scenarios. They all show average velocities of around 4 cm yr^{-1} , with the exception of Amasia (2.13 cm yr^{-1}). These velocities are close to the average paleo (Meso-Cenozoic) velocities reported by Young et al. (2019) of 6 cm yr^{-1} . Our lower average velocities mean that the timing of the next Supercontinent gathering may be overestimated in all the scenarios. Slightly higher velocities would probably result in a quicker supercontinent aggregation. For example, if the continent velocities were sped up, Amasia could form in 100 Ma or sooner.

It should be noted that these values are also consistent with the convergence rates at subduction zones, which have a global value of 5.6 cm yr^{-1} (Duarte et al., 2018). Convergence rates at subduction zones are an expression of the rate at which plates are consumed in the mantle. This makes sense and it means that in these scenarios plates (and therefore the continents) move on average at the velocity at which the slabs sink in the upper mantle.

Finally, it is worth remembering that these scenarios are useful idealizations based on concepts that describe end-members. For example, the classical introversion and extroversion scenarios were strongly conditioned by the misconception that Supercontinent cycles and Wilson cycles are the same thing. If this was the case, once a supercontinent, e.g., Pangea, breaks up it only has two options to reform the next supercontinent: by closing the Atlantic or by closing the Pacific. The problem is that this assumes that there were only two major continental masses travelling around the Earth. However, if more continents, and thus degrees of freedom, are considered, orthoversion and combination components are possible. One possibility is that whenever a supercontinent breaks up it may experience components of each of these scenarios during the corresponding Supercontinent cycle.

What is the use of modelling the remainder of the present Supercontinent cycle? Part of this work was motivated by ongoing parallel research on super-tidal cycles (Green et al., 2018), where it is suggested that the disposition of the continents and the geometry of the oceanic basins exert a first-order control on global tidal dynamics. Consequently, we hope to use the present scenarios as boundary condition in a global tidal model to further our understanding of the future Earth system.

5 Back to the future II: Tidal evolution of four supercontinent scenarios

Hannah S. Davies, J. A. Mattias Green, & João C. Duarte

(This chapter is presented in paper format as published in *Earth System Dynamics*, Davies et al. (2020))

5.1 Summary

The subject of this chapter presents results of tidal modelling of four future scenarios of the next supercontinent gathering. Tidal modelling with OTIS was carried out using the GPlates kinematic tectonic future reconstructions presented in Davies et al. (2018) to assess how the tide changes over geological time over the remainder of the current supercontinent cycle. We find the present day is in a state of elevated tidal dissipation due to North Atlantic resonance. As the Atlantic continues to open in each scenario, the resonance of the basin is lost, however resonance occurs in other ocean basins and again in the Atlantic in some scenarios as they progress. In general, we find that as an ocean basin develops through its respective Wilson cycle, it can (provided the ocean widens sufficiently i.e., widens as much as the present day Atlantic) support resonance multiple times in a supercontinent cycle.

5.2 Abstract

The Earth is currently 180 Myr into a supercontinent cycle that began with the break-up of Pangaea and which will end around 200–250 Myr (million years) in the future, as the next supercontinent forms. As the continents move around the planet they change the geometry of ocean basins, and thereby modify their resonant properties. In doing so, oceans move through tidal resonance, causing the global tides to be profoundly affected. Here, we use a dedicated and established global tidal model to simulate the evolution of tides during four future supercontinent scenarios. We show that the number of tidal resonances on Earth varies between one and five in a supercontinent cycle and that they last for no longer than 20 Myr. They occur in opening basins after about 140 – 180 Myr, an age equivalent to the present-day Atlantic Ocean, which is near resonance for the dominating semi-diurnal tide. They also occur when an ocean basin is closing, highlighting that within its lifetime, a large ocean basin – its history described by the Wilson cycle – may go through two resonances: one when opening and one when closing. The results further support the existence of a super-tidal cycle associated with the supercontinent cycle and gives a deep-time proxy for global tidal energetics.

5.3 Introduction

The continents have coalesced into supercontinents and then dispersed several times in Earth's history in a process known as the supercontinent cycle (Nance et al., 1988). While the cycle has an irregular period (Bradley, 2011), the breakup and reformation typically occurs over 500 – 600 Myr (Nance et al., 2014; Davies et al., 2018; Yoshida and Santosh, 2018). Pangea was the latest supercontinent to exist on Earth, forming ~ 300 Myr ago, and breaking up around 180 Myr ago, thus initiating the current supercontinent cycle (Scotese, 1991; Golonka, 2007). Another supercontinent should therefore form within the next 200 – 300 Myr (e.g., Scotese (2003); Yoshida (2016); Yoshida and Santosh (2011, 2018); Duarte et al. (2018); Davies et al. (2018)).

The supercontinent cycle is believed to be an effect of plate tectonics and mantle convection (Torsvik et al., 2010; Pastor-Galán et al., 2019), and the breakup and accretion of supercontinents are a consequence of the opening and closing of ocean basins (Wilson, 1966; Conrad and Lithgow-Bertelloni, 2002). The life cycle of each ocean basin is known as the Wilson cycle. A supercontinent cycle may comprise more than one Wilson cycle since several oceans may open and close between the breakup and reformation of a supercontinent (e.g., Hatton (1997); Murphy and Nance (2003); Burke (2011); Duarte et al. (2018); Davies et al. (2018)). As ocean basins evolve during the progression of the Wilson cycle (and associated supercontinent cycle), the energetics of the tides within the basins also change (Kagan, 1997; Green et al., 2017). Green et al. (2017, 2018) simulated the evolution of tides from the breakup of Pangea until the formation of a future supercontinent, thus spanning a whole supercontinent cycle, and found a link between Wilson cycles and tides. They also found that the unusually large present-day tides in the Atlantic, generated because of the near-resonant state of the basin (Platzman, 1975; Egbert et al., 2004; Green, 2010; Arbic and Garrett, 2010), have only been present for the past 1 Myr. However, because the Atlantic is still spreading apart, it will eventually become too wide to sustain resonant tides in the near (geological) future. But when exactly will this happen, and is it possible that while the continents diverge and converge, other basins will reach the right size to become resonant?

The initial simulation of deep-time future tides by Green et al. (2018) used a scenario of the Earth's tectonic future presented by Duarte et al. (2018), and strengthened the proof-of-concept for the existence of a super-tidal cycle associated with the supercontinent cycle. Their simulations were done using 50-100 Myr intervals between simulations. They acknowledged

that this was not enough to resolve details of the future tidal maxima, including their duration. In this work, we therefore revisit the future evolution of Earth’s tides by simulating the tide at 20 Myr intervals during the four different tectonic modes of supercontinent formation summarised by Davies et al. (2018): Pangea Ultima (based on Scotese (2003)), Novopangea (Nield, 2007), Aurica (Duarte et al., 2018) and Amasia (based on Mitchell et al. (2012)). Pangea Ultima is a scenario governed by the closing of the Atlantic – an interior ocean – leading to the reformation of a distorted Pangea (Murphy and Nance (2003, 2008) call this “closure through introversion”). Novopangea, in contrast, is dominated by the closing of the Pacific Ocean – an exterior ocean – and the formation of a new supercontinent at the antipodes of Pangea (this is closure through extroversion; Murphy and Nance (2003)). Aurica is a scenario in which the Atlantic and the Pacific close simultaneously and a new ocean opens across Siberia, Mongolia, and India, bisecting Asia (a combination scenario in which two oceans close, one by introversion and another by extroversion; Murphy and Nance (2005); Duarte et al. (2018)). Finally, in the Amasia scenario, the continents gather at the North Pole, 90° away from Pangea (this is known as orthoversion; Mitchell et al. (2012)). Every scenario has the potential to develop different tidal resonances in different ocean basins at different stages in each ocean’s evolution. We focus here on identifying the timing of the occurrence of resonant basins, and on mapping the large-scale evolution of tidal amplitudes and tidal energy dissipation rates in each of the investigated scenarios. We were particularly interested in understanding how common the resonant “super-tidal” states are, for how long they last, and their relationship with the Wilson cycle.

5.4 Methods

5.4.1 Tidal Modelling

The future tide was simulated using the Oregon State University Tidal Inversion Software, OTIS, which has been extensively used to simulate global-scale tides of the past, present, and future (Egbert et al., 2004; Green, 2010; Green and Huber, 2013; Wilmes and Green, 2014; Green et al., 2017, 2018). OTIS was benchmarked against other software that simulate global tides and it was shown to perform well (Stammer et al., 2014). It provides a solution to the linearized shallow water equations (Egbert et al., 2004):

$$\frac{\delta U}{\delta t} + f\mathbf{U} = gh\nabla(\eta - \eta_{SAL} - \eta_{EQ}) - \mathbf{F} \quad (5.1)$$

$$\frac{\delta \eta}{\delta t} - \nabla \cdot \mathbf{U} = 0 \quad (5.2)$$

Here, \mathbf{U} is the tidal volume transport vector defined as $\mathbf{u}h$, where \mathbf{u} is the horizontal velocity vector and h the water depth, f is the Coriolis parameter, g the acceleration due to gravity, η the sea surface elevation, η_{SAL} the self-attraction and loading elevation, η_{EQ} the elevation of the equilibrium tide, and \mathbf{F} the energy dissipation term. The latter is defined as $\mathbf{F} = \mathbf{F}b + \mathbf{F}w$, where $\mathbf{F}b = Cd\mathbf{u}\|\mathbf{u}\|$ parameterises energy due to bed friction using a drag coefficient, $Cd=0.003$, and $\mathbf{F}w = C\mathbf{U}$ represents losses due to tidal conversion. The conversion coefficient, C , is based on Zaron and Egbert (2006) and modified by Green and Huber (2013), computed from:

$$C(x,y) = \Upsilon \frac{N_H \bar{N}}{8\pi\omega} (\nabla H)^2 \quad (5.3)$$

In Eq. (5.3) $\Upsilon = 50$ is a dimensionless scaling factor accounting for unresolved bathymetric roughness, N_H is the buoyancy frequency (N) at seabed, \bar{N} is the vertically averaged buoyancy frequency, and ω is the frequency of the M_2 tidal constituent, the only constituent analysed here. The buoyancy frequency, N , is based on a statistical fit to present day climatology (Zaron and Egbert, 2006), and given by $N(x,y) = 0.00524 \exp(-z/1300)$, where z is the vertical coordinate counted positive upwards from the sea floor. We did not change N throughout the simulations because the stratification in the future oceans is yet to be quantified.

Each run simulated 14 days, of which 5 days were used for harmonic analysis of the tide. The model output consists of amplitudes and phases of the sea surface elevations and transports, which was used to compute tidal dissipation rates, D , as the difference between the time average of the work done by the tide generating force (W), and the divergence of the horizontal energy flux (\mathbf{P} ; see Egbert and Ray (2001) for details):

$$D = W - \nabla \cdot \mathbf{P} \quad (5.4)$$

where W and \mathbf{P} are given by:

$$W = g\rho\mathbf{U} \cdot \nabla(\eta_{EQ} + \eta_{SAL}) \quad (5.5)$$

$$\mathbf{P} = g\rho\mathbf{U}\eta \quad (5.6)$$

The orbital configuration of the Earth-Moon system, and thereby the tidal and lunar forcing was not changed during the future simulation. The difference in tidal period (+0.11 hr) and lunar forcing (-3%) that occurs after 250 Myr was applied to a sensitivity simulation which found that the altered parameters do not affect the results sufficiently to warrant changing the values from present-day.

5.4.2 Mapping of the future tectonic scenarios

We used the kinematic tectonic maps produced by Davies et al. (2018) with OTIS at incremental steps of 20 Myr by using the tectonic maps as boundary conditions in the tidal model. The maps were produced using GPlates, a software specifically designed for the visualisation and manipulation of tectonic plates and continents (e.g., Qin et al. (2012); Müller et al. (2018)). We used GPlates to digitise and animate a high resolution representation of present-day continental shelves and coastline (with no ice cover), created from the NOAA ETOPO1 global relief model of the Earth (see <https://data.nodc.noaa.gov/cgi-bin/iso?id=gov.noaa.ngdc.mgg.dem:316#> for details). For a matter of simplification, shelf extents are kept for the full duration of the scenarios. The continental polygons do not deform, though some overlap is allowed between their margins, to simulate rudimentary continental collision and shortening. Intracontinental breakup and rifting were introduced in three of the scenarios, allowing new ocean basins to form. No continental shelves were extrapolated along the coastlines of these newly formed basin's margins. For more details on the construction of the tectonic scenarios and the respective maps, see Davies et al. (2018).

The resulting maps were then given an artificial land mask 2° wide on both poles to allow for numerical convergence (simulations with equilibrium tides near the poles in Green et al. (2017, 2018) did not change the results there), and were constrained to a horizontal resolution of 0.25° in both latitude and longitude. They were then assigned a simplified bathymetry; continental shelves were set a depth of 150 m, and mid-ocean ridges were assigned a depth of 1600 m at the crest point and deepening to the abyssal plains within a width of 5° . Subduction trenches were made 5800 m deep. The depth of the abyssal plains in the maps changes dynamically to retain present-day ocean volume throughout the scenarios. This allows the tidal results of future simulations to be comparable to a present-day simulation, which was tested against real world tidal observations.

To test the accuracy of our results, we produced and used two present-day bathymetries. The first – a present-day control - is based on v13 of the Smith and Sandwell bathymetry (Smith and Sandwell (1997); https://topex.ucsd.edu/marine_topo/). A second map was then produced – the present-day degenerate bathymetry – which included a bathymetry created by using the depth values and the method described for the future slices (see Fig. 5.1 and corresponding description in section 5.4.2).

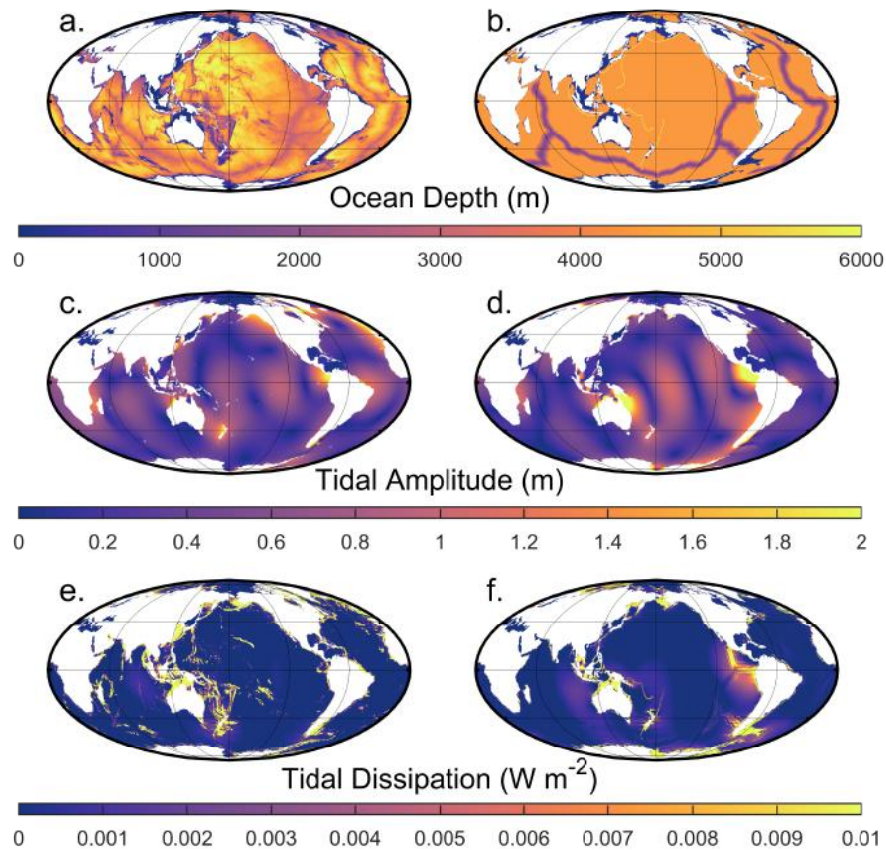


Figure 5.1: (a) The PD bathymetry in m. Panel (b) is the same as (a) but for the degenerate PD bathymetry (see text for details). (c–d) The simulated M_2 amplitudes (in m) for the control PD (c) and degenerate PD (d) bathymetries. Note that the colour scale saturates at 2 m. Panels (e–f) are the same as (c)–(d) but show M_2 dissipation rates in $W m^{-2}$.

5.5 Results

The tidal amplitude results for the present-day control simulation (Fig. 5.1c), when compared to the TPX09 satellite altimetry constrained tidal solution (Egbert and Erofeeva (2002); <http://volkov.oce.orst.edu/tides/tpxo9atlas.html>), produced an RMS error of ± 12 cm. Comparing the present-day degenerate simulation (Fig. 5.1d) results to TPX09, resulted in an RMS error of 13 cm. This is consistent with previous work (Green et al., 2017, 2018) and

gives us a quantifiable error of the model's performance when there is a lack of topographic detail (e.g., as in our future simulations).

The present-day control simulation (Fig. 5.1e) has a dissipation rate of 3.3 TW, with 0.6 TW dissipating in the deep ocean. This corresponds to 137% of the observed (real) global dissipation rate (2.4 TW for M_2 , see Egbert et al. (2004)), and 92% of the measured deep ocean rates (0.7 TW). The present-day degenerate bathymetry underestimates the globally integrated dissipation by a factor of 0.9, and the deep ocean rates by a factor of ~ 0.8 (Fig. 5.1f). Sensitivity tests for the present-day control simulation with varying bed friction and buoyancy frequency did not produce any significant difference in the result. The future tidal dissipation results (Fig. 5.3) were therefore normalised against the degenerate present-day value (2.2 TW), to account for the bias due to underrepresented bathymetry caused when using the simplified bathymetry in the future simulations (see Green et al. (2017) for a discussion).

The resulting tidal amplitudes and associated integrated dissipation rates are shown in Figs. (5.2), Figs. (5.4 - 5.6 - amplitudes), and Fig. (5.3 - dissipation). The latter is split into the global total rate, and rates in shallow (depths of $<500\text{m}$), and deep water (depths of $>500\text{m}$; Egbert and Ray (2001)), to highlight the mechanisms behind the energy loss. In the following we define a super-tide as occurring when: i) tidal amplitudes in a basin are on average meso-tidal or above, i.e., larger than 2 m, and ii) the globally integrated dissipation is equivalent to or larger than present-day values.

5.5.1 Pangea Ultima

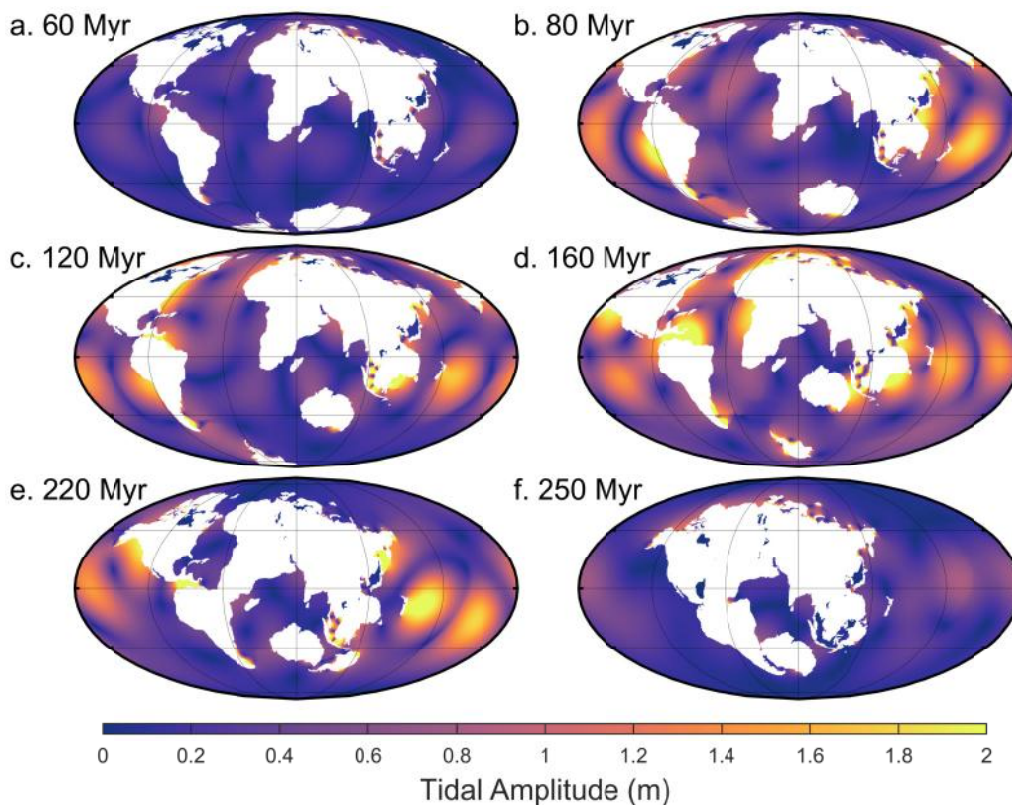


Figure 5.2: Global M_2 amplitudes for six representative time slices of the Pangea Ultima scenario. The colour scale saturates at 2 m. For the full set of time slices covering every 20 Myr, see the Supplement. Additionally, note that the figures presented for each scenario display different time slices to highlight periods with interesting tidal signals and that the centre longitude varies between panels to ensure the supercontinent forms in the middle of each figure (where possible).

In the Pangea Ultima scenario, the Atlantic Ocean continues to open for another 100 Myr, after which it starts closing, leading to the formation of a slightly distorted new Pangea in 250 Myr (Fig. 5.2). The continued opening of the Atlantic in the first 60 Myr moves the basin out of resonance, causing the M_2 tidal amplitude and dissipation to gradually decrease (Figs. 5.2 and 5.3a). During this period, the total global dissipation drops to below 30% of the PD (present-day) rate (note that this is equivalent to 2.2 TW because we compare to the degenerate bathymetry simulation), after which, at 80 Myr, it increases rapidly to 120% of PD (Figs. 5.3a and 5.2b). This peak at 80 Myr is due to a resonance in the Pacific Ocean initiated by the shrinking width of the basin (Fig. 5.2b). The dissipation then drops again until it recovers and peaks around 120 Myr at 130% above PD (Fig. 5.3a). This second peak is caused by another resonance in the Pacific, combined with a local resonance in the Northwest Atlantic (Fig. 5.2c). This period also marks the initiation of closure of the Trans-Antarctic ocean, a short-lived ocean which began opening at 40 Myr and was microtidal for its entire tenure (Fig.

5.2a-c). A third peak then occurs at 160 Myr, the most energetic period of the simulation, with the tides being 215% more energetic than at present due to both the Atlantic and the Pacific being resonant for M_2 frequencies (Fig. 5.2d). After this large-scale double resonance, the first described in detail in deep-time simulations, and the most energetic relative dissipation rate encountered, the tidal energy drops, with a small recovery occurring at 220 Myr due to a further minor Pacific resonance (Fig. 5.2e). When Pangea Ultima forms at 250 Myr (see Fig. 5.2f), the global energy dissipation has decreased to 25% of the PD value, or 0.5TW (Fig. 5.2f).

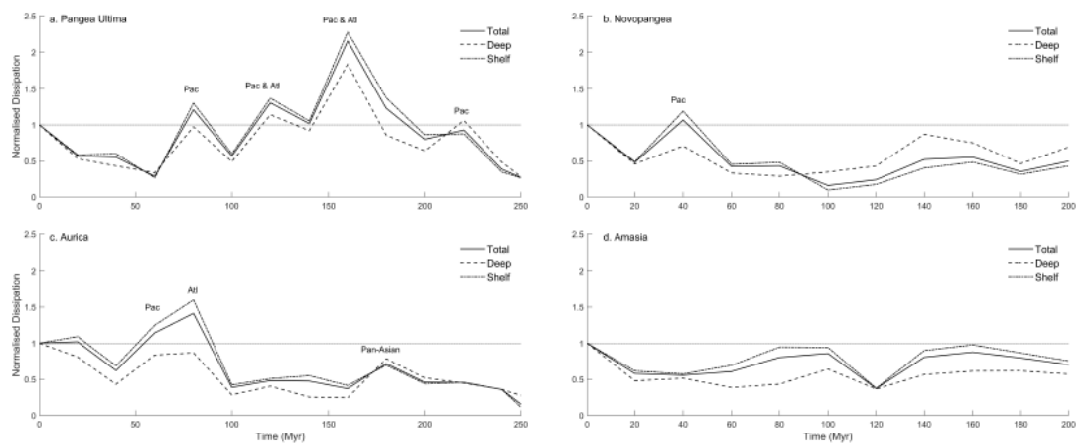


Figure 5.3: Normalized (against PD degenerate) globally integrated dissipation rates for the Pangaea Ultima (a), Novopangaea (b), Aurica (c), and Amasia (d) scenarios. The lines refer to total (solid line), deep (dashed line), and shelf (dotted–dashed line) integrated dissipation values. Each super-tidal peak is marked where it reaches its peak. Pac stands for Pacific and Atl stands for Atlantic.

5.5.2 Novopangea

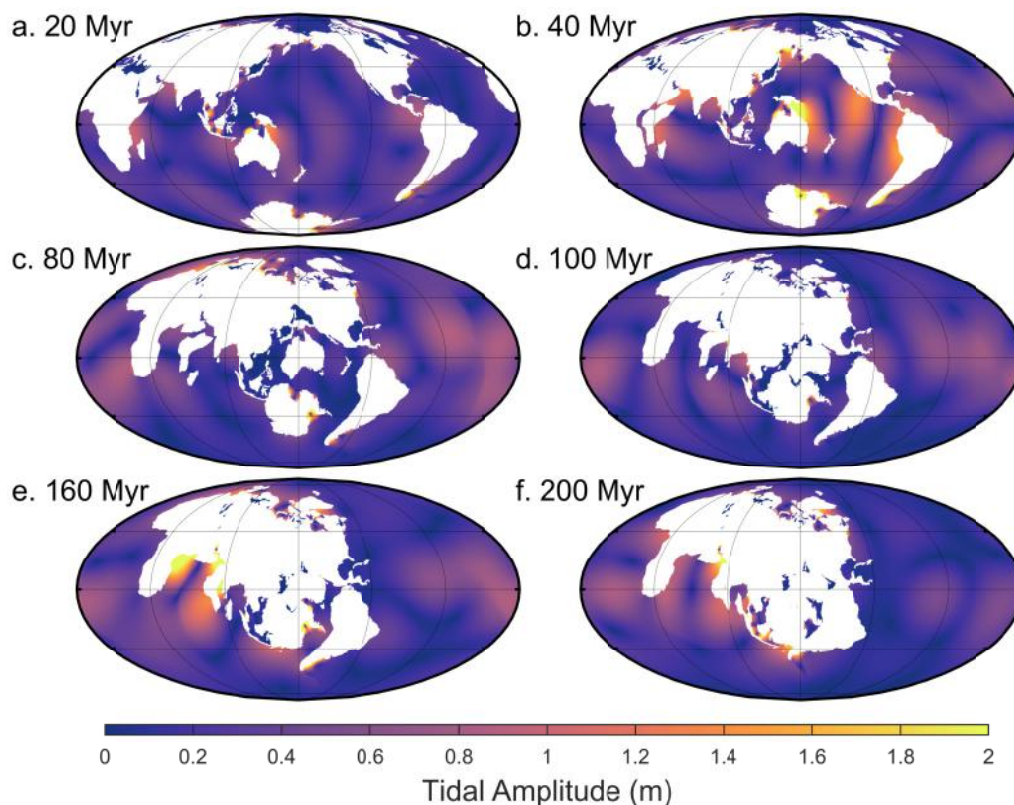


Figure 5.4: The same as in Fig. 5.2 but for the Novopangea scenario.

In the Novopangea scenario, the Atlantic Ocean continues to open for the remainder of the supercontinent cycle. Consequently, the Pacific closes, leading to the formation of a new supercontinent at the antipodes of Pangea in 200 Myr (Fig. 5.4). As a result, within the next 20 Myr the global M_2 dissipation rates decrease to half of present-day values (see Fig. 5.3b and 5.4 for the following discussion). The energy then recovers to PD levels at 40 Myr as a result of the Pacific Ocean becoming resonant. From 40 Myr to 100 Myr, the dissipation rates drop, reaching 15% of the PD value at 100 Myr. There is a subsequent recovery to values close to 50% of PD, with a tidal maximum at 160 Myr due to local resonance in the newly formed East-African Ocean (Davies et al., 2018). Even though the tidal amplitude in this new ocean reaches meso-tidal levels (i.e., 2-4 m tidal range, Fig. 5.3b), the increased dissipation in this ocean only increases the global total tidal dissipation to 50% PD (Fig. 5.4e). Therefore, this ocean cannot be considered super-tidal. The tides then remain at values close to half of present-day, i.e., equal to the long-term mean over the past 250 Myr in Green et al. (2017), until the formation of Novopangea at 200 Myr. After 100 Myr there is a regime shift in the location of the dissipation rates, with a larger fraction than before dissipated in the deep ocean (Fig. 5.3b).

5.5.3 Aurica

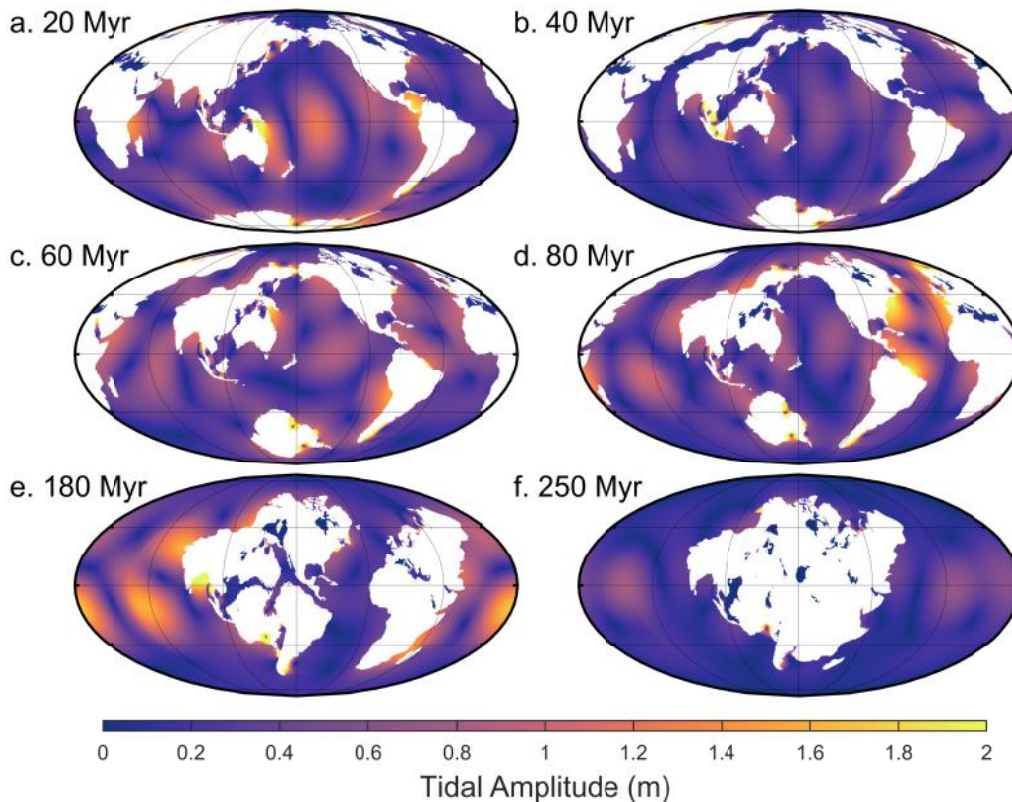


Figure 5.5: The same as in Fig. 5.2 but for the Aurica scenario.

Aurica is characterized by the simultaneous closing of both the Atlantic and the Pacific Oceans, and the emergence of the new Pan-Asian Ocean. This allows Aurica to form via combination in 250 Myr (Fig. 5.5). In this scenario, the tides remain close to present-day values for the next 20 Myr (see Fig. 5.3c and 5.5 for the results), after which they drop to 60% of PD at 40 Myr, only to rise to 114% of PD values at 60 Myr and then to 140% of PD rates at 80 Myr. This period hosts a relatively long super-tidal period, lasting at least 40 Myr as the Pacific and Atlantic go in and out of resonances at 60 Myr and 80 Myr, respectively. The dissipation then drops to 40-50% of PD, with a local peak of 70% of the PD value at 180 Myr due to resonance in the Pan-Asian Ocean. This is the same age as the North Atlantic today, which strongly suggests that oceans go through resonance around this age. By the time Aurica forms, at 250 Myr, the dissipation is 15% of PD, the lowest of all simulations presented here.

5.5.4 Amasia

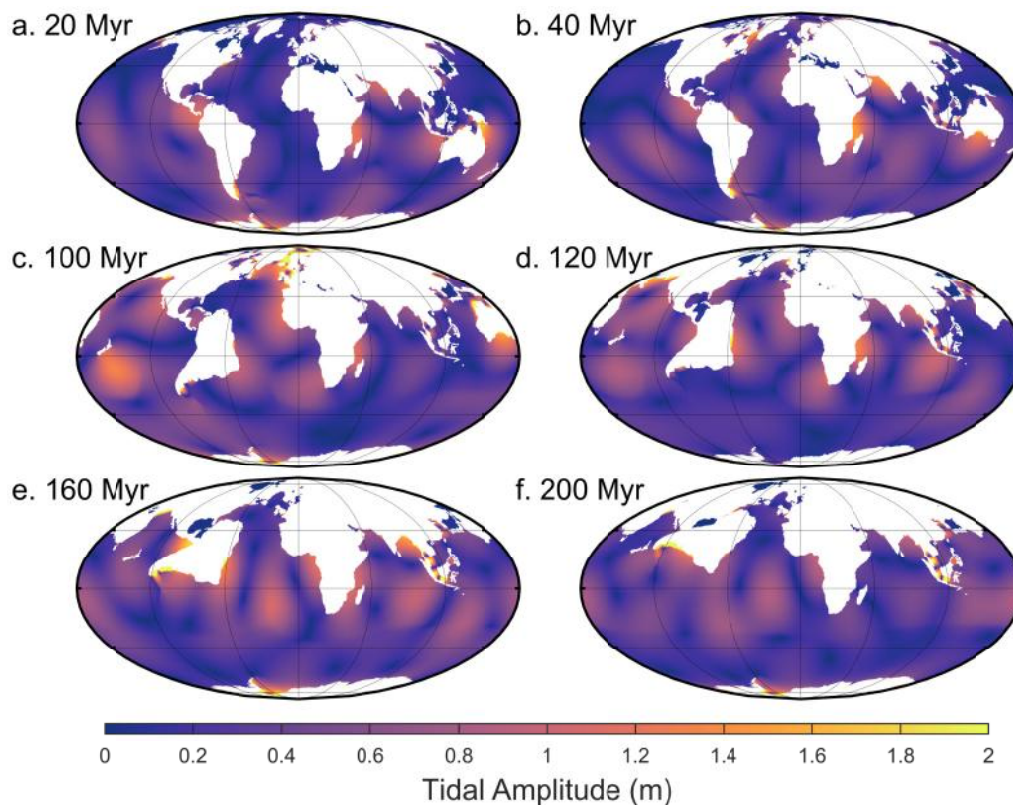


Figure 5.6: The same as in Fig. 5.2 but for the Amasia scenario.

In the Amasia scenario, all the continents except Antarctica move north, closing the Arctic Ocean and forming a supercontinent around the North Pole in 200 Myr (Fig. 5.6). The results show that the M_2 tidal dissipation drops to 60 % of PD rates within the next 20 Myr (Fig. 5.3d and 5.6 for continued discussion). This minimum is followed by a consistent increase, reaching 80% of PD rates at 100 Myr, and then, after another minimum of 40% of PD rates at 120 Myr, tidal dissipation increases until it reaches a maximum of 85% at 160 Myr. These two maxima are a consequence of several local resonances in the North Atlantic, North Pacific, and along the coast of South America, and the minimum at 120 Myr is a result of the loss of the dissipative Atlantic shelf areas due to continental collision. A major difference between Amasia and the scenarios previously described, is that here we never encounter a full basin-scale resonance. This is because the circumpolar equatorial ocean that forms is too large to host tidal resonances, and the closing Arctic Ocean is too small to ever become resonant. However, the scenario is still rather energetic, with dissipation rates averaging around 70% of PD rates because of several local areas of high tidal amplitudes and corresponding high shelf dissipation rates (Fig. 5.3d).

5.6 Discussion

Table 5.1: Summary of the number of super-tidal peaks for each scenario

Supercontinent Scenario	Mode of supercontinent formation	Number of super-tidal peaks, incl. PD	Resonant basins, incl. PD	Average normalised* dissipation
Pangea Ultima	Introversion	5	Atlantic, Pacific, Pacific and Atlantic, Pacific and Atlantic, Pacific	0.877
Novopangea	Extroversion	2	Atlantic, Pacific	0.520
Aurica	Combination	4	Atlantic, Pacific, Atlantic, Pan-Asian	0.647
Amasia	Orthoversion	1	Atlantic	0.723

*Against PD degenerate = 2.2 TW

Table 5.2: Summary of the total time each scenario was in a super-tidal state.

Supercontinent scenario	Number of super-tidal cycles	Time span of supercontinent cycle* (Myr)	Total time span of tidal maxima (Myr)	$T_{(future)}\%$
Pangea Ultima	5	730	100	13.7
Novopangea	2	680	40	5.9
Aurica	4	730	80	11.0
Amasia	1	680	20	2.9

*From the formation of Pangea to the break-up of the future supercontinent.

We investigated how the tides may evolve during four probable scenarios of the formation of Earth's future supercontinent. The results show large variations in tidal energetics between the scenarios (see Table 5.1 and Fig. 5.3), with the number of tidal maxima ranging from 1 (at present during the Amasia scenario) to 5 (including today's in the Pangea Ultima scenario) – see Table (5.1) for a summary. These maxima occur because of tidal resonances in the ocean basins as they open and close. Furthermore, we have shown that an ocean basin becomes resonant for the M_2 tide when it is around 140 – 180 Myr old (as is the PD Atlantic). The reason for this is simple: assuming the net divergence rate of two continents bordering each side of an ocean basin is $\sim 3 \text{ cm yr}^{-1}$ (which is close to the average drift rates today), after 140 Myr it will be 4500 km wide. Tidal resonance occurs when the basin width is half of the tidal wavelength (Arbic and Garrett, 2010):

$$L = c_g T \quad (5.7)$$

where the wave speed is given by:

$$c_g = (gh)^{\frac{1}{2}} \quad (5.8)$$

and T is the tidal period (12.42 hours). For a 4000 m deep ocean, resonance thus occurs when the ocean is 4429 km wide, i.e., at the age given above. The depth of the simulated oceans changes between the scenarios to preserve ocean volume at that of present day. These changes are too small to affect the resonant scales in the different simulations, especially at the resolution we are using here (0.25° in latitude and longitude). For example, in the Novopangea scenario, which has the shallowest average ocean depth at 3860 m, the resonant basin scale is 4350 km, whereas in the Pangea Ultima scenario, in the present-day the overall deepest at 4395 m, the basin scale would be 4642 km. This again highlights the relationship between the tidal and tectonic evolution of an ocean basin. It also reiterates that ocean basins must open for at least 140 Myr to be resonant during their opening at present day drift speeds (e.g., the Pan-Asian ocean). If an ocean opens for less than 140 Myr, e.g., the Trans-Antarctic (80 Myr of opening) or Arctic ocean (60 Myr of opening; Miller et al. (2006)), or if they drift slower than 3 cm yr^{-1} , they will not become resonant. After this 140 Myr/4500 km age/width threshold has been reached, the ocean may then be resonant again if it closes.

Therefore, if the geometry, and mode of supercontinent formation permits (i.e., multiple Wilson cycles are involved), several oceans may go through multiple resonances – sometimes simultaneously – as they open/close during a supercontinent cycle. For example, in the Pangea Ultima scenario, the Atlantic and Pacific are simultaneously resonant at 160 Myr (Table 5.1), and as Aurica forms, the Atlantic is resonant twice (at present, and when closing at 80 Myr), the Pacific once (closing) and the Pan-Asian ocean once (after 180 Myr, when opening; Table 5.1 and section 5.5.3).

The simulations here expand on the work of Green et al. (2018), regarding the tidal evolution of Aurica. They find a more energetic future compared to the present Aurica simulations (e.g., our Fig. 5.3c): their average tidal dissipation is 84% of the PD value, with a final state at 40% of PD, whereas we find dissipation at 64% of PD on average and 15% of PD at 250 Myr. This discrepancy can be explained by two factors present in the work of Green et al. (2018): a lack of temporal resolution, and a systematic northwards displacement in the configuration of the continents, meaning their tidal maxima are exaggerated. Despite these differences, the results are qualitatively similar, and we demonstrate here that under this future scenario the tides will be even less energetic than suggested in Green et al. (2018). This, along with results from tidal modelling of the deep past (Green et al. (2017) this paper, and unpublished results) lends further support to the super-tidal cycle concept, and again shows how strong the current

tidal state is.

All four scenarios presented have an average tidal dissipation lower than the present-day, and all scenarios, except Amasia, have a series of super-tidal periods analogous to present-day. The results presented here can supplement the fragmented tidal record of the deep past (Kagan (1997); Green et al. (2017)) and allow us to draw more detailed conclusions about the evolution of the tide over geological time, and the link between the tide, the supercontinent cycle, and the Wilson cycle.

We have estimated the number tidal maxima that have occurred in the Earth's history (N) and the total time that the Earth was in a super tidal state (T), as follows:

$$N = N_{sc} \cdot N_{wc} \cdot N_t \quad (5.9)$$

and:

$$T = \frac{N * T_{tm}}{T_E} \quad (5.10)$$

N_{sc} represents the Number of supercontinent cycles that have occurred on Earth, including the present one (we assume a minimum of 5 supercontinent cycles; e.g., Davies et al. (2018); and references therein), N_{wc} is the number of Wilson cycles per supercontinent cycle (we assume an average of 2), N_t is the number of tidal maxima per Wilson cycle (we assume an average of 2; this work). T_{tm} is a representative time duration for each tidal maximum (20 Myr) and T_E is the age of the Earth (4.5 Gyr; e.g., Dalrymple (2001)). This Fermi estimation suggests that there may have been ~ 20 super-tidal periods on Earth (N), spanning over 400 Myr (8.9%) of the Earth's history. This value is corroborated by the results in Table (5.2).

6 Analysing the tidal state of a pre-Plate tectonic Earth during the Archean Eon (3.9 Ga)

6.1 Preface

This chapter details a draft of my third first-author paper, currently in preparation to be included as a book chapter in 2022. The following sections cover tidal modelling of the Archean period (3.9 Ga).

6.2 Introduction

The relationship between tides and tectonics is a very important part of the Earth system as we have shown above. It has been demonstrated that as the continents move according to plate tectonics, they alter the shape of oceans which affects the open ocean tide. This has been established in the Cryogenian (Green et al., 2020), the Devonian (Byrne et al., 2020), the Cenozoic (Green et al., 2017) and in four potential scenarios of Earth's future (Davies et al., 2020). While it is still debated when plate tectonics became the dominant mechanism for plate recycling on Earth (Palin et al., 2020), we know that continental land masses, and oceans, did exist in the Archaean (4 - 2.5 Ga) (Tang et al., 2016). This means it is possible to assess the relationship between the tide and continental configuration during that period. Furthermore, the tidal state of this period is of particular interest in the context of the inception of life. An exchange via papers between Richard Lathe and Peter Varga (see Lathe (2004); Varga et al. (2006); Lathe (2006)) discusses the potential for tides to act as a chemical mixing mechanism to allow polymerase chain reactions (PCRs) to occur at the littoral zone; however none of these papers explicitly model the tide in this period.

The Archean is too remote a period in Earth history to allow accurate reconstructions of topography to be made; there is not enough extant Archean crust to extract paleolocations from to reconstruct a full view of the period (Condie, 1994). We therefore use an ensemble of randomised bathymetries from Blackledge et al. (2020), modified to have the land/ocean area of the Archean (~5 - 15% land) to establish a statistically significant approximation of the Archean Earth.

Using the 120 "Earths" Blackledge et al. (2020) created, in an established tidal model to simulate the Archean tide, we aim to establish a first order approximation of the Lunar and Solar

tide during the Archean. By doing this we aim to investigate the state of the tide in this remote epoch, focusing on whether or not there is a super-tidal signal. Furthermore, we also aim to discuss how the tide may have affected other components of the Earth system. Notwithstanding, establishing the tidal state of a primordial ocean on a young planet will further our knowledge of similar exoplanets.

6.3 Methods

6.3.1 Mapping of the Archean conceptual scenarios

The maps used as the boundary condition for the tidal modelling are modified versions of the ensemble presented in Blackledge et al. (2020). The original ensemble from Blackledge et al. (2020) are a matrix of 360 by 180 grid points (1° resolution) so they were extrapolated to a matrix of 1440 by 720 gridpoints ($1/4^\circ$ horizontal resolution in latitude and longitude). They were then given an artificial land mask 2° wide on both poles to allow for numerical convergence (simulations with equilibrium tides near the poles in Green et al. (2017, 2018) did not change the results there). Each map was then "flooded" until the land area averaged 5 - 15% retaining ocean volume at present day values by raising the ocean floor where needed. As these are randomly generated maps, they do not contain recognisable underwater features such as continental shelves, ridges, or subduction zones.

To show the effect of continent size, ocean basin size, and coastline complexity on the tide, we used the same non-dimensional R value presented in Blackledge et al. (2020), $R = L_{tot} / \sqrt{A_{ocean}}$, where L_{tot} is the total coastline length (in km) and A_{ocean} is the surface area of the ocean (in km^2). However due to the differences in method or defining what is land and ocean between Blackledge et al. (2020) and here, the R values are very different. Blackledge et al. (2020) defined coastline at a fixed value of the greyscale topographic ensemble where we "flooded" the maps to reach the coastline value thereby greatly altering the coastline length and therefore the R value.

Alongside the ensemble simulations, for each constituent we simulated the present day and Archean tide on a map with present day bathymetry (NOAA ETOPO1 - see <https://data.nodc.noaa.gov/cgi-bin/iso?id=gov.noaa.ngdc.mgg.dem:316#> for details). Consequently, we get two additional tidal simulation results for each constituent: PD bathymetry with PD tidal forcing, and PD bathymetry with Archean forcing, plotted with a triangle for present day and a

circle for Archean on Fig. (6.1) respectively.

While the same randomised topography ensemble was used here and in Blackledge et al. (2020), the method used to create the ocean bathymetries for tidal modelling differs between their and our work. They assign all values under 0.2 on the greyscale maps to 4500 Km with the rest being land, where we retain the random bathymetry by "flooding" maps until they are Archean-like, while also raising the abyssal plain to maintain present day ocean volume, meaning our oceans are shallower on average and retain more of the random bathymetry.

6.3.2 Tidal modelling

The Archean tide was simulated using the Oregon State University Tidal Inversion Software, OTIS, which has been extensively used to simulate global-scale tides of the past, present, and future (Egbert et al., 2004; Green, 2010; Green and Huber, 2013; Wilmes and Green, 2014; Green et al., 2017, 2018). OTIS was benchmarked against other software that simulate global tides and it was shown to perform well (Stammer et al., 2014). It provides a solution to the linearized shallow water equations (Egbert et al., 2004):

$$\frac{\delta U}{\delta t} + f\mathbf{U} = gh\nabla(\eta - \eta_{SAL} - \eta_{EQ}) - \mathbf{F} \quad (6.1)$$

$$\frac{\delta \eta}{\delta t} - \nabla \cdot \mathbf{U} = 0 \quad (6.2)$$

Here, \mathbf{U} is the tidal volume transport vector defined as $\mathbf{u}h$, where \mathbf{u} is the horizontal velocity vector and h the water depth, f is the Coriolis parameter, g the acceleration due to gravity, η the sea surface elevation, η_{SAL} the self-attraction and loading elevation, η_{EQ} the elevation of the equilibrium tide, and \mathbf{F} the energy dissipation term. The latter is defined as $\mathbf{F} = \mathbf{F}b + \mathbf{F}w$, where $\mathbf{F}b = Cd\mathbf{u}\|\mathbf{u}\|$ parameterises energy due to bed friction using a drag coefficient, $Cd=0.003$, and $\mathbf{F}w = C\mathbf{U}$ represents losses due to tidal conversion. The conversion coefficient, C , is based on Zaron and Egbert (2006) and modified by Green and Huber (2013), computed from:

$$C(x,y) = \Upsilon \frac{N_H \bar{N}}{8\pi\omega} (\nabla H)^2 \quad (6.3)$$

In Eq. 6.3 $\Upsilon = 50$ is a dimensionless scaling factor accounting for unresolved bathymetric roughness, N_H is the buoyancy frequency (N) at seabed, \bar{N} is the vertically averaged buoyancy frequency, and ω is the frequency of the M_2 tidal constituent, the only constituent analysed here.

The buoyancy frequency, N , is based on a statistical fit to present day climatology (Zaron and Egbert, 2006), and given by $N(x, y) = 0.00524 \exp(-z/1300)$, where z is the vertical coordinate counted positive upwards from the sea floor. We did not change N throughout the simulations because the stratification in the ancient oceans is yet to be quantified.

Each run simulated 14 days, of which 5 days were used for harmonic analysis of the M_2 , K_1 , S_2 , and O_1 tide. The model output consists of amplitudes and phases of the sea surface elevations and transports, which was used to compute tidal dissipation rates, D , as the difference between the time average of the work done by the tide generating force (W), and the divergence of the horizontal energy flux (\mathbf{P} ; see Egbert and Ray (2001) for details):

$$D = W - \nabla \cdot \mathbf{P} \quad (6.4)$$

where W and \mathbf{P} are given by:

$$W = g\rho\mathbf{U} \cdot \nabla (\eta_{EQ} + \eta_{SAL}) \quad (6.5)$$

$$\mathbf{P} = g\rho\mathbf{U}\eta \quad (6.6)$$

The tidal parameters for the Archean are very different to present day. Lunar distance is 263 000 Km compared to the present 384 400 Km (Waltham, 2015). This acts to enhance the equilibrium tide by 3.4x. Furthermore, the Earth was rotating much faster in this early eon of Earth history, meaning the day was 13.1 h (Waltham, 2015) and the semidiurnal tidal period was therefore 6.78 h. The orbit of the Earth relative to the sun has likely not changed significantly since the Archean therefore we kept the S_2 tidal parameters at present day values.

6.4 Results

On average we find an enhanced tidal signal for the ensemble bathymetry maps of the Archean, with average global M_2 tidal dissipation and amplitudes being around 40 - 60% higher than the present day (Figs. 6.1 and 6.2). Furthermore, the M_2 deep dissipation is almost twice as energetic as the present day equivalent. The K_1 and O_1 constituents are also more energetic, however by only a small margin when compared to the present day (Tables 6.1 and 6.2, and Fig. 6.1), and the S_2 tidal dissipation is less energetic in the Archean results than the present day.

The standard deviations of the Archean ensemble dissipations and amplitudes for all of the constituents is in general quite low (Tables 6.1 and 6.2). Except for deep dissipation in the M_2 constituent where it the same as the average.

Present day bathymetry with Archean forcing (Fig. (6.1 (top left figure, circle data point)) has the highest tidal dissipation for the M_2 constituent. In the K_1 , and O_1 constituents (Fig. 6.1 (bottom left and right respectively), Archean tidal forcing on PD bathymetry gives higher tidal dissipation rates than PD bathymetry and PD forcing, however, despite being more energetic than the PD bathymetry and forcing it is a median value when compared to the Archean ensemble. The S_2 tidal dissipation is highest in the PD bathymetry, PD forcing simulation, with the Archean S_2 ensemble, and Archean forcing on PD bathymetry values averaging less than half the PD value.

Table 6.1: Global average and standard deviation of the Archean ensemble maps' tidal dissipation (in TW) for the M_2 , S_2 , K_1 , and O_1 tidal constituents, along with the dissipation for Present day simulation with PD forcing and PD bathymetry.

Constituent	Avg. Archean Dissipation			SD Archean Dissipation			Present Day Dissipation		
	Total	Deep	Shelf	Total	Deep	Shelf	Total	Deep	Shelf
M_2	3.89	1.03	2.86	0.86	1.03	1.23	2.96	0.64	2.32
S_2	0.18	0.054	0.12	0.07	0.07	0.06	0.54	0.12	0.43
K_1	0.56	0.14	0.42	0.22	0.18	0.25	0.39	0.1	0.29
O_1	0.34	0.08	0.26	0.15	0.09	0.17	0.24	0.07	0.17

Table 6.2: Global average of the Archean ensemble maps' amplitude (in meters) for the M_2 , S_2 , K_1 , and O_1 tidal constituents, along with the amplitude for Present day simulation with PD forcing and PD bathymetry.

Constituent	Avg. Archean amplitude	SD Archean Amplitudes	Present Day Amplitude
M_2	0.47	0.12	0.29
S_2	0.06	0.02	0.11
K_1	0.10	0.02	0.08
O_1	0.08	0.02	0.07

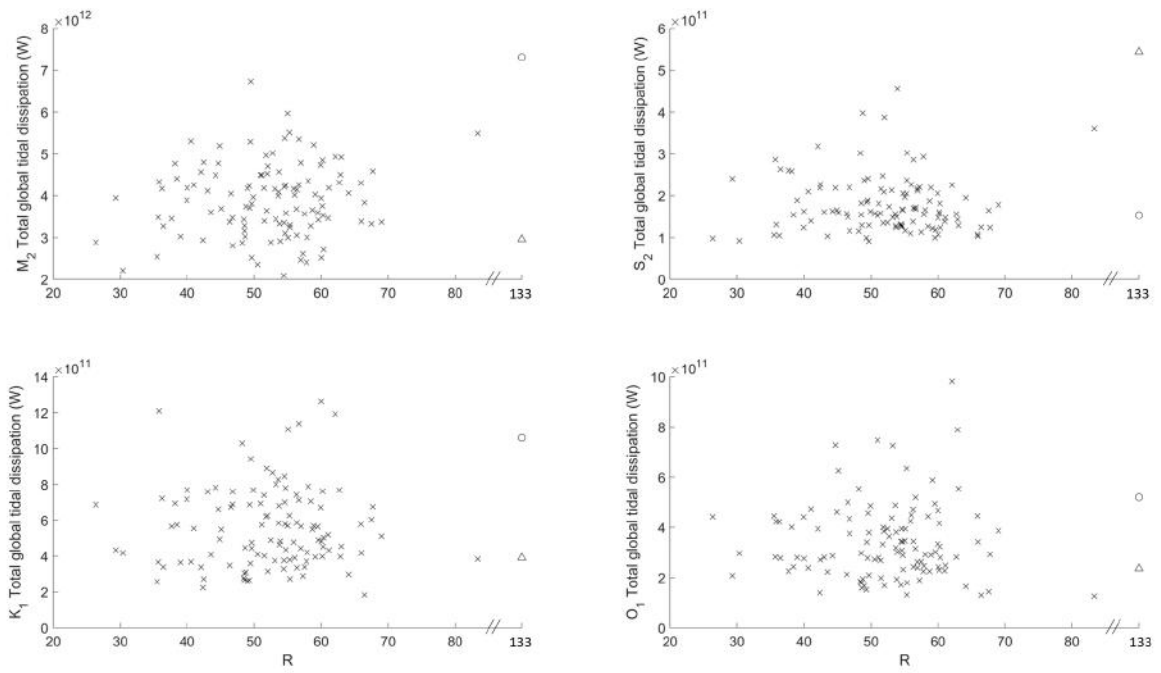


Figure 6.1: R versus the globally integrated dissipation rate for the M_2 (top left), S_2 (top right), K_1 (bottom left), and O_1 (bottom right) tide. The triangle marks present day dissipation and R value, and circle is present day with Archean tidal forcing. Note the discontinuous x-axis on all figures, also the y-scale is different for the M_2 tidal constituent.

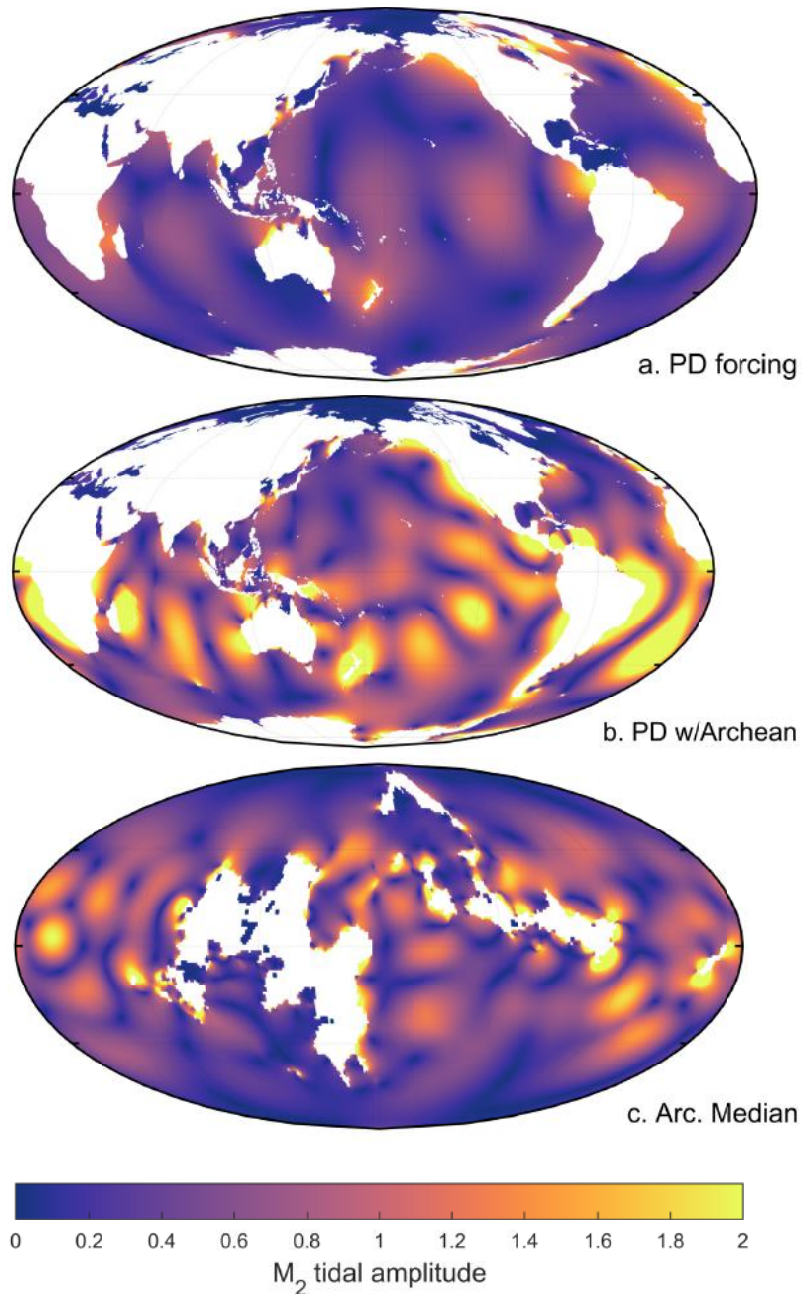


Figure 6.2: M_2 tidal amplitudes for (a) present day bathymetry with present day tidal forcing, (b) present day bathymetry and Archean tidal forcing, and (c) a representative map selected from the Archean ensemble because it has median tidal amplitudes.

We find a similar trend in our tidal dissipation results to those of Blackledge et al. (2020) where there is a weak correlation between higher R values and higher tidal dissipation. The ensemble average Archean M_2 tidal dissipation is higher than the average of the M_2 dissipation results presented in Blackledge et al. (2020). Their highest M_2 value is 1.9 TW where our highest result in the Archean ensemble was 6.7 TW. Notwithstanding, all four of the tidal constituents presented in Fig. (6.1) resemble Fig. (2b) of Blackledge et al. (2020), despite the the non-dimensional R value being much higher for all of the Archean simulations. Our

S_2 results are far less energetic than those presented in Blackledge et al. (2020). They report S_2 amplitudes $\sim 45\%$ of M_2 and dissipation rates of 0.67 TW. Here our Archean ensemble S_2 amplitudes are $1/8^{\text{th}}$ of the average Archean ensemble M_2 tidal amplitude, and the peak S_2 tidal dissipation is 0.45 TW. None of the configurations in the ensemble produce higher S_2 tidal dissipation rates than M_2 .

6.5 Discussion

Because the Archean M_2 tidal forcing is 3.4x the present day, we would expect to see higher values of tidal dissipation than that presented in Table (6.1). The lower than expected tidal dissipation (only 1.5x higher than PD) is likely a combination of the model underestimating the true tidal dissipation rates, as has been highlighted in previous papers using OTIS (Green et al., 2018, 2020; Davies et al., 2020), and the vast oceans of the period not being able to support any resonance. Looking at the half wavelength resonance equation $\lambda = \sqrt{gHT}$ (where H is ocean depth, T is the tidal period, and g is gravity) (Egbert et al., 2004; Arbic and Garrett, 2010; Green, 2010) in the Archean, the M_2 period for the Archean is just over half the PD value meaning the required width of an ocean 4 km deep for it to be resonant is just over 2200 Km. Oceans that narrow are uncommon in the ensemble because of the low land coverage. The results here agree with those of Blackledge et al. (2020) that low R value correlates with lower dissipation rates. Because of the large oceans and small area of coastline, dissipation is lower than it could potentially be if there was more resonant basins and embayments. Despite all this, the tidal dissipation is much higher than the PD value, due to the proximity of the Archean Moon, particularly in the deep ocean where most of the tidal energy would dissipate due to reduced area of continental shelves.

The overall standard deviations of the Archean ensemble tidal dissipations and amplitudes is low which indicates that (assuming the Archean was topographically similar to the ensemble - 5 - 15% land and no major underwater features) we have a reasonable approximation of the Archean tidal environment in this work. The highest standard deviation is in the M_2 deep dissipation which is understandable given a higher fraction of the Archean tide is dissipating in the deep ocean than the present day tide. Furthermore, we believe the Archean shelf dissipation value is overestimated because it is not a quantification of bodies of water near land, but water shallower than 1000 m. Much of the Archean ocean is therefore classified as "shelf" in this approximation. This value was kept the same to allow comparison with present day simulations

and with previous studies using the same method (e.g., Davies et al. (2020); Blackledge et al. (2020)).

Lathe (2004) argues that this enhanced tidal energy in the Archean lead to fast tidal cycling of the vast inter-tidal zone in the early Archean (3.9 Ga) is one mechanism by which early self-replicating molecules such as RNA and DNA might have developed. Despite the disparity in the length of day and period of the tide Lathe (2004) used compared to those used here, based on the tidal amplitude results presented above it is likely the Archean had large intertidal zones in some regions. Many of the scenarios have macrotidal (>4 m) regions along the small landmasses, however the conjecture of Lathe (2004) suggesting tidal zones were hundreds of kilometers wide is purely speculation. With regards to their hypothesis of the Archean intertidal zone acting as a natural "lab bench" for PCR (Polymerase Chain Reactions) to occur is not fully supported by the results presented here. The requisite temperatures (Catling and Zahnle, 2020) and periods (see above), are not present in the Archean, however there would likely have been periodic dilution and concentration of minerals on the intertidal zone.

The close proximity of the Moon in this early epoch exerts a strong tidal force on the young oceans which may have contributed to the emergence, growth in number and dispersal of life. Whether this is important for all habitable planets is still not fully investigated. Both here and in Blackledge et al. (2020) we find a link between ocean area, coastline complexity and tidal dissipation, however their work, while including rapid planetary rotation, did not include enhanced tidal energetics as a result of a close proximity moon, here that was included, however only for a sample which reflected the Archean continental area. Neither this or their study included potentially habitable gas giant moons, or planets in close proximity to their star where in both cases strong tidal forces are also exerted on the planet.

We believe future work should use the R value used here with caution. While it does approximate coastline complexity and ocean area, it is not a perfect quantification of ocean geometry. The ensemble maps used are each unique in continent layout however, because they were limited to 5 - 15% land coverage, many have similar R values. Future work should therefore include a further quantification of latitudinal concentration of landmasses and use either 1° or $1/4^\circ$ so the results are comparable with those here or in Blackledge et al. (2020).

7 Co-authored papers

7.1 Is there a tectonically driven supertidal cycle?

J. A. M. Green, J. L. Molloy, H. S. Davies, & J. C. Duarte

(This chapter is a summary of a paper I co-authored which was published in *Geophysical Research Letters*, Green et al. (2018))

7.1.1 Abstract

Earth is 180 Myr into the current supercontinent cycle, and the next supercontinent is predicted to form in 250 Myr. The continuous changes in continental configuration can move the ocean between resonant states, and the semi-diurnal tides are currently large compared to the past 252 Myr due to tidal resonance in the Atlantic. This leads to the hypothesis that there is a “super-tidal” cycle linked to the supercontinent cycle. Here this is tested using new tectonic predictions for the next 250 Myr as bathymetry in a numerical tidal model. The simulations support the following hypothesis: a new tidal resonance will appear 150 Myr from now, followed by a decreasing tide as the supercontinent forms 100 Myr later. This affects the dissipation of tidal energy in the oceans, with consequences for the evolution of the Earth-Moon system, ocean circulation and climate, and implications for the ocean’s capacity of hosting and evolving life.

7.1.2 Summary

The present day Atlantic is resonant with the M_2 tide (Platzman, 1975; Green, 2010). This elevates the global dissipation of energy in the oceans such that the present day dissipation rate (~ 2.5 TW) is anomalously high when compared to the deep time record of tidal dissipation (Green et al., 2017). According to the supercontinent cycle and more specifically, the Wilson cycle of the Atlantic, we know that the current Atlantic Wilson cycle began with the breakup of Pangea (Scotese, 1991). Since its inception, and in the present day, the Atlantic ocean is opening. Based on present day drift velocities (Schellart et al., 2007) we can assume the Atlantic ocean will continue opening into the near future and in every scenario presented in sections 4.6.1, 4.6.2, 4.6.3, and 4.6.4 the Atlantic does continue to open for at least the next 25 Ma. As the Atlantic continues to open it should widen to a point where it is no longer harmonically resonant with the M_2 tide.

To form the next supercontinent by introversion or extroversion either the Atlantic or Pacific (or both) must close. If the Atlantic continues to open before reversing and closing again then it could return to a resonant width. The same can be said of the Pacific it is closes also or instead of the Atlantic. Green et al. (2018) asks two questions considering the above: (i), when and where will a potential second tidal resonance occur in time and space on Earth, and (ii), is there a pattern of cyclicity in the relationship between the Wilson cycle and tidal resonance in ocean basins? - Is there a relationship between the energetics of tidal dissipation (i.e., the amount of energy the tide is dissipating in the Earth's oceans) over geological time, and the Supercontinent/Wilson cycle?

To best assess this relationship the future scenario with the most Wilson cycle initiations and terminations was chosen, Aurica. In the Aurica scenario the Atlantic and Pacific Wilson cycles terminate and a new Wilson cycle is initiated when the Pan-Asian ocean opens (section 4.6.3. A lower temporal resolution version of the Aurica scenario was used in Green et al. (2018) (Fig. 7.1)

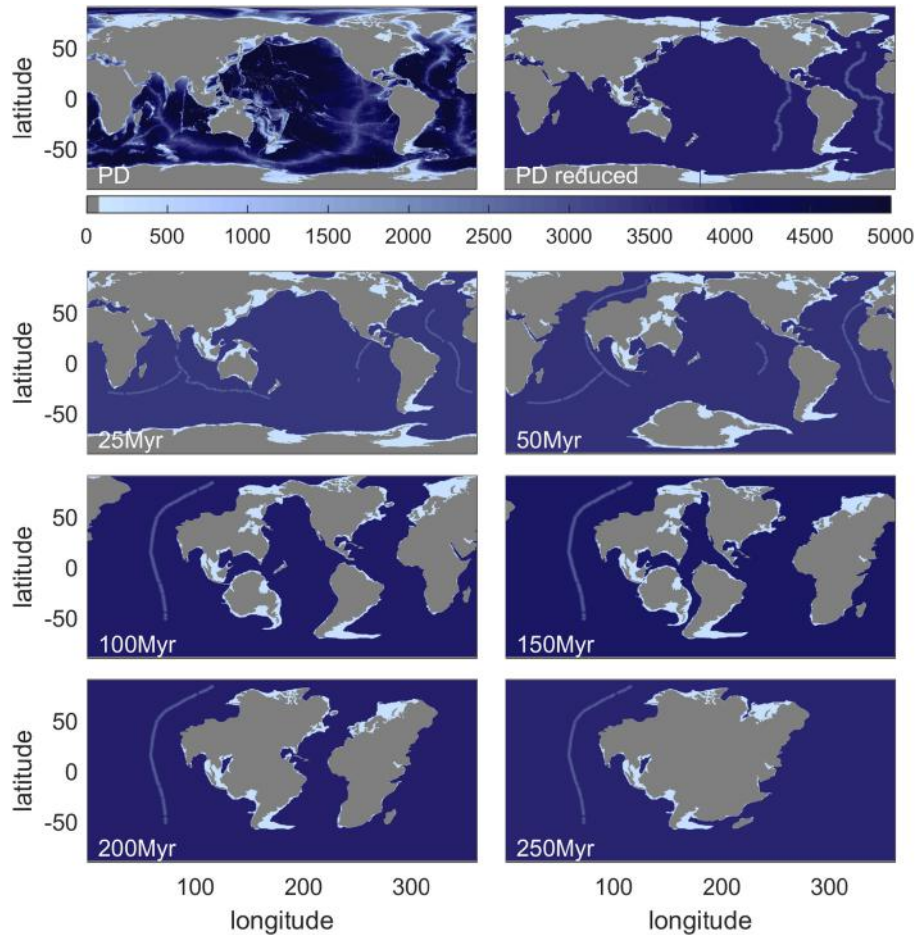


Figure 7.1: Figure 1 from Green et al. (2018) showing the progression of the next 250 Ma of Plate tectonics on Earth according to the Aurica scenario. The top two panels show present day (PD) and PD-reduced bathymetries respectively. Light blue is 200 m, intermediate blue (the ridges) is 2500 m and the majority of the ocean is <4000 m deep.

Changes in tidal dissipation over geological timescales can profoundly affect the rest of the Earth system. Herold et al. (2012) was unable to fully reproduce the conditions of the Miocene with the boundary conditions they prescribed, and Green and Huber (2013) found that enhanced abyssal tidal dissipation is necessary to recreate conditions around 55 Ma. Green and Huber (2013), and Green et al. (2017) both conclude that there must be periods in Earth history where the tidal dissipation was diminished from its present state, retro-polating Lunar recession rates confirm this (see section 2.7.3 for a full explanation).

The relationship between the tides and changing ocean basin geometry as a result of tectonic processes was already explored in the past by Green et al. (2017). Now this investigation will be continued 250 Ma into the future using the tectonic prediction of Duarte et al. (2018) to examine the relationship over a whole supercontinent cycle (Pangea - Aurica). Green et al. (2018) aims to conduct tidal modelling over an entire supercontinent cycle from the breakup of Pangea to the formation of Aurica to establish a first order predictability of when large tides

(Super-tides) may occur in Earth history.

7.1.3 Results - Tidal Amplitudes

Fig. (7.2) shows that the M_2 tidal amplitudes for the PD reduced are weaker than the PD simulation. This means the simulation could be underestimating the tide for the future scenarios. Reducing the bathymetric detail is enough to alter the tidal state in a number of regions, such as the Atlantic, Arctic ocean, and Antarctica. Conversely the K_1 tidal amplitudes appear to be larger for the PD-reduced than the PD (Fig. 7.3). The elevated tidal amplitude in the K_1 tide is likely because of the same reason as the reduction in the M_2 tide, reducing the complexity of the ocean bathymetry in the PD-reduced model alters the geometry of the Earth's basins allowing K_1 resonance to appear where it would not with the PD bathymetry.

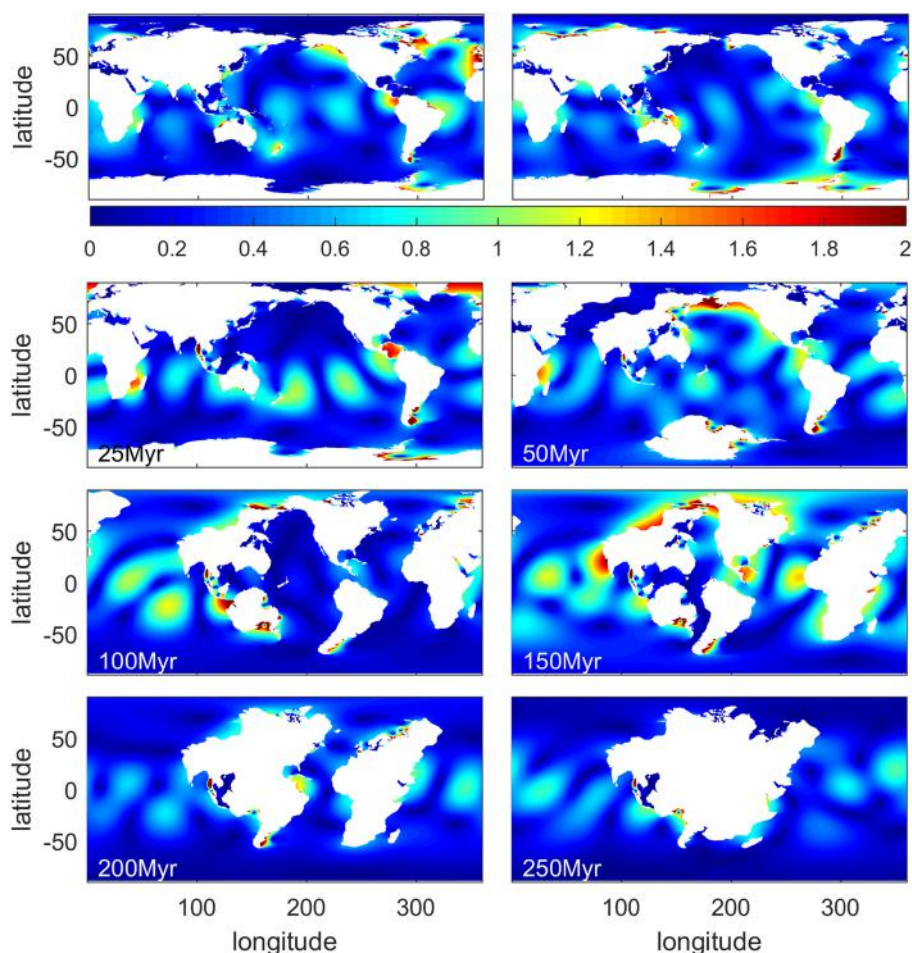


Figure 7.2: Figure 2 from Green et al. (2018) showing M_2 tidal amplitudes in meters for PD (top left) and PD-reduced (top right) simulations, along with the amplitudes at each time modelled in the future. The colour scale saturates at 2 m.

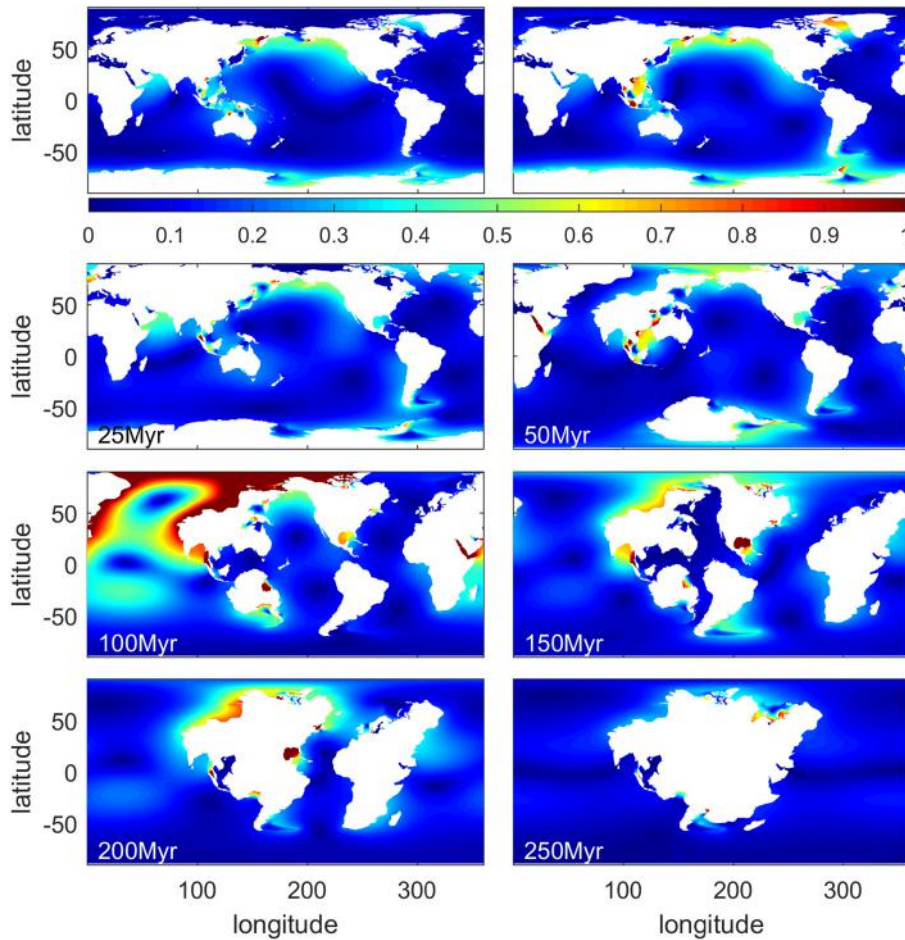


Figure 7.3: Figure 3 from Green et al. (2018) showing the same as Fig. 2, but for the K_1 constituent of the tide.

As the scenario progresses 25 Ma and 50 Ma into the future, M_2 tidal amplitudes increase. This is due to enhanced tides in both the Atlantic and Pacific oceans at these times; the Pacific is half-wavelength resonant at 25 Ma and 50 Ma. At 100 Ma large tides occur in the newly formed Pan-Asian ocean and Indian ocean - now one contiguous ocean running meridionally from Arctic to Southern oceans. As the Atlantic is closing at 150 Ma it returns to a width of half wavelength resonance. After this the tidal amplitudes globally drop as the Supercontinent begins to assemble. Once Aurica has formed only small regions such as embayements have large tides due to coastal geometry.

K_1 follows a somewhat different pattern of changing amplitudes through the scenario, however with some similarities. K_1 hits a global maximum at 100 Ma when M_2 is at a minimum. Then K_1 amplitude remains steady between 150 and 200 Ma before dropping off as Aurica forms, similarly to the M_2 amplitude. The M_2 experiences two resonances during the Aurica scenario where K_1 experiences only one. The K_1 tide is diurnal so according to the equations laid out in section 2.7.1 the width of an ocean required for K_1 resonance is larger. As the At-

lantic and Pacific oceans are both closing before reaching a width conducive to K_1 resonance, the only time it occurs in this scenario is in the Pan-Asian oceans at 100 Ma.

7.1.4 Results - Tidal Dissipation

Globally averaged tidal dissipation for the whole of the Aurica scenario showed the rates to be only 84% of Present day rates - ~ 2.2 TW (see Fig. 7.4b). This suggests the Present day tidal dissipation is elevated from the geological average, likely because of tidal resonance in the Atlantic ocean. Furthermore, the future dissipation result shows that the timing of the resonant states (or Super-Tides) in oceans is no longer than 50 Ma as no resonance observed persists for longer than that, and drift velocities are such that the ocean would widen or narrow too much in 50 Ma to retain a resonant width. The results suggest a Supercontinent cycle can support a number of resonances in both the M_2 and K_1 tide, although there is less chance K_1 will experience multiple resonances as it requires a wider ocean to be resonant.

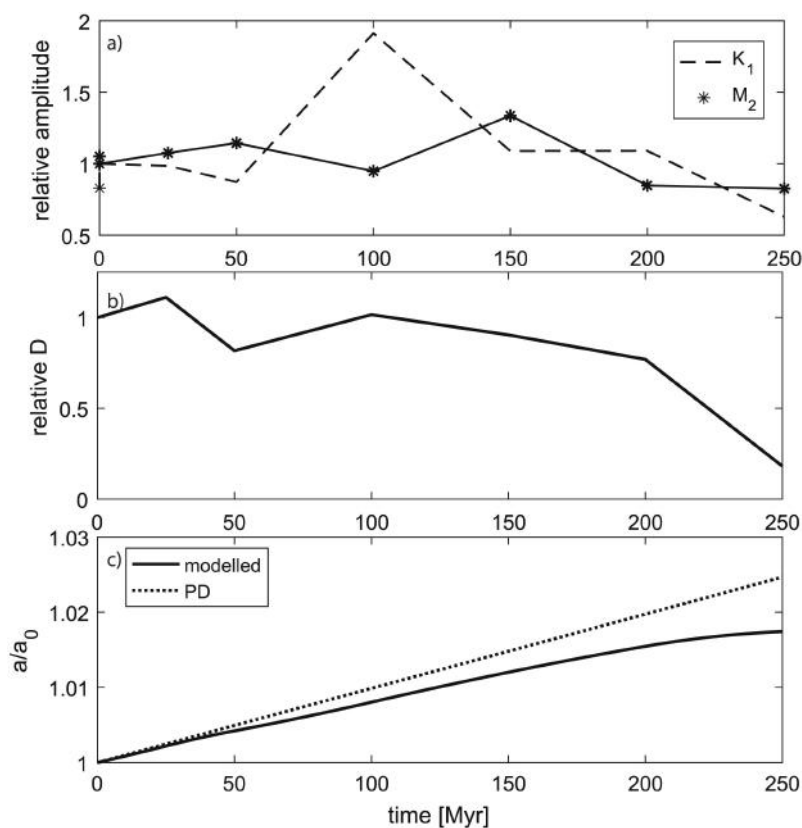


Figure 7.4: Figure 4 from Green et al. (2018) (a), Relative (to PD) tidal amplitudes for the K_1 (dashed line) and M_2 (Solid line) tidal constituents. (b), Globally integrated relative (to PD) dissipation rates for the M_2 tide. (c), Evolution of Lunar semi-major axis a over the scenario time frame, for the modelled (solid line) dissipation rate, and the present day (dashed) dissipation rate.

Weaker tidal dissipation on average, and for prolonged periods during the supercontinent

cycle further highlight the conclusions of Green et al. (2017), that the present day tide is more energetic than the geological average, and therefore should not be used in long term, or deep time investigations requiring accurate tidal dissipation rates. Furthermore, it confirms the present day Lunar recession rate is anomalously high meaning the disparity between recession age and radioisotope ages are not discordant (see section 2.7.3 for more details).

7.1.5 My contribution

My contribution to this work can be divided into two tasks: producing the kinematic tectonic maps of Aurica in enough detail that they can be used with the tidal model, and supervising a Masters student (Joe Molloy) who conducted the initial coupling of the kinematic and tidal models, thereby laying the foundation required to do the tidal modelling presented in Green et al. (2018).

For consistency the bathymetry used in these maps was made to be the same as that used in Green et al. (2017) (see their Figure 1, top left panel). This paper represents the first proper coupling of the kinematic and tidal models detailed in chapter 3 and the method here sets the precedent for the modelling done in Davies et al. (2020), and Green et al. (2020).

Joe's work during the summer of 2017 was to prepare all of the future scenarios for coupling with the tidal model, as detailed in section 3.2.1. Only the Aurica scenario was used in this work so of Joe's work, only the Aurica scenario was utilised.

7.2 Weak tides during Cryogenian glaciations

J. A. Mattias Green, Hannah S. Davies, João C. Duarte, Jessica R. Creveling, & Christopher Scotese.

(This chapter is a summary of a paper I co-authored which was published in *Nature Communications*, Green et al. (2020))

7.2.1 Abstract

The prolonged and severe “Snowball Earth” glaciations proposed to have existed during the Cryogenian period (720 to 635 million years ago (Ma)) coincided with the breakup of the supercontinent Rodinia and assembly of the supercontinent Pannotia. While the presence of extensive continental ice sheets predicts a tidally energetic Snowball ocean due to the reduced ocean depth, the supercontinent paleogeography predicts weak tides because the surrounding ocean is too large for tidal resonances to develop. Here we show, using an established numerical global tidal model and recent paleogeographic reconstructions, that the Cryogenian hosted diminished tidal amplitudes and tidal energy dissipation rates of 10-50% of today’s rates during the Snowball glaciations, and we argue that the near absence of Cryogenian tidal processes may have been one contributor to the prolonged Snowball glaciations. These results also better constrain lunar distance and orbital evolution throughout the Cryogenian, and highlight that simulations of past oceans should include explicit tidally driven mixing processes for the period under investigation.

7.2.2 Summary

During the Cryogenian period (720 - 635 Ma) it has been hypothesized that the Earth experienced severe glaciations which may have been near global in extent. Both glaciations which are proposed to have occurred during this period - The Sturtian (717 - 660 Ma) and the Marinoan (650 - 635 Ma) had continental ice advance to low latitudes (Macdonald et al., 2010). A "snowball state" for the Earth (i.e., large, low latitude extent glaciations) are climatically stable and only revert from "Snowball" when volcanic outgassing reach a threshold required for deglaciation (Hoffman et al., 2017). Along with the positive feedbacks which contribute to "Snowball" conditions - such as albedo, (Schrag et al., 2002), Green et al. (2020) proposes another positive feedback in the ocean system which may contribute to the duration of "snowball" glaciations. Tidal mixing underneath an ice sheet can rapidly increase melting from underneath as mixing removes the cold fresh water insulating the ice sheet away allowing warm saltier water to come into contact with the ice sheet enhancing melt rates. This can be observed in the Antarctic today (Makinson et al., 2011), and tidally driven mixing likely contributed to the collapse of the Laurentide ice sheet (Arbic et al., 2004). If the tides are weak during the "Snowball" glaciations, then under-ice mixing rate would be reduced and melting from under the ice sheet would occur slower.

As sections 2.7.1, and 2.7.3 outline, open ocean resonance occurs only when a basin's geometry (width and depth) is harmonic with the tide. In the period Green et al. (2020) covers the M_2 tide is 10.98 h instead of the present 12.42 h. Furthermore, the change in eustatic sea level between "snowball" and interglacial periods due to variation in land ice volume also alters basin geometry, as seen in the last glacial period (Wilmes and Green, 2014). The aims of Green et al. (2020) were twofold, to quantify tidal energetics for the cryogenian period, and to discuss how tidal energetics were effected by and could affect onset, tenure, and end of the "Snowball" glaciation periods.

7.2.3 Results - Tidal Amplitudes

At the beginning of the period modelled - until the beginning of the Sturtian glaciation at 715 Ma the tide goes from 0.2 m to 0.44 m, larger than the present day average tidal amplitude. As the Sturtian ice sheets form and the sea level drops continental shelf is exposed narrowing the oceans and allowing resonance to occur. The tidal amplitude drops over the next 25 Ma but does not drop down to microtidal levels because of emergence of land at the south pole

supporting further resonance. The large ocean appears to be on the cusp of being harmonically resonant as subtle changes at 680 and 655 Ma allow the basin to support larger tides than predicted. Onset of the Marinoan glaciation reduces the tidal energetics - This period has the most quiescent tides of any presented in this thesis, or in the other tidal modelling endeavours with OTIS. The tides return to around 0.2 m which is the average for the period modelled, around 60% of Present day values.

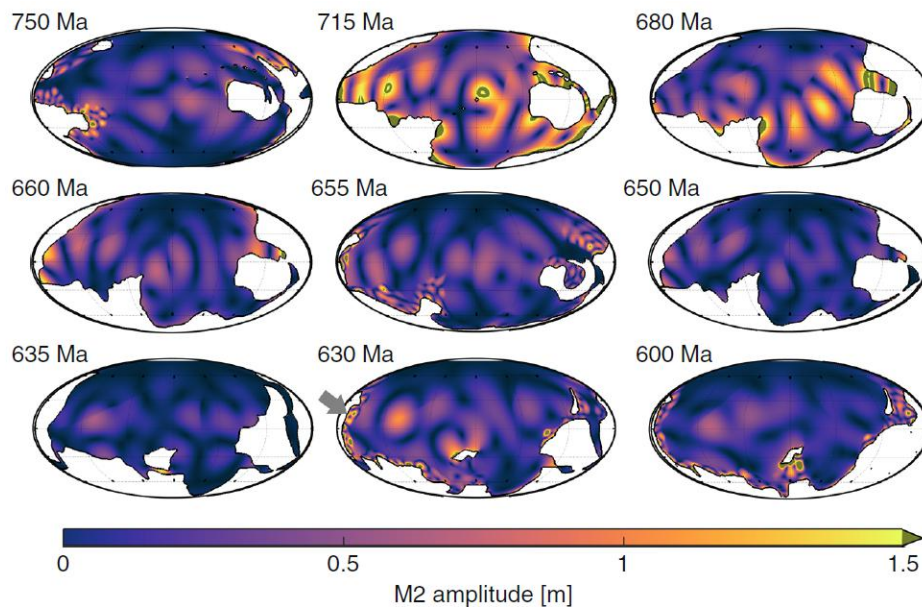


Figure 7.5: Figure 1 from Green et al. (2020) simulated M_2 tidal amplitudes for the 9 time slices represented in Fig. 7.3. Note that the colour scale saturates at 2 m. The grey arrow at 630 Ma is pointing to the Elatina formation in present day Aurstalia (Williams, 2000).

7.2.4 Results - Tidal Dissipation

As Fig. (7.6) shows, the tidal dissipation rates fail to come close to modern values. The closest value is at 715 Ma at 2 TW, around 80% of Present day. The lowest energetics to occur in this work were only around 10% of Present day. Despite the resonance which occurs at the onset of the Sturtian, both glaciations appear to dampen the tidal amplitude and dissipation. The tidal dissipation quickly increases after the end of the Marinoan, increasing from 0.2 - 1.4 TW between 635 Ma and 630 Ma. The difference between the two time slices observed is unlikely to be due to tectonic movement as little will change in only 5 Ma, therefore it is more likely the ice parameterisation affected the result more. This highlights the relationship between the ice in this period and tidal energetics. Furthermore, at 630 Ma large amplitudes (~ 2 m) are recorded along the Gondwanan coastline, now the Elatina formation in Australia (Fig. 7.5).

There is still debate whether during these glaciations the Earth was covered in solid ice or not. As Fig. (7.6) shows, the slushball simulations show, in general, weaker tidal amplitudes and dissipation for both glaciations, only strengthening slightly compared to snowball for the end of the Marinoan. In both scenarios the tidal environment is very quiescent and far below that seen during Present day.

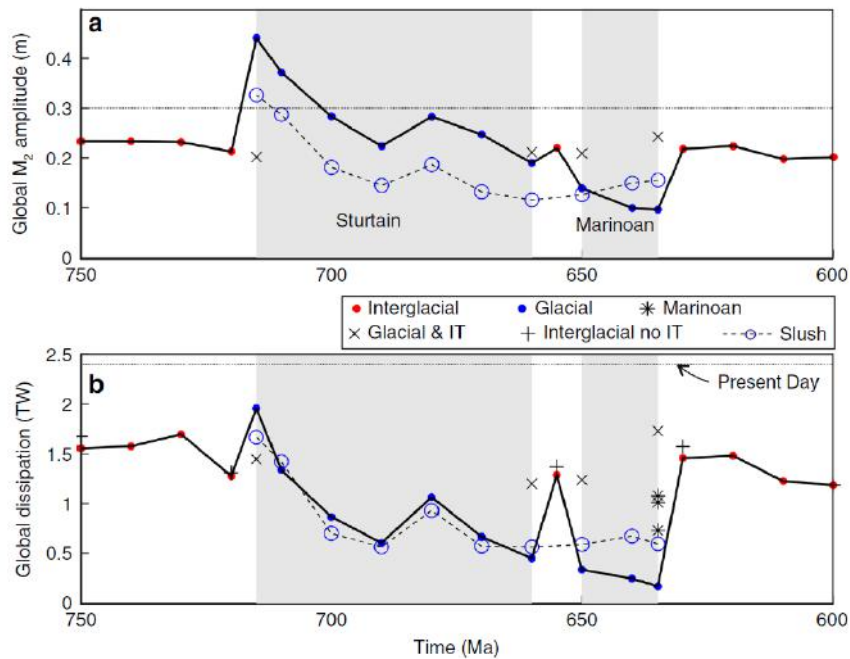


Figure 7.6: Figure 2 from Green et al. (2020) a) Globally averaged M_2 amplitudes and b) Globally averaged M_2 dissipation rates. The light grey shaded areas and data points marked by red dots are for interglacial periods, and the dark shaded areas and data points marked with blue dots are results for glacial periods. The black solid line represents simulations with conversion and no sea level change during interglacial periods, no conversion, and increased bed friction during the glacial periods. The "x" and "+" symbols represent sensitivity simulations for the onset of glaciations (although non-glacial parameters were used) and for interglacial periods with no tidal conversion respectively. The dashed line marked with blue circles represents a simulation with slushball conditions and an ice free band within 10° of the equator.

7.2.5 My contribution

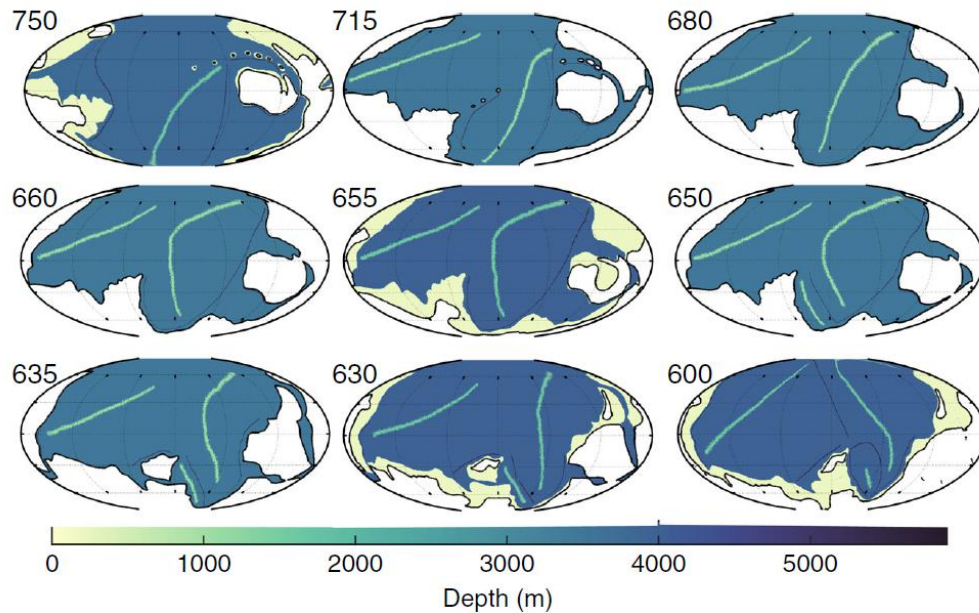


Figure 7.7: Figure 3 from Green et al. (2020) Ocean bathymetry for 9 key time slices. Land is shown in white and the ocean bathymetry in colour. Note the lack of (yellow) shelf seas during glaciations. The green lines in the oceans mark the peaks of the oceanic spreading centers and dark grey lines show subduction zones.

My contribution to this work involved creating a novel kinematic tectonic reconstruction of the period from 750 Ma to 600 Ma. GPlates has a data repository of raster maps for this time period at <https://www.earthbyte.org/paleomap-paleoatlas-for-gplates/>. The maps used from this repository covered only 750, 690, and 600 Ma so raster images from another source was also used (Scotese, 2017). Once all the relevant raster maps from both these repositories were compiled they were used to create a kinematic tectonic model compatible with OTIS by using the rasters as a base map from which to create shapefiles as detailed in section 3.1. Once the model was completed at a 50 Ma temporal resolution, the information was interpolated linearly to reconstruct plate movements to every 10 Ma between 750 and 600 Ma (a selected 9 maps are shown in Fig. 7.7). Finally, three extra slices were added to the scenario, at 635, 655, and 715 Ma as they represent the end of the Marinoan glaciation, an inter-glacial period, and the onset of the Sturtian glaciation respectively. The method to construct the bathymetries for this model are the same as described in sections 5.4.2, and 7.1.5.

7.3 Deep Future Climate on Earth: effects of tectonics, rotation rate, and insolation

M. J. Way, H. S. Davies, J. C. Duarte, & J. A. M. Green

(This chapter is a summary of a paper I co-authored which has currently been submitted to *Geophysical Research Letters*, Way et al. (2019))

7.3.1 Abstract

We explore two possible Earth climate scenarios, 200 and 250 million years into the future, using projections of the evolution of plate tectonics, solar luminosity, and rotation rate. In one scenario, a supercontinent forms at low latitudes, whereas in the other it forms at high northerly latitudes with an Antarctic subcontinent remaining at the south pole. The climates between these two end points are quite stark, with differences in mean surface temperatures approaching several degrees. The main factor in these differences is related to the topographic height of the high latitude supercontinents where higher elevations promote snowfall and subsequent higher planetary albedos. These results demonstrate the need to consider alternative boundary conditions when simulating Earth-like exoplanetary climates.

7.3.2 Summary

The study of the deep-future climate conducted in this paper is novel. Several studies of the deep past and near future have been carried out but none as ambitious as this one in its scope of exploration of the deep future.

The effects of tectonics on the surface of the Earth (i.e., Volcanism, rifting and orogeny) all have a strong influence on the climate of the planet. As the Supercontinent and related Wilson cycles progress towards the formation of the next supercontinent over the next 250 Myr, the surface of the Earth will change significantly (Davies et al., 2018). Since the breakup of the previous supercontinent Pangea, several tectonic events have occurred which have altered the climate of Earth. The opening of the Drake and Tasman passages led to the glaciation of Antarctica (Raymo and Ruddiman, 1992; DeConto and Pollard, 2003; Livermore et al., 2005). The formation of the Isthmus of Panama which strengthened the overturning circulation and formed the gulf stream (Montes et al., 2015). The formation of the Himalaya as a result of the collision of India with Asia leading to increased silicate weathering and the formation of a monsoon (Schmittner et al., 2011; Tada et al., 2016). As the supercontinent cycle continues more of these events will occur and they will also affect the climate. What is of particular interest is what the climate will be like once the next supercontinent has formed. Parrish (1993) explored the climate of the Pangea Supercontinent, concluding it was arid in the center and supported a large monsoon and large strong weather systems due to the size of the Panthalassa ocean. Aurica resembles Pangea in that it is a large equatorial supercontinent, however Amasia represents the opposite, a large polar supercontinent. Furthermore, Amasia is not contiguous, and retains an isolated Antarctica. Whether that means Amasia can or can not be considered a supercontinent because of this is besides the point, how Amasia's continental configuration affects the climate is the main focus of the investigation here.

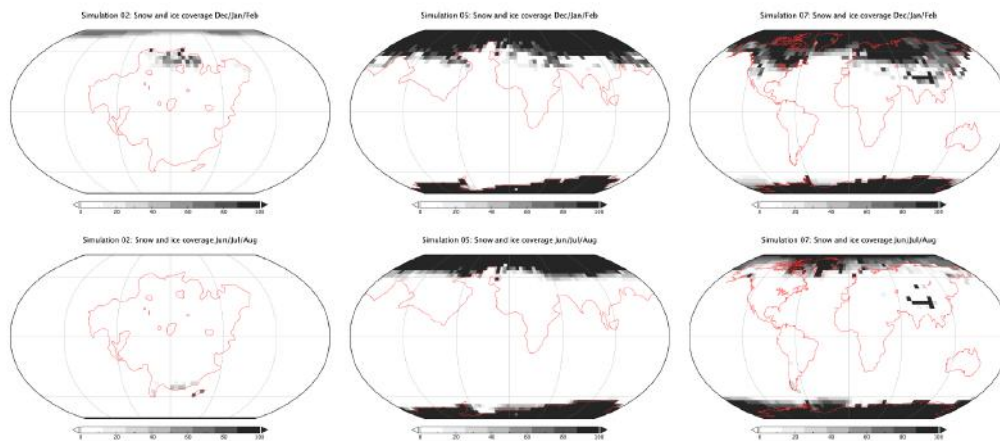


Figure 7.8: Figure 2 from Way et al. (2019), individual grid cell snow and ice fractional values for simulations 2 (Aurica_rand_PD), 5 (Amasia_rand_PD), and 7 (PD_control) show northern hemisphere winter (Dec, Jan & Feb) on the top row and northern hemisphere summer (Jun, Jul & Aug) on the bottom row.

If Plate tectonics represents a pre-requisite for a planet to maintain a stable biosphere for long enough to support complex life - i.e., its habitability lifetime is around the same length of Earth's ~ 6 Ga (Waltham, 2019) - then analysing the climate during the supercontinent phase of a supercontinent cycle is important. If habitable planets have active tectonic regimes they will most likely also have a supercontinent cycle. Using predictions of Earth's future supercontinents in global climate modelling will contribute to establishing sensitivity ranges for habitable exoplanets in the galaxy and wider universe and contribute to the search for planets similar to ours.

7.3.3 My contribution

My contribution to this work involved creating topographic maps of the future scenarios for coupling with ROCKE-3D. As ROCKE-3D is computationally expensive, and Novopangea, Pangea Ultima, and Aurica are all similarly shaped (equatorial, no polar land masses, similar size) it was decided to only use the Aurica and Amasia end members for the work. Of these, three subsets of maps were made, Low mean topography (CTRL), High mean topography (PD), and low topography with mountains (MTNS). CTRL was made with essentially no topography except for a random roughness applied randomly between 1 and 200 m. PD had a random mask applied using present day average land elevation and standard deviation. the resulting topography varies from 1 - 4000 m. Finally the MNTS subset had mountains applied to a CTRL land mask where they would geodynamically occur based on the scenario's development. For further information see section 3.3.1 and (Way et al., 2019).

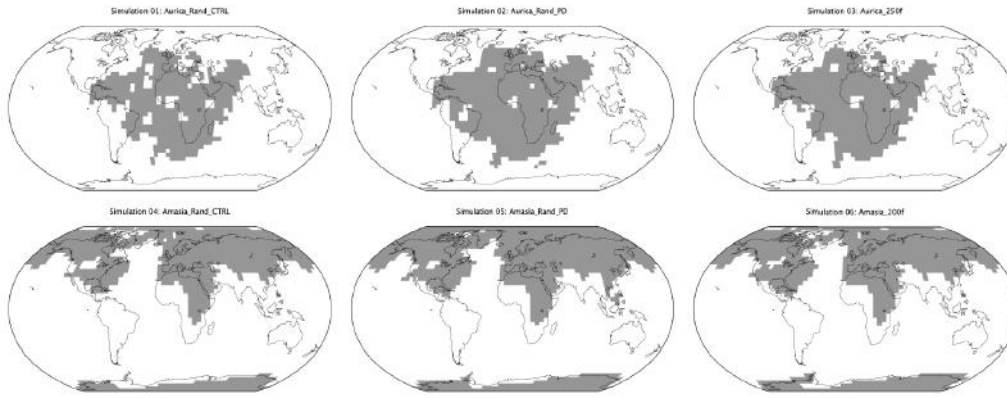


Figure 7.9: Figure 1 from Way et al. (2019) Land masks (grey) and ocean (white) used for this study, present day continental configurations have been overlain for reference.

8 Discussion

The primary research question of this work was "Is the Earth currently in a Global tidal maximum?" Green et al. (2017) shows tides during the tenure of Pangea, and for the past 200 Ma are quiescent, being around half present day values. The tidal modelling of Green et al. (2017) ends at the present day with a much more energetic tide showing that compared to the last 200 Myr since the breakup of Pangea, the present day tides are anomalously energetic. However, is this a unique phenomenon and how long will this period of more energetic tides last for?

Green et al. (2018) show using preliminary tidal modelling on the Aurica scenario of the future that the present day tides are also anomalously high when compared to the next 250 Myr. They identify other periods of enhanced tidal dissipation and amplitudes in the future, where the global tidal energetics are around twice the average for the scenario and around 80% of present day values. Furthermore, they show that the present period of more energetic tides occurs for approximately the next 20 Myrs and establish that because of the average drift velocity of continental plates in the present day, half wavelength resonance will rarely last longer than 20 Ma (see section 5.6 for a full explanation).

Davies et al. (2018) presented four scenarios of the next supercontinent gathering allowing us to further investigate tidal evolution into the geological future. In tidal modelling results of these scenarios, Davies et al. (2020) shows in all future scenarios, global tidal energetics decrease as the next supercontinent forms, regardless of which mode of ocean closing the supercontinent formed under. Despite this, periods of enhanced tidal energetics do emerge in the future (Fig. 5.3). All the periods of enhanced tidal dissipation or "super-tide" occur when the supercontinent is coalescing and ocean basins are widening and/or narrowing. As we know an ocean basin can only be resonant at a width equal to the half wavelength of the tidal wave, meaning very large and very small oceans cannot support resonant tides. Therefore tidal resonance should be most likely to occur in a supercontinent cycle when the supercontinent is dispersing or converging and ocean basins are moving through this resonant width, which is confirmed in Davies et al. (2020).

Compiling the results of Green et al. (2017, 2018); Davies et al. (2020) we can establish the tidal evolution of Earth for 500 Myrs, equivalent to an entire supercontinent cycle, beginning at the breakup of Pangea and ending in the formation of the next supercontinent. With this work we can confidently say that the present day is in a global tidal maximum. Furthermore, it is

not a unique occurrence on geological timescales. Notwithstanding, while it is likely a super-tidal period or global tidal maximum will occur at least once during a supercontinent cycle, the period of elevated tides (~ 20 Myr) is very short when compared to the whole period of the supercontinent cycle (~ 500 Myr).

Looking at the tidal dissipation over a whole supercontinent cycle, the global average is around half present day values for the majority of the supercontinent cycle, with periods of super-tide when resonance occurs. Once a supercontinent has fully coalesced, tidal dissipation decreases further, by as much as half again (25% of present day values). Illustrating the change in tidal energetics over a supercontinent cycle - very quiescent tides during supercontinent tenure and slightly elevated tides during the dispersed phase of the supercontinent cycle permeated by periods of harmonically enhanced tidal energetics.

Further studies revealed the above to be true in deep time periods of Earth history also. Based on the results detailed above in Green et al. (2020) of coupled tidal tectonic model results from the Cryogenian, the present day tides are anomalously high when compared to the geological average for the periods studied (Fig. 8.1). This is further corroborated by tidal modelling carried out during the Cenozoic (Green et al., 2017), Devonian (Byrne et al., 2020) and Phanerozoic (Hadley-Pryce & Green personal communication, June, 2020).

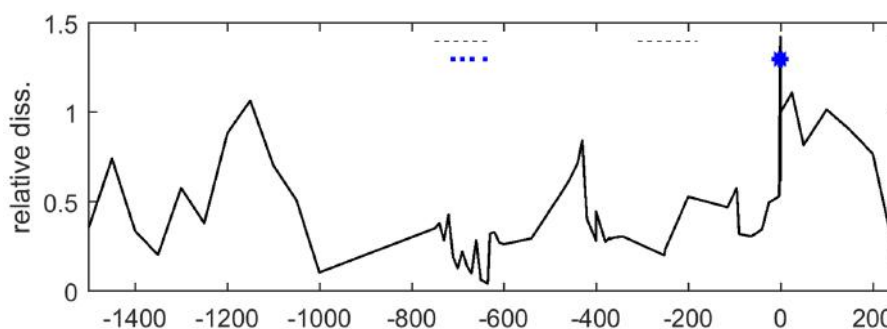


Figure 8.1: Relative tidal dissipation (Present-Day = 1) from 1500 Million years ago to 250 Million years in the future, dashed black lines represent supercontinent tenures, and blue dots represent ice ages (Green personal communication, Feb, 2020).

The anomalously energetic present day tide is due to harmonic open ocean resonance in the Atlantic (Green et al., 2017). We know the Atlantic has been opening for ~ 180 Myr and if the average divergence rate of the bordering continents is $\sim 3 \text{ cm yr}^{-1}$, after 140 Myr the ocean will be ~ 4500 km wide - which is near the harmonic width for an ocean 4 km deep (where 4 km is the average global ocean depth) (see section 2.7.1 for a full explanation). Therefore, if an ocean opens for at least 140 - 180 Myr, tidal resonance will likely develop within it. This is true for oceans which form at the beginning of the supercontinent cycle (i.e., when the supercontinent

breaks up) e.g., the Atlantic, and for oceans which form later in the supercontinent cycle, e.g., the Pan-Asian ocean. This holds true for all of the periods of dispersed continent phase where tidal modelling has been conducted, both in the past and the future (Green et al., 2020; Byrne et al., 2020; Davies et al., 2020). The best example in the future is during the Aurica scenario, the Pan-Asian ocean begins opening near the start of the Aurica scenario, and becomes harmonically resonant with the tide at 140 Ma (Fig. 5.5). Despite the fact that the Pan-Asian ocean is the second ocean to open sufficiently during the present cycle to be resonant, it still shows proof that a minimum age is required for an ocean to be harmonically resonant.

This result of a minimum age of 140 - 180 Myr before resonance is possible in an ocean can be seen in past supercycles also, the tidal modelling results of Byrne et al. (2020) show elevated global tidal amplitudes consistent with present day values (average M_2 amplitude 0.3 - 0.5 m) around 400 - 380 Ma, which is around 160 - 180 Ma after the breakup of Gondwana/Pannotia (Scotese, 2009; Merdith et al., 2017).

Looking at the tidal modelling results of the supercycle before Gondwana/Pannotia, beginning with the breakup of Rodinia at 800 Ma (Merdith et al., 2017), Green et al. (2020) finds enhanced tidal dissipation at 715, 680, and 630 Ma. The first two periods do not coincide with the prediction, however Green et al. (2020) attributes the resonance at 715 Ma to ocean basin shortening due to large scale eustatic sea level reduction as the Sturtian glaciation begins, this resonance is forced more by ice formation than geodynamics. This can be likened to the Atlantic resonance which occurred 21 Ka which was also due to ocean basin shortening as a result of eustatic sea level reduction during an ice age (Green et al., 2017). Green et al. (2020) attributes the enhanced tidal energetics at 680 to the emergence of land over the south pole, this is also not within the timing of the prediction (being only 120 Ma from the breakup of Rodinia) however, this period of enhanced tide is localised to the proto-tethys ocean and is more likely related to the continents orthoverting to form Gondwana/Pannotia. A similar period of enhanced tide is observed in the Amasia scenario at 100 Ma in Davies et al. (2020). The two periods also have similar energetics (680 Ma = $\sim 50\%$ PD and +100 Ma = $\sim 80\%$ PD dissipation). The third period of enhanced tidal dissipation during the Rodinia - Pannotia supercycle is at 630 Ma is when Gondwana/Pannotia has already arguably assembled (Murphy and Nance, 2005). This resonance is more local as Green et al. (2020) mentions, it mostly occurs in the Kipchak, Uralian, and Aegir seas, which surround the Proto-tethys ocean (Fig. 8.2).

The two snowball glaciations which occur during the Cryogenian period dampen any res-

onance which may have occurred. Furthermore, the breakup of Rodinia and the formation of Gondwana/Pannotia are only separated by around 150 Ma. This is a much shorter period of dispersed continents than other supercontinent cycles and may have made resonance far less likely.

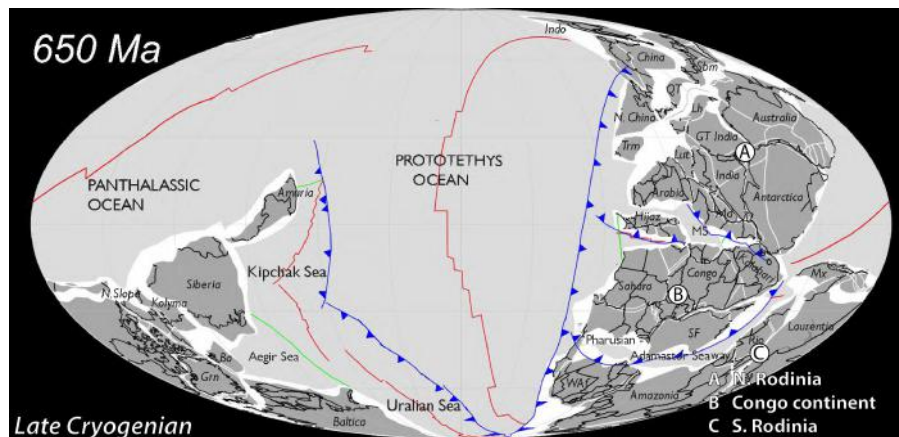


Figure 8.2: 650 Ma ago as represented by (Scotese, 2017) illustrating the landmasses, oceans, and seas of the time.

With regards to any tidal resonances which occurred as a result of the breakup of the supercontinent to precede Rodinia, the reconstructions begin to be too low resolution, both temporally and spatially to confidently predict and model the tidal environment. Figure (8.1) shows tidal results from this period conducted as a test of concept, and they do record a tidal peak at 1300 Ma, however it is smaller than the two neighbouring peaks at 1450 Ma and 1100 Ma, which occur just after the breakup of Columbia/Nuna, and during the formation of Rodinia respectively (Dalziel et al., 2000; Rogers and Santosh, 2003; Murphy and Nance, 2003; Merdith et al., 2017).

Going further back to the Archean, tidal modelling is only possible by using ensemble bathymetries to establish a statistically significant picture of the Archean tide which is in general far more energetic than the present day. In the context of open ocean resonance the Archean does exhibit some, however in general the continental area is too small to allow for the large scale open ocean resonance seen in the other periods modelled. The work presented in section 6 is preliminary however, meaning our conclusions here could change.

Including the results of Byrne et al. (2020); Green et al. (2017), and Hadley-Pryce (personal Communication, June, 2020) with those presented in this work, we now have tidal modelling results for over three supercontinent cycles and four supercontinents (Rodinia - Gondwana/Pannotia - Pangea - Future). Several distinct periods of enhanced tidal energetics have been identified, most due to open ocean resonance, and some due to regional resonances at

coastlines. Tidal resonance appears to be not uncommon at geological timescales. As concluded in 5.6 and presented in Table (5.1), each future scenario experiences a number of tidal maxima or Super-tides. Open ocean resonance is also recorded in the tidal modelling results of Green et al. (2017, 2018, 2020); Byrne et al. (2020), indicating that resonance may occur at least once or twice during the dispersed continent phase of a supercontinent cycle.

Above we have discussed how tidal resonance might arise while a Supercontinent is dispersing and new ocean(s) are being formed e.g. the Rheic, Tethys or Atlantic. We also established a method of predicting these initial open ocean resonances with geodynamic constraints (divergence rates and ocean depth). Predicting successive periods of tidal resonance in the supercontinent cycle is more difficult. As Table (5.1) shows, the four scenarios each have a different number of super-tidal peaks. This is because of the mode of formation each scenario illustrates. Different modes of supercontinent formation allow for different ocean morphologies and developments which can make harmonic resonance more or less likely. Based on the results of Davies et al. (2020), one might assume that each mode of supercontinent formation can be attributed to a generally more or less tidally active dispersed supercontinent phase i.e., Introversion (assuming the ocean opening does not fail) scenarios always exhibit a more tidally energetic dispersed continent phase than orthoversion scenarios. This appears to not be possible however. Comparing the Introversion scenario from Davies et al. (2020) with Byrne et al. (2020) and Hadley Pryce (personal communication, June, 2020) the tidal energetics for the period between the breakup of Pannotia/Gondwana and the formation of Pangea - which was an introversion event (Murphy and Nance, 2005), the results are not at all comparable. Only one period of enhanced tidal dissipation appears in the Devonian (Byrne et al., 2020). This is compared to the five of the Pangea Ultima introversion. Furthermore, when comparing the Amasia scenario with the period between the breakup of Rodinia and the formation of Pannotia/Gondwana - an orthoversion event (Murphy and Nance, 2005), Green et al. (2020) finds three periods of enhanced tidal dissipation, where the Amasia scenario is tidally quiescent throughout.

It must be noted that the deep-time periods highlighted cannot be faithfully compared with the scenarios of the future. Reconstructions of the Devonian and the Phanerozoic as a whole are not well resolved and fully agreed on. Not only are the continental geolocations debated but the mode of formation of Pangea is also debated, as it may have formed by Introversion, Orthoversion, or a combination of the both (see Davies et al. (2018) for a full explanation).

With regards to the Cryogenian, the maps used in Green et al. (2020) are rough estimations of the continental extent at the time and differences in the true continental extent could alter the results completely for some periods, particularly where resonance occurs. Furthermore, the tidal modelling conducted in Green et al. (2020) alters the tidal conversion and sea level to simulate the glaciations where the Amasia scenario retains present day ocean volume (and therefore sea level), and conversion throughout. That in mind, Way et al. (2019) finds significant ice sheet growth in ROCKE-3D models of the Amasia scenario which would alter eustatic sea level. If the Amasia scenario induced another "Snowball" glaciation, then the global sea level could be reduced by a similar amount to that estimated for the Sturtian or Marinoan glaciations. This would alter the effective shape of every ocean basin on Earth which could drastically alter the tidal energetics. Even regular ice ages such as the last glacial maximum are capable of altering ocean basin shape enough to alter the open ocean tidal energetics (Wilmes and Green, 2014). Even a small scale glaciation of the Amasia supercontinent could alter the results presented in Davies et al. (2020).

All of the periods of enhanced tidal energetics or Super-tides presented have two things in common, the timing of their emergence during the Supercontinent cycle, and their duration. As has been discussed above, around 140 - 180 Myr must pass for resonance to have a chance to occur in an ocean forming from the breakup of a supercontinent. Glaciations can alter ocean basin geometry significantly enough to expedite resonance in an ocean as seen in 715 Ma in Green et al. (2020), however this appears rare. After this period of 140 - 180 Myr, it appears resonance can develop at any time and any number of times during the dispersed phase of the Supercontinent cycle (Table 5.1). As the Supercontinent begins to enter a terminal stage of formation when its contingent parts are only separated by narrow seaways, resonance may still occur, however it is in surrounding oceans, not the seaways, which often resemble the Mediterranean sea in geology and tidal state. This is best illustrated at 220 Ma of the Pangea Ultima scenario (Fig. 5.2e), and 630 Ma of the Cryogenian simulations of Green et al. (2020) (Fig. 7.5). Pangea Ultima is only 30 Ma away from being fully assembled, the Atlantic now separated into two narrow seaways by a partial collision of Africa and South America, however the Pacific becomes resonant one last time before the Supercontinent fully forms. With the Cryogenian resonance at 630 Ma, it is arguably a regional case of resonance, as does occur once some supercontinents have assembled (e.g., Amasia, see Fig. 5.6f) however, it is still worth noting here as it was highlighted as a period of enhanced tidal energetics by Green et al.

(2020).

Therefore, while there appears to be a time after a supercontinent opens when resonance is not possible (or very unlikely) resonance can occur right up to the formation of a supercontinent. After a Supercontinent has formed, it may have some regional resonances at the coast, however these are localised and far weaker than when open ocean resonance occurs (Fig. 5.3). None of the supercontinents that have been tidally modelled have sustained large tides Green et al. (2017), Hadley-Pryce (personal communication June 2020), and Fig. (5.3). Geodynamically this makes sense, the majority of the Earth's water mass would be in a super ocean which would behave in a similar way to a water world exhibiting only small tides (Rohling (2020), and section 2.7). Furthermore, the supercontinent is fully assembled which means the Earth's continents are in a configuration with the smallest surface area. As coastlines (shelf seas) represent a major area of tidal dissipation on Earth, dissipating 1.8 TW of the M_2 tide in the Present Day (Munk and Wunsch, 1998), reducing that surface area will reduce the amount of tidal energy dissipated at the coast and thereby reduce global total ocean dissipation.

The Amasia scenario end member time slice (+200 Ma; Fig. 5.6f) represents the most tidally energetic supercontinent at $\sim 80\%$ of PD values. This we believe is a product of how the future supercontinents formed. Each scenario used present day coastlines with very detailed morphology ($<0.25^\circ$). As each supercontinent forms in the future scenarios the sum total surface area of the continent(s) drops. Amasia however retains a much larger portion of coastline than Pangea Ultima, Novopangea, or Aurica, and therefore has a much larger coastline surface area where the M_2 tide can dissipate. Where one or two large ocean basins (and their coastlines) close, and the supercontinent forms made up of every continent in the Pangea Ultima, Novopangea, and Aurica scenarios, the only ocean basin to close in the Amasia scenario is the Arctic ocean, a much smaller basin than the Atlantic or Pacific. Furthermore, Amasia forms with Antarctica remaining an independent separate continent. These both mean Amasia retains a much larger coastline area. It is therefore not prudent to use Amasia as a standard of tidal energetics during a supercontinent's tenure. Perhaps an upper bound, although this is uncertain as Davies et al. (2020) mentions, their tidal results may overestimate the true tidal energetics meaning the tidal state of the end member of the Amasia scenario could be more quiescent.

After modelling the tidal environment of several periods in Earth history the aim of this work was to quantify the relationship between tides and the supercontinent cycle. The tide represents a regular and predictable force in the Earth system, however the supercontinent

cycle is far less predictable and somewhat chaotic in its motions. Past work has attempted to predict the motions of the continents, i.e., a regular accordion like motion or introversion and extroversion (Murphy and Nance, 2003), or a regular polar to equatorial alternation of supercontinents (Mitchell et al., 2012). However, Davies et al. (2018) struggles to find this correlation, mainly because there have been so few complete, and well mapped supercontinent cycles on Earth.

It appears to be very difficult to objectively compare supercontinent cycles, either of the past or future. When looking at the different supercontinent cycles of Earth history it is tempting to try to find repetition and coincidences, however the motion of continents over geological time scales appears random. One could argue repetition can be found in the Wilson cycle as oceans close and re-open, however, the Rheic and Atlantic, while being similar oceans, are not identical and have different suture zones marking their closure and opening respectively (Burke et al., 1977). That in mind, as has been touched on above, the Wilson cycle dictates the mode of formation of supercontinents and that allows classification, however the fact that the mode of formation of Pannotia/gondwana and Pangea is still debated (Murphy and Nance, 2005; Mitchell et al., 2012) and that four completely different predictive scenarios of the Earth's future (among possibly more) exist and are debated, shows that understanding and predicting the motions of the continents as they progress through the supercontinent cycle is very difficult.

It may not be impossible to predict what the next supercontinent will look like however, and each academic will have their reasons for supporting one of the predictions in Davies et al. (2018). We know the primary forcing of plate tectonics is slab pull from sinking oceanic plate. We know that ocean plate is gravitationally unstable after 20 Ma (Condie, 1997), and will likely not remain on the surface of Earth for much longer after 180 Ma (Müller et al., 2008). We also know this sinking slab hydrates and disrupts the chemical equilibrium of the Mantle causing upwelling (Torsvik et al., 2016) which also plays a role in plate tectonics in the form of hot spots and LIPs argued to be the mechanism by which supercontinents break up (Pastor-Galán et al., 2019). We do not know how subduction initiates (Duarte et al., 2013; Marques et al., 2014; Stern and Gerya, 2018). If we are to assume the same as Davies et al. (2018) and simply assume subduction must somehow initiate in the present day Atlantic because of the average plate age at the boundaries of the ocean basin then it must be assumed the Atlantic will close. However the Pacific is already surrounded by subduction zones and the prevailing present day continental plate velocity suggests the Pacific is closing (Schellart et al., 2008). Here in lies the

problem, which Duarte et al. (2018) attempts to solve with the Aurica scenario.

Perhaps the question of "how a supercontinent forms" is not the correct one but instead "are supercontinents forming and dispersing" is more pertinent. Condie (1997); Pastor-Galán et al. (2019); Waltham (2019) and others emphasise that plate tectonics has impacted the Earth more than any other component of the Earth system, and that plate tectonics is necessary for a planet to have a long habitable period (~ 6 Ga). Regardless of how a supercontinent forms, its formation, tenure, and eventual breakup will affect the Earth system. As this thesis has shown, supercontinent formation is correlated with tidal quiescence which may in extreme cases result in ocean anoxia due to reduced mixing (Wignall and Hallam, 1992), however this link should be further investigated to confidently attribute anoxia to reduced tidal mixing during supercontinent tenure.

There is certainly also a link between supercontinents and climate. Supercontinents have fundamentally altered the climate in the past (Parrish, 1993; Santosh, 2010), and the formation of the next supercontinent in 250 Ma will also alter the climate significantly from its present day state (section 7.3). Way et al. (2019) shows that latitudinal concentration of landmasses significantly affects climate. When compared, the climate of the end member Aurica and Amasia scenario are very different (Fig. 7.8). Aurica being a mostly equatorial landmass experiences very little snow and ice cover, where in contrast the Amasia end member is almost completely covered $>30^\circ\text{N}$ in Northern hemisphere winter months. Where the Amasia end member is much colder, the Aurica end member is potentially more arid, and has weaker ocean circulation. The Aurica simulation has a weaker stream function meaning less moisture uptake to the atmosphere. Way et al. (2019) finds interesting results from climate modelling of Aurica and Amasia, however their study represents more of a test of concept than a complete investigation. Further multi-disciplinary modelling is required to fully resolve the relationship between climate the the supercontinent cycle over geological time.

This work has addressed the main question of if the present day has anomalously high tides when compared to the geological average, however the full relationship between tides and tectonics is very complex. This work has shown that the elevated tidal energetics of the present day is not unique in the tidal record over geological time but a result of a confluence of tectonics and tidal period. This has occurred several times in Earth history and will occur in Earth's future. This is not the only way tides affect Earth though, just as the supercontinent cycle is not the only way tectonics affects Earth. Chapter 6 shows that the early Earth Moon

relationship and the tide that occurred because of that may have impacted the development of life. It may not be necessary for a planet like ours to have a Moon to first cause life to develop, however the tides may have helped by mixing the primordial oceans.

8.1 Future work

In future work we believe the question of "are supercontinents forming and dispersing and how is that affecting the Earth system" should be further explored. Here, the supercontinent cycle has been found to fundamentally alter global tidal energetics and climate over geological timescales. The full effect of this on Earth and on Earth-like exo-planets remains to be investigated. Furthermore, how does the supercontinent cycle affect other components of the Earth system such as ocean chemistry and atmospheric composition? Understanding the true impact of plate tectonics and the supercontinent cycle on the Earth system will not only help us to understand our own planet but planets similar to our own in the wider universe.

Furthermore, the question "How has life shaped Earth and how has Earth shaped life" is among the top ten research questions of the 21st century. This work details a link between two seemingly disparate components of the Earth system - the tide and the supercontinent cycle, both forced by completely different mechanisms yet which interact to alter the surface of the Earth potentially also impacting life (Balbus (2014), Chapter 6). There is already an abundance of literature illustrating how different components of the Earth system affect each other, e.g., silicate weathering where climate and marine productivity are balanced by tectonic uplift. Earth's geodynamic evolution is intimately linked to the evolution of the atmosphere, oceans and life. As the Earth has aged it has changed fundamentally in each of these components however, it has remained habitable. Quantifying the relationship and feedbacks between these components is essential to fully understanding the Earth system and its dynamism over geological time.

Future work should therefore generally focus on two things - how each component of the Earth system is linked, and why Earth has been (and will continue to be) habitable for so long (~6 Ga). Feedbacks in the Earth system appear to be tuned to anthropic selection, i.e., they occur over timescales conducive (at least on Earth) to allowing the evolution of "observers". Is Earth unique in this, is it an outlier or are there billions of "Earth twins" in the universe?

References

Arbic, B. K. and Garrett, C. (2010), 'A coupled oscillator model of shelf and ocean tides', *Continental Shelf Research* **30**(6), 564 – 574. Tides in Marginal Seas - A special issue in memory of Prof Alexei Nekrasov.

URL: <http://www.sciencedirect.com/science/article/pii/S0278434309002271>

Arbic, B. K., Karsten, R. H. and Garrett, C. (2009), 'On tidal resonance in the global ocean and the back-effect of coastal tides upon open-ocean tides', *Atmosphere-Ocean* **47**(4), 239–266.

URL: <https://doi.org/10.3137/OC311.2009>

Arbic, B. K., MacAyeal, D. R., Mitrovica, J. X. and Milne, G. A. (2004), 'Ocean tides and heinrich events', *Nature* **432**, 460.

URL: <https://doi.org/10.1038/432460a>

Balbus, S. A. (2014), 'Dynamical, biological and anthropic consequences of equal lunar and solar angular radii', *Proceedings of the Royal Society A: Mathematical, Physical and Engineering Sciences* **470**(2168), 20140263.

URL: <https://royalsocietypublishing.org/doi/abs/10.1098/rspa.2014.0263>

Billen, M. I. (2008), 'Modeling the dynamics of subducting slabs', *Annual Review of Earth and Planetary Sciences* **36**(1), 325–356.

URL: <https://doi.org/10.1146/annurev.earth.36.031207.124129>

Blackledge, B. W., Green, J. A. M., Barnes, R. and Way, M. J. (2020), 'Tides on other earths: Implications for exoplanet and palaeo-tidal simulations', *Geophysical Research Letters* **47**(12), e2019GL085746. e2019GL085746 10.1029/2019GL085746.

URL: <https://agupubs.onlinelibrary.wiley.com/doi/abs/10.1029/2019GL085746>

Boschman, L. M. and van Hinsbergen, D. J. J. (2016), 'On the enigmatic birth of the pacific plate within the panthalassa ocean', *Science Advances* **2**(7).

URL: <https://advances.sciencemag.org/content/2/7/e1600022>

Bossard, D. C. (2004), 'Report of the scientific results of the voyage of h.m.s. challenger during the years of 1873 - 76.'. [Online; accessed: 22.10.2020].

URL: <http://www.19thcenturyscience.org/HMSC/README.htm>

- Bradley, D. C. (2008), ‘Passive margins through earth history’, *Earth-Science Reviews* **91**(1), 1 – 26.
URL: <http://www.sciencedirect.com/science/article/pii/S0012825208000871>
- Bradley, D. C. (2011), ‘Secular trends in the geologic record and the supercontinent cycle’, *Earth-Science Reviews* **108**(1), 16 – 33.
URL: <http://www.sciencedirect.com/science/article/pii/S0012825211000717>
- Burke, K. (2011), ‘Plate tectonics, the wilson cycle, and mantle plumes: Geodynamics from the top’, *Annual Review of Earth and Planetary Sciences* **39**(1), 1–29.
URL: <https://doi.org/10.1146/annurev-earth-040809-152521>
- Burke, K., Dewey, J. and Kidd, W. (1977), ‘World distribution of sutures—the sites of former oceans’, *Tectonophysics* **40**(1-2), 69–99.
- Burke, K., Steinberger, B., Torsvik, T. H. and Smethurst, M. A. (2008), ‘Plume generation zones at the margins of large low shear velocity provinces on the core–mantle boundary’, *Earth and Planetary Science Letters* **265**(1), 49 – 60.
URL: <http://www.sciencedirect.com/science/article/pii/S0012821X07006036>
- Byrne, H. M., Green, J. A. M., Balbus, S. A. and Ahlberg, P. E. (2020), ‘Tides: A key environmental driver of osteichthyan evolution and the fish-tetrapod transition?’, *Proceedings of the Royal Society A: Mathematical, Physical and Engineering Sciences* **476**(2242), 20200355.
URL: <https://royalsocietypublishing.org/doi/abs/10.1098/rspa.2020.0355>
- Cande, S. C. and Stegman, D. R. (2011), ‘Indian and african plate motions driven by the push force of the réunion plume head’, *Nature* **475**, 47–52.
URL: <https://doi.org/10.1038/nature10174>
- Catling, D. C. and Zahnle, K. J. (2020), ‘The archean atmosphere’, *Science Advances* **6**(9).
URL: <https://advances.sciencemag.org/content/6/9/eaax1420>
- Cawood, P. A. (2020), ‘Earth Matters: A tempo to our planet’s evolution’, *Geology* **48**(5), 525–526.
URL: <https://doi.org/10.1130/focus052020.1>
- Cawood, P. A., Hawkesworth, C. J., Pisarevsky, S. A., Dhuime, B., Capitanio, F. A. and Nebel, O. (2018), ‘Geological archive of the onset of plate tectonics’, *Philosophical*

Transactions of the Royal Society A: Mathematical, Physical and Engineering Sciences **376**(2132), 20170405.

URL: <https://royalsocietypublishing.org/doi/abs/10.1098/rsta.2017.0405>

Cloos, M. (1993), 'Lithospheric buoyancy and collisional orogenesis: Subduction of oceanic plateaus, continental margins, island arcs, spreading ridges, and seamounts', *GSA Bulletin* **105**(6), 715–737.

URL: [https://doi.org/10.1130/0016-7606\(1993\)105<0715:LBACOS>2.3.CO;2](https://doi.org/10.1130/0016-7606(1993)105<0715:LBACOS>2.3.CO;2)

Cocks, L. R. M. and Torsvik, T. H. (2011), 'The palaeozoic geography of laurentia and western laurussia: A stable craton with mobile margins', *Earth-Science Reviews* **106**(1), 1 – 51.

URL: <http://www.sciencedirect.com/science/article/pii/S001282521100016X>

Coltice, N., Rolf, T., Tackley, P. J. and Labrosse, S. (2012), 'Dynamic causes of the relation between area and age of the ocean floor', *Science* **336**(6079), 335–338.

URL: <https://science.sciencemag.org/content/336/6079/335>

Condie, K. C. (1994), *Archean crustal evolution*, Elsevier.

Condie, K. C. (1997), Chapter 2 - the earth's crust, in K. C. Condie, ed., 'Plate Tectonics and Crustal Evolution (Fourth Edition)', fourth edition edn, Butterworth-Heinemann, Oxford, pp. 36 – 68.

URL: <http://www.sciencedirect.com/science/article/pii/B9780750633864500070>

Conrad, C. P. and Lithgow-Bertelloni, C. (2002), 'How mantle slabs drive plate tectonics', *Science* **298**(5591), 207–209.

URL: <https://science.sciencemag.org/content/298/5591/207>

Dalrymple, G. B. (2001), 'The age of the earth in the twentieth century: a problem (mostly) solved', *Geological Society, London, Special Publications* **190**(1), 205–221.

URL: <https://sp.lyellcollection.org/content/190/1/205>

Dalziel, I. W. D., Mosher, S. and Gahagan, L. M. (2000), 'Laurentia-kalahari collision and the assembly of rodinia', *The Journal of Geology* **108**(5), 499–513.

URL: <https://doi.org/10.1086/314418>

- Dalziel, I. W., Lawver, L. A., Norton, I. O. and Gahagan, L. M. (2013), 'The scotia arc: Genesis, evolution, global significance', *Annual Review of Earth and Planetary Sciences* **41**(1), 767–793.
URL: <https://doi.org/10.1146/annurev-earth-050212-124155>
- Dannowski, A., Kopp, H., Grevemeyer, I., Lange, D., Thorwart, M., Bialas, J. and Wollatz-Vogt, M. (2020), 'Seismic evidence for failed rifting in the ligurian basin, western alpine domain', *Solid Earth* **11**(3), 873–887.
URL: <https://se.copernicus.org/articles/11/873/2020/>
- Davies, H. S., Green, J. A. M. and Duarte, J. C. (2020), 'Back to the future ii: tidal evolution of four supercontinent scenarios', *Earth System Dynamics* **11**(1), 291–299.
URL: <https://esd.copernicus.org/articles/11/291/2020/>
- Davies, H. S., Green, J. M. and Duarte, J. C. (2018), 'Back to the future: Testing different scenarios for the next supercontinent gathering', *Global and Planetary Change* **169**, 133 – 144.
URL: <http://www.sciencedirect.com/science/article/pii/S0921818118302054>
- DeConto, R. M. and Pollard, D. (2003), 'Rapid cenozoic glaciation of antarctica induced by declining atmospheric co₂', *Nature* **421**, 245–249.
URL: <https://doi.org/10.1038/nature01290>
- Dewey, J. F. and Burke, K. (1974), 'Hot Spots and Continental Break-up: Implications for Collisional Orogeny', *Geology* **2**(2), 57–60.
URL: [https://doi.org/10.1130/0091-7613\(1974\)2<57:HSACBI>2.0.CO;2](https://doi.org/10.1130/0091-7613(1974)2<57:HSACBI>2.0.CO;2)
- Dewey, J. and Spall, H. (1975), 'Pre-Mesozoic plate tectonics: How far back in Earth history can the Wilson Cycle be extended?', *Geology* **3**(8), 422–424.
URL: [https://doi.org/10.1130/0091-7613\(1975\)3<422:PPTHFB>2.0.CO;2](https://doi.org/10.1130/0091-7613(1975)3<422:PPTHFB>2.0.CO;2)
- Dietz, R. S. (1977), 'Plate tectonics: A revolution in geology and geophysics', *Tectonophysics* **38**(1), 1 – 6. Present State of Plate Tectonics.
URL: <http://www.sciencedirect.com/science/article/pii/0040195177901974>
- Duarte, J. C., Rosas, F. M., Terrinha, P., Schellart, W. P., Boutelier, D., Gutscher, M.-A. and Ribeiro, A. (2013), 'Are subduction zones invading the Atlantic? Evidence from the south-

west Iberia margin', *Geology* **41**(8), 839–842.

URL: <https://doi.org/10.1130/G34100.1>

Duarte, J. C. and Schellart, W. P. (2016), *Plate boundaries and natural Hazards*, Vol. 219, John Wiley & Sons.

Duarte, J. C., Schellart, W. P. and Rosas, F. M. (2018), 'The future of earth's oceans: consequences of subduction initiation in the atlantic and implications for supercontinent formation', *Geological Magazine* **155**(1), 45–58.

Eagles, G. and Jokat, W. (2014), 'Tectonic reconstructions for paleobathymetry in drake passage', *Tectonophysics* **611**, 28 – 50.

URL: <http://www.sciencedirect.com/science/article/pii/S0040195113006860>

Egbert, G. D., Bennett, A. F. and Foreman, M. G. G. (1994), 'Topex/poseidon tides estimated using a global inverse model', *Journal of Geophysical Research: Oceans* **99**(C12), 24821–24852.

URL: <https://agupubs.onlinelibrary.wiley.com/doi/abs/10.1029/94JC01894>

Egbert, G. D. and Erofeeva, S. Y. (2002), 'Efficient Inverse Modeling of Barotropic Ocean Tides', *Journal of Atmospheric and Oceanic Technology* **19**(2), 183–204.

URL: [https://doi.org/10.1175/1520-0426\(2002\)019<0183:EIMOBO>2.0.CO;2](https://doi.org/10.1175/1520-0426(2002)019<0183:EIMOBO>2.0.CO;2)

Egbert, G. D. and Ray, R. D. (2001), 'Estimates of m2 tidal energy dissipation from topex/poseidon altimeter data', *Journal of Geophysical Research: Oceans* **106**(C10), 22475–22502.

URL: <https://agupubs.onlinelibrary.wiley.com/doi/abs/10.1029/2000JC000699>

Egbert, G. D., Ray, R. D. and Bills, B. G. (2004), 'Numerical modeling of the global semidiurnal tide in the present day and in the last glacial maximum', *Journal of Geophysical Research: Oceans* **109**(C3).

URL: <https://agupubs.onlinelibrary.wiley.com/doi/abs/10.1029/2003JC001973>

Foley, B. J. and Driscoll, P. E. (2016), 'Whole planet coupling between climate, mantle, and core: Implications for rocky planet evolution', *Geochemistry, Geophysics, Geosystems* **17**(5), 1885–1914.

URL: <https://agupubs.onlinelibrary.wiley.com/doi/abs/10.1002/2015GC006210>

- Gerkema, T. (2019), *An Introduction to Tides*, Cambridge University Press.
- Golonka, J. (2007), 'Late triassic and early jurassic palaeogeography of the world', *Palaeogeography, Palaeoclimatology, Palaeoecology* **244**(1), 297 – 307. Triassic-Jurassic Boundary events: problems, progress, possibilities.
URL: <http://www.sciencedirect.com/science/article/pii/S003101820600455X>
- Granot, R. (2016), 'Palaeozoic oceanic crust preserved beneath the eastern mediterranean', *Nature Geoscience* **9**, 701–705.
URL: <https://doi.org/10.1038/ngeo2784>
- Green, J. A. M. (2010), 'Ocean tides and resonance', *Ocean Dynamics* **60**, 1243–1253.
URL: <https://doi.org/10.1007/s10236-010-0331-1>
- Green, J. A. M. and Huber, M. (2013), 'Tidal dissipation in the early eocene and implications for ocean mixing', *Geophysical Research Letters* **40**(11), 2707–2713.
URL: <https://agupubs.onlinelibrary.wiley.com/doi/abs/10.1002/grl.50510>
- Green, J. A. M., Molloy, J. L., Davies, H. S. and Duarte, J. C. (2018), 'Is there a tectonically driven supertidal cycle?', *Geophysical Research Letters* **45**(8), 3568–3576.
URL: <https://agupubs.onlinelibrary.wiley.com/doi/abs/10.1002/2017GL076695>
- Green, J., Draper, D., Boardsen, S. and Dong, C. (2020), 'When the moon had a magnetosphere', *Science Advances* **6**(42).
URL: <https://advances.sciencemag.org/content/6/42/eabc0865>
- Green, J., Huber, M., Waltham, D., Buzan, J. and Wells, M. (2017), 'Explicitly modelled deep-time tidal dissipation and its implication for lunar history', *Earth and Planetary Science Letters* **461**, 46 – 53.
URL: <http://www.sciencedirect.com/science/article/pii/S0012821X16307518>
- Hatton, C. J. (1997), 'The superocean cycle', *South African Journal of Geology* **100**(4), 301–310.
- Herold, N., Huber, M., Müller, R. D. and Seton, M. (2012), 'Modeling the miocene climatic optimum: Ocean circulation', *Paleoceanography* **27**(1).
URL: <https://agupubs.onlinelibrary.wiley.com/doi/abs/10.1029/2010PA002041>

Hess, H. H. (1962), History of Ocean Basins, in 'Petrologic Studies', Geological Society of America.

URL: <https://doi.org/10.1130/Petrologic.1962.599>

Hoffman, P. F. (1999), 'The break-up of roдинia, birth of gondwana, true polar wander and the snowball earth', *Journal of African Earth Sciences* **28**(1), 17 – 33.

URL: <http://www.sciencedirect.com/science/article/pii/S0899536299000184>

Hoffman, P. F., Abbot, D. S., Ashkenazy, Y., Benn, D. I., Brocks, J. J., Cohen, P. A., Cox, G. M., Creveling, J. R., Donnadieu, Y., Erwin, D. H., Fairchild, I. J., Ferreira, D., Goodman, J. C., Halverson, G. P., Jansen, M. F., Le Hir, G., Love, G. D., Macdonald, F. A., Maloof, A. C., Partin, C. A., Ramstein, G., Rose, B. E. J., Rose, C. V., Sadler, P. M., Tziperman, E., Voigt, A. and Warren, S. G. (2017), 'Snowball earth climate dynamics and cryogenian geology-geobiology', *Science Advances* **3**(11).

URL: <https://advances.sciencemag.org/content/3/11/e1600983>

Holmes, A. (1931), 'Xviii. radioactivity and earth movements', *Transactions of the Geological Society of Glasgow* **18**(3), 559–606.

URL: <https://trngl.lyellcollection.org/content/18/3/559>

Iaffaldano, G., Davies, D. R. and DeMets, C. (2018), 'Indian ocean floor deformation induced by the reunion plume rather than the tibetan plateau', *Nature Geoscience* **11**, 362–366.

URL: <https://doi.org/10.1038/s41561-018-0110-z>

Kagan, B. A. (1997), 'Earth—moon tidal evolution: model results and observational evidence', *Progress in Oceanography* **40**(1), 109 – 124. Tidal Science In Honour of David E. Cartwright.

URL: <http://www.sciencedirect.com/science/article/pii/S007966119700027X>

King, S. D. (2018), 'Venus resurfacing constrained by geoid and topography', *Journal of Geophysical Research: Planets* **123**(5), 1041–1060.

URL: <https://agupubs.onlinelibrary.wiley.com/doi/abs/10.1002/2017JE005475>

Kleine, T., Palme, H., Mezger, K. and Halliday, A. N. (2005), 'Hf-w chronometry of lunar metals and the age and early differentiation of the moon', *Science* **310**(5754), 1671–1674.

- Lathe, R. (2004), 'Fast tidal cycling and the origin of life', *Icarus* **168**(1), 18 – 22.
URL: <http://www.sciencedirect.com/science/article/pii/S001910350300383X>
- Lathe, R. (2006), 'Early tides: Response to varga et al.', *Icarus* **180**(1), 277–280.
URL: <https://www.sciencedirect.com/science/article/pii/S0019103505003271>
- Le Pichon, X. (1968), 'Sea-floor spreading and continental drift', *Journal of Geophysical Research (1896-1977)* **73**(12), 3661–3697.
URL: <https://agupubs.onlinelibrary.wiley.com/doi/abs/10.1029/JB073i012p03661>
- Lithgow-Bertelloni, C. and Richards, M. A. (1995), 'Cenozoic plate driving forces', *Geophysical Research Letters* **22**(11), 1317–1320.
URL: <https://agupubs.onlinelibrary.wiley.com/doi/abs/10.1029/95GL01325>
- Livermore, R., Nankivell, A., Eagles, G. and Morris, P. (2005), 'Paleogene opening of drake passage', *Earth and Planetary Science Letters* **236**(1), 459 – 470.
URL: <http://www.sciencedirect.com/science/article/pii/S0012821X05002785>
- Macdonald, F. A., Schmitz, M. D., Crowley, J. L., Roots, C. F., Jones, D. S., Maloof, A. C., Strauss, J. V., Cohen, P. A., Johnston, D. T. and Schrag, D. P. (2010), 'Calibrating the cryogenian', *Science* **327**(5970), 1241–1243.
URL: <https://science.sciencemag.org/content/327/5970/1241>
- Makinson, K., Holland, P. R., Jenkins, A., Nicholls, K. W. and Holland, D. M. (2011), 'Influence of tides on melting and freezing beneath filchner-ronne ice shelf, antarctica', *Geophysical Research Letters* **38**(6).
URL: <https://agupubs.onlinelibrary.wiley.com/doi/abs/10.1029/2010GL046462>
- Marques, F., Cabral, F., Gerya, T., Zhu, G. and May, D. (2014), 'Subduction initiates at straight passive margins', *Geology* **42**(4), 331–334.
URL: <https://doi.org/10.1130/G35246.1>
- Matthews, K. J., Maloney, K. T., Zahirovic, S., Williams, S. E., Seton, M. and Müller, R. D. (2016), 'Global plate boundary evolution and kinematics since the late paleozoic', *Global and Planetary Change* **146**, 226 – 250.
URL: <http://www.sciencedirect.com/science/article/pii/S0921818116302417>

- Mccully, J. G. (2006a), *Beyond the Moon: a conversational, common sense guide to understanding the tides*, World scientific publishing company, chapter 8, pp. 113–144.
URL: https://www.worldscientific.com/doi/abs/10.1142/9789812774330_0008
- Mccully, J. G. (2006b), *Beyond the Moon: a conversational, common sense guide to understanding the tides*, World scientific publishing company, chapter 7, pp. 97–111.
URL: https://www.worldscientific.com/doi/abs/10.1142/9789812774330_0008
- McKenzie, D. P. and Parker, R. L. (1967), ‘The north pacific: an example of tectonics on a sphere’, *Nature* **216**, 1276–1280.
URL: <https://doi.org/10.1038/2161276a0>
- Meert, J. G. (2012), ‘What’s in a name? the columbia (paleopangaea/nuna) supercontinent’, *Gondwana Research* **21**(4), 987 – 993. Advances in High-Resolution Ion-Microprobe Geochronology.
URL: <http://www.sciencedirect.com/science/article/pii/S1342937X11003479>
- Meert, J. G. (2014), ‘Strange attractors, spiritual interlopers and lonely wanderers: The search for pre-pangean supercontinents’, *Geoscience Frontiers* **5**(2), 155 – 166.
URL: <http://www.sciencedirect.com/science/article/pii/S1674987113001576>
- Merdith, A. S., Collins, A. S., Williams, S. E., Pisarevsky, S., Foden, J. D., Archibald, D. B., Blades, M. L., Alessio, B. L., Armistead, S., Plavsa, D., Clark, C. and Müller, R. D. (2017), ‘A full-plate global reconstruction of the neoproterozoic’, *Gondwana Research* **50**, 84 – 134. Gondwana Research Golden Jubilee Volume.
URL: <http://www.sciencedirect.com/science/article/pii/S1342937X16305093>
- Miller, E. L., Toro, J., Gehrels, G., Amato, J. M., Prokopyev, A., Tuchkova, M. I., Akinin, V. V., Dumitru, T. A., Moore, T. E. and Cecile, M. P. (2006), ‘New insights into arctic paleogeography and tectonics from u-pb detrital zircon geochronology’, *Tectonics* **25**(3).
URL: <https://agupubs.onlinelibrary.wiley.com/doi/abs/10.1029/2005TC001830>
- Mitchell, R. N., Kilian, T. M. and Evans, D. A. D. (2012), ‘Supercontinent cycles and the calculation of absolute palaeolongitude in deep time’, *Nature* **482**, 208–211.
URL: <https://doi.org/10.1038/nature10800>

- Montes, C., Cardona, A., Jaramillo, C., Pardo, A., Silva, J. C., Valencia, V., Ayala, C., Pérez-Angel, L. C., Rodríguez-Parra, L. A., Ramirez, V. and Niño, H. (2015), 'Middle miocene closure of the central american seaway', *Science* **348**(6231), 226–229.
URL: <https://science.sciencemag.org/content/348/6231/226>
- Moresi, L. and Solomatov, V. (1998), 'Mantle convection with a brittle lithosphere: thoughts on the global tectonic styles of the Earth and Venus', *Geophysical Journal International* **133**(3), 669–682.
URL: <https://doi.org/10.1046/j.1365-246X.1998.00521.x>
- Morgan, W. J. (1972), 'Plate motions and deep mantle convection', *Geological Society of America Memoirs* **132**, 7–22.
- Morley, L. and Larochelle, A. (1964), 'Paleomagnetism as a means of dating geological events', *Geochronology in Canada* **8**, 39–51.
- Mueller, S. and Phillips, R. J. (1991), 'On the initiation of subduction', *Journal of Geophysical Research: Solid Earth* **96**(B1), 651–665.
URL: <https://agupubs.onlinelibrary.wiley.com/doi/abs/10.1029/90JB02237>
- Munk, W. and Wunsch, C. (1998), 'Abyssal recipes ii: energetics of tidal and wind mixing', *Deep Sea Research Part I: Oceanographic Research Papers* **45**(12), 1977 – 2010.
URL: <http://www.sciencedirect.com/science/article/pii/S0967063798000703>
- Murphy, J. B. and Nance, R. D. (2003), 'Do supercontinents introvert or extrovert?: Sm-Nd isotope evidence', *Geology* **31**(10), 873–876.
URL: <https://doi.org/10.1130/G19668.1>
- Murphy, J. B. and Nance, R. D. (2005), 'Do supercontinents turn inside-in or inside-out?', *International Geology Review* **47**(6), 591–619.
URL: <https://doi.org/10.2747/0020-6814.47.6.591>
- Murphy, J. B. and Nance, R. D. (2008), 'The Pangea conundrum', *Geology* **36**(9), 703–706.
URL: <https://doi.org/10.1130/G24966A.1>
- Murphy, J. B., Nance, R. D. and Cawood, P. A. (2009), 'Contrasting modes of supercontinent formation and the conundrum of pangea', *Gondwana Research* **15**(3), 408 – 420. Special

Issue: Supercontinent Dynamics.

URL: <http://www.sciencedirect.com/science/article/pii/S1342937X08001469>

Müller, R. D., Cannon, J., Qin, X., Watson, R. J., Gurnis, M., Williams, S., Pfaffelmoser, T., Seton, M., Russell, S. H. J. and Zahirovic, S. (2018), 'Gplates: Building a virtual earth through deep time', *Geochemistry, Geophysics, Geosystems* **19**(7), 2243–2261.

URL: <https://agupubs.onlinelibrary.wiley.com/doi/abs/10.1029/2018GC007584>

Müller, R. D., Sdrolias, M., Gaina, C. and Roest, W. R. (2008), 'Age, spreading rates, and spreading asymmetry of the world's ocean crust', *Geochemistry, Geophysics, Geosystems* **9**(4).

URL: <https://agupubs.onlinelibrary.wiley.com/doi/abs/10.1029/2007GC001743>

Nance, R. D., Gutiérrez-Alonso, G., Keppie, J. D., Linnemann, U., Murphy, J. B., Quesada, C., Strachan, R. A. and Woodcock, N. H. (2012), 'A brief history of the rheic ocean', *Geoscience Frontiers* **3**(2), 125 – 135.

URL: <http://www.sciencedirect.com/science/article/pii/S1674987111001113>

Nance, R. D., Murphy, J. B. and Santosh, M. (2014), 'The supercontinent cycle: A retrospective essay', *Gondwana Research* **25**(1), 4 – 29.

URL: <http://www.sciencedirect.com/science/article/pii/S1342937X13000506>

Nance, R. D., Worsley, T. R. and Moody, J. B. (1988), 'The supercontinent cycle', *Scientific American* .

URL: <https://www.osti.gov/biblio/6742273>

Nield, T. (2007), *Supercontinent: 10 Billion Years in the Life of Our Planet*, Granta Books.

Nimmo, F. and Stevenson, D. J. (2000), 'Influence of early plate tectonics on the thermal evolution and magnetic field of mars', *Journal of Geophysical Research: Planets* **105**(E5), 11969–11979.

URL: <https://agupubs.onlinelibrary.wiley.com/doi/abs/10.1029/1999JE001216>

Palin, R. M., Santosh, M., Cao, W., Li, S.-S., Hernández-Uribe, D. and Parsons, A. (2020), 'Secular change and the onset of plate tectonics on earth', *Earth-Science Reviews* **207**, 103172.

URL: <http://www.sciencedirect.com/science/article/pii/S001282522030218X>

- Parrish, J. T. (1993), 'Climate of the supercontinent pangea', *The Journal of Geology* **101**(2), 215–233.
URL: <https://doi.org/10.1086/648217>
- Pastor-Galán, D., Nance, R. D., Murphy, J. B. and Spencer, C. J. (2019), 'Supercontinents: myths, mysteries, and milestones', *Geological Society, London, Special Publications* **470**(1), 39–64.
URL: <https://sp.lyellcollection.org/content/470/1/39>
- Pinet, P. R. (2008), *Invitation to Oceanography*, Jones & Bartlett Publishers.
- Platzman, G. W. (1975), 'Normal Modes of the Atlantic and Indian Oceans', *Journal of Physical Oceanography* **5**(2), 201–221.
URL: [https://doi.org/10.1175/1520-0485\(1975\)005<0201:NMOTAA>2.0.CO;2](https://doi.org/10.1175/1520-0485(1975)005<0201:NMOTAA>2.0.CO;2)
- Pugh, D. and Woodworth, P. (2014), *Sea-Level Science: Understanding Tides, Surges, Tsunamis and Mean Sea-Level Changes*, Cambridge University Press.
- Qin, X., Müller, R. D., Cannon, J., Landgrebe, T. C. W., Heine, C., Watson, R. J. and Turner, M. (2012), 'The gplates geological information model and markup language', *Geoscientific Instrumentation, Methods and Data Systems* **1**, 111–134.
URL: <https://gi.copernicus.org/articles/1/111/2012/>
- Raymo, M. E. and Ruddiman, W. F. (1992), 'Tectonic forcing of late cenozoic climate', *Nature* **359**, 117–122.
URL: <https://doi.org/10.1038/359117a0>
- Riofrio, L. (2012), 'Calculation of lunar orbit anomaly', *Planetary Science* **1**, 1.
URL: <https://doi.org/10.1186/2191-2521-1-1>
- Rogers, J. J. and Santosh, M. (2003), 'Supercontinents in earth history', *Gondwana Research* **6**(3), 357 – 368.
URL: <http://www.sciencedirect.com/science/article/pii/S1342937X0570993X>
- Rohling, E. J. (2020), *The oceans: A deep history*, Princeton University Press.

- Rolf, T., Coltice, N. and Tackley, P. J. (2014), ‘Statistical cyclicity of the supercontinent cycle’, *Geophysical Research Letters* **41**(7), 2351–2358.
URL: <https://agupubs.onlinelibrary.wiley.com/doi/abs/10.1002/2014GL059595>
- Santosh, M. (2010), ‘Supercontinent tectonics and biogeochemical cycle: A matter of ‘life and death’’, *Geoscience Frontiers* **1**(1), 21 – 30.
URL: <http://www.sciencedirect.com/science/article/pii/S167498711000006X>
- Schellart, W. P., Freeman, J., Stegman, D. R., Moresi, L. and May, D. (2007), ‘Evolution and diversity of subduction zones controlled by slab width’, *Nature* **446**, 308–311.
URL: <https://doi.org/10.1038/nature05615>
- Schellart, W. and Rawlinson, N. (2010), ‘Convergent plate margin dynamics: New perspectives from structural geology, geophysics and geodynamic modelling’, *Tectonophysics* **483**(1), 4 – 19. Convergent plate margin dynamics: New perspectives from structural geology, geophysics and geodynamic modelling.
URL: <http://www.sciencedirect.com/science/article/pii/S0040195109004818>
- Schellart, W., Stegman, D. and Freeman, J. (2008), ‘Global trench migration velocities and slab migration induced upper mantle volume fluxes: Constraints to find an earth reference frame based on minimizing viscous dissipation’, *Earth-Science Reviews* **88**(1), 118 – 144.
URL: <http://www.sciencedirect.com/science/article/pii/S0012825208000184>
- Schmittner, A., Silva, T. A. M., Fraedrich, K., Kirk, E. and Lunkeit, F. (2011), ‘Effects of mountains and ice sheets on global ocean circulation’, *Journal of Climate* **24**(11), 2814 – 2829.
URL: <https://journals.ametsoc.org/view/journals/clim/24/11/2010jcli3982.1.xml>
- Schrag, D. P., Berner, R. A., Hoffman, P. F. and Halverson, G. P. (2002), ‘On the initiation of a snowball earth’, *Geochemistry, Geophysics, Geosystems* **3**(6), 1–21.
URL: <https://agupubs.onlinelibrary.wiley.com/doi/abs/10.1029/2001GC000219>
- Scotese, C. (2017), ‘Atlas of ancient oceans and continents: Plate tectonics during the last 1.5 billion years’.
URL: <https://tinyurl.com/94wtupzd>

Scotese, C. R. (1991), 'Jurassic and cretaceous plate tectonic reconstructions', *Palaeogeography, Palaeoclimatology, Palaeoecology* **87**(1), 493 – 501. Palaeogeography and Paleocceanography of Tethys.

URL: <http://www.sciencedirect.com/science/article/pii/003101829190145H>

Scotese, C. R. (2003), 'Palaeomap project'. [Online; accessed: 25.10.2017].

URL: <http://www.scotese.com/earth.htm>

Scotese, C. R. (2009), 'Late proterozoic plate tectonics and palaeogeography: a tale of two supercontinents, rodinia and pannotia', *Geological Society, London, Special Publications* **326**(1), 67–83.

URL: <https://sp.lyellcollection.org/content/326/1/67>

Silver, P. G. and Behn, M. D. (2008), 'Intermittent plate tectonics?', *Science* **319**(5859), 85–88.

URL: <https://science.sciencemag.org/content/319/5859/85>

Smith, D. K. and Cann, J. R. (1993), 'Building the crust at the mid-atlantic ridge', *Nature* **365**, 707–715.

URL: <https://doi.org/10.1038/365707a0>

Smith, W. H. F. and Sandwell, D. T. (1997), 'Global sea floor topography from satellite altimetry and ship depth soundings', *Science* **277**(5334), 1956–1962.

URL: <https://science.sciencemag.org/content/277/5334/1956>

Stammer, D., Ray, R. D., Andersen, O. B., Arbic, B. K., Bosch, W., Carrère, L., Cheng, Y., Chinn, D. S., Dushaw, B. D., Egbert, G. D., Erofeeva, S. Y., Fok, H. S., Green, J. A. M., Griffiths, S., King, M. A., Lapin, V., Lemoine, F. G., Luthcke, S. B., Lyard, F., Morison, J., Müller, M., Padman, L., Richman, J. G., Shriver, J. F., Shum, C. K., Taguchi, E. and Yi, Y. (2014), 'Accuracy assessment of global barotropic ocean tide models', *Reviews of Geophysics* **52**(3), 243–282.

URL: <https://agupubs.onlinelibrary.wiley.com/doi/abs/10.1002/2014RG000450>

Stern, R. J. (2002), 'Subduction zones', *Reviews of Geophysics* **40**(4), 3–1–3–38.

URL: <https://agupubs.onlinelibrary.wiley.com/doi/abs/10.1029/2001RG000108>

Stern, R. J. (2016), 'Is plate tectonics needed to evolve technological species on exoplanets?',

Geoscience Frontiers **7**(4), 573 – 580.

URL: <http://www.sciencedirect.com/science/article/pii/S1674987115300062>

Stern, R. J. and Gerya, T. (2018), ‘Subduction initiation in nature and models: A review’, *Tectonophysics* **746**, 173 – 198. Understanding geological processes through modelling - A Memorial Volume honouring Evgenii Burov.

URL: <http://www.sciencedirect.com/science/article/pii/S0040195117304390>

Stern, R. J., Gerya, T. and Tackley, P. J. (2018), ‘Stagnant lid tectonics: Perspectives from silicate planets, dwarf planets, large moons, and large asteroids’, *Geoscience Frontiers* **9**(1), 103 – 119. Lid Tectonics.

URL: <http://www.sciencedirect.com/science/article/pii/S1674987117301135>

Tada, R., Zheng, H. and Clift, P. D. (2016), ‘Evolution and variability of the asian monsoon and its potential linkage with uplift of the himalaya and tibetan plateau’, *Progress in Earth and Planetary Science* **3**, 4.

URL: <https://doi.org/10.1186/s40645-016-0080-y>

Tang, M., Chen, K. and Rudnick, R. L. (2016), ‘Archean upper crust transition from mafic to felsic marks the onset of plate tectonics’, *Science* **351**(6271), 372–375.

URL: <https://science.sciencemag.org/content/351/6271/372>

Thorkelson, D. J. (1996), ‘Subduction of diverging plates and the principles of slab window formation’, *Tectonophysics* **255**(1), 47 – 63.

URL: <http://www.sciencedirect.com/science/article/pii/0040195195001069>

Torsvik, T. H., Burke, K., Steinberger, B., Webb, S. J. and Ashwal, L. D. (2010), ‘Diamonds sampled by plumes from the core–mantle boundary’, *Nature* **466**, 352–355.

URL: <https://doi.org/10.1038/nature09216>

Torsvik, T. H., Steinberger, B., Ashwal, L. D., Doubrovine, P. V. and Trønnnes, R. G. (2016), ‘Earth evolution and dynamics—a tribute to kevin burke’, *Canadian Journal of Earth Sciences* **53**(11), 1073–1087.

URL: <https://doi.org/10.1139/cjes-2015-0228>

Torsvik, T. H., van der Voo, R., Doubrovine, P. V., Burke, K., Steinberger, B., Ashwal, L. D., Trønnnes, R. G., Webb, S. J. and Bull, A. L. (2014), ‘Deep mantle structure as a reference

- frame for movements in and on the earth’, *Proceedings of the National Academy of Sciences* **111**(24), 8735–8740.
URL: <https://www.pnas.org/content/111/24/8735>
- Varga, P., Rybicki, K. and Denis, C. (2006), ‘Comment on the paper “fast tidal cycling and the origin of life” by richard lathe’, *Icarus* **180**(1), 274–276.
URL: <https://www.sciencedirect.com/science/article/pii/S0019103505003283>
- Vine, F. J. and Matthews, D. H. (1963), ‘Magnetic anomalies over oceanic ridges’, *Nature* **199**, 947–949.
URL: <https://doi.org/10.1038/199947a0>
- Waltham, D. (2015), ‘Milankovitch Period Uncertainties and Their Impact On Cyclostratigraphy’, *Journal of Sedimentary Research* **85**(8), 990–998.
URL: <https://doi.org/10.2110/jsr.2015.66>
- Waltham, D. (2019), ‘Is earth special?’, *Earth-Science Reviews* **192**, 445 – 470.
URL: <http://www.sciencedirect.com/science/article/pii/S0012825218306524>
- Wang, C., Mitchell, R. N., Murphy, J. B., Peng, P. and Spencer, C. J. (2020), ‘The role of megacontinents in the supercontinent cycle’, *Geology* .
URL: <https://doi.org/10.1130/G47988.1>
- Way, M., Davies, H. S., Duarte, J. C. and Green, M. (2019), ‘Deep future climate on earth: effects of tectonics, rotation rate, and insolation’, *Earth and Space Science Open Archive* p. 41.
URL: <https://doi.org/10.1002/essoar.10501348.1>
- Way, M. J., Aleinov, I., Amundsen, D. S., Chandler, M. A., Clune, T., Del Genio, A. D., Fujii, Y., Kelley, M., Kiang, N. Y., Sohl, L. and Tsigaridis, K. (2017), ‘Resolving orbital and climate keys of earth and extraterrestrial environments with dynamics 1.0: A general circulation model for simulating the climates of rocky planets’, *Astrophys. J. Supp. Series* **231**(1), 12.
- Wegener, A. (1912), ‘Die entstehung der kontinente’, *Geologische Rundschau* **3**, 276–292.
URL: <https://doi.org/10.1007/BF02202896>

- Whattam, S. A. and Stern, R. J. (2011), ‘The ‘subduction initiation rule’: a key for linking ophiolites, intra-oceanic forearcs, and subduction initiation’, *Contributions to Mineralogy and Petrology* **162**, 1031–1045.
URL: <https://doi.org/10.1007/s00410-011-0638-z>
- Wignall, P. and Hallam, A. (1992), ‘Anoxia as a cause of the permian/triassic mass extinction: facies evidence from northern italy and the western united states’, *Palaeogeography, Palaeoclimatology, Palaeoecology* **93**(1), 21 – 46.
URL: <http://www.sciencedirect.com/science/article/pii/0031018292901825>
- Williams, G. E. (2000), ‘Geological constraints on the precambrian history of earth’s rotation and the moon’s orbit’, *Reviews of Geophysics* **38**(1), 37–59.
URL: <https://agupubs.onlinelibrary.wiley.com/doi/abs/10.1029/1999RG900016>
- Wilmes, S.-B. and Green, J. A. M. (2014), ‘The evolution of tides and tidal dissipation over the past 21,000 years’, *Journal of Geophysical Research: Oceans* **119**(7), 4083–4100.
URL: <https://agupubs.onlinelibrary.wiley.com/doi/abs/10.1002/2013JC009605>
- Wilson, J. T. (1965), ‘A new class of faults and their bearing on continental drift’, *Nature* **207**, 343–347.
URL: <https://doi.org/10.1038/207343a0>
- Wilson, J. T. (1966), ‘Did the atlantic close and then re-open?’, *Nature* **211**, 676–681.
URL: <https://doi.org/10.1038/211676a0>
- Wilson, R. W., Houseman, G. A., Buitert, S. J. H., McCaffrey, K. J. W. and Doré, A. G. (2019), Fifty years of the Wilson Cycle concept in plate tectonics: an overview, in ‘Fifty Years of the Wilson Cycle Concept in Plate Tectonics’, Geological Society of London.
URL: <https://doi.org/10.1144/SP470-2019-58>
- Wright, J. E. and Wyld, S. J. (2011), ‘Late Cretaceous subduction initiation on the eastern margin of the Caribbean-Colombian Oceanic Plateau: One Great Arc of the Caribbean (?)’, *Geosphere* **7**(2), 468–493.
URL: <https://doi.org/10.1130/GES00577.1>
- Yoshida, M. (2016), ‘Formation of a future supercontinent through plate motion–driven flow

coupled with mantle downwelling flow', *Geology* **44**(9), 755–758.

URL: <https://doi.org/10.1130/G38025.1>

Yoshida, M. and Santosh, M. (2011), 'Future supercontinent assembled in the northern hemisphere', *Terra Nova* **23**(5), 333–338.

URL: <https://onlinelibrary.wiley.com/doi/abs/10.1111/j.1365-3121.2011.01018.x>

Yoshida, M. and Santosh, M. (2018), 'Voyage of the Indian subcontinent since Pangea breakup and driving force of supercontinent cycles: Insights on dynamics from numerical modeling', *Geoscience Frontiers* **9**(5), 1279 – 1292. SPECIAL ISSUE: Frontiers in geoscience: A tribute to Prof. Xuanxue Mo.

URL: <http://www.sciencedirect.com/science/article/pii/S1674987117301536>

Young, A., Flament, N., Maloney, K., Williams, S., Matthews, K., Zahirovic, S. and Müller, R. D. (2019), 'Global kinematics of tectonic plates and subduction zones since the late Paleozoic era', *Geoscience Frontiers* **10**(3), 989 – 1013. Special Issue: Advances in Himalayan Tectonics.

URL: <http://www.sciencedirect.com/science/article/pii/S1674987118301373>

Zaron, E. and Egbert, G. (2006), 'Verification studies for a z-coordinate primitive-equation model: Tidal conversion at a mid-ocean ridge', *Ocean Modelling* **14**(3), 257 – 278.

URL: <http://www.sciencedirect.com/science/article/pii/S1463500306000564>

Appendix

A1 Is there a tectonically driven supertidal cycle?

J. A. M. Green, J. L. Molloy, H. S. Davies, & J. C. Duarte

(The full copy of "Is there a tectonically driven supertidal cycle?" published in *Geophysical Research Letters*, Green et al. (2018))



Geophysical Research Letters

RESEARCH LETTER

10.1002/2017GL076695

Key Points:

- Earth is in a semidiurnal tidal maximum and will go through another during the supercontinent cycle
- The average dissipation rates over the supercontinent cycle are lower than present rates
- This highlights a deep-time cycle of importance for past and future Earth system studies

Correspondence to:

J. A. M. Green,
m.green@bangor.ac.uk

Citation:

Green, J. A. M., Molloy, J. L., Davies, H. S., & Duarte, J. C. (2018). Is there a tectonically driven supertidal cycle? *Geophysical Research Letters*, 45, 3568–3576. <https://doi.org/10.1002/2017GL076695>



Received 7 DEC 2017

Accepted 13 MAR 2018

Accepted article online 11 APR 2018

Published online 23 APR 2018

Is There a Tectonically Driven Supertidal Cycle?

J. A. M. Green¹ , J. L. Molloy^{1,2}, H. S. Davies^{3,4} , and J. C. Duarte^{3,4,5}

¹School of Ocean Sciences, Bangor University, Menai Bridge, UK, ²Department of Geography, University of Sheffield, Sheffield, UK, ³Departamento de Geologia, Faculdade de Ciências, Universidade de Lisboa, Lisbon, Portugal, ⁴Instituto Dom Luiz, Faculdade de Ciências, Universidade de Lisboa, Lisbon, Portugal, ⁵School of Earth, Atmosphere and Environment, Monash University, Melbourne, Victoria, Australia

Abstract Earth is 180 Myr into the current supercontinent cycle, and the next supercontinent is predicted to form in 250 Myr. The continuous changes in continental configuration can move the ocean between resonant states, and the semidiurnal tides are currently large compared to the past 252 Myr due to tidal resonance in the Atlantic. This leads to the hypothesis that there is a “supertidal” cycle linked to the supercontinent cycle. Here this is tested using new tectonic predictions for the next 250 Myr as bathymetry in a numerical tidal model. The simulations support the following hypothesis: a new tidal resonance will appear 150 Myr from now, followed by a decreasing tide as the supercontinent forms 100 Myr later. This affects the dissipation of tidal energy in the oceans, with consequences for the evolution of the Earth-Moon system, ocean circulation and climate, and implications for the ocean’s capacity of hosting and evolving life.

Plain Language Summary Earth goes through cycles over 400–450 million years (Myr), during which all landmasses are brought together in a supercontinent, which breaks up, disperse, and then reform in a new supercontinent. We are currently 180 Myr into a cycle, and the next supercontinent will form in 250 Myr. During these cycles oceans open and close. The Atlantic is widening, and it has the largest tides found on Earth during the current supercontinent cycle. The reason is that the Atlantic is currently in tidal resonance because of its shape, but as it widens more it may move away from this state. This led us to ask if there is a supertidal cycle linked to the supercontinent cycle. We test the idea using new tectonic predictions for the next 250 Myr in a numerical tidal model. The results support the following idea: the tides will drop over the next 100 Myr, only to light up again 150 Myr from now. They then become very quiescent when the new supercontinent has formed. This affects the loss of tidal energy, with consequences for the evolution of the Earth-Moon system, ocean circulation, and climate and for the ocean’s capacity of hosting and evolving life.

1. Introduction

The Earth moves through a cyclic dispersion and aggregation of supercontinents over a period of 400–500 Myr in what is known as the supercontinent cycle (Matthews et al., 2016; Nance et al., 1988; Rogers & Santosh, 2003). Pangea, the latest supercontinent, broke up around 180 Ma (Golonka, 2007, 1991), and it is predicted that a new supercontinent will form over the next 200–250 Myr (e.g., Duarte et al., 2018; Yoshida & Santosh, 2011). The breakup of a supercontinent may lead to the formation of several internal oceans that will grow and eventually close. The lifecycle of each of these oceans is known as the Wilson cycle (Burke & Dewey, 1974; Wilson, 1966). Consequently, the completion of a supercontinent cycle through the formation of a supercontinent is generally preceded by the termination of several Wilson cycles (e.g., Burke, 2011). There is strong evidence that the tides are currently unusually large and that for most of the current supercontinent cycle, they have been less energetic than at present (Green et al., 2017; Kagan & Sundermann, 1996). The exception is the past 2 Myr, during which the continental configuration has led to a tidal resonance in the Atlantic (e.g., Green, 2010; Platzman, 1975). This (near-)resonant state has led to increased global tidal dissipation rates, which were further enhanced during glacial low stands in sea level (Arbic & Garrett, 2010; Egbert et al., 2004; Green, 2010; Green et al., 2017; Griffiths & Peltier, 2008; Wilmes & Green, 2014). An ocean basin can house resonant tides when the width of the basin, L is equal to a multiple of half wavelengths, $\lambda = \sqrt{gHT}$ (T is the tidal period, g is gravity, and H is water depth) of the tidal wave. Because today’s resonant basin, the Atlantic,

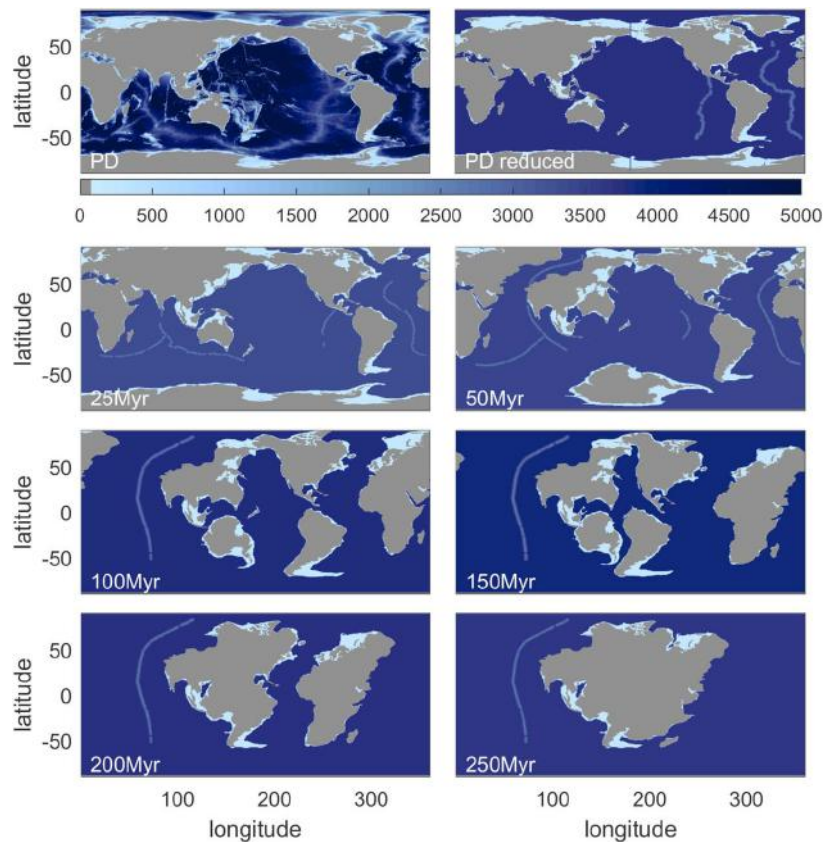


Figure 1. Shown is the tectonic evolution and eventual formation of the next supercontinent, Aurica. The top two panels show present-day (PD) and PD-reduced bathymetries, respectively (section 2.2 for details). The timings for the other slices are noted in the lower left corner of each panel. The colors mark the depths used in the tidal model simulations: light blue is 200 m, intermediate blue is 2,500 m, and the majority of the ocean is less than 4,000 m deep (section 2.2 below for details).

is currently opening, we would expect it to move away from the resonant state as it continues to widen, if we assume that the water depth and tidal period remain constant. Later on during the supercontinent cycle, we would expect either another basin to become resonant, that is, the Pacific if the Atlantic continues to open, or the Atlantic to become resonant again if it starts to close. This leads us to ask two questions: (i) when and where does this second resonance occur, if at all? and (ii) is there a supertidal cycle, that is, a cycle in the tidal amplitudes, associated with the supercontinent cycle? Here the questions will be answered by new simulations of the possible evolution of the tide over the next 250 Myr. This is done by implementing the tectonic scenario in Duarte et al. (2018) as the bathymetric boundary condition in the tidal model described by Green et al. (2017).

Duarte et al. (2018) describe one possible scenario for the formation of the next supercontinent, Aurica, 250 Myr into the future. Aurica is predicted to be fairly circular and located in the present-day (PD) equatorial Pacific Ocean (see Duarte et al., 2018, and our Figure 1). It is formed by the closure of both the PD Atlantic and Pacific Oceans, which can only happen if a new ocean opens up. In the scenario, a bisection of Eurasia leads to the formation of a new ocean basin via intracontinental rifting. The motivation for the double-basin closure is that both the Atlantic and the Pacific oceanic lithospheres are already, in some regions, 180 Ma old (although the Pacific oceanic basin is much older; Boschman & van Hinsbergen, 2016; Golonka, 1991; Müller et al., 2008), and oceanic plates older than 200 Ma are rare in the geological record (Bradley, 2011). Consequently, it can be argued that both the Pacific and Atlantic must close to form the new supercontinent.

Changes in the tides, and the associated tidal dissipation rates, on geological timescales have had profound implications for the Earth system. Herold et al. (2012) and Green and Huber (2013) show that the changed location of abyssal tidal dissipation during the Eocene (55 Ma) can explain the reduced meridional temperature

gradients seen in the proxy record for sea surface temperature that coupled climate models have struggled to reproduce (see Herold et al., 2012, for a summary). Furthermore, the reduced tidal dissipation during the Mesozoic and Cenozoic eras reported by Green et al. (2017) had implications for lunar recession rates and hence for interpreting cyclostratigraphy and long-term climate cycles (Waltham, 2015), for the evolution of the Earth-Moon system (Green et al., 2017), and for the evolution of life (Balbus, 2014).

The disposition of the continents on Earth over geological timescales consequently has a direct and major impact in the evolution of the Earth-Moon system, and tidal dissipation should be included in global ocean- and climate models, especially over long timescales (Green & Huber, 2013). The overall aim of this paper is to evaluate if there is a supertidal cycle linked to the supercontinent cycle. We do this by expanding the work of Green et al. (2017) by adding tidal simulations 250 Myr into the future using the tectonic predictions in Duarte et al. (2018) as bathymetric boundary conditions. Consequently, this paper will increase our fundamental understanding of the Earth system, and it will, if the hypothesis is correct, lead to a first-order predictability of when large supertides may occur in Earth's history. To obtain this knowledge, we want to cover a full supercontinent cycle to see if there is a supertidal cycle. The logical thing to do is to expand the supercontinent cycle we are currently in into the future, because the first part of it has already been covered and shown to be tidally less energetic than PD (Green et al., 2017). In the next section we describe the tidal model and the bathymetric time slices used to obtain the results in section 3. Section 4 closes the paper with a discussion, conclusions, and an outlook into further work.

2. Modeling Future Tides

2.1. Tides

We use OTIS—the Oregon State University Tidal Inversion Software—to simulate the evolution of the future tides. OTIS is a portable, dedicated, numerical shallow-water tidal model, which has been used extensively for both global and regional modeling of past, present, and future ocean tides (e.g., Egbert et al., 2004; Green, 2010; Green & Huber, 2013; Green et al., 2017; Pelling & Green, 2013; Wilmes & Green, 2014). It is highly accurate both in the open ocean and in coastal regions (Stammer et al., 2014), and it is computationally efficient. The model solves the linearized shallow-water equations (e.g., Hendershott, 1977):

$$\frac{\partial \mathbf{U}}{\partial t} + \mathbf{f} \times \mathbf{U} = -gH\nabla(\zeta - \zeta_{EQ} - \zeta_{SAL}) - \mathbf{F} \quad (1)$$

$$\frac{\partial \zeta}{\partial t} = -\nabla \cdot \mathbf{U} \quad (2)$$

Here \mathbf{U} is the depth-integrated volume transport (i.e., tidal current velocity \mathbf{u} times water depth H), f is the Coriolis vector, g denotes the gravitational constant, ζ is the tidal elevation, ζ_{SAL} denotes the tidal elevation due to self-attraction and loading (SAL), and ζ_{EQ} is the equilibrium tidal elevation. For simplicity we used a constant SAL correction with $\beta = 0.1$ (Egbert et al., 2004). \mathbf{F} represents energy losses due to bed friction and tidal conversion. The former is represented by the standard quadratic law:

$$\mathbf{F}_B = C_d \mathbf{u} |\mathbf{u}| \quad (3)$$

where $C_d = 0.003$ is a drag coefficient, and \mathbf{u} is the total velocity vector for all the tidal constituents. The conversion, $\mathbf{F}_w = C |\mathbf{U}|$, includes a conversion coefficient C , which is here defined as (Green & Huber, 2013; Zaron & Egbert, 2006)

$$C(x, y) = \gamma \frac{(\nabla H)^2 N_b \bar{N}}{8\pi^2 \omega} \quad (4)$$

Here $\gamma = 50$ is a scaling factor, N_b is the buoyancy frequency at the seabed, \bar{N} is the vertical average of the buoyancy frequency, and ω is the frequency of the tidal constituent under evaluation. The buoyancy frequency is given by $N = N_0 \exp(-z/1,300)$, where $N_0 = 5.24 \times 10^{-3} \text{ s}^{-1}$ and based on a least squares fit to PD climatology values (Zaron & Egbert, 2006). The future stratification is obviously unknown, and to estimate potential effects of altered stratification, we did a set of sensitivity simulations in which C was doubled or halved. As in other tidal simulations this had a relatively minor effect on the global tides, and we will not discuss these results further (see, e.g., Egbert et al., 2004; Green & Huber, 2013).

The model solves equations 1 and (2) using the astronomic tide-generating force as the only forcing (represented by ζ_{EQ} in equation (1)). An initial spin-up from rest of over 7 days is followed by a further 5 days of simulation time, on which harmonic analysis is performed to obtain the tidal elevations and transports. Here we focus on the M_2 and K_1 constituents only.

2.2. Bathymetry Data

2.2.1. PD Bathymetries

The PD bathymetry is the same as in Green et al. (2017): see our Figure 1, top left panel. To avoid open boundaries, the equilibrium tide was used as forcing at 88° when appropriate. Tests with a vertical wall at the poles (not shown) did not change the results. All simulations were done with $1/4^\circ$ horizontal resolution. The PD control simulation was compared to the elevations in the TPX08 database, and the root-mean-square errors (RMSEs) were computed from the difference between modeled and observed elevations. TPX08 is an inverse tidal solution for both elevation and velocity based on satellite altimetry and the shallow-water equations and is commonly taken as the truth for tidal elevations (see Egbert & Erofeeva, 2002, and http://volkov.oce.orst.edu/tides/tpxo8_atlas.html for details).

To evaluate the sensitivity of our solutions to the lack of detail in the future bathymetries, we constructed a simplified PD bathymetry having the same (lack of) detail as the future bathymetries (see Figure 1, top right panel). This case is denoted PD reduced in the following, and it is the simulation we use as a benchmark for the evolution of the tide. In PD reduced any water currently shallower than 200 m was set to 200 m. PD oceanic ridges were smoothed out and set to have a peak depth of 2,500 m and a total width of 5° over which the ridge approaches the depth of the deep ocean linearly, whereas subduction zones were set to be 1° wide and 6,000 m deep with a triangular cross section. The remaining ocean was set to a depth computed to conserve the ocean's PD total volume. The same values were used in the construction of the future bathymetries shown in Figure 1.

2.2.2. Future Bathymetries

We used GPlates for the kinematic tectonic modeling of the future scenario (see Duarte et al., 2018; Qin et al., 2012, and <https://www.gplates.org/> for a description). The continental polygons provided in the GPlates data repository were used as the starting point for the PD ocean, as in Matthews et al. (2016). The drift paths of the continental plates were constrained for the first 25 Myr by the drift velocities in Schellart et al. (2007). For the remaining 225 Myr, we used the PD globally averaged plate velocity of 5.6 cm year^{-1} (see Duarte et al., 2018, for a summary) but applied deviations from the average based on the observations in Zahirovic et al. (2016). The plate and land boundaries from the model were output as digital gray scale images, which were used to build the model bathymetries based on the details given for the PD sensitivity bathymetry.

2.3. Dissipation Computations

The computation of tidal dissipation rates, D , was done following Egbert and Ray (2001) and thus given by

$$D = W - \nabla \cdot P. \quad (5)$$

Here W is the work done by the tide-generating force and P is the energy flux given by

$$W = g\rho\langle \mathbf{U} \cdot \nabla(\eta_{SAL} + \eta_{EQ}) \rangle \quad (6)$$

$$P = g\langle \eta \mathbf{U} \rangle \quad (7)$$

where the angular brackets mark time averages over a tidal period.

3. Results

3.1. PD Sensitivity

The PD control simulation (Figure 2, top left) has an RMSE of 11 cm when compared to TPX08; the same computation for the reduced M_2 tide gives 23 cm. The K_1 RMSE are 2 cm for PD and 10 cm for PD reduced, respectively. As discussed above, we did a series of sensitivity simulations for both bathymetries in which the tidal conversion coefficient was changed within a factor of 2, and the RMSE and dissipation rates did not change significantly (not shown). Green and Huber (2013) and Green et al. (2017) did an extensive series of sensitivity simulations and came to the same conclusion. Consequently, we have confidence in the robustness of our results, and we have a well-constrained error bound on the simulations.

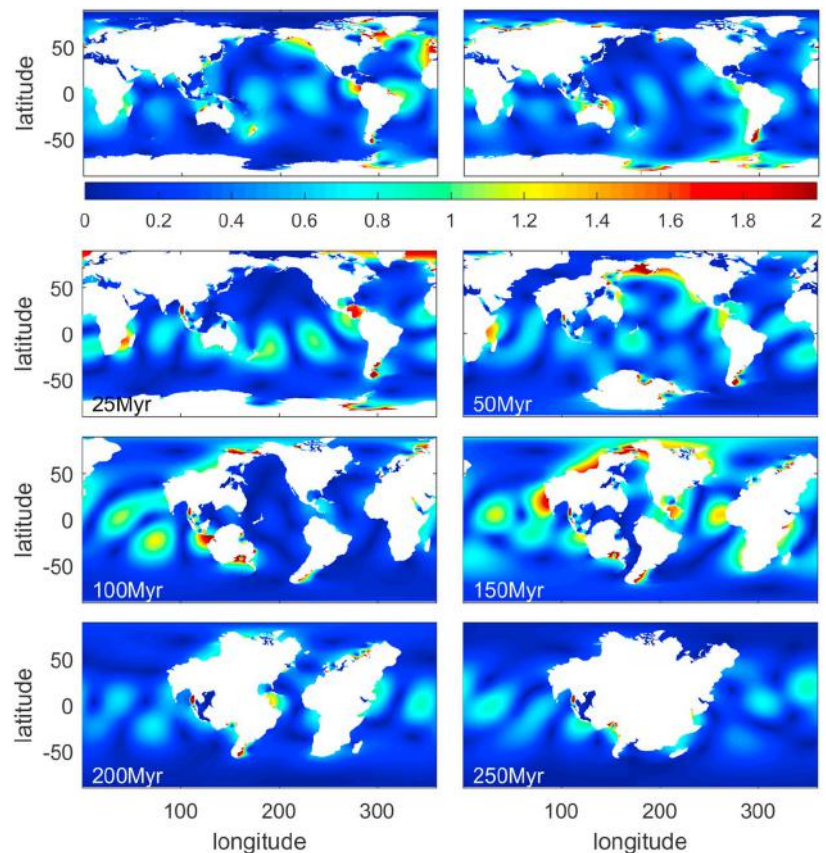


Figure 2. Shown are the M2 tidal amplitudes, in meters, for the PD (top left) and PD-reduced (top right) simulations, along with the future time slices. Note that the color scale saturates in the more energetic scenarios.

The PD sensitivity simulation reveals a less energetic global tide (Figure 2, top right), with reduced M2 tidal amplitudes in the Atlantic and the emergence of fairly large M2 tides along the Siberian shelf and around Antarctica. The new tides along the northern coast of Eurasia are due to the sub-Arctic seas being deeper, allowing the tide to propagate into the Arctic Basin. The large PD Atlantic tides are reduced because of the water-world-like ocean and reduced shelf sea area, leading to a more equilibrium-like tide (see Egbert et al., 2004, for a discussion). The weaker M2 tide in the PD reduced scenario means that we are potentially underestimating the M2 amplitudes for all future scenarios. For K1 we see a different pattern in Figure 3 (top row): our synthetic bathymetry appears to produce a larger K1 amplitude than the PD bathymetry. This is likely because the changed water depth allows the K1 tide to be nearer resonance in some areas, such as around Greenland and Indonesia. It is thus possible that we are overestimating K1 in the future scenarios. Note that this is a reversed response to that in Green et al. (2017), where their simplified bathymetry gives an enhanced M2 tide. The bathymetries in Green et al. (2017), however, have more topographic detail, especially in shallow water, than the ones used here. For clarity, we will describe our globally averaged or integrated metrics in relative terms by normalizing by the respective values from the simplified PD bathymetry.

3.2. Tidal Amplitudes

The global M2 tidal amplitude increases slightly over the next 50 Myr (refer to Figures 2 and 4a for the following discussion) due to an enhanced tide in the North Atlantic and Pacific at 25 Myr, followed by a very large Pacific tide at 50 Myr. This is because the equatorial Pacific becomes half-wavelength resonant at these ages. At 100 Myr, there are large tides in the newly formed Pan-Asian Ocean (in the Asian rift) and in the Indian Ocean. This signal persists to 150 Myr when the Atlantic comes back into resonance to form the next tidal maximum. After 150 Myr, there is a decline of the global amplitudes as the new supercontinent starts to come together and the resonant properties of the basins are lost. When Aurica has formed fully at 250 Myr, we only see large tides locally, in embayments with a geometry allowing for local resonances.

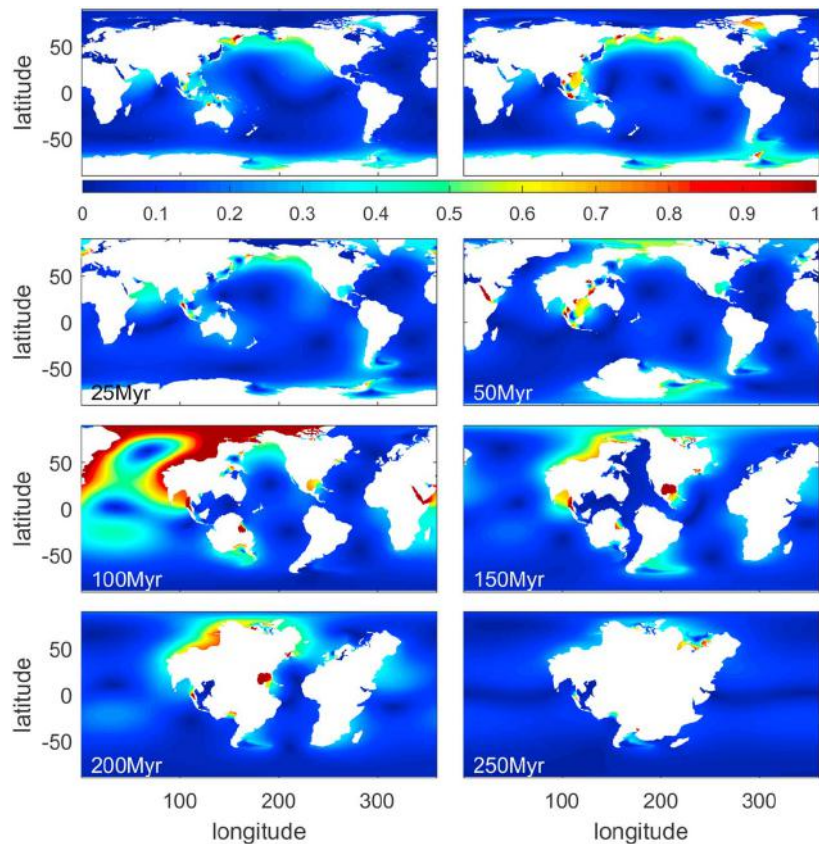


Figure 3. As in Figure 2, but showing K1 amplitudes (again in meters). Note the different color scale between this figure and Figure 2.

K1 follows a different pattern to M2, with a global tidal maximum when M2 hits a minimum at 100 Myr (the maximum K1 amplitude is then about 5 m). The average K1 amplitude remains relatively constant between 150 and 200 Myr, before a very sharp decline as the next continent forms (Figures 3 and 4a). It appears that K1 does not have two resonances in this tectonic scenario, whereas M2 does, because it becomes resonant again when the Atlantic closes, as well as in what is left of the Pacific at 150 Myr (Figure 2). This makes sense from a basin size perspective: because the Atlantic continues to open for a while before closing again, K1 will never have an opportunity to become resonant in the Atlantic, whereas M2 will be. Because of the changing size of the Pacific, it will be resonant for the K1 tide at 100 Myr only.

3.3. Dissipation and Earth-Moon Evolution

Overall, the global M2 dissipation rates for the remainder of the supercontinent cycle is 84% of the present values, or 2.2 TW (Figure 4b). This expands the results in Green et al. (2017) 250 Myr into the future and strongly suggests that Earth is presently in an M2 tidal maximum. It also suggests that the maximum has a width of 50 Myr or less and that there will be another M2 maximum occurring during the cycle around 150 Myr from now, i.e., 100 Myr before the formation of the next supercontinent. K1, in contrast, will be resonant only once in the current cycle, at 100 Myr. This is in agreement with results for the late Silurian (430 Ma), which showed more energetic tides than during the Early Devonian (400 Ma; H. Byrne, personal communication, 2017; Balbus, 2014). Pangea, the previous supercontinent, formed around 330 Myr ago and started breaking up some 180 Myr ago. It thus seems plausible that Earth's oceans go through tidal maxima some 150–200 Myr after supercontinental break up (i.e., at present) and around 100 Myr before a supercontinent forms (i.e., during the Silurian, before Pangea, and 150 Myr into the future for Aurica).

Following the lunar recession model in Waltham (2015) and summarized in Green et al. (2017), the recession rate, $\partial a / \partial t$, can be written as

$$\frac{\partial a}{\partial t} = fa^{-5.5} \quad (8)$$

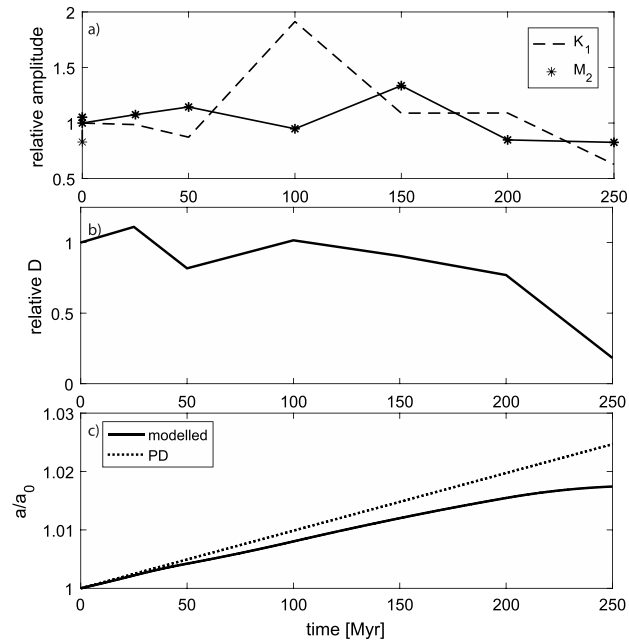


Figure 4. (a) Shown are time series of the evolution of the tidal constituents. The solid line, with markers, represents the globally averaged M₂ amplitude, whereas the dashed line shows K₁ amplitudes. (b) Globally integrated M₂ tidal dissipation rates normalized with the PD dissipation. (c) The evolution of the lunar distance, a , over time using the dissipation in panel b (solid) and the PD dissipation rate (dashed). Both are computed from equations (8) and (9). The distance is normalized by the PD distance, a_0 .

where f is the tidal factor given by

$$f = \frac{2Da^6}{m' \sqrt{\omega^2 a^3 (\Omega - \omega)}} \quad (9)$$

Here $m' = mM/(m + M)$ is the reduced mass of the Moon ($M = 5.972 \times 10^{24}$ kg and $m = 7.348 \times 10^{22}$ kg are the masses of the Earth and the Moon, respectively), and $\Omega = 7.2923 \times 10^{-5} \text{ s}^{-1}$ ($\omega = 2.6616 \times 10^{-6} \text{ s}^{-1}$) is the rotation rate of the Earth (Moon). Using the dissipation rates in Figure 4b, interpolated to every 1 Myr using linear interpolation to produce a smoother curve, we obtain the result in Figure 4c. We have also, for comparison, computed the lunar distance assuming a continuous PD dissipation rate (dashed). These results further highlight the conclusions in Green et al. (2017): appropriate tidal dissipation rates should be used in investigations involving lunar recession rates or distances, especially over long periods of time. Consequently, the PD recession rate is anomalously high because of the current tidal resonance in the Atlantic and PD tides are a poor proxy for past or future tides over large parts of the supercontinent cycle.

4. Discussion

Our results support previous ideas that the tides are at their lowest when the Earth is in the supercontinent configuration. The dissipation is then less than 40% of the PD value in our simulations. The tenure of a supercontinent varies, but both Pangaea and Rodinia, the two most recent supercontinents, maintained their formation for over 100 Myr (Rogers & Santosh, 2003). This means that dissipation rates could remain at this very low level for long periods of time—much longer than the timescale of its resonant peaks, which here are less than 50 Myr (see below for a tighter constraint).

This project aimed to evaluate if there is a supertidal cycle. The results strongly suggest that the answer is yes: there is a repeated gradual change between states of high and low tidal dissipation levels over the period of Aurica forming. However, there is more than one supertidal cycle within the supercontinent cycle. Combined with the results in Green et al. (2017), who goes back to Pangea 252 Myr ago, we suggest that the oceans will go through two M₂ supertidal cycles and at least one K₁ cycle during the current supercontinent cycle. Consequently, the global tides are weak for long periods of time and then pass through several quite narrow

(on geological timescales) resonances. This is because there are several Wilson cycles involved in one supercontinent cycle, and as the basins open and close there can be several supertidal cycles associated with the Wilson cycles. This also means that the supertidal cycle is not necessarily in phase with the supercontinent cycle. The mechanism behind the supertidal cycle is tidal resonance, which is set up by the continental configurations: peak resonance occurs when the continental configuration results in an ocean basin of a length that is an exact multiple of half wavelengths of the M2 tidal wave. Theoretically, one would therefore be able to predict when each basin may be resonant, without being able to provide any details of the actual magnitude. To lowest order, one can assume that the tide will be large when the natural frequency of a basin is within, say, 20% of the tidal period (see Figure 11 in Egbert et al., 2004, for a theoretical estimate). For the present, this would give a period window of about 3 hr in which the basin is close enough to resonance to support a large tide. If the ocean is 4,000 m deep and we are looking at a half-wavelength resonance, we get a range of the width of the basin in which it is resonant of about 1,100 km. With a continental drift rate of 6 cm year⁻¹, the width of the resonant peak would then be some 18 Myr, implying that Earth is currently in the beginning of the tidal maximum. There is further support for this in our results here and in Green et al. (2017). They show that the tides were weak 2 Myr before present, and the 25 Myr time slice in the present paper still shows a rather large tide. This is an interesting idea worth pursuing in a future paper, which would look into the time span of the resonances in more detail by simulating more time slices between now and 25 Myr.

Ocean basin closure is a result of consumption of oceanic plate at subduction zones within the basin and sea floor spreading in a neighboring basin. This means that there are long periods where the direction of closure is mostly fixed, with two continental plates being pulled or pushed together. The observation that there are multiple peaks in tidal dissipation makes sense in this context. There will be multiple modes of resonance for each ocean basin as it reaches the dimensions that are resonant for smaller or larger multiples of the tidal wavelength. The implication of these observations is that the length of a supertidal cycle is directly related to the length of the supercontinent cycle. Consequently, the period of the supertidal cycle is set by how quickly the continental configurations move from one resonant mode to another. There are of course other factors that contribute to the total tidal dissipation, such as sea level changes and variations in the extent of continental shelves, but through this study we have a clear indication that changing the position of the continents alone is enough to elicit significant changes in the energy of the tidal system. However, if an ocean basin is close to resonance it is much more sensitive to relative sea level changes and/or continental shelf configurations than when its not in a near-resonant state. This was the case for the Last Glacial Maximum (21–18 kyr) where Green et al. (2017) find the largest M2 amplitude in their 252 Myr time series. This exceptionally large tide is explained by a low stand in sea level, exposing the dissipative shelf seas (Egbert et al., 2004; Wilmes & Green, 2014).

The results here are promising, and further investigations will focus on other tectonic scenarios and increasing the temporal resolution of our simulations. This will provide a further understanding of the future Earth system and will, along with more simulations of the past, allow us to build a better picture of the variability in tides and tidal dissipation rates over long time periods.

Acknowledgments

J. A. M. G. acknowledges funding from the Natural Environmental Research Council through grants NE/F014821/1 and NE/I030224/1. J. C. D. acknowledges an FCT Researcher contract, an exploratory project grant ref. IF/00702/2015, and the FCT project UID/GEO/50019/2013-IDL. H. S. D. was supported by FCT (ref. UID/GEO/50019/2013—Instituto Dom Luiz; FCT PhD grant ref. PD/BD/135068/2017). Kara Matthews (Oxford University) provided invaluable support on using GPlates. Comments from Sophie Wilmes, Jeroen Ritsema (Editor), Dietmar Müller (reviewer), and an anonymous reviewer greatly improved the manuscript. The data are available from the Open Science Framework (osf.io/8ydwv).

References

- Arbic, B. K., & Garrett, C. (2010). A coupled oscillator model of shelf and ocean tides. *Continental Shelf Research*, 30, 564–574.
- Balbus, S. A. (2014). Dynamical, biological and anthropic consequences of equal lunar and solar angular radii. *Proceeding of the Royal Society of London, A*, 470, 20140263.
- Boschman, L. M., & van Hinsbergen, D. J. J. (2016). On the enigmatic birth of the Pacific Plate within the Panthalassa Ocean. *Science Advances*, 2, e1600022.
- Bradley, D. (2011). Secular trends in the geologic record and the supercontinent cycle. *Earth-Science Reviews*, 108, 16–33.
- Burke, K. (2011). Plate tectonics, the Wilson cycle, and mantle plumes: Geodynamics from the top. *Annual Review of Earth and Planetary Sciences*, 39, 1–29.
- Burke, K., & Dewey, J. F. (1974). Hot spots and continental breakup: Implications for collisional orogeny. *Geology*, 2, 57–60.
- Duarte, J., Schellart, W., & Rosas, F. (2018). The future of Earth's oceans: Consequences of subduction initiation in the Atlantic and implications for supercontinent formation. *Geological Magazine*, 155, 45–58.
- Egbert, G. D., & Erofeeva, S. (2002). Efficient inverse modeling of barotropic ocean tides. *Journal of Atmospheric and Oceanic Technology*, 19, 183–204.
- Egbert, G. D., & Ray, R. D. (2001). Estimates of M2 tidal energy dissipation from Topex/Poseidon altimeter data. *Journal of Geophysical Research*, 106, 22,475–22,502.
- Egbert, G. D., Bills, B. G., & Ray, R. D. (2004). Numerical modeling of the global semidiurnal tide in the present day and in the Last Glacial Maximum. *Journal of Geophysical Research*, 109, C03003. <https://doi.org/10.1029/2003JC001973>
- Golonka, C. R. (1991). Jurassic and Cretaceous plate tectonic reconstructions. *Paleogeography, Palaeoecology, Palaeoclimatology*, 87, 493–501.



- Golonka, J. (2007). Late Triassic and early Jurassic palaeogeography of the world. *Paleogeography, Palaeoecology, Palaeoclimatology*, *244*, 297–307.
- Green, J., Huber, M., Waltham, D., Buzan, J., & Wells, M. (2017). Explicitly modeled deep-time tidal dissipation and its implication for lunar history. *Earth and Planetary Science Letters*, *461*, 46–53.
- Green, J. A. M. (2010). Ocean tides and resonance. *Ocean Dynamics*, *60*, 1243–1253. <https://doi.org/10.1007/s10236-010-0331-1>
- Green, J. A. M., & Huber, M. (2013). Tidal dissipation in the early Eocene and implications for ocean mixing. *Geophysical Research Letters*, *40*, 2707–2713. <https://doi.org/10.1002/grl.50510>
- Griffiths, S. D., & Peltier, W. R. (2008). Megatides in the Arctic Ocean under glacial conditions. *Geophysical Research Letters*, *35*, L08605. <https://doi.org/10.1029/2008GL033263>
- Hendershott, M. C. (1977). Numerical models of ocean tides. In *The sea* (Vol. 6, pp. 47–89). New York: Wiley Interscience Publication.
- Herold, N., Huber, M., Müller, R. D., & Seton, M. (2012). Modeling the Miocene climatic optimum: Ocean circulation. *Paleoceanography*, *27*, PA1209. <https://doi.org/10.1029/2010PA002041>
- Kagan, B., & Sundermann, A. (1996). Dissipation of tidal energy, paleotides, and evolution of the Earth-Moon system. *Advances in Geophysics*, *38*, 179–266.
- Matthews, K., Maloney, K., Zahirovic, S., Williams, S., Seton, M., & Müller, R. D. (2016). Global plate boundary evolution and kinematics since the late Paleozoic. *Global and Planetary Change*, *146*, 226–250.
- Müller, R. D., Sdrolias, M., Gaina, C., & Roest, W. R. (2008). Age, spreading rates, and spreading asymmetry of the world's ocean crust. *Geochemistry, Geophysics, Geosystems*, *9*, Q04006. <https://doi.org/10.1029/2007GC001743>
- Nance, R. D., Worsley, T. R., & Moody, J. B. (1988). The supercontinent cycle. *Scientific American*, *256*, 72–79.
- Pelling, H. E., & Green, J. A. M. (2013). Sea-level rise, tidal power, and tides in the Bay of Fundy. *Journal of Geophysical Research: Oceans*, *118*, 2863–2873. <https://doi.org/10.1002/jgrc.20221>
- Platzman, G. W. (1975). Normal modes of the Atlantic and Indian Oceans. *Journal of Physical Oceanography*, *5*, 201–221.
- Qin, X., Muller, R., Cannon, J., Landgrebe, T., Heine, C., Watson, R., & Turner, M. (2012). The GPlates Geological Information Model and Markup Language. *Geoscientific Instrumentation, Methods and Data Systems*, *1*, 111–134.
- Rogers, J., & Santosh, M. (2003). Supercontinents in Earth history. *Gondwana Research*, *6*, 357–368. [https://doi.org/10.1016/S1342-937X\(05\)70993-X](https://doi.org/10.1016/S1342-937X(05)70993-X)
- Schellart, W. P., Freeman, J., Stegman, D. R., Moresi, L., & May, D. (2007). Evolution and diversity of subduction zones controlled by slab width. *Nature*, *446*, 308–311.
- Stammer, D., Ray, R. D., Andersen, O. B., Arbic, B. K., Bosch, W., Carrère, L., et al. (2014). Accuracy assessment of global ocean tide models. *Reviews of Geophysics*, *52*, 243–282. <https://doi.org/10.1002/2014RG000450>
- Waltham, D. (2015). Milankovitch period uncertainties and their impact on cyclostratigraphy. *Journal of Sedimentary Research*, *85*, 990–998.
- Wilmes, S.-B., & Green, J. A. M. (2014). The evolution of tides and tidally driven mixing over 21,000 years. *Journal of Geophysical Research: Oceans*, *119*, 4083–4100. <https://doi.org/10.1002/2013JC009605>
- Wilson, J. T. (1966). Did the Atlantic close and then re-open? *Nature*, *211*, 676–681.
- Yoshida, M., & Santosh, M. (2011). Future supercontinent assembled in the Northern Hemisphere. *Terra Nova*, *23*, 333–338.
- Zahirovic, S., Matthews, K. J., Flament, N., Müller, R. D., Hill, K. C., Seton, M., & Gurnis, M. (2016). Tectonic evolution and deep mantle structure of the eastern Tethys since the latest Jurassic. *Earth-Science Reviews*, *162*, 293–337.
- Zaron, E. D., & Egbert, G. D. (2006). Estimating open-ocean barotropic tidal dissipation: The Hawaiian Ridge. *Journal of Physical Oceanography*, *36*, 1019–1035.

A2 Weak tides during Cryogenian glaciations

J. A. Mattias Green, Hannah S. Davies, João C. Duarte, Jessica R. Creveling, & Christopher Scotese.

(The full copy of "Weak tides during Cryogenian glaciations" published in *Nature Communications*, Green et al. (2020))

Weak tides during Cryogenian glaciations

J. A. Mattias Green ^{1✉}, Hannah S. Davies^{2,3}, Joao C. Duarte ^{2,3,4}, Jessica R. Creveling⁵ & Christopher Scotese⁶

The severe “Snowball Earth” glaciations proposed to have existed during the Cryogenian period (720 to 635 million years ago) coincided with the breakup of one supercontinent and assembly of another. Whereas the presence of extensive continental ice sheets predicts a tidally energetic Snowball ocean due to the reduced ocean depth, the supercontinent palaeogeography predicts weak tides because the surrounding ocean is too large to host tidal resonances. Here we show, using an established numerical global tidal model and paleogeographic reconstructions, that the Cryogenian ocean hosted diminished tidal amplitudes and associated energy dissipation rates, reaching 10–50% of today’s rates, during the Snowball glaciations. We argue that the near-absence of Cryogenian tidal processes may have been one contributor to the prolonged glaciations if these were near-global. These results also constrain lunar distance and orbital evolution throughout the Cryogenian, and highlight that simulations of past oceans should include explicit tidally driven mixing processes.

¹School of Ocean Sciences, Bangor University, Menai Bridge, UK. ²Instituto Dom Luiz (IDL), Faculdade de Ciências, Universidade de Lisboa, Lisboa, Portugal. ³Departamento de Geologia, Faculdade de Ciências, Universidade de Lisboa, Lisboa, Portugal. ⁴School of Earth, Atmosphere and Environment, Monash University, Melbourne, VIC, Australia. ⁵College of Earth, Ocean, and Atmospheric Sciences, Oregon State University, Corvallis, OR, USA. ⁶Earth and Planetary Sciences, Northwestern University, Evanston, IL, USA. ✉email: m.green@bangor.ac.uk

It has been suggested that the Earth experienced near-global severe glaciations during the Cryogenian period (720–635 Ma), events which earned the nickname “Snowball Earth”^{1,2}. The earliest Cryogenian glaciation proposed, the Sturtian from 717–660 Ma^{1–3}, and the younger Marinoan glaciation, from 650–635 Ma^{1,3}, had continental ice advance down to very low latitudes⁴, possibly leaving an open equatorial ocean (the latter known as a “Slushball Earth”⁵). A Snowball state is climatologically stable, with the predicted duration of long-lived glaciation commensurate with the time for volcanic outgassing of greenhouse gases to reach a threshold for deglaciation^{1,6–8}, leading to abrupt warming and hothouse conditions after the glaciations^{7,9}. Here we propose that a second factor, ocean tides, influenced the duration of Cryogenian Snowball glaciations. Coupled ice flow–ocean circulation models^{10,11} suggest that there was only a single vigorous meridional overturning circulation cell, and hence stratification, near the equator in the Snowball ocean. The rest of the ocean was most likely vertically mixed or only very weakly stratified because of strong convective overturns from geothermal heating^{11,12}. If tidal dissipation, i.e., the loss of tidal energy due to boundary friction and tidal conversion (the generation of internal tidal waves), was then added to the background flow, the stratification could break down further¹³. This scenario predicts negligible tidal conversion (i.e., the generation of an internal tide), and tidal dissipation would be limited to the frictional boundary layer near the sea floor and underneath the ice. It has been suggested that tides in the vicinity of the Laurentide ice sheet during the last deglaciation probably contributed to its rapid collapse¹⁴. The melt rate in cavities under the ice shelf in present day Antarctica is largely controlled by tidally driven mixing, because mixing stirs the cold and fresh meltwater under the ice down into the water column, thus allowing saltier and warmer water to be brought into contact with the ice¹⁵. Breaking down the saline stratification in the ice–ocean boundary layer is a key process that will happen even if the rest of the ocean is only weakly stratified. Thus, weak tides would reduce under-ice mixing rates, which could prolong the duration of a Snowball glaciation, with far-reaching consequences for the Earth system.

Tides are known to fluctuate on geological time scales^{16,17} due to changes in the basin geometries induced by the motion of the Earth’s tectonic plates^{18,19}. The main mechanism for amplification of the tides is tidal resonance, which occurs when the size of a basin is equal to half a wave length of the tidal wave^{20,21}. Because of movements of the tectonic plates, we can therefore expect the tides to change on scales of millions of years. Also, because the wavelength is set by the tidal period (here taken to be 10.98 h throughout the period under investigation^{22,23}—see our methods for more details) and the speed of the wave, which in turn is set by the water depth, large-scale variations in depth due to the appearance of ice can also move a basin towards, or away from, resonance on scales shorter than those of tectonic motions.

Here, we aim to quantify Cryogenian tidal energetics by simulating the evolution of the global tides using 20 recent paleogeographic reconstructions covering 750–500 Ma¹⁸ in a numerical tidal model¹⁷ (see Methods for details and sensitivity simulations). We discuss how Cryogenian tidal amplitude and dissipation was affected by and could have contributed to the onset and termination of Snowball glaciation, and wider implications of the tidal results. The investigation covers the late Neoproterozoic, including the Cryogenian, and spans 750–600 Ma. We model a Sturtian and Marinoan glaciation duration from 715–660 Ma and 650–635 Ma, respectively.

Results

Tidal amplitudes. The numerical simulations predict global mean M2 tidal amplitudes of ~0.2 m prior to the onset of the Sturtian glaciation (Figs. 1 and 2a, and Supplementary Fig. 1; note that the tidal range is twice the amplitude). At 715 Ma, model glacial tidal amplitudes rapidly increase to 0.44 m, higher than present-day tidal amplitudes (Fig. 2), due to sea-level fall below the continental shelf. This allows a tidal resonance to develop, much like the enhanced resonance during the Last Glacial Maximum^{21,24}. The tidal amplitude in the simulations then decreases during the next 25 Ma due to a tectonic configuration that was unable to host a large tide because the basins were too large to be near resonance for the semidiurnal tide^{21,25–27}. The model suggests that at 680 Ma, the tide became more energetic again because the tectonic emergence of land over the South Pole

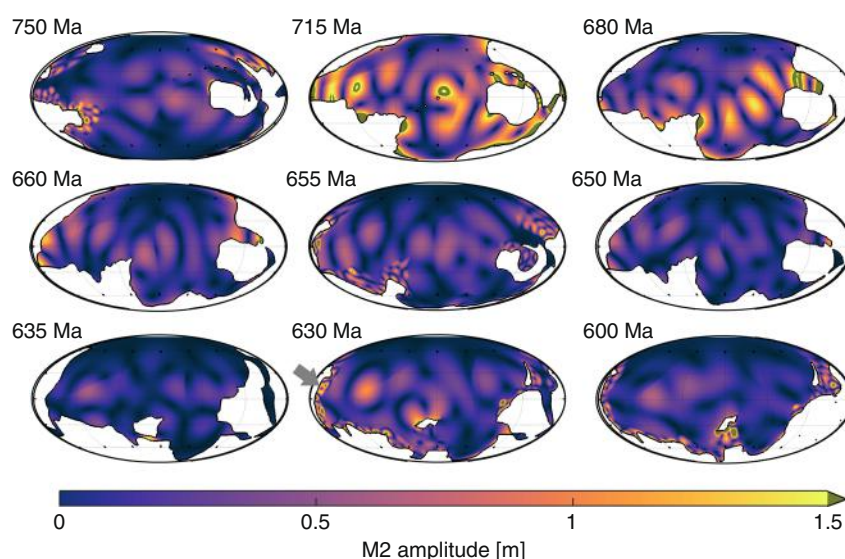


Fig. 1 Simulated M2 tidal amplitudes in metres for the time slices representing 750, 715, 680, 660, 655, 650, 635, 630 and 600 Ma (see labels in the top left hand corner of each panel; note that all global maps are plotted on a Mollweide projection). Note that the colour scale saturates at 1.5 m, in a grey-green colour, for clarity. The grey arrow at 630 Ma point to the coastline where the Elatina formation³¹ is now located. The formation gives a tidal proxy showing a range consistent with the one presented from the model.

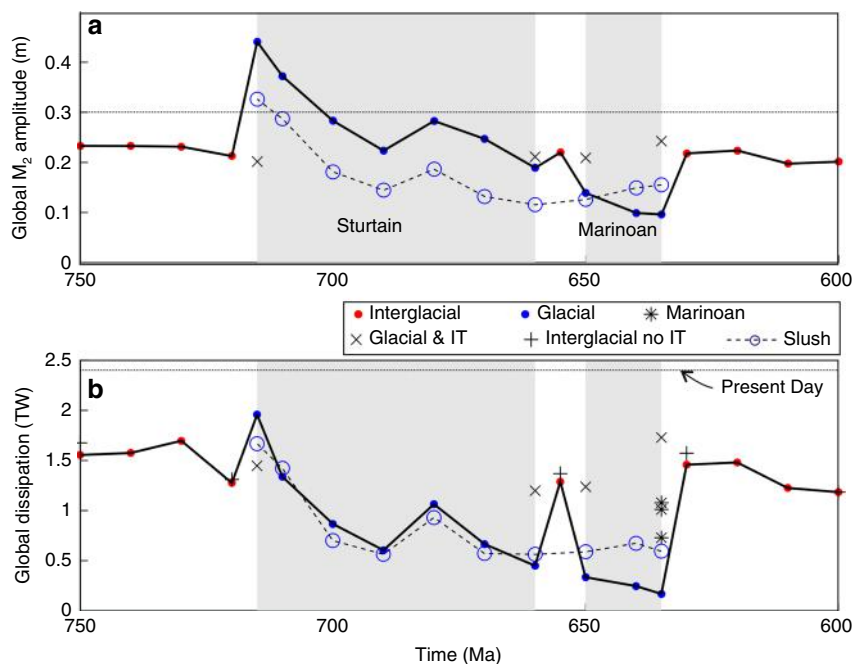


Fig. 2 The evolution of globally averaged tidal parameters during the Cryogenian. Globally averaged M_2 amplitudes (a) and integrated dissipation rates (b) throughout the period under consideration. The black solid line is the result from the set of simulations with conversion and no sea level change during interglacial periods (red dots), and a 500 m lowstand, no conversion, and increased bed friction during the glacial periods (blue dots). The x-symbols mark sensitivity simulations at the onset and end of glacial periods, in which non-glacial conditions were used, and the plus signs (+) mark simulations during interglacial periods without tidal conversion. The blue dashed line with circle markers shows the results for the Slushball with an ice-free band within 10° from the equator. The horizontal black dotted lines mark present day values and the blue shaded areas mark the spans of the two glaciations.

and a convergence of the main continental landmasses in the southern hemisphere changed the geometry of the large super-ocean basin to a size that was closer to that required for tidal resonance. Another decrease in tidal amplitude would have occurred through ~660 Ma because the continental configuration would only have allowed for small tidal amplitudes. The tide at 655 Ma, however, is slightly elevated in the model because the continental configuration allowed for a large tide between the glaciations. The onset of the model Marinoan glaciation at 650 Ma again reduced the tidal amplitude, resulting in the most tidally quiescent period in all deep-time simulations to date^{17,28}. Finally, deglaciation tidal amplitudes recover in the model to about 0.2 m between 630 and 600 Ma. The results highlight a tide-ice feedback in which the tidal dissipation response for the Sturtian glaciation is similar to that during the Pleistocene glaciations, where the sea-level lowstand enhanced dissipation due to ocean resonances^{21,24,29}. In contrast, during the Marinoan glaciation, the ice weakened the tides by an enhanced friction and changes in water depth that prohibited resonances to develop.

The modelled amplitudes are on average around 0.2 m throughout the Cryogenian, or about 2/3 of present-day values. This may not amount to a very large difference, but it is generally the tidal dissipation rates that are of importance to the wider Earth system, including driving under ice melting and large-scale ocean circulation patterns.

Tidal dissipation. The tidal dissipation rates computed from the simulations (Fig. 2b) are consistently below modern values. The estimated peak tidal dissipation rate at 715 Ma is 2TW, or 80% of today's rate (dashed line in Fig. 2b), while the minimum tidal dissipation rate in the Marinoan simulation is only about 10% of modern values³⁰. This supports the hypothesis put forward here that Cryogenian glaciations damped global tides and tidally

driven processes. A key feature, however, is the very sharp rise in the dissipation rates at the end of the Marinoan; over 5 Myr the tidal dissipation rate increases from 0.2 to 1.4 TW. Deglacial ice melt thus had important effects on the tides as ocean circulation and tidally driven mixing recovered. As the reconstructed continental configuration changed minimally between 635 and 630 Ma, the change in tidal amplitude and dissipation in the model arises from the parametrization of the ice sheets (i.e., the lowstand in sea level and changes in friction and tidal conversion discussed above). Glacial suppression of the tides is supported by simulations using interglacial conditions (i.e., sea level high-stand, reduced friction, and tidal conversion) for the beginning and end points for each glaciation, which show results in line with the nearby interglacial time slices (x symbols in Fig. 2b). In contrast, sensitivity simulations for interglacial time slices without tidal conversion (+ symbols in Fig. 2b) show only a minor change in the tides, further supporting the robustness of these results. Also, the simulations from 630 Ma show localised large amplitudes of over 2 m along the coastline of what is today south Australia (see the grey arrow in Fig. 1 for the location). This is the location of the tidally influenced Elatina formation³¹, and our amplitudes match those described from the site.

In our Snowball simulations we assume that the entire ocean was ice covered. As mentioned above, Earth may instead have been in a Slushball state, where the equatorial ocean was ice free³². Consequently, we simulated the Slushball for the glaciated time slices by allowing a full water depth within 10° from the equator and having a weak stratification throughout the ocean (see Methods for details and Supplementary Figs. 2 and 3). The average M_2 amplitude and associated integrated dissipation rates are again shown in (Fig. 2 as blue circles on a dashed line). Interestingly, these simulations show weaker tidal amplitudes, except for the end of the Marinoan, and the tidal dissipation rates

are below those of the snowball for most time slices. The reason for this response is that when tidal conversion is re-introduced in the deep ocean, the amplitudes are reduced, especially in the shallow shelf seas present, and thus there is less dissipation of energy in total. This is due to the non-linear interplay between friction and conversion, as seen in simulations for the Last Glacial Maximum (21ka)^{29,33}. These results further show that the Cryogenian tides were weak, regardless of how severe the glaciations were, and we argue that this supports our idea that weak tides were a key process in the Cryogenian ocean.

Details of the Marinoan deglaciation: The duration of deglaciation predicted by the Snowball hypothesis¹ is shorter than the 5 Myr model resolution adopted here. The increase in tidal amplitude after the glaciations, at both 655 Ma and 630 Ma, raises the question of how fast tides respond to deglaciation? To address this question, we used the three Marinoan deglacial bathymetries³⁴ with higher temporal resolution, covering 0 kyr, 2 kyr and 10 kyr from the initiation of the deglaciation (these simulations were done for a Snowball state only, as the tides were weakest in this state for this period, see; Fig. 2). The results show a rapid increase in tidal dissipation, from 0.7 TW at 0 kyr to 1.1 TW at 10 kyr, consistent with the deglacial signal between 635 and 630 Ma (note that the simulations, shown as black asterisks in Fig. 2b, appear at the same point on the x-axis because of the short time span relative to the full simulation). Thus, the deglacial rise in the tidal amplitude and dissipation would have occurred over millennia, rather than millions of years. Notably, the difference in tidal dissipation between the 635 Ma and the 0 kyr simulation, a factor 3.5 (from 0.2 to 0.7 TW), provides an estimate of uncertainty in the simulations. The 635 Ma simulation likely underestimates tidal dissipation due to the uniform 500 m sea level decrease, whereas the 0 kyr simulation includes a spatially varying sea level fingerprint. Furthermore, by excluding deep ocean bathymetry in the Marinoan reconstructions we overestimate tidal dissipation rates by up to a factor 2^{17,24}. The key conclusion of this investigation, however, is not in the exact amplitude or dissipation rate—they both require knowledge of the Late Neoproterozoic Earth system beyond that preserved in the rock record—but rather the robust result that Snowball glaciation led to generally very small tidal amplitudes, and that rapid deglaciation allowed the tides to recover.

Discussion

There is uncertainty in the paleogeographic reconstructions for the Cryogenian^{18,34}. Our tidal results are representative of scenarios of global glaciation of a specific ice/ocean volume, and may differ substantially under alternative scenarios of ice volume and distribution³⁵. The sea-level changes we used here are based on the commonly cited assumptions of glacial volume and deglacial timescale¹. Our globally integrated results are robust and the sensitivity simulation only change the globally integrated tidal dissipation rates by less than 10%. This holds for our Slushball simulations as well. These have an ice-free ocean around the Equator, and a weak stratification allowing for open ocean energy losses through tidal conversion (blue dashed lines in Fig. 2). The largest difference in the tides is seen at the onset and end of the glaciations, in simulations both with and without the ice parameterisation (i.e., double friction, lower sea-level, and no conversion—see Methods for details; Fig. 2b). The tidal signal that then emerges can be explained by how the differences in glacial reconstructions would affect tides, and it shows the effect of the deglaciation on the tides.

These results highlight a connection between oceanography (tides) and palaeogeography (ultimately set by tectonics) in the climatic stability of a Snowball Earth. Quiescent tides during

Snowball glaciations could have contributed to climate stability, because tidally driven processes, acting to melt ice by destabilising the freshwater stratification near the ice and allowing warmer water into contact with the ice, were severely muted for millions of years (or longer for the Sturtian). Tides are of course not the only process influencing the ice-sheets – if they were the main controller the Marinoan should have lasted longer than the Sturtian. However, the tides are a potential mechanism for destabilization of the ice once it starts to collapse. We also show that tides and tectonics are not independent on geological time scales: for a large fraction of the late Neoproterozoic, including the Cryogenian, Earth was in a supercontinent state. This led to weak late Neoproterozoic tides because of a lack of resonant ocean basins, except locally during a few time slices. The Cryogenian is the most quiescent period of the 1 Gyr of Earth's tides simulated to date^{17,28}. The resulting low tidal energy and tidal mixing would have had consequences for other components of the Earth system, including ocean circulation patterns and vertical fluxes of mass, salt, heat, and tracers, and for the evolution and dispersion of Neoproterozoic life. Detailed investigations of these consequences are left for future studies. The results also suggest that conceptual models of Cryogenian tides on Earth³⁶, may not necessarily provide converging results when compared to explicitly simulated tides with realistic paleo-geographies. We confirm the existence of the supertidal cycle, a long-term cycle of tidal strength, which is tied to the supercontinent assembly and dispersal²⁸. This has further implications for the Earth system, because tidal drag induces lunar recession¹⁷, and the current recession rate is too large to support the old Moon age model³⁷. The tidal dissipation rates must therefore have been weaker than at present for prolonged periods of Earth's history, and our results provide support for this being the case.

Methods

Late Neoproterozoic tides were simulated using a dedicated numerical tidal model^{17,21,24,28,29,38} that parameterizes energy losses due to both friction at the sea floor and tidal conversion. The latter includes the buoyancy frequency as a measure of vertical stratification, which is uncertain for ancient oceans. Consequently, we adopted values based on observed present day values for non-glaciated time slices³⁹ and a non-stratified ocean for all time slices representing Snowball states¹¹. The effect of friction in the glaciated time slices was enhanced with respect to the non-glaciated time slices to represent the presence of thick ice covering the ocean (see below for details). We adopt an Earth-moon orbital configuration consistent with the Late Neoproterozoic, including a 21.9 h solar day³¹, a 10.98 h lunar period, and a lunar forcing 15% larger than the modern. Neoproterozoic paleobathymetries were created from recent reconstructions¹⁸ and interpolated using the GPlates software^{40,41} to obtain bathymetries every 10 Myr from 750–600 Ma interval, with three extra slices produced for 715 Ma (the onset of the Sturtian), 655 Ma (the interglacial), and 635 Ma (the end of the Marinoan). In the non-glacial time slices, ocean volume was set to the same as for present day, whereas glaciated time slices included a lowstand of 500 m. We also used three slices from Creveling and Mitrovica³⁴ representing the termination of the Marinoan glaciation (0 kyr), and 2 kyr and 10 kyr into the deglaciation, respectively³⁴.

Tidal modelling. The Oregon State University Tidal Inversion Software (OTIS) has been used extensively to simulate deep-time, present day, and future tides^{17,21,24,28,29,38}, and it has been benchmarked against other forward tidal models⁴². It provides a numerical solution to the linearised shallow water equations, with the non-linear advection and horizontal diffusion excluded without a loss in accuracy²⁴:

$$\frac{\partial \mathbf{U}}{\partial t} + f \times \mathbf{U} = gH\nabla(\eta - \eta_{\text{SAL}} - \eta_{\text{EQ}}) - \mathbf{F} \quad (1)$$

$$\frac{\partial \eta}{\partial t} - \nabla \cdot \mathbf{U} = 0 \quad (2)$$

Here, $\mathbf{U} = \mathbf{u}H$ is the tidal volume transport (\mathbf{u} is the horizontal velocity vector and H is the water depth), f is the Coriolis parameter, g is acceleration due to gravity, η is the sea-surface elevation, η_{SAL} is the self-attraction and loading elevation, η_{EQ} is the elevation of the equilibrium tide, and \mathbf{F} the tidal energy dissipation term. This consists of two parts, $\mathbf{F} = \mathbf{F}_B + \mathbf{F}_W$, where \mathbf{F}_B parameterizes bed friction and \mathbf{F}_W represents energy losses due to tidal conversion, i.e., due to the generation of a baroclinic tide. Bed friction is parameterised through the standard quadratic law,

$F_B = C_D \mathbf{u} | \mathbf{u} |$, where $C_D = 0.003$ is a dimensionless drag coefficient. In the glaciated time slices, $C_d = 0.006$ was used to represent the effect of the ice covering the ocean as it effectively sets up a second boundary layer. The tidal conversion term is given by $F_W = C U$, and the conversion coefficient, C , was given by^{39,43,44}

$$C(x, y) = \gamma \frac{N_H \bar{N}}{8\pi\omega} (\nabla H)^2 \tag{3}$$

Here, $\gamma = 100$ represents a dimensionless scaling factor representing unresolved bathymetric roughness, N_H is the buoyancy frequency at the seabed, \bar{N} represents the vertical average of the buoyancy frequency, and ω is the frequency of the tide. The buoyancy frequency, N , is given by $N^2 = -g/\rho \partial\rho/\partial z$, where ρ is the density. The distribution of N is based on a statistical fit to observed present day values³⁹, or $N(x, y) = 0.00524 \exp(-z/1300)$, where z is the vertical coordinate, and the constants 0.00524 and 1300 have units of s^{-1} and m, respectively. We do not change these values of N in our simulations, but rather test sensitivity by modifying γ (because details of N is largely unknown for the period). The exception is the Snowball oceans, which were only weakly stratified¹¹, and the conversion was then switched off by setting $\gamma = 0$. To test the robustness of the parameterisation, sensitivity simulations were done for several time slices. For those at the beginning and end of each glaciation (i.e., 715, 660, 650, and 635 Ma), we did further simulations with $\gamma = 100$, and for select non-glacial states (600, 630, 655, 720, and 750 Ma) sensitivity tests were done with $\gamma = 200$ or $\gamma = 0$, representing a strongly stratified or unstratified ocean, respectively.

Our Slushball state was simulated by allowing for an open ocean within 10° of the equator. This was implemented by an exponential change in water depth over 1° in latitude from the 500 m lowstand to the ice-free ocean and then doubling the bed friction under the ice only. The Slushball ocean was likely weakly stratified, so we re-introduced a weak tidal conversion by setting $\gamma = 50$ in Eq. (3).

Bathymetry. The paleo-bathymetries for the Snowball simulations were created by digitising reconstructions of the late Proterozoic¹⁸, using GPlates^{40,41}. The original reconstructions covered every 50 Ma between 600–750 Ma, so to improve the temporal resolution, the information was interpolated linearly between these slices to obtain bathymetries every 10 Ma in our 600–750 Ma interval. Furthermore, three extra slices were produced for 635 Ma (end of the Marinoan), 655 Ma (interglacial),

and 715 Ma (onset of the Sturtian). The resulting 19 images were then translated to ocean bathymetries by setting continental shelf seas to 200 m depth, and subduction zones to 5900 m. Mid-oceanic ridges were 2500 m deep at the crest, and sloped linearly into the abyss over 5° in width. The abyssal plains were set to a depth that conserved present day ocean volume once all the other bathymetric features were set. There is obviously uncertainty in the Cryogenian sea level, although it is clear that it must have been low during the glaciations; Creveling & Mitrovica³⁴ suggest a lowstand of up to 1500 m below interglacial levels at some locations, and a mean sea level 500–800 m below interglacial levels. Consequently, we reduced the depth in our glaciated time slices by 500 m to represent the lowstand (simulations with 800 m lowstand do not change the qualitative results). The grids used in the simulation for selected time slices are shown in Fig. 3.

When we mention glacial conditions, we thus refer to a situation with a doubled bed friction (to represent the ice boundary layer), $g = 0$ (to represent an unstratified ocean), and sea-level lowered by 500 m, and non-glacial simulation uses the default parameters discussed above.

Furthermore, simulations of the relative sea level changes during the Marinoan deglaciation around 635 Ma for three slices were also used³⁴. These represent the termination of the glaciation (i.e., 0 kyr after our 635 Ma slice), and then 2 kyr and 10 kyr into the deglaciation (this last slice represents the end of the deglaciation; see Fig. 4). We used these slices for a set of sensitivity simulations and refer to them as 0 kyr, 2 kyr, and 10 kyr in the following, or as “the Marinoan” when discussed as a group. This gives us a unique opportunity to add 3 simulations at higher temporal resolution to further evaluate the influence of the glaciations on the tides.

Simulations and computations. The Earth-moon system’s orbital configuration was different during the Cryogenian, and here we used a 21.9 h solar day⁴⁵, a 10.98 h lunar period, and lunar forcing 15% larger than at present day^{17,23}. Simulations were done for all 19 time slices with a range of parameter choices to ensure the results were robust. The effect of the ice-sheet was parameterised in the Snowball time slices by neglecting conversion (i.e., with $\gamma = 0$ in Eq. (3)); the Snowball state was most likely unstratified¹⁰), a doubled drag coefficient (i.e., $C_d = 0.006$) and with a 500 m uniform lowstand in sea level to represent the effect of the ice. Note that floating ice does not impose a rigid lid for the tide because the ice moves with

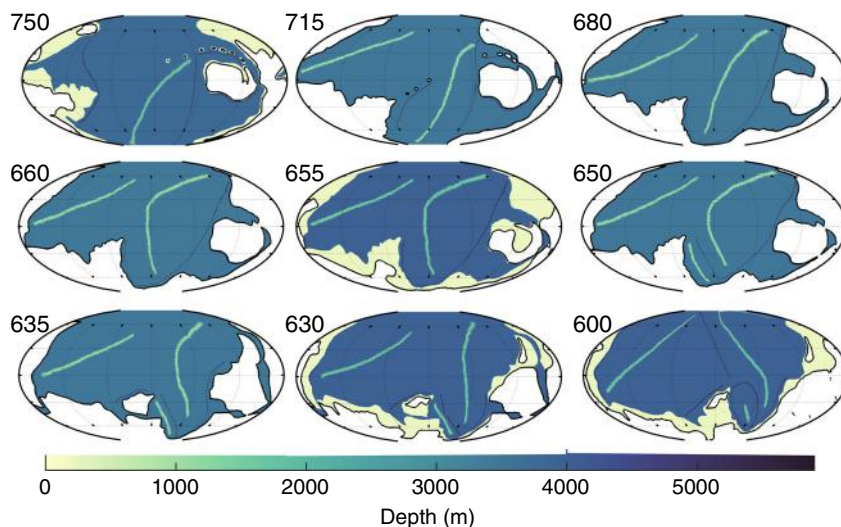


Fig. 3 The ocean bathymetry for nine key time slices. Shown is the ocean bathymetry, with depths in colour land white. Note the age for each time slice marked by the label at top left corner, and the black contour marking the coastline and the lack of shelf seas during the glaciations (715–660 Ma and 650–635 Ma). The green lines in the deep ocean mark the peaks of the oceanic ridges and the dark grey lines show trenches.

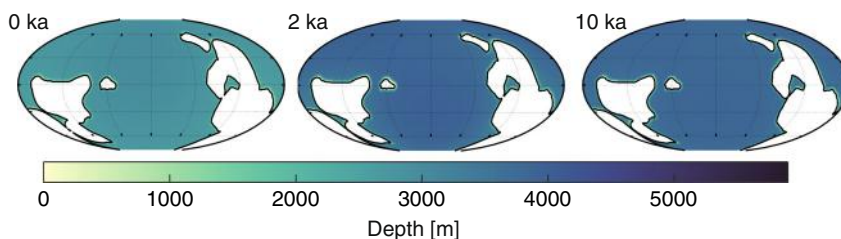


Fig. 4 The ocean bathymetry during the Marinoan deglaciation. From left to right are the bathymetry for the 0 kyr, 2 kyr, and 10 kyr time slices, with times measured from onset of the Marinoan deglaciation³⁴.

sea surface. Landfast ice without fractures may act as a lid in smaller regions not resolved here. The enhanced drag coefficient is justified by the rough underside of the ice, which leads to effective energy losses in ice covered areas⁴⁶. This may lead to tidally driven residual currents as well, and these may be important because of the quiescent ocean. Analysing them is left for future studies. The time slices at onset and termination of the glaciations (i.e., 715, 660, 650, and 635 Ma) were also simulated without the lowstand and with conversion to represent non-glaciated states. Furthermore, the non-glaciated time slices at 750, 720, 655, 630 and 600 were used to test the robustness of the conversion parameterisation and rerun with $\gamma = 200$ (i.e., representing a very strong, doubled, vertical stratification). A further set of sensitivity simulations for these slices had further doubling and halving of the drag coefficient, C_d , and/or the conversion scaling factor, γ . As in other deep-time studies^{17,43}, the sensitivity simulations (not shown) only led to limited changes in global dissipation rates, and we conclude that the results presented here are robust. The Slushball simulations are described above.

Simulations for all of our time slices were done at $1/4^\circ$ horizontal resolution in both latitude and longitude, achieved through linear interpolation from the original data described above. Each simulation covered 14 days, of which 5 days were used for harmonic analysis of the tide. Simulations were done for the two dominating constituents, M2 (principle lunar) and K1 (luni-solar declination), although focus in the following is on M2. The model outputs amplitudes and phases for the surface elevation and transport vector for each simulated tidal constituent.

The model output was used to compute tidal dissipation rates, D , as the difference between the time average of the work done by the tide generating force (\mathbf{W}) and the divergence of the horizontal energy flux (\mathbf{P})⁴⁷:

$$D = \mathbf{W} - \nabla \cdot \mathbf{P} \quad (4)$$

where \mathbf{W} and \mathbf{P} are given by

$$\mathbf{W} = g\rho(\mathbf{U} \cdot \nabla(\eta_{EQ} + \eta_{SAL})) \quad (5)$$

and

$$\mathbf{P} = g\rho(\mathbf{U}\eta) \quad (6)$$

In Eqs. (5) and (6) the angular brackets mark time-averages over a tidal period.

Present day validation. The core model set-up used here is the same as in other deep-time tidal simulations^{17,48}, and it is briefly described here. A present day control simulation¹⁷ gives a root-mean-square error of about 11 cm for the M2 tidal amplitudes when compared to the data in TPXO8 (<http://www.tpxo.net>). A simulation with a degenerated present day bathymetry, with less resolution to represent reconstructed bathymetry, produced an error of about 20 cm⁴³. It also produces an M2 dissipation rate that is 75% higher than in the present day simulation because of a lack of deep-ocean bathymetry¹⁷. It is thus highly likely that our simulations overestimate the Cryogenian tidal dissipation rates, especially in the Marinoan simulations.

Data availability

The manuscript data are available from the Open Science Framework (https://osf.io/wnyhr/?view_only=bae47b065db24d97b79d106536a59549).

Received: 1 November 2019; Accepted: 3 November 2020;

Published online: 04 December 2020

References

- Hoffman, P. F. et al. Snowball Earth climate dynamics and Cryogenian geology-geobiology. *Sci. Adv.* **3**, e1600983 (2017).
- Hoffman, P. F., Kaufman, A. J., Halverson, G. P. & Schrag, D. P. A neoproterozoic snowball earth. *Science* **281**, 1342–1346 (1998).
- Rooney, A. D., Strauss, J. V., Brandon, A. D. & Macdonald, F. A. A Cryogenian chronology: two long-lasting synchronous Neoproterozoic glaciations. *Geology* **43**, 459–462 (2015).
- Macdonald, F. A. et al. Calibrating the Cryogenian. *Science* **327**, 1241–1243 (2010).
- Allen, P. A. & Etienne, J. L. Sedimentary challenge to Snowball Earth. *Nat. Geosci.* **1**, 817–825 (2008).
- Pierrehumbert, R. T., Abbot, D. S., Voigt, A. & Koll, D. Climate of the Neoproterozoic. *Annu. Rev. Earth Planet. Sci.* **39**, 417–460 (2011).
- Pierrehumbert, R. T. High levels of atmospheric carbon dioxide necessary for the termination of global glaciation. *Nature* **429**, 646–649 (2004).
- Harland, W. B. Origins and assessment of snowball Earth hypotheses. *Geol. Mag.* **144**, 633–642 (2007).
- Shields, G. A. Marinoan meltdown. *Nat. Geosci.* **1**, 351–353 (2008).
- Ashkenazy, Y. et al. Dynamics of a snowball earth ocean. *Nature* **495**, 90–93 (2013).
- Ashkenazy, Y., Gildor, H., Losch, M. & Tziperman, E. Ocean circulation under globally glaciated snowball Earth conditions: steady-state solutions. *J. Phys. Oceanogr.* **44**, 24–43 (2014).
- Pollard, D. & Kasting, J. F. Snowball Earth: a thin-ice solution with flowing sea glaciers. *J. Geophys. Res. C. Ocean* **110**, 1–16 (2005).
- Jansen, M. F. The turbulent circulation of a snowball earth ocean. *J. Phys. Oceanogr.* **46**, 1917–1933 (2016).
- Arbic, B. K., MacAyeal, D. R., Mitrovica, J. X. & Milne, G. A. Palaeoclimate: ocean tides and Heinrich events. *Nature* **432**, 460 (2004).
- Makinson, K., Holland, P. R., Jenkins, A., Nicholls, K. W. & Holland, D. M. Influence of tides on melting and freezing beneath Filchner-Ronne Ice Shelf, Antarctica. *Geophys. Res. Lett.* **38**, 4–9 (2011).
- Kagan, B. A. & Sündermann, J. Dissipation of tidal energy, paleotides, and evolution of the Earth-Moon system. *Adv. Geophys.* **38**, 179–266 (1996).
- Green, J. A. M., Huber, M., Waltham, D., Buzan, J. & Wells, M. Explicitly modelled deep-time tidal dissipation and its implication for Lunar history. *Earth Planet. Sci. Lett.* **461**, 46–53 (2017).
- Scotese, C. R. Late Proterozoic plate tectonics and palaeogeography: a tale of two supercontinents, Rodinia and Pannotia. *Geol. Soc. Lond., Spec. Publ.* **326**, 67–83 (2009).
- Merdith, A. S. et al. A full-plate global reconstruction of the Neoproterozoic. *Gondwana Res.* **50**, 84–134 (2017).
- Arbic, B. K. & Garrett, C. A coupled oscillator model of shelf and ocean tides. *Cont. Shelf Res.* <https://doi.org/10.1016/j.csr.2009.07.008> (2009).
- Green, J. A. M. Ocean tides and resonance. *Ocean Dyn.* **60**, 1243–1253 (2010).
- Williams, G. E. Late Proterozoic tidal rhythmites, South Australia: sedimentary features, deposition, and implications for the Earth's paleorotation. *Can. Soc. Pet. Geol. Memo.* **16**, 161–178 (1991).
- Waltham, D. Milankovitch period uncertainties and their impact on cyclostratigraphy. *J. Sediment. Res.* **85**, 990–998 (2015).
- Egbert, G. D., Ray, R. D. & Bills, B. G. Numerical modeling of the global semidiurnal tide in the present day and in the last glacial maximum. *J. Geophys. Res. Ocean.* **109**, 1–15 (2004).
- Arbic, B. K., Karsten, R. H. & Garrett, C. On tidal resonance in the global ocean and the back-effect of coastal tides upon open-ocean tides. *Atmosphere-Ocean* **47**, 239–266 (2009).
- Platzman, G. W. Normal modes of the {Atlantic and Indian Oceans}. *J. Phys. Oceanogr.* **5**, 201–221 (1975).
- Longuet-Higgins, M. S. & Pond, G. S. The free oscillations of fluid on a hemisphere bounded by meridians of longitude. *Philos. Trans. R. Soc. Lond.* **266**, 193–223 (2020).
- Green, J. A. M., Molloy, J. L., Davies, H. S. & Duarte, J. C. Is there a tectonically driven supertidal cycle? *Geophys. Res. Lett.* **45**, 3568–3576 (2018).
- Wilmes, S.-B. & Green, J. A. M. The evolution of tides and tidal dissipation over the past 21,000 years. *J. Geophys. Res. Ocean.* **119**, 4083–4100 (2014).
- Egbert, G. D. & Ray, R. D. Significant dissipation of tidal energy in the deep ocean inferred from satellite altimeter data. *Nature* **405**, 775–778 (2000).
- Williams, G. E. Geological constraints on the Precambrian history of Earth's rotation and the Moon's orbit. *Rev. Geophys.* **38**, 37–59 (2000).
- Fairchild, I. J. & Kennedy, M. J. Neoproterozoic glaciation in the Earth System. *J. Geol. Soc. Lond.* **164**, 895–921 (2007).
- Egbert, G. D., Bills, B. G. & Ray, R. D. Numerical modeling of the global semidiurnal tide in the present day and in the last glacial maximum. *J. Geophys. Res.* **109**, C03003 (2004).
- Creveling, J. R. & Mitrovica, J. X. The sea-level fingerprint of a Snowball Earth deglaciation. *Earth Planet. Sci. Lett.* **399**, 74–85 (2014).
- Benn, D. I. et al. Orbitally forced ice sheet fluctuations during the Marinoan Snowball Earth glaciation. *Nat. Geosci.* **8**, 704–707 (2015).
- Wunsch, C. Tides of global ice-covered oceans. *Icarus* **274**, 122–130 (2016).
- Munk, W. Once Again - Tidal Friction. *Q. J. R. Astron. Soc.* **9**, 352–375 (1968).
- Wilmes, S.-B., Green, J. A. M., Gomez, N., Rippeth, T. P. & Lau, H. Global tidal impacts of large-scale ice sheet collapses. *J. Geophys. Res. Ocean.* **122**, (2017).
- Zaron, E. D. & Egbert, G. D. Verification studies for a z-coordinate primitive-equation model: tidal conversion at a mid-ocean ridge. *Ocean Model* **14**, 257–278 (2006).
- Müller, R. D. et al. GPlates: building a virtual Earth through deep time. *Geochem. Geophys. Geosystems* **19**, 2243–2261 (2018).
- Qin, X. et al. The GPlates geological information model and markup language. *Geosci. Instrumentation Methods Data Syst.* **1**, 111–134 (2012).
- Stammer, D. et al. Accuracy assessment of global barotropic ocean tide models. *Rev. Geophys.* **52**, 243–282 (2014).
- Green, J. A. M. & Huber, M. Tidal dissipation in the early Eocene and implications for ocean mixing. *Geophys. Res. Lett.* **40**, 2707–2713 (2013).

44. Green, J. A. M. & Nycander, J. A comparison of tidal conversion parameterizations for tidal models. *J. Phys. Oceanogr.* **43**, 104–119 (2013).
45. Williams, G. E., Gostin, V. A., McKirdy, D. M. & Preiss, W. V. The Elatina glaciation, late Cryogenian (Marinoan Epoch), South Australia: Sedimentary facies and palaeoenvironments. *Precambrian Res.* **163**, 307–331 (2008).
46. Makinson, K. & Nicholls, K. W. Modeling tidal currents beneath Filchner-Ronne Ice Shelf and on the adjacent continental shelf: Their effect on mixing and transport. *J. Geophys. Res. Ocean.* **104**, 13449–13465 (1999).
47. Egbert, G. D. & Ray, R. D. Estimates of M2 tidal energy dissipation from Topex/Poseidon altimeter data. *J. Geophys. Res.* **106**, 22475–22502 (2001).
48. Davies, H. S., Green, J. A. M. & Duarte, J. C. J. Back to the future: testing different scenarios for the next supercontinent gathering. *Glob. Planet. Change* **169**, 133–144 (2018).

Acknowledgements

The tidal simulations were done on Supercomputing Wales (project SCW1343). JAMG acknowledges funding from NERC (MATCH, NE/S009566/1) and from the College of Natural Science, Bangor University. JCD acknowledges an FCT Researcher contract, an exploratory project grant ref. IF/00702/2015, and the FCT project UID/GEO/50019/2020-IDL. HSD acknowledges the Fundação para a Ciência e a Tecnologia a PhD grant no. PD/BD/135068/2017 - Earthsystems/IDL. JCD and HSD also acknowledge support from the Fundação para a Ciência e a Tecnologia through project no. UIDB/50019/2020 - Instituto Dom Luiz. Comments from Dr Paul Myrow, two anonymous reviewers, and Prof Melissa Plail (editor) greatly improved the manuscript.

Author contributions

The work was led by J.A.M.G. with support from J.D. J.A.M.G. wrote the core of the paper with input from all authors. H.S.D. made the bathymetry grids from initial projections by CS; J.R.C. provided the additional material for the Marinoan and provided extensive writing support.

Competing interests

The authors declare no competing interests.

Additional information

Supplementary information is available for this paper at <https://doi.org/10.1038/s41467-020-20008-3>.

Correspondence and requests for materials should be addressed to J.A.M.G.

Peer review information *Nature Communications* thanks Yonggang Liu, Paul Myrow and the other, anonymous, reviewer(s) for their contribution to the peer review of this work.

Reprints and permission information is available at <http://www.nature.com/reprints>

Publisher's note Springer Nature remains neutral with regard to jurisdictional claims in published maps and institutional affiliations.



Open Access This article is licensed under a Creative Commons Attribution 4.0 International License, which permits use, sharing, adaptation, distribution and reproduction in any medium or format, as long as you give appropriate credit to the original author(s) and the source, provide a link to the Creative Commons license, and indicate if changes were made. The images or other third party material in this article are included in the article's Creative Commons license, unless indicated otherwise in a credit line to the material. If material is not included in the article's Creative Commons license and your intended use is not permitted by statutory regulation or exceeds the permitted use, you will need to obtain permission directly from the copyright holder. To view a copy of this license, visit <http://creativecommons.org/licenses/by/4.0/>.

© The Author(s) 2020

A3 The climates of Earth's next supercontinent: effects of tectonics, rotation rate, and insolation

M. J. Way, H. S. Davies, João C. Duarte, & J. A. M. Green.

(The full copy of "The climates of Earth's next supercontinent: effects of tectonics, rotation rate, and insolation" submitted to *Geophysical Research Letters*, Way et al. (2019))

1 **The climates of Earth's next supercontinent: effects of**
2 **tectonics, rotation rate, and insolation**

3 **M. J. Way^{1,2,3}, H. S. Davies^{4,5}, J. C. Duarte^{4,5,6}, and J. A. M. Green⁷**

4 ¹NASA Goddard Institute for Space Studies, New York, USA

5 ²Goddard Space Flight Center Sellers Exoplanet Environments Collaboration

6 ³Theoretical Astrophysics, Department of Physics and Astronomy, Uppsala University, Uppsala, Sweden

7 ⁴Instituto Dom Luiz (IDL), Faculdade de Ciências, Universidade de Lisboa, Lisbon, Portugal

8 ⁵Departamento de Geologia, Faculdade de Ciências, Universidade de Lisboa, Lisbon, Portugal

9 ⁶School of Earth, Atmosphere and Environment, Monash University, Melbourne, Victoria, Australia

10 ⁷School of Ocean Sciences, Bangor University, Menai Bridge, UK

11 **Key Points:**

- 12 • The climate of a distant future Earth is modeled for two different supercontinent
13 scenarios.
- 14 • The latitudinal location and topographic height of the supercontinents are crit-
15 ical to mean surface temperatures.

Corresponding author: Michael Way, michael.way@nasa.gov

Abstract

We explore two possible Earth climate scenarios, 200 and 250 million years into the future, using projections of the evolution of plate tectonics, solar luminosity, and rotation rate. In one scenario, a supercontinent forms at low latitudes, whereas in the other it forms at high northerly latitudes with an Antarctic subcontinent remaining at the south pole. The climates between these two end points are quite stark, with differences in mean surface temperatures approaching several degrees. The main factor in these differences is related to the topographic height of the high latitude supercontinents where higher elevations promote snowfall and subsequent higher planetary albedos. These results demonstrate the need to consider alternative boundary conditions when simulating Earth-like exoplanetary climates.

Plain Language Summary

We investigate two tantalizing Earth climate scenarios 200 and 250 million years into the future. We show the role played by plate tectonics, the sun's increase in brightness, and a slightly slower rotation rate in these future climate scenarios. In one case the present day continents form into a single land-mass near the equator, and in the other case Antarctica stays put, but the rest of the present day continents are mostly pushed well north of the equator. The difference in the mean surface temperatures of these two cases differ by several degrees Celsius, while also being distinct in the total surface area in which they maintain temperatures allowing liquid water to exist year round.

1 Introduction

Earth's near-future climate has been extensively explored via the IPCC and associated CMIP studies (e.g. Collins et al., 2013). Earth's ancient climate has also been studied at various levels of detail, including the Cretaceous greenhouse (e.g., Huber et al., 2018), the Neoproterozoic Snowball (Pierrehumbert et al., 2011), and on the supercontinent Pangea (e.g., Parrish, 1993; Dunne et al., 2021). However, Earth's deep time future is a novel research discipline, and changes in deep-time future climate, induced by changes in topography and land/sea masks (e.g., Davies et al., 2018), have yet to be explored until now.

The geological formations on the ever-changing surface of the Earth have a strong influence on our climate. The transition to a cold climate in the Cenozoic, including the glaciation of Antarctica, was induced by opening of ocean gateways and reduced atmospheric CO₂ concentrations (Barker, 2001; DeConto & Pollard, 2003; Smith & Pickering, 2003). The development of the Caribbean arc and closing of the Panama Isthmus allowed the Gulf Stream to form, with major consequences for global climate (Montes et al., 2015), whereas the closure of the Strait of Gibraltar led to the Messinian Salinity Crisis (Krijgsman et al., 1999). Furthermore, the Himalayas, a consequence of the India-Eurasia collision, allows for the monsoon (Tada et al., 2016). Recently, Farnsworth et al. (2019) showed that the climate sensitivity for the period 150–35 million years ago is dependent on the continental configuration, particularly ocean area. Schmittner et al. (2011) investigated the effects of mountains on ocean circulation patterns of present day Earth and concluded that the current configuration of mountains and ice sheets determines the relative deep-water formation rates between the Atlantic and the Pacific Oceans.

The tectonic plates on Earth aggregate into supercontinents and then disperse on a cycle of 400-600 million years – the supercontinent cycle (Davies et al., 2018; Pastor-Galán et al., 2019; Yoshida, 2016; Yoshida & Santosh, 2018). The latest supercontinent Pangea formed around 310 million years ago and started breaking up around 180 million years ago. The next supercontinent will most likely form in 200–250 million years,

64 meaning Earth is currently about halfway through the scattered phase of the current su-
 65 percontinent cycle (Davies et al., 2018).

66 There are obvious and strong links between large-scale tectonics and climate. It
 67 would be interesting to know what Earth’s climate could be like in the distant future when
 68 continental movements will have taken Earth away from the current continental config-
 69 uration (Davies et al., 2018). Here, we investigate what a climate may look like on Earth
 70 in a future supercontinent state. A secondary application of climate modelling of the deep-
 71 time future is to create a climate model of an Earth-like exoplanet using the param-
 72 eters known to sustain habitability and a stable biosphere (Earth). Using the Deep-time
 73 future Earth as a basis for exoplanetary climate studies allows us to establish sensitiv-
 74 ity ranges for the habitability and climate stability of the future Earth and its distant
 75 cousins in our galaxy.

76 2 Methods

77 2.1 Tectonic maps

78 Maps of the future Earth were produced based on two plausible scenarios for fu-
 79 ture Earth: Aurica (forming around 250 million years from now; Duarte et al., 2018)
 80 and Amasia (forming around 200 million years from now; Mitchell et al., 2012) – see
 81 Davies et al. (2018) for a summary. In both cases the ocean bathymetry was kept as in
 82 Davies et al. (2020), with continental shelf seas 150 m deep, mid-ocean ridges 1600 m
 83 deep at the crest point and deepening to the abyssal plains within 5° , and subduction
 84 zones 6000 m deep. The abyssal plain was set to a depth maintaining the present day
 85 ocean volume. Each topographic file was generated with a $1/4^\circ$ horizontal resolution in
 86 both latitude and longitude.

87 We generated three subsets of maps for each of the two supercontinent scenarios
 88 (see Table 1):

- 89 1. CTRL: Low mean topography (land close to sea level, 1–200 m), without moun-
 90 tains
- 91 2. PD: Higher mean topography (land close to present day mean topography, 1–4000
 92 m) without mountains
- 93 3. MNTS: Low topography (1–200 m) with mountains (land close to sea level 1–200
 94 m interspersed with mountains 2000–7000 m high)

95 The first subset of maps serve as a control (CTRL), allowing us to test the effect
 96 of the position and geometry of the continents without the influence of high topographies
 97 and particular features such as mountain ranges. It could also simulate a supercontinent
 98 that has existed long enough to have been almost fully eroded. The land here has been
 99 assigned topography with a normal distribution (mean = 1 m and standard deviation
 100 = 50 m), giving topographic heights varying from 1 to 200 m.

101 The second set of maps assume mean topographic values close to those of present
 102 day (PD) but with no significant variation (e.g., no high mountains). This was made by
 103 applying a random topography following a normal distribution with mean and standard
 104 deviations closer to those of present day Earth’s topography (i.e., mean of 612 m and
 105 standard deviation of 712 m). The resulting topography varies between 1 and 4000 m
 106 in height.

107 In the third set mountain ranges (MTNS) are included. The land of the supercon-
 108 tinent was first given a random topography similar to the control map (varying randomly
 109 between 1 and 200 m), after which mountains were added manually. The mountains are
 110 of three types: 1) Himalaya-type, which result from the collision of continents during the
 111 formation of the supercontinent, with an average peak elevation of 7500 m; 2) Andes-

Table 1. A summary list of the simulations & results.

Sim	Name	Topography	Ins ^a	LoD ^b (hrs)	Runtime (years)	T ^c (C)	Balance (Wm ⁻²)	A ^d (%)	SnowFr ^e (%).	Hab ^f (%).
Aurica 250Myr into the Future										
01	Aurica	CTRL	1.0260	24.5	2000	20.5	0.2	30.5	0.5	1.000/1.000
02	"	PD	"	24.5	2500	20.6	0.1	30.1	0.6	0.955/0.956
03	"	MTNS	"	24.5	2000	20.6	0.2	30.3	1.5	0.974/0.983
Amasia 200Myr into the Future										
04	Amasia	CTRL	1.0223	24.5	3000	19.5	0.3	30.2	5.0	0.932/0.983
05	"	PD	"	24.5	3000	16.9	0.2	31.3	10.2	0.862/0.901
06	"	MTNS	"	24.5	3000	20.2	0.2	30.0	4.7	0.926/0.976
Modern Earth										
07	Earth_noAer_noO3		1.0	24.0	2000	13.5	-0.1	31.1	9.3	0.869/0.953
08	Earth_noAer_noO3_Rot		1.0	24.5	2000	13.3	0.2	31.0	9.5	0.865/0.951
09	Earth_noAer_noO3_Rot_Ins		1.0260	24.5	2000	17.7	-0.0	30.6	6.4	0.930/0.974

^a Insolation, where 1.0 = 1361 W m⁻² (Modern Earth).

^b LoD = Length of Day in hours.

^c Global mean surface temperature in degrees Celsius from an average over the last 10 years of the model run.

^d Planetary Albedo.

^e Snow and Ice, global fractional area.

^f Habitable fraction (Spiegel et al., 2008) T>0/T>-15°.

112 type, located at the margins of the continents along major subduction zones, with an
 113 average peak elevation of 4000 m; and 3) Appalachian-type, which correspond to eroded
 114 orogens that were formed and then partially eroded during the supercontinent cycle, with
 115 an average peak elevation of 2000 m. In all cases, the width of the mountains is 5° from
 116 peak to base.

117 2.2 Rotation changes

118 Day-length for the future was computed based on the simulated tidal dissipation
 119 rates presented in Green et al. (2018). The average dissipation during the remaining part
 120 of the supercontinent cycle is approximately half of the present day value (Green et al.,
 121 2018), leading to a change in day length that cannot be ignored. Consequently, we ex-
 122 pect a change in daylength at approximately half the rate of present day, or about 1×10^{-3}
 123 s per 100 years (Bills & Ray, 1999) over the next 200 My. This leads to a day at the su-
 124 percontinent state being ~30 minutes longer than today, and this length of day (24.5 hours)
 125 was consequently used in all of the Future Climate General Circulation Model simula-
 126 tions discussed below.

127 2.3 General Circulation Model set up

128 The ROCKE-3D General Circulation Model (GCM) version Planet_1.0 (R3D1) as
 129 described in Way et al. (2017) is used for this study. A fully coupled dynamic ocean is
 130 utilized. Using data generated via Claire et al. (2012) we use an insolation value of
 131 $1361 \times 1.0223 = 1391.3$ W m⁻² for the Amasia simulations (04–06) 200 Myr into the fu-
 132 ture. We use a value of $1361 \times 1.0260 = 1396.4$ W m⁻² for the Aurica Simulations (01–
 133 03) 250 My into the future. We do not change the solar spectrum as the changes for such
 134 a small leap into the future will be minimal in terms of its effect on the planet’s atmo-
 135 sphere.

136 We use a 50/50 clay/sand mix for the soil given that we have no constraints on what
 137 the surface will be like in the deep future and is a value commonly used in the exoplanet
 138 community (e.g. Yang et al., 2014; Way et al., 2018). 40 cm of water is initially distributed
 139 into each soil grid cell. We use a ground albedo of 0.2 at model start, but the albedo will

140 change via snow deposition (brighter), or from rainfall (darker) as the GCM moves for-
141 ward in time.

142 The original topography resolution of $1/4^\circ \times 1/4^\circ$ from the tectonic maps discussed
143 in Section 2.1 is down-sampled to a resolution of $4^\circ \times 5^\circ$ in latitude by longitude, which
144 is the default R3D1 resolution. The standard deviation from the down-sampling is used
145 to set the roughness length of the surface in each grid cell. River flow direction is based
146 on the resulting topography and exits to the ocean when possible. Large inland seas (typ-
147 ically less than 15 contiguous grid cells) are defined as lakes rather than ocean grid cells.
148 The GCM allows lakes to expand and contract as dictated by the competition between
149 evaporation and precipitation. The same holds for the possible creation and disappear-
150 ance of lakes. This allows the model to handle inland surface water in a more sophisti-
151 cated manner than making all surface water defined as ocean grid cells. This is highly
152 desirable because ocean grid cells cannot be created or destroyed during a model run.

153 Any ocean grid cell with a depth less than 150 meters (from the down-sampled $4^\circ \times$
154 5° data) was set to have a value of 204 meters (the mean depth of ocean model level 6).
155 This is especially important at high latitudes where shallow ocean cells may freeze to the
156 bottom causing the model to crash due to its inability to dynamically change surface types
157 from ocean to land ice.

158 The down-sampling has a side effect in that the land-sea mask will differ slightly
159 between the three topographic types (CTRL, PD, MTNS). For example, in a case with
160 a collection of ocean or lake grid cells adjacent to a number of high elevation land to-
161 pography grid cells the down-sampling may change the combined ocean + land grid cells
162 into a land grid cell, or vice-versa if the mean depth of the ocean grid cells is larger than
163 the height of the land grid cells. This is why the land/sea masks differ between CTRL,
164 PD and MTNS in Figure 1, even though their $1/4^\circ \times 1/4^\circ$ parents had exactly the same
165 land-sea mask.

166 One side-effect of having quite distinct land elevations and a lack of oceans in po-
167 lar regions in the Amasia runs (Simulations 04–06) is that snow accumulation can re-
168 sult in the growth of ice sheets akin to that of Earth’s last glacial maximum (LGM) when
169 the Earth was cooler than present day (Argus et al., 2014; Peltier et al., 2015). The in-
170 crease in ice sheet height can influence the climate as there may be substantially more
171 snow accumulation at higher elevations, whereas rain would normally fall at lower ele-
172 vations, due to differences in the lapse rate. To accommodate this reality we ran mod-
173 els with the original Amasia topography and allowed snow to accumulate unhindered.
174 Once these runs reached equilibrium we then used these snow accumulations as the bases
175 for modified production runs. Fifty year climatological averages of snow accumulation
176 (see Figure 2 middle panels) over N. Hemisphere summer months (June, July & August)
177 was used to increase the elevations where necessary. We choose summer months since
178 those minimum northern hemisphere accumulations work well to allow accumulation in
179 the Fall/Winter months and evaporation in the Spring/Summer months. The same pro-
180 cedure is used in the southern hemisphere with 50 year climatological averages over the
181 months of December, January & February. We then perform small areal averages over
182 the highest latitudes to simulate the effect of ice sheet movement. These summer min-
183 ima with snow accumulations are then labeled as permanent ice sheets (with appropri-
184 ate albedo) in the model topography boundary condition files. We adopt this approach
185 because R3D1 does not have a dynamic ice sheet model. An offline ice sheet model would
186 be preferred as is typical in LGM studies (Argus et al., 2014; Peltier et al., 2015) but is
187 beyond the scope of the present exploratory work. Figure S4 includes original topogra-
188 phy plus snow accumulations (denoted as ‘with ice sheets’ in red dotted lines) versus the
189 original topography (blue solid lines). For comparison purposes Figure S4d over plots
190 the LGM data from Argus et al. (2014); Peltier et al. (2015). Recall that the LGM was
191 at a time of lower solar insolation and differing orbital parameters from our future Earth

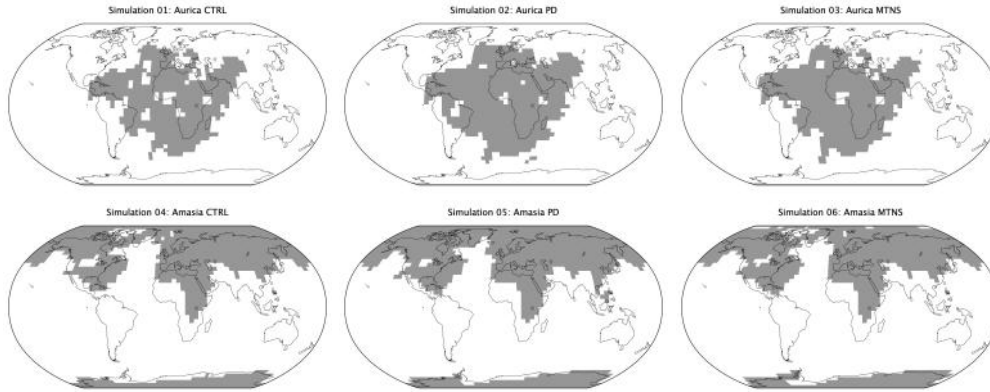


Figure 1. Land (grey) and Ocean/Lake (white) masks used in experiments of Table 1. Present day Earth continental outlines are shown for reference.

192 scenarios. We believe that Figure S4d with the LGM over plotted demonstrates that our
 193 approach to dealing with the ice sheets is not unreasonable.

194 The atmosphere is set to roughly Earth constituents in the year 1850: Nitrogen dom-
 195 inated with 21% Oxygen, 285 ppmv CO₂, 0.3 ppmv N₂O, and 0.79 ppmv CH₄. No aerosols
 196 or Ozone (O₃) are included. For comparison purposes with related work (Way et al., 2018)
 197 we include a modern Earth-like land/sea mask in Simulations 07–09 (Table 1) with these
 198 same atmospheric constituents and a bathtub ocean. The Earth-like land/sea mask used
 199 in these simulations is described in Way et al. (2018) and shown in Figure 8 of that pa-
 200 per. These changes do not greatly effect the mean surface temperature and make the model
 201 more resistant to crash conditions often associated with shallow ocean cells freezing to
 202 the bottom as would be likely in some of the cases herein. To better understand the pos-
 203 sible effects of rotation rate and insolation (given such parameters used in Simulations
 204 01–06) we take the same Earth model (Simulation 07) and slow the rotation rate (Sim-
 205 ulation 08) to be the same as Simulations 01–06, and then increase the insolation (Sim-
 206 ulation 09) to be the same as that of Simulations 01–03 as shown in Table 1 (the higher
 207 of the two insolutions used at 200 and 250 Myr into the future).

208 3 Results

209 Let’s first attempt to disentangle any effects of the slower rotation rate. We do this
 210 by looking at the modern Earth simulations (07–08). Table 1 shows a minimal differ-
 211 ence between the mean surface temperature between our Earth-like world with modern
 212 rotation rate (Sim 07) and the 24.5 hour rotation for Sim 08 that is used by our Aurica
 213 and Amasia simulations (01–06). Planetary Albedo and snow+ice fraction are also nearly
 214 the same. In Figure S0a visible high latitude regional temperature differences ($\sim 5^\circ\text{C}$)
 215 are seen between simulations 07 and 08 even if mean difference is only 0.2°C .

216 Looking at Figure S1 (left panels) we see that simulations 07 and 08 also have very
 217 similar atmospheric, ocean and total meridional transport. If one compares the min and
 218 max stream functions in the tropics in Figure S2a and S2b (simulations 07 and 08) the
 219 differences are small: $-9.1 \times 10^{10} / -9.2 \times 10^9 \sim 1\%$, $1.2 \times 10^{11} / 1.19 \times 10^{11} < 1\%$.

220 Work by Showman et al. (2013, Figure 5) has shown that pole to equator temper-
 221 ature differences should decrease as rotation rate slows. There is a marginal difference
 222 at high northerly latitudes that in fact goes in the opposite direction (Figure S5a). With
 223 the slower rotating Sim 08 having a very small increase in equator-to-pole temperature

224 difference. Note that the Showman et al. (2013) result is for much larger changes in ro-
 225 tation rate. Finally in Figure S5b we plot the eddy energy transport fluxes for simula-
 226 tions 07 and 08. One can see that the mid-latitude eddy energy flux in simulations 07
 227 is slightly larger than that of 08, which would be consistent with that of Showman et al.
 228 (2013), but again the differences are marginal. In the end we find very little evidence that
 229 the additional 30 minutes in the length of day has any effect on the climate dynamics.

230 Next the rotation rate is fixed at 24.5 hours, but the insolation is increased from
 231 simulation 08 ($1361 = \text{W m}^{-2}$) to simulation 09 ($1361 \times 1.0260 = 1396.4 \text{ W m}^{-2}$). The
 232 differences are much clearer here with a $\sim 5^\circ\text{C}$ difference in the mean surface tempera-
 233 ture. The planetary albedo has decreased $\sim 0.5\%$ which tracks the decrease in Snow+Ice
 234 fraction of $\sim 3\%$.

235 It should be noted that previous work has shown that some ancient Earth super-
 236 continent phases, which are comparable to our Aurica simulations 01–03, have had more
 237 arid interiors where weathering effects and CO_2 draw down may have been less efficient
 238 (e.g. Jellinek et al., 2019). This would increase surface temperatures as the balance of
 239 CO_2 would tend to be larger than present day because volcanic outgassing (sources) would
 240 likely remain constant while CO_2 drawdown (sinks) would decrease. However, there are
 241 other climatic effects to consider. For example, the Amasia reconstruction is essentially
 242 an arctic supercontinent with an independent and isolated antarctic continent, mean-
 243 ing both poles are covered by land, and much of that is covered by ice. Amasia is thus
 244 in essence a shift to consolidate the present day domination of northern latitude land masses
 245 even further north.

246 This increase in land masses at northerly latitudes means that there is less ocean
 247 heat transport to melt the ice in the northern hemisphere summers as happens on mod-
 248 ern Earth. Some of the heat differences can be seen in the middle right panel of Figure
 249 S1 where the oceanic meridional transport for the modern Earth simulations (07–09) is
 250 lower at lower latitudes than the Amasia simulations (04–06). This is because there are
 251 no southern low latitude continents (e.g. S. America or S. Africa) and the northern hemi-
 252 sphere continents are now pushed to higher northern latitudes in the Amasia runs. At
 253 the same time in Figure S3 we see that there are active ocean currents in the modern
 254 Earth simulation 09 (bottom panel) near the northern polar regions, but none are pos-
 255 sible in the Amasia simulation 05 run (middle panel).

256 The lack of a northern polar ocean means that more ice resides on land and in lakes
 257 all year round near the north pole, as we see in present day Antarctica, for the three Ama-
 258 sia simulations. This is the well known ice-albedo climate feedback and explains why the
 259 Amasia simulations tend to be cooler than the Aurica ones. Simulation 05 (Amasia PD)
 260 is the coolest of the Amasia simulations. This is because its mean topographic height
 261 is higher (especially near the north polar regions) than in simulations 04 and 06 (See Fig-
 262 ure S4e versus S4d and S4f). The higher relief means simulation 05’s lapse rate is lower
 263 on average and as discussed in the Methods section above it is cooler and hence instead
 264 of rainfall we tend to get snowfall at high latitudes. This fact is also born out in Figure
 265 2 where grid snow+ice fractional amounts are quite high in the northern hemisphere win-
 266 ter months (top center) and southern hemisphere winter months (bottom center) in com-
 267 parison with the modern Earth simulation 09 with the same rotation rate and insola-
 268 tion. Note that in Sim 09 in the lower right panel of Figure 2 has snow coverage on Green-
 269 land in the northern hemisphere summer. This is because we have not adjusted the height
 270 of Greenland assuming it no longer has an ice sheet, so it will accumulate snow and main-
 271 tain it because of its higher altitude. In reality it would likely not be snow covered at
 272 this higher insolation as its topographic height would surely be far lower, although one
 273 would also have to consider the effects of any land rebound height from the removal of
 274 the ice sheets.

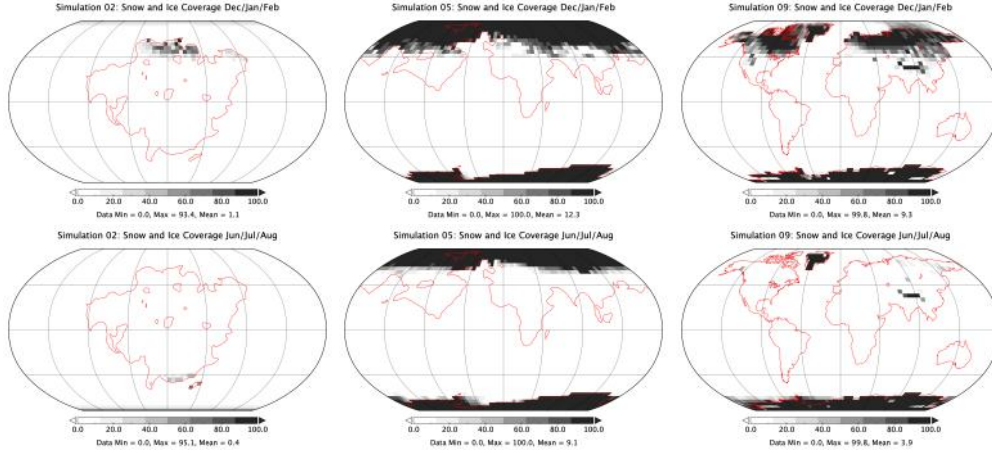


Figure 2. Individual grid cell snow+ice fractional amounts. For simulation 02 (left), simulation 05 (middle) and simulation 09 (right) for a 50-year climatological mean (from the last 50 years of each run) of the months of December, January and February (top) and June, July and August (bottom).

275 It is informative to contrast simulation 02 (Aurica PD) with simulation 05 (Ama-
 276 sia PD). Simulation 02 has land at lower latitudes and uses the same “present day” (PD)
 277 topographic height values for inputs as simulation 05 where the landmasses reside at high
 278 latitudes. In Table 1 we give their mean surface temperatures, planetary albedo, frac-
 279 tional snow & ice coverage and “Habitable Fraction.” The snow & ice coverage as illus-
 280 trated in Figure 2 is clearly related to the planetary albedo and mean surface temper-
 281 atures in Table 1. In Table 1 it is clear that the snow & ice fractions are much higher
 282 for the Amasia runs (04–06) compared to the Aurica runs (01–03), and highest for simu-
 283 lation 05 in particular. Simulation 05 has the highest snow fraction amount correspond-
 284 ing directly to the lowest mean surface temperature of simulations 01–06. This coldest
 285 of the future climates (simulation 05) is nearly 1°C cooler than its corresponding mod-
 286 ern Earth-like simulation (09). We see a lower fractional snow+ice coverage for simu-
 287 lation 09 in Figure 2 versus that of simulation 05. This in turn is related to the fact that
 288 simulation 09 maintains open ocean at northern pole which prevents the year round land
 289 ice seen in simulation 05 (see Figure S3). Hence simulation 05 has 10.2% for the snow+ice
 290 versus a mere 6.4% for simulation 09 at the same rotation and insolation.

291 The general effect of the different land/sea masks between simulations 01–03 and
 292 04–06 and how they compare with the modern Earth-like mask in simulations 07–09 are
 293 seen in Supplementary Material Figures S1 and S2. In Figure S1 The largest differences
 294 are seen in the oceanic meridional transport between the Aurica & Earth-like simula-
 295 tions. The weaker values seen for simulations 01–03 are likely explained by the large low
 296 latitude landmass restricting meridional heat transport over a large longitudinal range
 297 (left middle panel). In the right middle panel of Figure S1 we see how having larger low-
 298 latitude open-ocean increases the oceanic meridional transport for the Amasia simula-
 299 tions (04–06) versus the modern Earth-like simulations (07–09). Total (atmosphere +
 300 ocean) meridional heat transport is very similar between simulations where the only dis-
 301 cernible differences manifest themselves in the larger northern hemisphere transport for
 302 simulations 07–09 versus 01–03, which certainly related to the differences in oceanic trans-
 303 port as discussed above.

304 These general trends are repeated in Figure S2 where we plot the stream function
 305 which indicates the strength of the Hadley circulation. The Aurica (Sim 02) stream func-

306 tion is the weaker of the three as we saw in Figure S1 (lower panels). Looking at Ama-
 307 sia (simulation 05) versus Earth-like (simulation 09) the northern hemisphere values are
 308 very similar, but the southern values differ likely because of the low-mid latitude south
 309 American, south African, and Australian continents in simulation 09 that do not exist
 310 in simulation 05.

311 Work by Spiegel et al. (2008) uses a metric of “climatic habitability” that defines
 312 the amount of surface area of a planet that can host liquid water (e.g., surface temper-
 313 atures in the range $0 < T < 100^{\circ}\text{C}$) at modern Earth atmospheric pressures. In the right-
 314 most column of Table 1 the left values are given using this metric, while the right val-
 315 ues utilize a larger temperature range since life on Earth has been found to thrive in tem-
 316 peratures as high as 121°C and as low as -15°C (e.g. NRC, 2007, Table 3.1). These met-
 317 rics are calculated from 10 year averages (post-equilibrium) of the ground and sea tem-
 318 peratures. From Table 1 it is clear that the Aurica simulations (01–03) have the largest
 319 surface habitable fraction amongst all of the simulations. Since none of our simulations
 320 approach the boiling part of water in any region this is clearly due to the high-latitude
 321 continents found in simulations 04–09 that manifest below freezing temperatures not widely
 322 present in simulations 01–03. Simulations 07–08 have large areas with temperatures be-
 323 low freezing – not unexpected given their lower insulations. What is perhaps most sur-
 324 prising are the values for Amasia PD (simulation 05) which are lower than the Earth sim-
 325 ulations at lower insolation (07–08). As noted above, this is attributable to the large ice
 326 sheets in the high latitude northern and southern hemispheres. Even though simulation
 327 05 has a higher mean surface temperature than simulations 07–08 the higher global snow
 328 fraction appears to influence this metric more than may be expected. However, caution
 329 is warranted when using this habitability metric as other work (e.g. Sparrman, 2021) has
 330 shown that applying the Spiegel et al. (2008) temperature definition in a 3-D sense re-
 331 veals little difference in “climatic habitability” between worlds that otherwise appear quite
 332 climatically distinct. On Earth life has been found to withstand pressures beyond those
 333 of deep sea trenches on Earth (Sharma et al., 2002; Vanlint et al., 2011), at the bottom
 334 of thick ice sheets (Griffiths et al., 2021) and in extremely deep mines (Lollar et al., 2019).
 335 Given enough time life has found a way to fill nearly every ecological niche on the mod-
 336 ern Earth. While a habitability metric like that used herein may be imperfect it can still
 337 provide us a simple way to compare the surface climates of different worlds.

338 4 Conclusions

339 The supercontinents of the future can provide us some guidance on how surface tem-
 340 peratures will increase or decrease depending on how the continents are distributed, with
 341 implications for exoplanet climate and habitability. But there are other factors to con-
 342 sider related to weathering rates and volcanic outgassing (e.g. Jellinek et al., 2019), not
 343 to mention the related role of atmospheric pressure (Gaillard & Scaillet, 2014). We have
 344 also used a fixed atmospheric CO_2 concentration in this paper to avoid introducing a fur-
 345 ther parameter that can add climate variability and, interesting as it would be, explor-
 346 ing the climate with a dynamic carbon cycle is left for future work.

347 The 30 minute increase in the length of day between simulations 07 and 08 appears
 348 to play little to no role in the climate dynamics as there is little discernible difference
 349 in the strength or distribution of the Hadley or eddy transport diagnostics. This implies
 350 the same for simulations 01–06 with their 30 min longer day lengths than present day
 351 Earth.

352 While we discuss the future climate of Earth we do not touch on the future of life.
 353 There are too many uncertainties for us to speculate, but recent work provides some guide-
 354 lines (Mello & Friaça, 2019). The reduced tides during the supercontinent stage (Davies
 355 et al., 2020) will lead to reduced vertical mixing rates, i.e. a reduced vertical diffusiv-
 356 ity in the abyssal ocean (Munk, 1966; Wunsch & Ferrari, 2004). This may have impli-

357 cations for ocean ecosystems, and biodiversity. At the same time it appears that the for-
 358 mation of Pangea had little effect on the global biodiversity of marine animals (Zaffos
 359 & Peters, 2017) and Pangea was in a very weak tidal state (Green et al., 2017).

360 It would be interesting to compare the GCM derived climates for the superconti-
 361 nent at low latitude in the Aurica runs with previous work on Pangea (e.g. Chandler et
 362 al., 1992; Chandler, 1994; Fluteau et al., 2001; Gibbs et al., 2002; Roscher et al., 2011).
 363 Unfortunately it is difficult to make a proper comparison for a number of reasons. First,
 364 all of these previous works use either atmosphere only GCMs (i.e., no ocean) or shallow
 365 mixed layer oceans with either prescribed horizontal heat transport or none at all. Sec-
 366 ondly, unlike Aurica, Pangea spanned not only lower latitudes (like Aurica), but also high
 367 southern latitudes where ice/snow forms easily (e.g. Chandler et al., 1992, Figure 5). Fi-
 368 nally, there are different reconstructions for different time periods and not all are directly
 369 comparable to those we simulate herein. This makes a direct comparison with Pangea
 370 complicated and we leave such an analysis for the future.

371 These new reconstructions may prove useful for exoplanetary where researchers will
 372 have a larger library of topographies and land/sea masks to chose from when estimat-
 373 ing the probability of surface habitability on neighboring worlds.

374 Acknowledgments

375 Thanks goes to Jeffrey Jonas, Linda Sohl and Chris Colose at The Goddard Institute
 376 for Space Studies for their help with the map overlays in Figure 2 and useful discussions.
 377 This work was supported by NASA’s Nexus for Exoplanet System Science (NExSS). Re-
 378 sources supporting this work were provided by the NASA High-End Computing (HEC)
 379 Program through the NASA Center for Climate Simulation (NCCS) at Goddard Space
 380 Flight Center. MJW acknowledges support from the GSFC Sellers Exoplanet Environ-
 381 ments Collaboration (SEEC), which is funded by the NASA Planetary Science Division’s
 382 Internal Scientist Funding Model. HSD acknowledges funding from FCT (ref. UID/GEO/50019/2019—Institut
 383 Dom Luiz; FCT PhD grant ref. PD/BD/135068/2017). JCD acknowledges an FCT Re-
 384 searcher contract, an exploratory project grant ref. IF/00702/2015, and the FCT project
 385 UID/GEO/50019/2021-IDL. JAMG acknowledges funding from NERC, grant NE/S009566/1
 386 (MATCH). All GCM NetCDF data used in this publication can be downloaded from the
 387 NCCS data portal:
 388 https://portal.nccs.nasa.gov/GISS_modelE/ROCKE-3D/publication-supplements/The_climates_of_Earths_next_supe

389 References

- 390 Argus, D. F., Peltier, W. R., Drummond, R., & Moore, A. W. (2014, 05). The
 391 Antarctica component of postglacial rebound model ICE-6G_C (VM5a) based
 392 on GPS positioning, exposure age dating of ice thicknesses, and relative sea
 393 level histories. *Geophysical Journal International*, *198*(1), 537-563. Retrieved
 394 from <https://doi.org/10.1093/gji/ggu140> doi: 10.1093/gji/ggu140
- 395 Barker, P. F. (2001). Scotia sea regional tectonic evolution: implications for mantle
 396 flow and palaeocirculation. *Earth-Science Reviews*, *55*, 1-39.
- 397 Bills, B. G., & Ray, R. D. (1999). Lunar orbital evolution: A synthesis of recent re-
 398 sults. *Geophysical Research Letters*, *26*(19), 3045–3048.
- 399 Chandler, M. A. (1994, 01). Depiction of modern and Pangean deserts: Evaluation
 400 of GCM hydrological diagnostics for paleoclimate studies. In *Pangea:
 401 Paleoclimate, Tectonics, and Sedimentation During Accretion, Zenith, and
 402 Breakup of a Supercontinent*. Geological Society of America. Retrieved from
 403 <https://doi.org/10.1130/SPE288-p117> doi: 10.1130/SPE288-p117
- 404 Chandler, M. A., Rind, D., & Ruedy, R. (1992, 05). Pangaeon climate during
 405 the Early Jurassic: GCM simulations and the sedimentary record of pa-
 406 leoclimate. *GSA Bulletin*, *104*(5), 543-559. Retrieved from <https://>

- doi.org/10.1130/0016-7606(1992)104<0543:PCDTEJ>2.3.CO;2 doi:
10.1130/0016-7606(1992)104<0543:PCDTEJ>2.3.CO;2
- Claire, M. W., Sheets, J., Cohen, M., Ribas, I., Meadows, V. S., & Catling, D. C.
(2012, September). The Evolution of Solar Flux from 0.1 nm to 160 μ m:
Quantitative Estimates for Planetary Studies. *Astrophysical Journal*, 757, 95.
doi: 10.1088/0004-637X/757/1/95
- Collins, M., Knutti, R., Arblaster, J., Dufresne, J.-L., Fichet, T., Friedling-
stein, P., ... Wehner, M. (2013). Long-term Climate Change: Projections,
Commitments and Irreversibility. *Climate Change 2013: The Physical Sci-
ence Basis. Contribution of Working Group I to the Fifth Assessment Re-
port of the Intergovernmental Panel on Climate Change*, 1029–1136. doi:
10.1017/CBO9781107415324.024
- Davies, H. S., Green, J. A. M., & Duarte, J. C. (2018). Back to the future: Test-
ing different scenarios for the next supercontinent gathering. *Global Planetary
Change*, 169, 133–144.
- Davies, H. S., Matthias Green, J. A., & Duarte, J. C. (2020, March). Back to the fu-
ture II: tidal evolution of four supercontinent scenarios. *Earth System Dynam-
ics*, 11(1), 291–299. doi: 10.5194/esd-11-291-2020
- DeConto, R. M., & Pollard, D. (2003). Rapid Cenozoic glaciation of Antarctica in-
duced by declining atmospheric CO₂. *Nature*, 421, 245–249.
- Duarte, J. C., Schellart, W. P., & Rosas, F. M. (2018). The future of Earth's
oceans: Consequences of subduction initiation in the Atlantic and implica-
tions for supercontinent formation. *Geological Magazine*, 155(1), 45–58. doi:
10.1017/S0016756816000716
- Dunne, E. M., Farnsworth, A., Greene, S. E., Lunt, D. J., & Butler, R. J. (2021).
Climatic drivers of latitudinal variation in Late Triassic tetrapod diversity.
Paleontology, 64, 101–117.
- Farnsworth, A., Lunt, D., O'Brien, C., Foster, G., Inglis, G., Markwick, P., ...
Robinson, S. (2019). Climate sensitivity on geological timescales controlled
by non-linear feedbacks and ocean circulation. *Geophysical Research Letters*,
2019GL083574.
- Fluteau, F., Besse, J., Broutin, J., & Ramstein, G. (2001). The late permian cli-
mate. what can be inferred from climate modelling concerning pangea scenar-
ios and hercynian range altitude? *Palaeogeography, Palaeoclimatology, Palaeoe-
cology*, 167(1), 39 - 71. Retrieved from [http://www.sciencedirect.com/
science/article/pii/S0031018200002303](http://www.sciencedirect.com/science/article/pii/S0031018200002303) doi: [https://doi.org/10.1016/
S0031-0182\(00\)00230-3](https://doi.org/10.1016/S0031-0182(00)00230-3)
- Gaillard, F., & Scaillet, B. (2014, Oct). A theoretical framework for volcanic de-
gassing chemistry in a comparative planetology perspective and implications
for planetary atmospheres. *Earth and Planetary Science Letters*, 403, 307–316.
doi: 10.1016/j.epsl.2014.07.009
- Gibbs, M. T., Rees, P. M., Kutzbach, J. E., Ziegler, A. M., Behling, P. J., & Row-
ley, D. B. (2002). Simulations of permian climate and comparisons with
climate-sensitive sediments. *The Journal of Geology*, 110(1), 33–55. Retrieved
from <https://doi.org/10.1086/324204> doi: 10.1086/324204
- Green, J. A. M., Huber, M., Waltham, D., Buzan, J., & Wells, M. (2017). Ex-
plicitly modelled deep-time tidal dissipation and its implication for lun-
ar history. *Earth and Planetary Science Letters*, 461, 46–53. doi:
10.1016/j.epsl.2016.12.038
- Green, J. A. M., Molloy, J. L., Davies, H. S., & Duarte, J. C. (2018). Is there a tec-
tonically driven supertidal cycle? *Geophysical Research Letters*, 45, 3568–3576.
doi: 10.1002/2017GL076695
- Griffiths, H. J., Anker, P., Linse, K., Maxwell, J., Post, A. L., Stevens, C., ...
Smith, J. A. (2021). Breaking all the rules: The first recorded hard sub-
strate sessile benthic community far beneath an antarctic ice shelf. *Frontiers*

- 462 *in Marine Science*, 8, 76. Retrieved from [https://www.frontiersin.org/](https://www.frontiersin.org/article/10.3389/fmars.2021.642040)
 463 [article/10.3389/fmars.2021.642040](https://www.frontiersin.org/article/10.3389/fmars.2021.642040) doi: 10.3389/fmars.2021.642040
- 464 Huber, B. T., MacLeod, K. G., Watkins, D. K., & Coffin, M. F. (2018). The rise and
 465 fall of the cretaceous hot greenhouse climate. *Global and Planetary Change*,
 466 167, 1 - 23. doi: <https://doi.org/10.1016/j.gloplacha.2018.04.004>
- 467 Jellinek, M., Lenardic, A., & Pierrehumbert, R. (2019, 06). Ice, fire or fizzle: The
 468 climate footprint of earth's supercontinental cycles. *Geochemistry, Geophysics,*
 469 *Geosystems*, 10.
- 470 Krijgsman, W., Hilgen, F. J., Raffi, I., Sierro, F. J., & Wilson, D. S. (1999).
 471 Chronology, causes and progression of the Messinian salinity crisis. *Nature*,
 472 400(6745), 652–655.
- 473 Lollar, G. S., Warr, O., Telling, J., Osburn, M. R., & Lollar, B. S. (2019). 'follow
 474 the water': Hydrogeochemical constraints on microbial investigations 2.4 km
 475 below surface at the kidd creek deep fluid and deep life observatory. *Geomicro-*
 476 *biology Journal*, 36(10), 859-872. Retrieved from [https://doi.org/10.1080/](https://doi.org/10.1080/01490451.2019.1641770)
 477 [01490451.2019.1641770](https://doi.org/10.1080/01490451.2019.1641770) doi: 10.1080/01490451.2019.1641770
- 478 Mello, F. d. S., & Friça, A. C. S. (2019). The end of life on earth is not the end
 479 of the world: converging to an estimate of life span of the biosphere? *Interna-*
 480 *tional Journal of Astrobiology*, 1-18. doi: 10.1017/S1473550419000120
- 481 Mitchell, R. N., Kilian, T. M., & Evans, D. A. D. (2012). Supercontinent cycles
 482 and the calculation of absolute palaeolongitude in deep time. *Nature*, 482,
 483 208–211.
- 484 Montes, C., Cardona, A., Jaramillo, C., Pardo, A., Silva, J. C., Valencia, V., ...
 485 Niño, H. (2015). Middle Miocene closure of the Central American Seaway.
 486 *Science*, 348, 226–229.
- 487 Munk, W. H. (1966). Abyssal recipes. *Deep-Sea Research and Oceanographic Ab-*
 488 *stracts*, 13(4), 707–730. doi: 10.1016/0011-7471(66)90602-4
- 489 NRC. (2007). *The limits of organic life in planetary systems*. Washington, DC:
 490 The National Academies Press. Retrieved from [https://www.nap.edu/](https://www.nap.edu/catalog/11919/the-limits-of-organic-life-in-planetary-systems)
 491 [catalog/11919/the-limits-of-organic-life-in-planetary-systems](https://www.nap.edu/catalog/11919/the-limits-of-organic-life-in-planetary-systems) doi:
 492 10.17226/11919
- 493 Parrish, J. (1993, 03). Climate of the supercontinent pangea. *Journal of Geology*,
 494 101, 215-233. doi: 10.1086/648217
- 495 Pastor-Galán, D., Nance, R. D., Murphy, J. B., & Spencer, C. J. (2019). Su-
 496 percontinents: myths, mysteries, and milestones. *Geological Society,*
 497 *London, Special Publications*, 470(1), 39–64. Retrieved from [https://](https://sp.lyellcollection.org/content/470/1/39)
 498 sp.lyellcollection.org/content/470/1/39 doi: 10.1144/SP470.16
- 499 Peltier, W. R., Argus, D. F., & Drummond, R. (2015). Space geodesy constrains
 500 ice age terminal deglaciation: The global ice-6g_c (vm5a) model. *Journal of*
 501 *Geophysical Research: Solid Earth*, 120(1), 450-487. Retrieved from [https://](https://agupubs.onlinelibrary.wiley.com/doi/abs/10.1002/2014JB011176)
 502 agupubs.onlinelibrary.wiley.com/doi/abs/10.1002/2014JB011176 doi:
 503 <https://doi.org/10.1002/2014JB011176>
- 504 Pierrehumbert, R. T., Abbot, D. S., Voigt, A., & Koll, D. (2011). Climate of the
 505 neoproterozoic. *Annual Reviews of Earth and Planetary Sciences*, 417-460.
- 506 Roscher, M., Stordal, F., & Svensen, H. (2011). The effect of global warming and
 507 global cooling on the distribution of the latest permian climate zones. *Palaeo-*
 508 *geography, Palaeoclimatology, Palaeoecology*, 309(3), 186 - 200. Retrieved from
 509 <http://www.sciencedirect.com/science/article/pii/S0031018211002987>
 510 doi: <https://doi.org/10.1016/j.palaeo.2011.05.042>
- 511 Schmittner, A., Silva, T. A. M., Fraedrich, K., Kirk, E., & Lunkeit, F. (2011). Ef-
 512 fects of Mountains and Ice Sheets on Global Ocean Circulation. *Journal of Cli-*
 513 *mate*, 24, 2814–2829.
- 514 Sharma, A., Scott, J. H., Cody, G. D., Fogel, M. L., Hazen, R. M., Hemley, R. J., &
 515 Huntress, W. T. (2002). Microbial activity at gigapascal pressures. *Science*,
 516 295(5559), 1514–1516. Retrieved from <https://science.sciencemag.org/>

- 517 content/295/5559/1514 doi: 10.1126/science.1068018
- 518 Showman, A. P., Wordsworth, R. D., Merlis, T. M., & Kaspi, Y. (2013). Atmo-
 519 spheric Circulation of Terrestrial Exoplanets. In S. J. Mackwell, A. A. Simon-
 520 Miller, J. W. Harder, & M. A. Bullock (Eds.), *Comparative climatology of*
 521 *terrestrial planets* (p. 277). doi: 10.2458/azu_uapress_9780816530595-ch12
- 522 Smith, A. G., & Pickering, K. T. (2003). Oceanic gateways as a critical factor to ini-
 523 tiate icehouse Earth. *Journal of the Geological Society, London, 160*, 337-340.
- 524 Sparrman, V. (2021). Estimates of fractional habitability for proxima centauri b
 525 using a 3d gcm. *Dissertation, 1*, 1–16. Retrieved from [http://urn.kb.se/
 526 resolve?urn=urn:nbn:se:uu:diva-415703](http://urn.kb.se/resolve?urn=urn:nbn:se:uu:diva-415703)
- 527 Spiegel, D. S., Menou, K., & Scharf, C. A. (2008, Jul). Habitable Climates. *Astro-
 528 physical Journal, 681*(2), 1609-1623. doi: 10.1086/588089
- 529 Tada, R., Zheng, H., & Clift, P. D. (2016). Evolution and variability of the Asian
 530 monsoon and its potential linkage with uplift of the Himalaya and Tibetan
 531 Plateau. *Progress in Earth and Planetary Science, 3*, 4.
- 532 Vanlint, D., Hazeel, R., Bailey, E., Meersman, F., McMillan, P., Michiels, C., &
 533 Aertsen, A. (2011, 12). Rapid acquisition of gigapascal-high-pressure resistance
 534 by escherichia coli. *mBio, 2*, e00130-10. doi: 10.1128/mBio.00130-10
- 535 Way, M. J., Aleinov, I., Amundsen, D. S., Chandler, M. A., Clune, T. L., Del
 536 Genio, A. D., ... Tsigaridis, K. (2017, July). Resolving Orbital and Cli-
 537 mate Keys of Earth and Extraterrestrial Environments with Dynamics
 538 (ROCKE-3D) 1.0: A General Circulation Model for Simulating the Climates
 539 of Rocky Planets. *Astrophysical Journal Supplement Series, 231*, 12. doi:
 540 10.3847/1538-4365/aa7a06
- 541 Way, M. J., Del Genio, A. D., Aleinov, I., Clune, T. L., Robinson, T. D., Kelly, M.,
 542 & Kiang, N. Y. (2018). Climates of warm earth-like planets. i. 3d model
 543 simulations. *The Astrophysical Journal Supplement Series, 239*(2).
- 544 Wunsch, C., & Ferrari, R. (2004). Vertical mixing, energy, and the general circula-
 545 tion of the oceans. *Annual Review of Fluid Mechanics, 36*(1), 281–314.
- 546 Yang, J., Boué, G., Fabrycky, D. C., & Abbot, D. S. (2014). Strong dependence of
 547 the inner edge of the habitable zone on planetary rotation rate. *Astrophysical
 548 Journal Letters, 787*(1). doi: 10.1088/2041-8205/787/1/L2
- 549 Yoshida, M. (2016, 09). Formation of a future supercontinent through plate mo-
 550 tion-driven flow coupled with mantle downwelling flow. *Geology, 44*(9), 755-
 551 758. Retrieved from <https://doi.org/10.1130/G38025.1> doi: 10.1130/
 552 G38025.1
- 553 Yoshida, M., & Santosh, M. (2018). Voyage of the indian subcontinent since pangea
 554 breakup and driving force of supercontinent cycles: Insights on dynamics from
 555 numerical modeling. *Geoscience Frontiers, 9*(5), 1279 - 1292. Retrieved from
 556 <http://www.sciencedirect.com/science/article/pii/S1674987117301536>
 557 (SPECIAL ISSUE: Frontiers in geoscience:A tribute to Prof. Xuanxue Mo)
 558 doi: <https://doi.org/10.1016/j.gsf.2017.09.001>
- 559 Zaffos, S., A. Finneganb, & Peters, S. E. (2017). Plate tectonic regulation of
 560 global marine animal diversity. *PNAS, 114*(22), 5653–5658. Retrieved from
 561 <https://www.pnas.org/content/114/22/5653> doi: [https://doi.org/10.1073/
 562 pnas.1702297114](https://doi.org/10.1073/pnas.1702297114)